

# Development of Low Temperature Catalysts for an Integrated Ammonia PEM Fuel Cell

Hill, Alfred

*Award date:*
2017

*Awarding institution:*
University of Bath

# Development of Low Temperature Catalysts for an Integrated Ammonia PEM Fuel Cell

Alfred Hill

A thesis submitted for the degree of Doctor of Philosophy

University of Bath
Department of Chemical Engineering

November 2014

Supervisors:

Dr Laura Torrente-Murciano
Prof. Frank Marken
Dr Pejman Iravani

## COPYRIGHT

# Contents

# List of Figures

# List of Tables

# Acknowledgements

I would like to thank the EPSRC and the Doctoral Training Centre in Sustainable Chemical Technologies for providing funding, support and training as part of my integrated PhD. In particular Dr Janet Scott for guidance on PhD selection and especially Sheila Apps who made all sorts of problems go away. My supervisors have provided support throughout this project and I am particularly indepted to my lead supervisor for her being available for advice and guidance throughout this project. The support of my fellow students within the catalysis and process integration group have made this project a pleasure to undertake and the sharing of best practices and camaraderie in the group made the journey easier.

Special thanks are due to Dr Davide Mattia for providing access to the ultra-high vacuum furnace as well as lots of help and advice and the Plucinski group who have kindly allowed access to gas analytical equipment and also the research complex at Harwell (RCaH) who have provided access to their electron microscopy suite; I note the assistance provided by Andrew Allen and Jennifer Holter in this regard. John Mitchells and Ursula Potter provided a great deal of expertise and assistance during microscopy experiments. Technical support within the Chemical Engineering Department at Bath have been invaluable in enabling me to construct and commission the ammonia decomposition catalyst testing rig and have enabled me to surmount numerous challenges encountered in this project.

Great appreciation is due to Sam Capper and Husni Abboushi, Masters students who undertook some of the experimental work presented in Chapter 5 as well as preliminary work that formed background to the sustainability and feasibility study in chapter 6. All of their work was done under the direct supervision of this author and it is identified as such in the locations where it is used. They were exceptional students who brought intelligence, curiosity and application to their work in the lab.

# Abstract

It is proposed that an integrated ammonia-PEM fuel cell could unlock the potential of ammonia to act as a high capacity chemical hydrogen storage vector and enable renewable energy to be delivered effectively to road transport applications.

Catalysts are developed for low temperature ammonia decomposition with activity from 450 $K$ (ruthenium and cesium on graphitised carbon nanotubes). Results strongly suggest that the cesium is present on the surface and close proximity to ruthenium nanoparticles and that it produces activity in ruthenium by donation of electrons.

The activity of sustainable cobalt for ammonia decomposition is shown to be a function of particle size and is more active on microporous carbon supports compared to mesoporous ones. Unlike ruthenium, activity for cobalt was not influenced by the degree of surface graphitic nature and cobalt supported on microporous carbon approached the activity of ruthenium on the same support.

In accordance with the sustainable objectives of this thesis, a case-study on the sustainability of ammonia as a sustainable hydrogen storage vector was undertaken. In this scheme, hydrogen produced from renewable electricity by electrolysis is converted to ammonia by the Haber-Bosch process and then converted back to deliver pure hydrogen at the point of use. The energy efficiency and carbon footprint fell short of targets set by the US Department of Energy and the UK Department for Transport, the biggest impact was the production of hydrogen by electrolysis and not the Haber-Bosch process which accounts for only 9 % of total energy losses.

To assess the feasibility of the ammonia-PEM fuel cell, a conceptual design was undertaken to quantify the palladium membrane size and catalyst quantity required for a typical road transport vehicle. The predicted quantity of palladium was excessive and future work must consider improvements to membrane technology.

# Dissemination of Work from this Thesis

## Publications

- Results from this thesis have been published in the following journal article. Hill, A. and Torrente Murciano, L. (2014) "In-situ H2 production via low temperature decomposition of ammonia : Insights into the role of cesium as a promoter". International Journal of Hydrogen Energy, 39 (15). pp. 7646-7654. ISSN 0360-3199
- Results from this thesis have been accepted for publication in the article titled: "Low Temperature H2 production from ammonia using ruthenium based catalysts: synergetic effect of promoters and support." Applied Catalysis B: Environmental, 172-173 (2015), pp129-135.
- This author contributed to the following mini-review: Puertolas, B., Hill, A.K., Garcia, T., Torrente-Murciano, L. (In Press). In-situ synthesis of hydrogen peroxide in tandem with selective oxidation reactions: A mini-review. Catalysis Today, DOI: 10.1016/j.cattod.2014.03.054.

## Presentations

The following presentations were made by the author comprising work from this thesis.

- Oral presentation entitled: *"The Role of Cesium in Ammonia Decomposition"* was presented at Europacat XIV (oral and poster), Lyon, September 2014.
- Oral presentation entitled: *"The Role of Cesium in Ammonia Decomposition"* at Hydrogen: A Vital Element for our Sustainable Future. A symposium for

the Centre for Sustainable Chemical Technologies at the University of Bath, 29th January 2013.

- Oral presentation entitled: *"Developing Low Temperature Activity for Ammonia Decomposition in Heterogeneous Catalysts"* at Sustainable Industrial Catalysis. A symposium for the Centre for Sustainable Chemical Technologies at the University of Bath, 30th January 2014.

- A poster presentation entitled: *"Design of Low Temperature Catalysts for H2 Release from Ammonia"* at Chem Eng Day, University of Manchester, 7-8 April, 2014.

# Chapter 1

# Introduction

The fifth assessment by the international panel on climate change (IPCC) has further strengthened the link between anthropogenic carbon dioxide emissions and climate change [2]. In order to minimise the future impact of climate change, researchers are urged to develop carbon free energy vectors to cater for the full range of existing energy demands including portable applications such as road transport.

The provision of sustainable energy to mobile applications is significantly more challenging than providing it to fixed locations where the existing electrical networks can be utilised. Also, whereas buses and trains can be electrified using fixed wires, this is not practical for road transport vehicles that can range over a much broader area. If this problem is to be addressed, the development of new technologies is required to replace existing fossil fuels.

There are two main technologies competing to provide clean energy to road transport vehicles: electrical energy, stored in batteries for use with electric motors and hydrogen powered polymer exchange membrane (PEM) fuel cells which generate the electrical energy from the stored chemical energy of hydrogen. Although battery technologies have become widely available, they are still expensive to manufacture, have a small driving range between charges and require long periods of time to recharge which makes them unsuitable for most commercial applications. Hydrogen London chose to use hydrogen hybrid fuel cell buses rather than a battery storage technology because the fast refuelling rate of pressurised hydrogen maximised the proportion of buses in service at a given time [3]. Unlike urban buses which tend to remain in close proximity to re-fuelling locations, the success of hydrogen vehicles has been restricted because no technologies have been found to safely store sufficient quantities of hydrogen for longer range vehicles [4]. New ideas are required to enable greater hydrogen storage capacity and to release the latent potential of hydrogen fuel cell vehicles.

Hydrogen storage technologies have been in development for many years; the most popular technologies include high pressure (200 - 700 *bar*), cryogenic, adsorption in porous carbons or metal-organic frameworks or a combination of these technologies [5, 6]. Despite many advancements, the technologies available fall substantially short of the targets for hydrogen storage density set by the US Department of Energy (DoE) [7]. It is in response to this shortfall in hydrogen storage density that this thesis sets out to consider ammonia as a chemical hydrogen storage vector.

If ammonia is to be used as an effective hydrogen storage vector, then it should be considered as part of a carbon-free energy system. Sustainable hydrogen, produced using electricity from renewable generation, can be converted to ammonia by the Haber-Bosch process, stored and converted back to hydrogen at the point of use for mobile PEM fuel cell applications. This proposed system can be compared directly to conventional physical hydrogen storage, but to be compared to other portable renewable energy systems such as batteries, the boundaries of the system must be enlarged to consider hydrogen production by electrolysis. It is not envisaged that the hydrogen would be sourced from methane because this would generate substantial carbon dioxide emissions and undermine the sustainable objectives for this concept.

Ammonia is of great interest as a hydrogen storage medium; it has a very high hydrogen storage capacity and it can be easily stored and transported. The ammonia molecule contains 17.6 wt.% hydrogen. It can be stored as a liquid at around 10 *bar* and at ambient temperature, far simpler and cheaper than the extremely high pressure containment currently required for gaseous hydrogen storage [8]. Although ammonia has the potential to solve the problem of high capacity hydrogen storage, it also presents a number of potential problems which must be addressed.

The first challenges presented by the use of ammonia as a hydrogen storage medium is around energy efficiency. The conversion of hydrogen to ammonia for storage and its subsequent conversion back to hydrogen will result in the loss of energy. These energy losses must be examined thoroughly to demonstrate the viability of this proposal. The decomposition of ammonia typically requires temperatures around 700 $K$ to generate significant kinetic activity and to reach an equilibrium conversion of around 99 %; the reduction of this temperature is one of the key challenges identified by the US DoE to minimise the energy losses and lower the cost for ammonia decomposition technology [9]. There are also safety considerations related to the toxicity and flammability of ammonia and finally, ammonia is a poison to the PEM fuel cell nafion™ membrane [10].

## 1.1 Objectives

The objectives of this project are directly related to the challenges presented by the storage of hydrogen in ammonia and are summarised as follows:

1. Assess the sustainability of ammonia as a hydrogen storage medium. This considers the energy losses of the system and compares them to appropriate benchmarks.

2. Assess the practicality of an integrated ammonia decomposition and hydrogen purification system for on-board hydrogen production.

3. Develop catalysts with low temperature activity for ammonia decomposition (close to the PEM fuel cell temperature of 370 $K$) and improve the understanding of the key factors that influence activity at low temperature.

## 1.2 Impact

Addressing these challenges can have impact not just on catalysts for ammonia decomposition but it also has wider applicability. The investigation into low temperature activity in catalysis requires a study of fundamental aspects of catalytic activity and design and accordingly, the outcomes of this work have wider significance. The design of an integrated ammonia-PEM fuel cell requires a consideration of membrane technologies for the provision of pure hydrogen for the fuel cell. Addressing the questions of sustainability of integrated ammonia-PEM fuel cell involves a study of energy efficiency and a consideration of the wider life cycle implications.

## 1.3 Structure of Thesis

The thesis is structured into the following chapters:

- Chapter 1: Introduction.

- Chapter 2: Literature Review. *This summarises the state-of-the-art in the areas of relevance to this work including understanding of the sustainability aspects; fuel cell technolog; catalyst design synthesis and characterisation and membrane technology.*

- Chapter 3: Experimental. *This section details the main experimental techniques used in this work.*

- Chapter 4: Development of Ruthenium Catalysts for Low Temperature Generation of Hydrogen from Ammonia. *This chapter comprises the development of catalysts for low temperature activity for ammonia decomposition. The catalysts combined ruthenium as active metal, cesium as promoter and carbon nanotubes as the catalytic support.*

- Chapter 5: Development of Sustainable Catalysts for the Decomposition of Ammonia. *This chapter identifies and develops the potential of more sustainable metals than ruthenium for ammonia decomposition: it considers the relationship between the metal and the catalyst support as well as the possibilities of enhancing activity through bi-metallic catalyst systems.*

- Chapter 6: The Sustainable Case for Ammonia as a Chemical Storage Vector for Hydrogen. *This chapter presents a conceptual design for an integrated ammonia-PEM fuel cell and a sustainability analysis of using ammonia as a hydrogen storage vector, it includes a comparison with benchmark targets set by the US DoE and the UK Department for Transport (DfT).*

- Chapter 7: Conclusions and Further Work.

# Chapter 2

# Literature Review

## 2.1 Introduction

The objectives of this project are to investigate the sustainability of using ammonia as a hydrogen storage vector with the primary focus on the development of catalysts for the low temperature decomposition of ammonia. In consideration of the practicality of on-board hydrogen generation from ammonia, membrane reactor technologies are investigated to assess whether it can improve the effective conversion when operating under thermodynamic equilibrium limitations. This literature review evaluates the current progress in addressing these problems and identifies the areas where further work is required.

## 2.2 The Sustainability of Ammonia as a Hydrogen Storage Medium

This section addresses the sustainability aspects related to the use of ammonia as a hydrogen storage vector. To do this, it is necessary to consider the capacity that ammonia has for hydrogen storage, the practicalities of the hydrogen - ammonia - hydrogen cycle and the safety considerations around flammability and toxicity.

The capacity of ammonia to act as a hydrogen storage vector was illustrated by Klerke *et al.* [11] who showed that the volume required to store 10 kg of hydrogen as liquid ammonia was only 13 % of that occupied by gaseous hydrogen at 200 *bar* and only 66 % of the volume occupied by liquid hydrogen (Figure 2.1). Clearly ammonia has a storage potential for hydrogen that vastly outstrips conventional physical hydrogen storage methods.

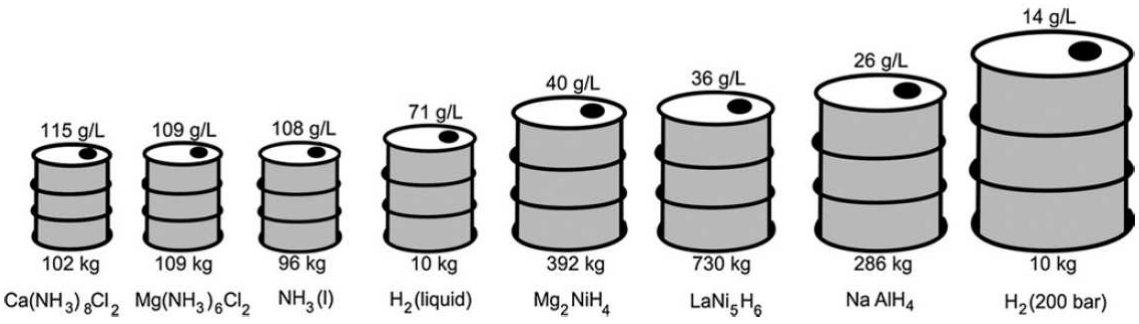


**Figure 2.1:** Depiction of the hydrogen storage densities of a range of storage media with 10 $kg$ of hydrogen. Directly reproduced from Klerke *et al.* [11] with permission from the Royal Society of Chemistry.

Another advantage of using ammonia as a fuel is that it is already widely stored and distributed. Ammonia synthesis is the oldest chemical industrial process and there is an existing infrastructure. For example, the USA has 4,950 $km$ of ammonia pipelines [9]. In small quantities below 1,500 $t$ it is typically stored at 10 $bar$ and in larger quantities it is liquefied at 238 $K$ [11].

Similarly to ammonia storage, the technical challenges around the production of ammonia are also well understood. However, most ammonia is generated using hydrogen derived from methane. For a carbon free future, ammonia must be generated from renewably derived hydrogen and the processes for achieving this require further study.

Although it is established that generation and storage of ammonia is technically feasible, the energetic efficiency of doing so is not well understood. If ammonia is to be used for hydrogen storage in an energy scarce world then any significant energy losses incurred would be problematic. In an attempt to better understand this aspect, Schuth *et al.* [12] considered the energy cost of generating ammonia from methane. It was found that the typical ammonia synthesis process has an overall energy efficiency of 75 % calculated as the chemical energy of the products as a ratio of the total energy of feed materials and energy inputs. This finding suggests that while conventional ammonia synthesis is not the most efficient of processes, the analysis does not address a carbon free scenario and further work is required to estimate the carbon free ammonia generation energy cost.

In their review on hydrogen storage in ammonia, Schuth *et al.* [12] identified insufficient catalyst activity as being the most important area for technical improvement. This view is shared by the US Department of Energy (DoE) [9] who found that the efficiency of present ammonia decomposition reactor and catalyst systems must be increased by around two orders of magnitude. They recommended that future

research should focus upon alignment with the conditions available on-board a PEM fuel-cell vehicle. PEM fuel cells typically operate at around 370 K [13] suggesting that an ammonia decomposition reactor would need to operate at a similar temperature.

The safety issues related to the use of ammonia were of concern to Schuth *et al.* [12]. It was believed that despite the feasibility of ammonia transportation and storage, the toxicity and smell of ammonia would prevent its wider utilisation in road transport vehicles. They concluded that ammonia as a hydrogen storage medium would be viable for niche applications that required a supply of hydrogen. The authors also highlight the work on metal ammine complexes by Klerke *et al.* [11], notably $Mg(NH_3)_6Cl_2$ and $Ca(NH_3)_8Cl_2$ which can be safely handled and releases ammonia upon heating which would alleviate the problems of toxicity by reducing the ammonia vapour pressure by many orders of magnitude. They can be regenerated with fresh ammonia and would seem to address many of the safety concerns around ammonia handling [11].

With further regard to the safety aspects around the use of ammonia, Klerke *et al.* [11] evaluated the relative toxicity of ammonia, which they define as the vapour pressure divided by the concentration at which the material is immediately dangerous to life or health (IDLH). They found that the IDLH for ammonia was three orders of magnitude higher than for gasoline and methanol. Although this is a significant problem, they also suggest that it can be remedied by storage in metal ammine solid tablets which reduces the IDLH to less than 1/10th that of gasoline. Klerke *et al.* [11] also considered the explosive limits of ammonia in air compared to other fuels. The range at which the concentration in air that would be required for an ammonia explosion are far higher than gasoline, 16 - 25 *vol.*% as opposed to 1.1 - 3.3 *vol.*%. This means that a small ammonia leak presents a much reduced explosion risk than a similar gasoline leak as any leak will quickly dilute below the lower explosive limit. Ammonia also compares favourably to hydrogen which presents the widest risk of explosion from 18.3 - 59 *vol.*%. The US DoE reviewed the safety case for using ammonia as a widespread hydrogen storage medium and recommended that more research should be directed towards lightweight indestructible tanks, cheap ammonia detectors and a better understanding of the health effects [9].

It can be concluded that the explosion and flammability risks presented by ammonia are similar to or less than those presented by current liquid fossil fuels and are much less significant than those presented by hydrogen. Of greater concern is the issue of toxicity and it is suggested that much more effort should be expended in the research of enhanced containment systems to sufficiently mitigate this risk. The use of metal ammines would also appear to greatly offset this toxicity risk.

The toxicity issues associated with ammonia can be compared to a historic example where a toxic and flammable gas was piped into the homes of the general population. Up until the 1970s, town gas consisting of hydrogen and highly toxic carbon monoxide was widely used as a domestic energy source until it was superseded by the safer and more energy rich natural gas. That people were prepared to accept the toxic town gas into their homes illustrates the public acceptance of risk that a populace will accept in exchange for the necessities of life such as heating and cooking. The toxicity of ammonia may appear unpalatable now in the context of widely available and safer carbon based fuels, but it may look far more acceptable in a future carbon free world.

In conclusion, the sustainable use of ammonia as a hydrogen storage medium depends firstly upon the development of better catalysts to enable a faster rate of reaction at lower temperature. Secondly, the current understanding of the lifecycle energy costs of ammonia as a sustainable hydrogen storage medium are poorly understood and more work is required to consider the energy costs of this system. Finally, the toxicity hazard posed by ammonia is a substantial problem and although potential solutions have been highlighted here, it is clear that more work is required.

## 2.3 Alternative Ammonia Fuel Cell Technologies

Ammonia does not need to be considered solely as a hydrogen vector, it can also be considered as a direct fuel based on its chemical energy content. There are fuel cell technologies available that accept ammonia as a direct fuel, thus eliminating the ammonia decomposition and hydrogen purification steps. In this section these technologies will be reviewed and considered as alternatives to the hydrogen from ammonia PEM fuel cell proposal.

All fuel cells convert chemical energy into electrical energy via chemical reaction, the fuel is introduced at the anode and oxygen or air at the cathode. The fuel cells differ in regards to the method for ion transportation. Schematics of three example fuel cell technologies are shown in Figure 2.2. The most common type, the proton exchange membrane (PEM) fuel cell, transports protons from the anode to the cathode where catalytic oxidation occurs. This type of design is inherently more fuel-selective because the fuel must be convertible into hydrogen as the precursor to proton transfer, it is for this reason that high purity hydrogen is generally used as fuel in PEM fuel cells. A number of fuel cell technologies exist that can accept ammonia as a direct fuel, these facilitate transfer of the oxidising group via the membrane to oxidise the fuel directly at the anode. Examples shown here are the

alkali exchange membrane fuel cell and the solid oxide fuel cell which have membrane technologies for the transfer of $OH^-$ and $O^{2-}$ ions respectively.

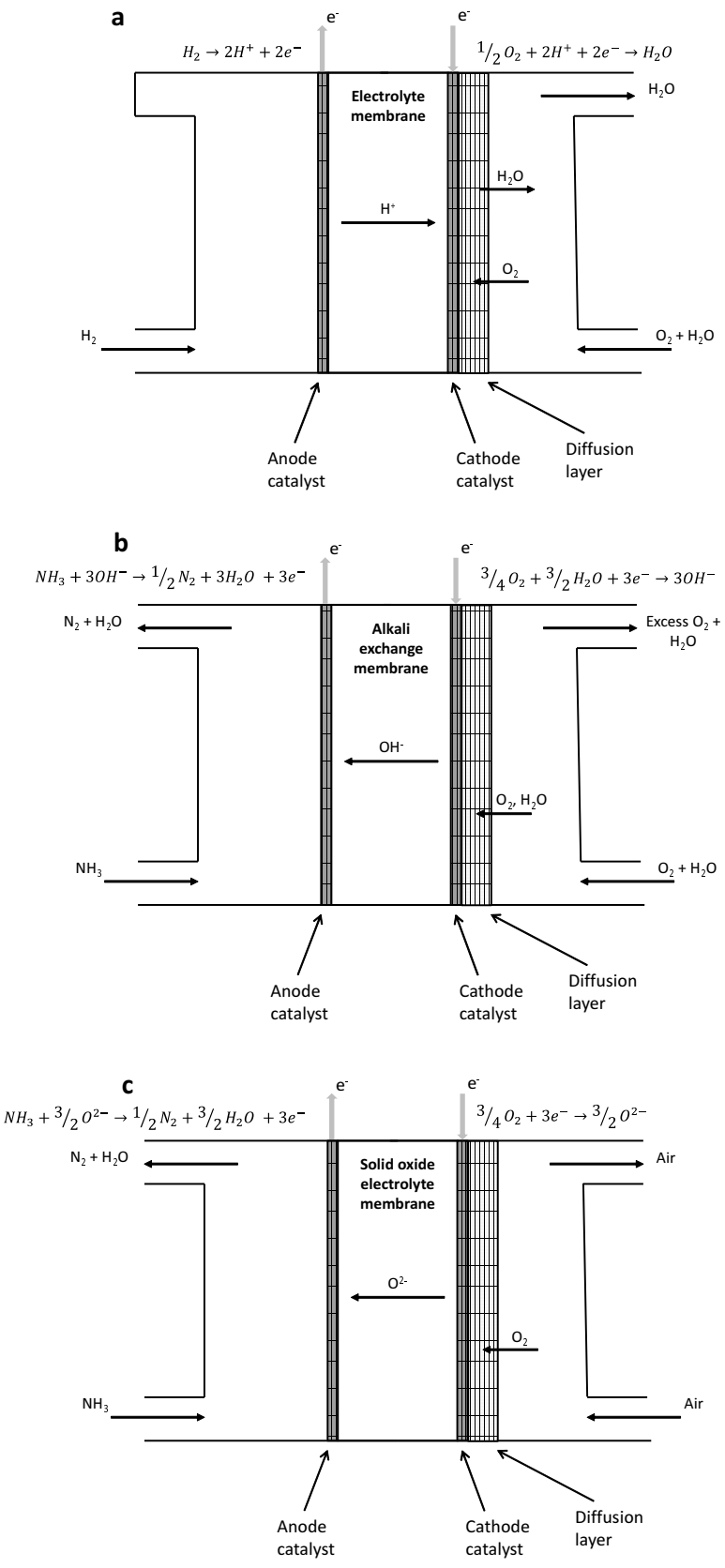


**Figure 2.2:** Schematics of different fuel cell technologies. **a** - PEM fuel cell, **b** - alkali exchange membrane fuel cell and **c** - oxide conducting solid oxide fuel cell.

The performance of a selection of fuel cell technologies is briefly summarised in Table 2.1. Operating temperature and power density information is included for the hydrogen fed PEM, phosphoric acid and proton solid oxide fuel cells as well as the ammonia fed alkaline and oxide solid oxide fuel cells.

PEM fuel cells have the greatest commercial viability as they exhibit high efficiency (40 - 60 % rising to a theoretical maximum of 83.0 %) and the lowest materials cost [13]. PEM fuel cell electrodes typically consist of platinum supported on carbon, which has excellent activity for the hydrogen and oxygen dissociation reactions. Use of platinum has reduced to 0.2 $mg/cm^2$ which enables costs to be kept reasonably low [14]. Despite the high efficiency and low cost of PEM fuel cells, implementation of ammonia - PEM technologies has been held back because of ammonia poisoning of the Nafion™ polymer membrane at ammonia concentrations greater than 0.1 *ppm* [15]. Equilibrium conversion for ammonia decomposition increases as a function of temperature but even at 1173 $K$ the ammonia concentration is still 150 *ppm* [9], a separation step must be used to achieve the 0.1 *ppm* figure. Furthermore, the high temperature that all catalytic systems require in order to decompose ammonia into hydrogen (typically above 570 $K$) is substantially more than the maximum PEM fuel cell operating temperature of around 370 $K$ [13]. Significant advances are required in reactor, separator and catalyst technologies to realise the ammonia - PEM fuel cell.

Phosphoric acid fuel cells also operate by the transfer of protons and although they show some promise, they offer no advantage in fuel flexibility over the PEM fuel cell [16].

Fuel cells that transport the oxidising anion species from the cathode to the anode enable far greater fuel flexibility and there are a number of examples in which ammonia has been used as a direct fuel. One example is the alkaline fuel cell that transfers $OH^-$ ions. This technology can achieve a maximum efficiency of 88.7 % compared to 83.0 % for a PEM fuel cell [13]. They are often made using conventional bases such as KOH but they are readily deactivated by carbon dioxide which prevents their use with air as an oxidant. This limitation was overcome by Lan *et al.* [16] who developed a membrane consisting of quaternary ammonium hydroxide linked to a polymer that is resistant to carbon dioxide. Some direct ammonia fuel cells have been developed using alkaline anion exchange membranes [17]. Although they have demonstrated the feasibility of this method, the power density achieved is an order of magnitude lower than PEM and solid oxide alternatives (see Figure 2.1).

Another type of anion transfer fuel cell that can accept ammonia as a fuel is the solid oxide fuel cell in which $O^{2-}$ ions are transferred to the anode. Proton conducting

solid oxide fuel cells have a higher efficiency compared to anion transfer but they cannot process the same range of fuels [18]. Solid oxide fuel cells have not been widely implemented as a transport solution due to cost, long startup time, high operating temperature and brittleness of the ceramic components [17]. The high operating temperature means that operating efficiencies are likely to be lower than other fuel cell technologies due to system thermal losses. A number of researchers have developed ammonia fuel cells using solid oxide fuel cells [19], catalytic ammonia decomposition to hydrogen occurs easily at the anode due to the high fuel cell operating temperature of 920 - 1270 K [20]. The implementation of this fuel cell technology is currently held back by the high cost and operability limitations.

**Table 2.1: Performance comparison of fuel cell technologies**

| **Fuel Cell Electrolyte Technology** | **Fuel** | **Power Density** $mWcm^{-2}$ | **Temperature** $K$ | |
|---|---|---|---|---|
| PEM | $H_2$ | 600 | 333 - 373 | [21, 13] |
| Alkaline (CPPO-PVA electrolyte) | $H_2$ or $NH_3$ | 11 - 16 | 273 | [17] |
| Acid (phosphoric) | $H_2$ or $NH_3$ | 350 | 273 - 470 | [16] |
| SOFC - H | $H_2$ or $NH_3$ | 410 | 920 - 1270 | [19, 20] |
| SOFC - O | $H_2$ or $NH_3$ | 380 | 920 - 1270 | [19, 20] |

PEM - Polymer exchange membrane fuel cell.
CPPO-PVA - chloroacetyl poly2,6-dimethyl-1,4-phenylene oxide - poly vinyl alcohol.
SOFC - Solid oxide fuel cell.

Of the fuel cell options outlined here, the anion transfer potential of the alkali and some solid oxide fuel cells are attractive options because ammonia can be fed directly to the anode. This approach avoids the ammonia decomposition and hydrogen purification steps and would simplify the overall design. The downsides of these technologies are increased cost and poorer efficacy when compared to PEM fuel cells and substantial further work is required to make them competitive with the PEM fuel cell.

The PEM fuel cell has great advantages in cost, efficiency and operability and so a combined technology that incorporates ammonia decomposition and hydrogen purification with a PEM fuel cell could be competitive. The ammonia PEM fuel cell that this work focuses on has the advantage of using the most competitive fuel cell technology but still faces a number of challenges including the high temperature required for ammonia decomposition and the need for hydrogen purification.

## 2.4 Catalysis For The Ammonia Decomposition Reaction

The most important challenge to be overcome to achieve an effective ammonia PEM fuel cell is to reduce the temperature for decomposition of ammonia from the current range of 570 - 670 $K$ required by current catalysts [22]. Although low temperature activity for ammonia decomposition can be considered as any temperature below this for which a catalyst has significant activity, the ultimate objective is to push toward 370 $K$ to enable easier integration with PEM fuel cell applications. Significant advances in catalyst design will be required if this objective is to be achieved.

This section provides an overview of the ammonia decomposition reaction, current ammonia decomposition catalysts are considered with a focus on low temperature activity. To achieve a step change in low temperature activity, it is necessary to explore the potential of new techniques and ideas in the field of heterogeneous catalysis. Accordingly, this review also considers a number of these new developments including bi-metallic catalysts.

### 2.4.1 Reaction Scheme and Mechanism

Ammonia decomposition is a reversible reaction where one mole of ammonia decomposes to form one and a half moles of hydrogen gas and one half mole of nitrogen gas (2.1). The reaction is endothermic and proceeds readily on catalytic surfaces where the reaction intermediates are thermodynamically stable.

$$NH_{3(g)} \rightleftharpoons {}^{3}/_{2}H_{2(g)} + {}^{1}/_{2}N_{2(g)} \qquad \Delta H^{o} = 46.19\ kJ/mol \quad (2.1)$$

A widely accepted twelve step reversible mechanism for the heterogeneous decomposition of ammonia is shown in equations 2.2 to 2.13. The figure is reproduced from Hansgen *et al.* [23], asterisks represent active sites on the catalyst surface. The reaction proceeds via adsorption of ammonia (2.2), successive cleavage of N-H bonds (2.4, 2.6 and 2.8) and recombinative desorption of molecular nitrogen and hydrogen (2.10 and 2.12) [24]. The mechanism is the reverse of the extensively studied ammonia synthesis reaction. Although a catalyst active for ammonia synthesis will be active for ammonia decomposition, there are differences in the interaction energies with reacting species that means that the best catalyst for one direction is not

necessarily the best in reverse [25]. A catalyst more active for ammonia decomposition than synthesis tends to have a weaker nitrogen interaction energy to facilitate combination of surface nitrogen adatoms (2.10).

$$NH_3 + * \rightarrow NH_3* \tag{2.2}$$
$$NH_3* \rightarrow NH_3 + * \tag{2.3}$$
$$NH_3* + * \rightarrow NH_2* + H* \tag{2.4}$$
$$NH_2* + H* \rightarrow NH_3* + * \tag{2.5}$$
$$NH_2* + * \rightarrow NH* + H* \tag{2.6}$$
$$NH* + H* \rightarrow NH_2* + * \tag{2.7}$$
$$NH* + * \rightarrow N* + H* \tag{2.8}$$
$$N* + H* \rightarrow NH* + * \tag{2.9}$$
$$N* + N* \rightarrow N_2 + 2* \tag{2.10}$$
$$N_2 + 2* \rightarrow N* + N* \tag{2.11}$$
$$H* + H* \rightarrow H_2 + 2* \tag{2.12}$$
$$H_2 + 2* \rightarrow H* + H* \tag{2.13}$$

Much effort has been expended to determine the rate limiting step in the ammonia decomposition reaction mechanism. In 1960, Tamaru [26] investigated ammonia decomposition using a tungsten wire catalyst and found that although the reaction proceeded below 723 $K$, only hydrogen was produced and all nitrogen remained bound to the catalyst acting as a temporary poison. In 1970, Matsushita and Hansen [27] studied the desorption of hydrogen and nitrogen from polycrystaline tungsten filament during the decomposition of ammonia. They found that while ammonia was partially decomposed at 300 $K$, the hydrogen desorption was not complete until 900 $K$, nitrogen desorption started at 870 $K$ and peaked at 1100 $K$. These findings suggest that nitrogen desorption from the catalyst is the rate limiting step at low temperatures. However in 1978, Danielson *et al.* [28] found that molecular nitrogen does not adsorb appreciably on a ruthenium surface, thus implying that the desorption of molecular nitrogen would be a rapid event and not limiting. It must therefore be true that the rate limiting step is not molecular nitrogen desorption but the recombination of nitrogen adatoms to form molecular nitrogen on the catalyst surface. This was confirmed experimentally by Tsai and Weinberg [29] who showed by thermal desorption measurements that the surface of a ruthenium was increasingly saturated with nitrogen adatoms below 650 $K$ (see Figure 2.3). The surface nitrogen recombination and desorption are commonly combined and referred

to as recombinative desorption (2.10) with the removal of surface molecular nitrogen being very fast.

The temperature at which the rate dependency transitions from N-H bond scission to the recombination of nitrogen adatoms is a function of many factors. Ganley *et al.* [30] found that the rate limiting step depended upon the catalytic metal. Recombination of nitrogen adatoms was found to be limiting for iron, cobalt and nickel and N-H bond scission was limiting for rhodium, iridium, palladium, platinum and copper.

Given the low target temperature of the ammonia PEM fuel cell, the rate limiting step for the ammonia decomposition reaction cell is likely to be the recombination of nitrogen adatoms on the catalyst surface. This knowledge will dictate many aspects of the catalyst design, in particular the selection of catalytic metal which should be selected to give the most advantageous nitrogen interaction energy.

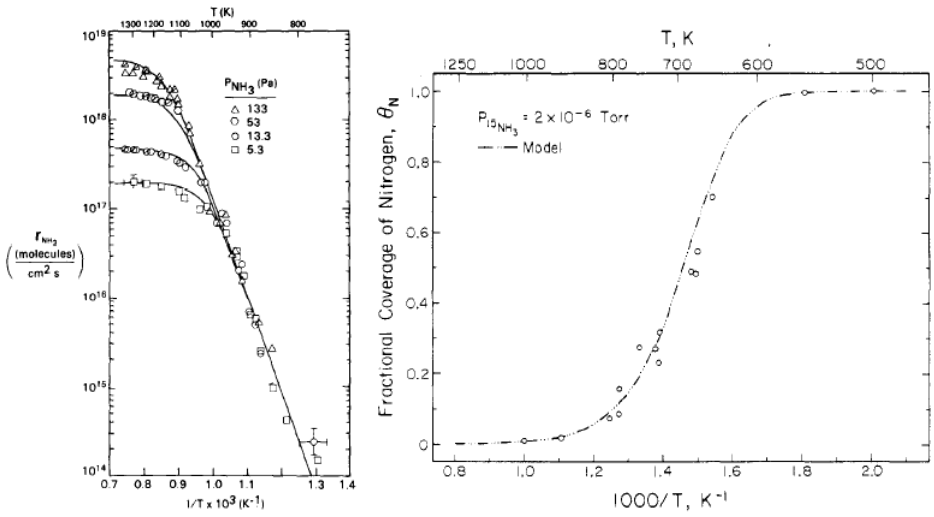


**Figure 2.3:** The transition between two rate limiting steps for ammonia decomposition: **1-** the rate of reaction as a function of temperature and ammonia partial pressure and **2-** nitrogen saturation of a ruthenium crystal surface below 650 $K$. [31, 29]

### 2.4.2 Ammonia Decomposition Thermodynamics

An understanding of the reaction equilibrium for ammonia decomposition is also a very important factor in the design and development of the ammonia PEM fuel cell. It may be possible to carry out the reaction at a set of conditions in which the equilibrium ammonia concentration is lower than 0.1 *ppm* that would avoid poisoning of the PEM fuel cell [9]. If this could be achieved, it would eliminate the requirement for a hydrogen purification step. It is also important to know

the equilibrium conversion at temperature closer to the PEM fuel cell operating temperature between 370 - 470 $K$.

The decomposition of ammonia is endothermic and increases the net moles of gas leading to an increase in system entropy. High equilibrium conversion is favoured by low pressure and high temperature. The equilibrium conversion curve at 1 *bar* is shown in Figure 2.4. At 673 $K$ the ammonia decomposition equilibrium is 99.12 *mol.*% rising to 99.90 *mol.*% at 873 $K$ and 99.97 *mol.*% at 1073 $K$ [9]. Even at 1173 $K$ there is 150 *ppm* of ammonia remaining at completion which is far in excess of the 0.1 *ppm* specification for hydrogen to be used in a PEM fuel cell [9]. Therefore reaction conditions alone are not sufficient and a separation step must be employed to purify the produced hydrogen.

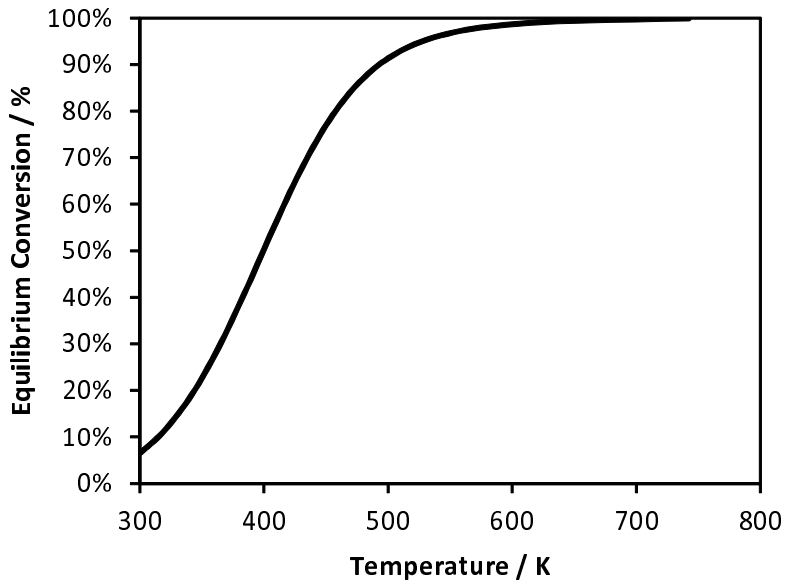


**Figure 2.4:** Reaction equilibrium for ammonia decomposition, data from Aspen™ simulation with the ideal thermodynamic package.

Under the target reaction conditions for the ammonia PEM fuel cell of 370 - 470 $K$ and 1 *bar*, the equilibrium conversion ranges from 34.4 % at the lower temperature to 84.9 *mol.*% at the higher. A single pass reactor would waste substantial ammonia operating under these conditions and a more advanced engineering solution is required. A membrane reactor that can remove product hydrogen could achieve greater overall conversion of ammonia, in Figure 2.5 an analysis is made showing the effect of hydrogen removal upon the overall ammonia conversion at 370 $K$. It can be seen that to achieve 90 % ammonia conversion, 94 % of hydrogen must be removed from the reactor and to achieve 99 % ammonia conversion, 99.5 % of hydrogen must be removed. Thus the separation of hydrogen from the ammonia decomposition

reactor operating at low temperature will be a difficult challenge to overcome and much effort will be needed in the development of membrane technologies to achieve this.

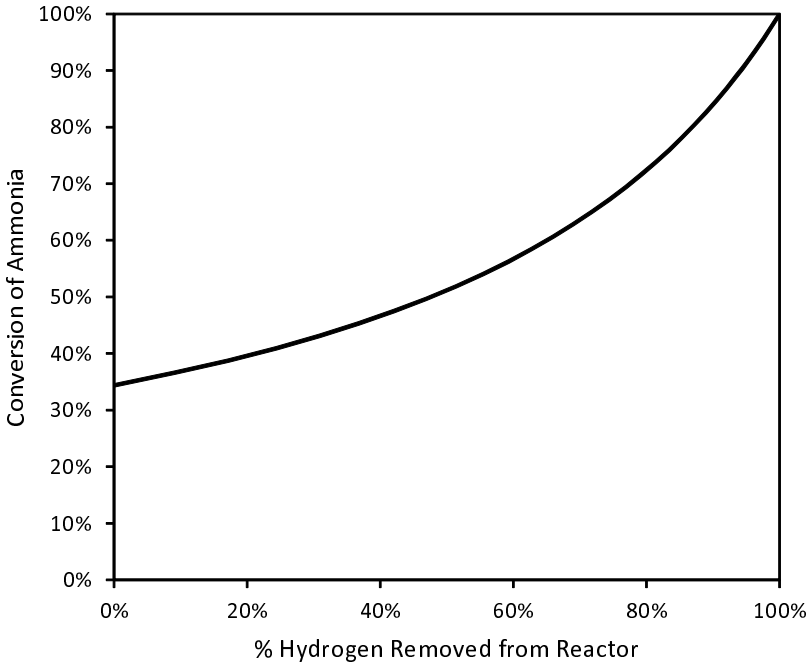


**Figure 2.5:** Analysis of Conversion vs Hydrogen Removal at 370 $K$.

It can be concluded that a hydrogen purification step is required as part of the design of the ammonia PEM fuel cell and that the ammonia decomposition reactor design must account for lower equilibrium conversions. Both of these problems can be addressed by using a hydrogen permeation membrane reactor which would enhance the effective overall conversion of ammonia by reducing the partial pressure of hydrogen in the reactor while also producing very high purity hydrogen.

### 2.4.3 Kinetic Models for Ammonia Decomposition

A number of researchers have attempted to model the ammonia decomposition reaction. Of particular interest are the predicted activation energies, orders of reaction with respect to reagents and products and the treatment of the reaction steps within the models as these yield insight into the ammonia decomposition mechanism.

$$-r_{NH_3} = k_o e^{\frac{E_a}{RT}} P_{NH_3}^{\alpha} P_{H_2}^{\beta} \tag{2.14}$$

The ammonia decomposition reaction is often modelled using a simple Arrhenius relationship (as shown in equation 2.14) where $k_0$ is the frequency factor, $E_a$ is the

activation energy, $R$ is the universal gas constant, $T$ is temperature and $\alpha$ and $\beta$ are the orders of reaction with respect to ammonia and hydrogen partial pressure.

A selection of reported Arrhenius parameters are shown in Table 2.2. Researchers have reported substantial variation in the order of reaction with respect to ammonia and hydrogen, however the order of reaction with respect to nitrogen is uniformly reported as zero. Few of the experiments listed consider temperatures much below 650 $K$ and so kinetic behaviour below this temperature is not well known. It might be expected that there would be a step change at around 650 $K$ to account for the change in reaction mechanism claimed by Tsai and Weinberg [29]. Egawa *et al.* [24], Logan and Kemball [32] and Tsai and Weinberg [29] all investigated the kinetics below 650 $K$ but their reported orders of reaction are not in good agreement. These discrepancies are probably the result of variations in catalyst design.

**Table 2.2: Kinetic parameters reported for ammonia decomposition** (adapted from Bradford *et al.* [22]).

| **Catalyst** | **Temperature** $K$ | **Activation Energy** $kJ\,mol^{-1}$ | **α** | **β** | |
|---|---|---|---|---|---|
| Ru(0 0 1) | <650 | 180.0 | 0 | - | [29] |
| Ru(0 0 1) | >750 | 20.9 | 1 | - | [29] |
| Ru(1 1 10) & Ru(0 0 1) | <500 | - | 0 | - | [24] |
| Ru(1 1 10) & Ru(0 0 1) | 520 | - | 0.4 | -0.6 | [24] |
| Ru(1 1 10) & Ru(0 0 1) | >600 | - | 1 | 0 | [24] |
| Ru | 543 - 748 | 188.4 | 0.83 to 1.56 | -1.59 to -2.56 | [32] |
| $Ru/Al_2O_3$ | 623 - 673 | 129.8 | 0.6 | -0.9 | [33] |
| Ru/C | 623 - 723 | 96.3 | 0.69 to 0.75 | -2 -to -1.56 | [22] |
| $Ir(100)/Al_2O_3$ | 200 - 800 | 84 | 0.9 | -0.7 | [34] |

A number of published micro-kinetic models for ammonia decomposition are summarised in Table 2.3. The models for nickel and ruthenium catalyst show the highest activation energy for the combination of nitrogen adatoms and this is expected to be the rate determining step.

**Table 2.3: Summary of microkinetic models for the decomposition of ammonia**

| Reaction Step | Pt (5 5 7) [35] | Ru-Cs on MgO [36] | Ru [37] | Ni [38] |
|---|---|---|---|---|
| $NH_{3(g)} + \bullet \rightarrow NH_3\bullet$ | $c_s = 0.54$ | $2.1 \cdot 10^6$ | $c_s = 1$ | $c_s = 0.011$ |
| $NH_3\bullet \rightarrow NH_{3(g)} + \bullet$ | $2.2 \cdot 10^{17} e^{\left(\frac{-161,000}{RT}\right)} s^{-1}$ | $5.9 \cdot 10^{13} e^{\left(\frac{-83,700}{RT}\right)}$ | $1.0 \cdot 10^{13} e^{\left(\frac{-76,200}{RT}\right)}$ | $8.210 \cdot 10^{14} e^{\left(\frac{-78,630}{RT}\right)}$ |
| $NH_3\bullet + \bullet \rightarrow NH_2\bullet + H\bullet$ | $2.5 \cdot 10^{11} e^{\left(\frac{-55,700}{RT}\right)} s^{-1}$ | $9.3 \cdot 10^{12} e^{\left(\frac{-64,600}{RT}\right)}$ | $1.0 \cdot 10^{11} e^{\left(\frac{-73,300}{RT}\right)}$ | $5.723 \cdot 10^{22} e^{\left(\frac{-78,990}{RT}\right)}$ |
| $NH_2\bullet + H\bullet \rightarrow NH_3\bullet + \bullet$ | - | $3.3 \cdot 10^{13} e^{\left(\frac{-17,200}{RT}\right)}$ | $1.0 \cdot 10^{11} e^{\left(\frac{-55,300}{RT}\right)}$ | $1.320 \cdot 10^{24} e^{\left(\frac{-48,810}{RT}\right)}$ |
| $NH_2\bullet + \bullet \rightarrow NH\bullet + H\bullet$ | $4.9 \cdot 10^8 e^{\left(\frac{-83,700}{RT}\right)} s^{-1}$ | $1.8 \cdot 10^{13} e^{\left(\frac{-8,600}{RT}\right)}$ | $1.0 \cdot 10^{11} e^{\left(\frac{-80,000}{RT}\right)}$ | $2.718 \cdot 10^{22} e^{\left(\frac{-75,740}{RT}\right)}$ |
| $NH\bullet + H\bullet \rightarrow NH_2\bullet + \bullet$ | - | $4.7 \cdot 10^{13} e^{\left(\frac{-60,400}{RT}\right)}$ | $1.0 \cdot 10^{11} e^{\left(\frac{-72,900}{RT}\right)}$ | $3.702 \cdot 10^{19} e^{\left(\frac{-74,870}{RT}\right)}$ |
| $NH\bullet + \bullet \rightarrow N\bullet + H\bullet$ | $1.0 \cdot 10^8 e^{\left(\frac{-16,500}{RT}\right)} s^{-1}$ | $2.8 \cdot 10^{14} e^{\left(\frac{-41,200}{RT}\right)}$ | $1.0 \cdot 10^{11} e^{\left(\frac{-24,300}{RT}\right)}$ | $6.213 \cdot 10^{19} e^{\left(\frac{-22,930}{RT}\right)}$ |
| $N\bullet + H\bullet \rightarrow NH\bullet + \bullet$ | - | $6.0 \cdot 10^{13} e^{\left(\frac{-86,500}{RT}\right)}$ | $1.0 \cdot 10^{11} e^{\left(\frac{-156,000}{RT}\right)}$ | $2.870 \cdot 10^{19} e^{\left(\frac{-156,040}{RT}\right)}$ |
| $H\bullet + H\bullet \rightarrow H_{2(g)} + 2\bullet$ | Fast | $2.3 \cdot 10^{13} e^{\left(\frac{-89,400}{RT}\right)}$ | $1.0 \cdot 10^{13} e^{\left(\frac{-99,200}{RT}\right)}$ | $3.315 \cdot 10^{19} e^{\left(\frac{-82,210}{RT}\right)}$ |
| $H_{2(g)} + 2\bullet \rightarrow H\bullet + H\bullet$ | - | $5.5 \cdot 10^5$ | $c_s = 1$ | $c_s = 0.01$ |
| $N\bullet + N\bullet \rightarrow N_{2(g)} + 2\bullet$ | Slow | $2.0 \cdot 10^{10} e^{\left(\frac{-137,000}{RT}\right)}$ | $1.0 \cdot 10^{13} e^{\left(\frac{-211,000}{RT}\right)}$ | $4.442 \cdot 10^{22} e^{\left(\frac{-210,840}{RT}\right)}$ |
| $N_{2(g)} + 2\bullet \rightarrow N\bullet + N\bullet$ | - | $5.6 \cdot 10^1 e^{\left(\frac{-33,000}{RT}\right)}$ | $c_s = 1$ | $c_s = 1.000 \cdot 10^{-6}$ |

Where $c_s$ is the sticking coefficient defined as the ratio of the number of incident molecules which adsorb to a surface to the total number of incident molecules.

Although there is substantial variation between the studies summarised here, it can be concluded that the reaction is zero order with respect to nitrogen, around 0.5 - 1 with respect to ammonia and -1 to -2 with respect to hydrogen. A wide range of reaction activation energies are reported, this is unsurprising given the variation of catalysts and conditions employed. Finally the micro-kinetic models suggest that recombination of surface adatoms is the rate determining step for the ammonia decomposition reaction at low temperature.

### 2.4.4 Catalytic Systems for Ammonia Decomposition

This review considers supported metal nanoparticles with promoters. Catalysts of this type have been widely used for ammonia decomposition and have been shown to be highly active. Important considerations include selection of the support with attention to the surface area, pore-structure, electrical interactions and electrical conductivity. Selection of the active metals is considered with focus upon their electrical and structural properties as well as the strength of interaction with the reacting species. Finally, findings on the roles of the promoter are evaluated.

Recent developments in nano-structured catalyst design are also considered including bi-metallic, alloys and core-shell catalysts. Further developments in nanoparticle size and structure, metal dispersion and alternative supports and promoters are also examined.

### Active Metals

Research into active metals for ammonia decomposition is one of the oldest areas of research within the field of catalysis. The first metals identified as catalysts for ammonia decomposition were found by Thenard and Dulong in 1823 [39], who reported the following activities in descending order: Fe $>$ Cu $>$ Ag $>$ Au $>$ Pt. Amano and Taylor [33] found that ruthenium was active from 623 $K$, rhodium from 633 $K$ and palladium from 783 $K$. In 1997, Papapolymerou and Bontozoglou [40] discovered that iridium was an order of magnitude more reactive than rhodium which in turn was more active than platinum and palladium. A similar comparison made by Choudhary *et al.* [41] found that activity decreases in the order Ru $>$ Ir $>$ Ni. More recently in 2004, Yin *et al.* [42] concluded that ruthenium is the most active metal for ammonia decomposition. Relative activities of metals for ammonia decomposition are shown in Figures 2.6 and 2.7.

More recently, researchers have attempted to correlate activity of a metal with thermodynamically calculated interaction energies. Ganley *et al.* [30] related the activity of a metal for ammonia decomposition with the nitrogen - hydrogen bond scission energy estimated using density functional theory (Figure 2.6). The results show a linear relationship for the metals for which breaking of the nitrogen hydrogen bond is limiting however other metals such as nickel, cobalt and iron do not fit this trend. It was postulated that the limiting step for these metals was the recombination of nitrogen adatoms. Ruthenium is generally reported to be the most active single metal for both ammonia decomposition and ammonia synthesis across the literature, it sits at the pinnacle of the volcano curves shown in Figures 2.6 and 2.7 and represents the best compromise between the competing limiting steps in the reaction mechanism.

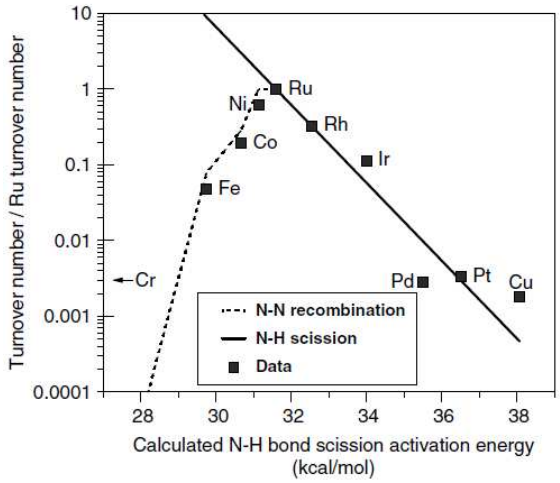


**Figure 2.6:** Correlation between the activation energy for N-H bond scission and measured relative TOF for ammonia decomposition at 853 K. Directly reproduced with permission from Ganley *et al.* [30].

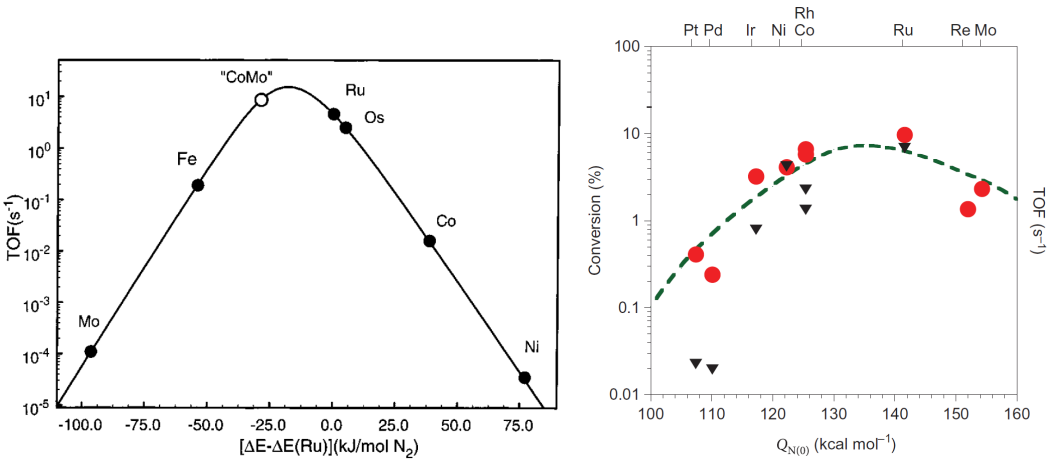


**Figure 2.7:** Volcano curves for the predicted binding energy of nitrogen vs turnover frequency: 1. Synthesis of ammonia at 673 $K$ and 50 $bar$ (left) reprinted directly from Jacobsen *et al.* and 2. decomposition of ammonia at 850 K (right) reprinted directly with permission from Hangsen *et al.* (the triangles are from experiment and the circles are predicted conversion). [23, 43]

These interaction energies are a crucial part of understanding the activity of a catalyst. Further insight here can be gleaned by considering catalysts for the more heavily studied ammonia synthesis reaction. While it is true that the best metal for ammonia synthesis is not the same as for ammonia decomposition, metals active for ammonia synthesis will also have some activity for ammonia decomposition because they will stabilise the same reaction intermediates [25]. Jacobsen *et al.* [43] found that the activation energy for $N_2$ dissociation on transition metal surfaces was directly proportional to the binding energy of nitrogen. They predicted the

best catalyst by using a volcano curve of activity plotted against nitrogen binding energy (rather than N-H scission energy) estimated using density functional theory (DFT) (see Figure 2.7). Jacobsen *et al.* [43] stated that the two desirable catalyst qualities for ammonia decomposition are a small activation energy barrier for nitrogen dissociation and a surface with a low coverage of adsorbed atomic nitrogen. These properties can only be achieved if the catalyst possesses both a strong and weak nitrogen interaction energy and are therefore inherently opposed. This is reflected in work by Ganley *et al.* [30] (Figure 2.6) showing that ruthenium is the optimum mono-metallic catalyst as it possesses the best compromise between these two properties. Jacobsen *et al.* [43] proposed that this problem could be overcome by use of a dual metal system comprising cobalt and molybdenum ($Co_3Mo_3N$). Thermodynamic models predicted that molybdenum binds nitrogen strongly and facilitates N-H bond cleavage and cobalt binds nitrogen weakly which facilitates nitrogen atom combination. They propose that chemisorbed species can transition from one active site to another. Experimental results showed that this catalyst is more active than ruthenium when the ammonia mole fraction is less than 5.6 mol.% [43].

Core-shell and alloy nanoparticle catalysts could be a route to a new generation of more active catalysts at low temperatures. Jiang and Xu [44] stated that alloy materials often possess "distinct binding properties with reactants in contrast to those for monometallic metal catalysts" and core-shell catalysts have a performance which is "strongly dependent on the structure of the core, shell and interface, and also quite different from those of monometallic counterparts and alloys".

The presence of a second less active metal can alter the activity of the more active metal in a number of ways. A core metal can change the electronic structure (d-band shift) of the metal surface as the bi-metallic bonds act as pseudo-ligands by either donating or withdrawing electrons from the more active metal. Further to this, the metal bond lengths can be altered by strain effects [45, 46]. This enhanced tuneability of alloys and core-shell catalysts presents new opportunities to optimise the design of catalysts and enable the replacement of rare and precious metals such as ruthenium with more abundant metals.

The prediction of the properties of a core-shell or alloy nanoparticle catalyst present a number of problems because of the number of factors which can influence the configuration of the two metals within the nanoparticle. Ferrando *et al.* [47] summarised some key characteristics that could be used to predict the alloy properties:

1. If inter-metal bond strength is greater than intra-metal bond strength then this favours a core-shell structure, in the reverse case an alloy is more likely.

2. The metal with the lowest surface energy will tend to migrate to the surface in preference to the other metal (some surface segregation energies relative to platinum are shown in Figure 2.4).

3. A metal with a smaller atomic size would tend to migrate to the more sterically confined core.

4. The degree of electron charge transfer between metals increases the likelihood of an alloy formation.

5. The metal with a stronger interaction with surface species (reacting species for example) will tend to migrate to the surface. Other researchers have shown that core-shell nanoparticles can flip the core and shell depending upon whether they are in a reducing or oxidising environment [48].

**Table 2.4: Surface segregation energies of common catalytic metals in bi-metallic systems with platinum [49].**

| **Metal** | **Surface segregation energy** $eV$ |
|---|---|
| Re | -2.08 |
| Mo | -1.3 |
| Ru | -0.83 |
| Co | -0.61 |
| Fe | -0.41 |
| Ni | -0.38 |
| Rh | -0.35 |
| Pd | -0.03 |
| Pt | 0 |
| Au | 0.36 |

Metals used as nanoparticles in bi-metallic catalysts have a tendency to either remain in the starting condition, form an alloy or to promote one metal to the surface at the expense of the other depending upon the temperature and their intrinsic properties. Naitabdi *et al.* [50] investigated the effect of temperature upon the nano-structure of Fe-Au core-shell nanoparticles supported upon titania. They found that alloy formation began around 973 $K$ and that gold had a tendency to migrate to the surface above 1073 $K$. The temperature at which the phenomenon occurred depended upon the starting metal ratios. Wang *et al.* [51] made a theoretical investigation of the Ni-Pt, Re-Pt and Mo-Pt core shell nanoparticles and found that at 600 $K$ the equilibrium comprised a majority of platinum in the shell layer in all cases. In a similar thermodynamic study, Ma *et al.* [49] found that in a bi-metallic

M-Pt system (where M is the second metal): Ag, Au, Cr, Mn and Ti would tend to migrate toward the surface whereas Co, Cu, Fe, Ir, Mo, Ni, Pd, Re, Rh & Ru migrate away from the surface. It should be noted that they did not consider the kinetics of metal migration within a core-shell nanoparticle and it is not clear whether this would be a slow or a fast process.

A number of studies have considered the potential of bi-metallic heterogeneous catalysts for ammonia decomposition and ammonia synthesis. A Co-Mo nitride catalyst was shown by Jacobsen *et al.* to have more activity for ammonia decomposition at low conversions than ruthenium [52]. Several other papers have followed this work, including Ji *et al.* who synthesised cobalt-molybdenum bimetallic nanoparticles supported on gamma alumina showing that the combined activity was greater than for the individual metals [53]. A series of bimetallic Co-Mo nanoparticle catalysts were supported on carbon MCM-41 with 3.0 - 3.5 nm pore size and silica. The catalysts were prepared by incipient wetness impregnation, there were shown to have bimetallic interactions by TPR experiments and the best activity was achieved with a 7 - 3 ratio of Co-Mo [54]. Other combinations include commercially sourced Ni-Pt on alumina [55], nitrided Ni-Mo catalysts supported on alumina by incipient wetness impregnation [56], Ni-Fe supported on alumina by incipient wetness impregnation [57] and Fe-Co alloy nanoparticles on CNTs [58]. Hansgen *et al.* who showed computationally and experimentally that Fe and Co monolayers on a Pt(111) surface [59]. Core-shell nanoparticle catalysts have also been applied successfully for the decomposition of formic acid using Pd over Ag nanoparticles by Tedsree *et al.* [60]. The shells were 1 - 10 Pd atoms thick and exhibited a terraced structure, they outperformed Pd-Ag alloys working best with a 1:1 molar ratio. Pd/Au core-shell nanoparticles supported on carbon for the decomposition of formic acid were found to possess superior activity, selectivity and stability at low temperature compared to the mono-metallic catalysts [61]. There is currently no consensus on the optimum combination of metals for a bimetallic ammonia decomposition catalyst and much research will be required before this can be achieved.

Zhang *et al.* [58] investigated Fe-Co alloy nano particles supported on carbon nanotubes and found that the alloy had the activity of cobalt but with improved stability. A study of ammonia decomposition was undertaken by Hansgen *et al.* [23] that showed that core-shell catalysts with Ni, Fe and Co on a Pt(111) core exceeded the activity of ruthenium [23, 62, 59]. They show that the performance of a catalyst can be predicted by calculating the atomic nitrogen adsorption energy (using a similar DFT function as Jacobsen *et al.* [43]) and confirmed these predictions through experimentation (see Figure 2.7).

The properties of the shell of the core-shell metal are very important with regards

to activity. Hansgen *et al.* [62] observed that the shell metals deposited in core shell nanoparticles did not cover the entire surface and subsequent layers grew preferentially upon the first metal to form islands (this growth mechanism is known as Volmer-Weber [63]). The presence of metal islands means that there are sites on the catalyst where the active species can engage with both the core and shell metals simultaneously. Hansgen *et al.* [62] proposed that in the decomposition reaction on the nickel active site, the bound nitrogen could transition onto a platinum site which has a much lower adsorption energy enabling easier desorption. The implication is that this island growth of the second metal is superior to a shell covering in which only a single metal is available. This finding is in agreement with that of Jacobsen *et al.* [43] who developed the Co-Mo alloy specifically to express two different binding energies for nitrogen.

In the selection of the active metal for a catalyst, some thought should be given to the corresponding negative ion of the precursor salt. Murata and Aika [64] investigated the performance of ruthenium on $Al_2O_3$ for ammonia decomposition using six different precursor salts for ruthenium. They found that performance was in order carbonate $>$ nitrate $>$ oxide $>$ acetate $>$ chloride. They also highlight that ruthenium dispersion varied substantially depending upon which precursor salt was used and carbonate achieved the best dispersion. This finding agrees with the claim by Yin *et al.* [42] that species tend to have a positive or detrimental effect on the rate of ammonia decomposition reaction depending upon their tendency to donate or withdraw electrons respectively.

In conclusion, many researchers have suggested that it is possible to predict the activity of an active metal or a bi-metallic composite through an understanding of the metal properties in relation to the key reaction steps and reacting species. It has been suggested that there is an optimal nitrogen interaction energy for an active metal and that this property can be predicted by thermodynamic modelling. Other authors have suggested that the structural organisation of a bi-metallic nanoparticle can also be predicted by an understanding of the key properties of each metal and their interaction with the reacting species. Although there is scope for much more work to be done in this area, these findings can be considered as aids to help other researchers to design effective single metal and bi-metal catalysts in a more efficient manner.

### The Effect of Active Metal Nano-Structure

Further to the intrinsic properties of the active metal, there are many other important aspects to consider such as the surface structure of the deposited metal

nanoparticle. The shape of the active metal surface will in part define the interaction energies with reacting species and thus will alter the catalyst activity. In order to understand this effect in more depth, it is necessary to consider the typical structural properties of these metals.

Transition metals tend to form a characteristic crystal structure, these are body centred cubic (BCC), face centred cubic (FCC) or hexagonal close packed (HCP) (see Figure 2.8). These crystal structures feature characteristic plane surfaces, edges and nodes and are commonly described using Miller indices [65]. These surfaces can exhibit different interaction energies with reacting species. Loffler and Schmidt [66] found that the activity of the face centred cubic (FCC) platinum crystals for ammonia decomposition decreased in the order from (2 1 0) > (1 1 0) > (1 1 1) > (1 0 0). The more complex (2 1 0) structure exhibited higher activity than the lower energy (1 0 0).

| | | | | | | | | | | | |
|---|---|---|---|---|---|---|---|---|---|---|---|
| Li hcp | Be hcp | | | | | | | | | | |
| Na hcp | Mg hcp | | | | | | | | | | |
| K bcc | Ca fcc | Sc hcp | Ti hcp | V bcc | Cr bcc | Mn (bcc) | Fe bcc | Co hcp | Ni fcc | Cu fcc | Zn hcp |
| Rb bcc | Sr fcc | Y hcp | Zr hcp | Nb bcc | Mo bcc | Tc hcp | Ru hcp | Rh fcc | Pd fcc | Ag fcc | Cd hcp |
| Cs bcc | Ba bcc | Lu hcp | Hf hcp | Ta bcc | W bcc | Re hcp | Os hcp | Ir fcc | Pt fcc | Au fcc | Hg (fcc) |
| Fr | Ra bcc | | | | | | | | | | |

**Figure 2.8:** Trends in metal crystal structure in the periodic table at low temperature [67]. Bcc refers to body centred cubic structure, fcc to face centred cubic and hcp to hexagonal close packed.

Metal nanoparticles do not tend to form into the perfectly ordered crystal structures because they typically have an insufficient number of atoms in the cluster. This produces a number of surface defects such as step sites that can be advantageous because the defects tend to have higher activity. A good example are stepped crystal surfaces that have been shown to be substantially more active than flat ones for the synthesis reaction for both nitrogen - hydrogen bond cleavage and nitrogen recombination [24, 66, 35].

Research into ammonia synthesis using density functional theory have found that switching from Ru(0001) to a stepped surface reduced the activation energy for nitrogen dissociation and recombination from 190 $kJ\,mol^{-1}$ to 40 $kJ\,mol^{-1}$ [68].

Rosenthal [69] goes further to state that "for the ammonia synthesis on ruthenium single crystalline surfaces, both the geometric and electronic functionalities of step edges are crucial to dissociate nitrogen". Egawa *et al.* [24] experimented with stepped (1 1 10) and flat (0 0 1) facets of ruthenium, for ammonia decomposition, concluding that $N_2$ formation was an order of magnitude faster upon the stepped surface which they suggested to be advantageous in breaking the N-H bond. Guthrie *et al.* [35] showed that the stepped (5 5 7) facets of platinum crystals was 16 times more active for ammonia decomposition than the flat (1 1 1) facets.

Given that it is the most active metal for ammonia decomposition, much investigation has been made into the surface structure of ruthenium nanoparticles. Jacobsen *et al.* [70] found an orientation of ruthenium atoms which was particularly active for ammonia synthesis. It consists of a step between three atoms in one layer and two atoms in an adjacent layer and is referred to as a $B_5$ site (see Figure 2.9). They found that ruthenium nanoparticles were most active with diameters between 1 - 3 nm and these nanoparticles were also shown to have the highest concentration of $B_5$ sites. Garcia-Garcia *et al.* [71] found that the highest proportion of ruthenium $B_5$ sites of supported ruthenium occurred with particle diameters between 3 - 5 nm. Duan *et al.* [72] found that the optimum particle size for ammonia decomposition on nickel supported on carbon was 3.1 - 3.6 nm which suggests that a similar effect may occur with other metals.

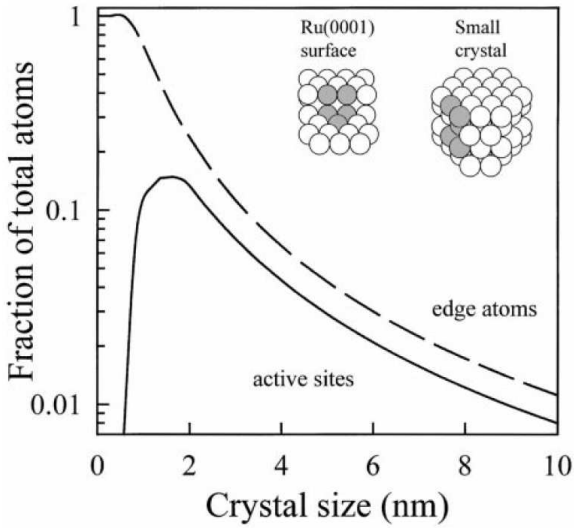


**Figure 2.9:** Occurrence of active Ru(0001) $B_5$sites vs nanoparticle size. Reproduced directly with permission from Jacobsen *et al.* [70].

Given the desirability of these high energy crystal structures, some effort has been expended to develop synthesis techniques by which they can be selectively produced.

Sun *et al.* [73] grew copper nano-crystals upon multi-walled carbon nanotubes by electro-deposition. They have shown that by increasing the applied potential, not only are higher energy crystal facets achieved, but also the growth pattern changes from van der Merwe growth (deposition in even layers) to Volmer-Weber growth in which deposition occurs in multi-layered islands (depicted in Figure 2.10). The Volmer-Weber growth pattern can be advantageous for catalytic applications as it exposes potential high activity interfaces between metals and supports [62].

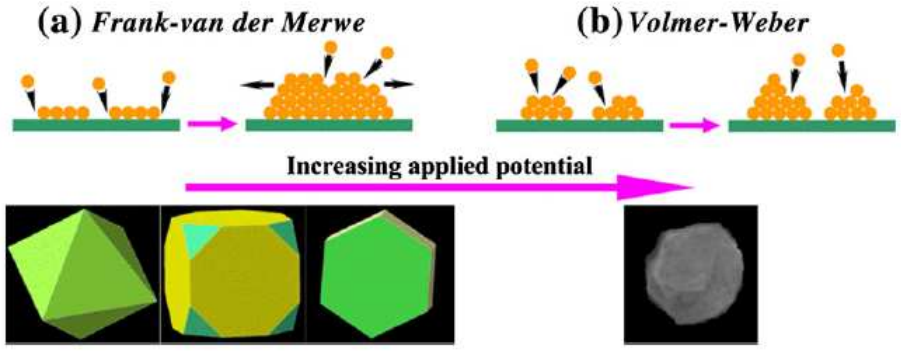


**Figure 2.10:** Crystal structures of copper supported on carbon nanotubes achieved as a function of applied potential during electro-deposition. Reproduced directly with permission from Sun et al. [73]

In conclusion, it has been shown that the activity of an active metal is a strong function of its surface structure. This structure is a function not only of the metal properties but more critically of the nanoparticle size and synthesis method. The control of nanoparticle size is one of the more important factors influencing the activity of any nanoparticle based catalyst.

### The Influence of Reduction Conditions on Metal Nanoparticle Catalysts

All metal nanoparticle catalysts require a reduction step to prepare them prior to use. The temperature at which this step occurs is specific to each metal. This section considers the information available in literature on the typical reduction conditions used for metals active for ammonia decomposition.

Yin *et al.* [74] undertook temperature programmed reduction studies of Ru, Rh, Pt, Pd, Ni & Fe nanoparticles supported on carbon nanotubes (see Figure 2.11). Although most metals required temperatures between 400 - 600 $K$, iron and nickel were reduced above 900 $K$. Four different studies on the temperature programmed reduction of ruthenium nanoparticles on carbon nanotubes have been compared in Figure 2.12. Peak hydrogen consumption temperature varied from 390 $K$ for functionalised carbon nanotubes [75] to 560 $K$ for ruthenium nanoparticles supported

outside the nanotubes. For ruthenium particles supported inside carbon nanotubes the peak reduction temperature was 480 $K$ [76]. It is likely that the reduction temperature of a particular metal will vary as a function of particle size, support interaction and the presence of promoters however it is difficult to predict the effect in each case.

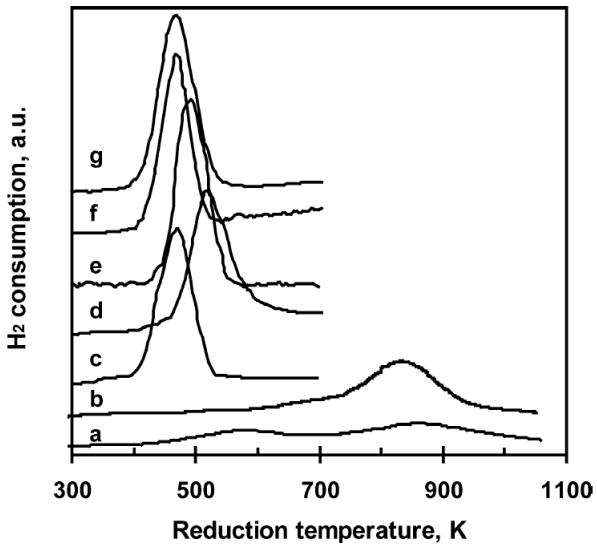


**Figure 2.11:** TPR profiles of metal catalysts supported on carbon nanotubes. **(a)** - Ni, **(b)** - Fe, **(c)** - unsupported $RuO_2$, **(d)** - Ru, **(e)** - Pd, **(f)** - Rh and **(g)** - Pt. Directly reproduced with permission from Yin *et al.*[74]

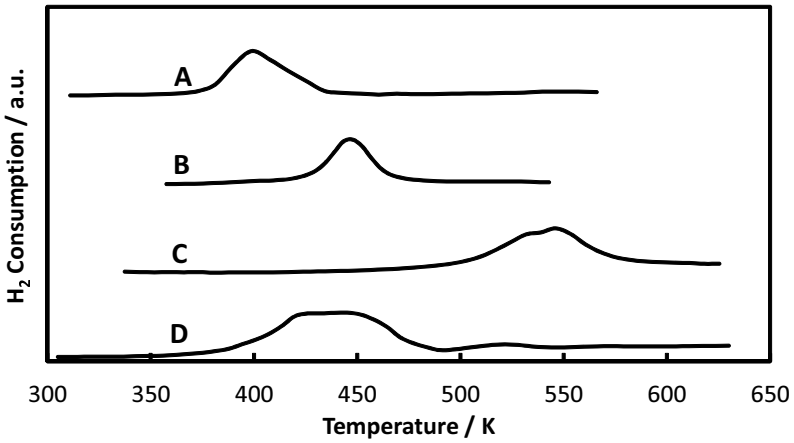


**Figure 2.12:** TPR profiles of ruthenium catalysts supported on carbon nanotubes. **A** is from Deng *et al.* [75], **B** is from Garcia-Garcia *et al.* [77], **C** is from Guo *et al.* [76] and **D** is from Yang *et al.* [78].

### The Role of Catalyst Support and Promoter

The catalyst support material performs a number of important roles within the catalyst for the ammonia decomposition reaction. It must provide sufficient surface area so that a high loading of active metal can be well dispersed as nanoparticles increasing metal surface area and lessening the potential for agglomeration. It can additionally provide containment of the nanoparticle within pore structures that can be highly valuable in prevention of nanoparticle translation and agglomeration at higher temperature. The support also influences the electrical environment of the nanoparticle and can participate in the withdrawing or donation of electrons.

Yin *et al.* [42] stated that carbon nanotubes are the best performing support for an ammonia decomposition catalyst. They quote relative activities as $Ru/CNT > Ru/MgO > /Ru/TiO_2 = Ru/Al_2O_3 = Ru/ZrO_2 > Ru/AC > Ru/ZrO_wBD$. They claim that the recombinative desorption of nitrogen is related to the electrical conductivity of the support that enables electron transfer to the active site. This finding is supported by Li *et al.* [79] who made extensive studies of CMK-3 activated carbon supports for ammonia decomposition and concluded that its poor activity might be due to its amorphous structure resulting in poor electron conductivity.

Carbon nanotubes are known to possess many favourable properties as a catalyst support, particularly high surface area and high electrical conductivity [80]. However, they pose handling problems because of the smaller powder particle size and poor flow characteristics. They are also susceptible to methanation after extensive use [81]. Carbon nanotubes are available as single wall nanotubes (SW CNTs) or as multi-wall (MW CNTs). MW CNTs are generally meso-porous (2 - 50 nm) which is substantially larger than the micro-porous SW CNTs ($<$ 2 nm) [80]. MW CNTs have better electrical conductivity than SWCNTs [82] and are more widely available and hence they are normally selected above SW CNTs as a catalyst support material even though they have significantly lower specific surface area [80].

Acid pre-treatment to oxidise carbon nanotubes (normally concentrated nitric acid or nitric-sulphuric acid mixtures) has consistently been shown to produce smaller, more disperse and more uniformly sized nanoparticles [80]. This finding has been applied to ammonia decomposition catalysts by a number of researchers, including Yin *et al.* [74] who applied a 2 hour reflux in 5 M nitric acid. This process is sometimes referred to as functionalising the nanotubes and it creates anionic groups upon the nanotubes which act as anchoring points for the metal ion to be adsorbed and thus form the location for a nanoparticle [80].

Nanoparticles can be deposited within carbon nanotubes by utilising the capillary effect. The active metal precursor is deposited with a low surface tension solvent to

achieve greater pore filling and the precursor is distributed both inside and outside of the nanotubes. Then, the proto-catalyst is dried to remove solvent and repeated solvent applications are applied to re-dissolve the ions and transports them into the nanotubes by capillary action where they can be reduced to form confined nanoparticles [58]. This approach improves temperature stability of the catalyst but it also introduces an elongated diffusion pathway to reaction as reagents and products will have to travel through the tubes to reach the active sites. Furthermore, it was found by Guo *et al.* [76] that ruthenium nanoparticles supported on the outside of carbon nanotubes had greater activity for ammonia synthesis than similar sized nanoparticles supported within the nanotubes. The variation in activity was attributed to higher electron density upon the external surface. This is conducive for the dissociative adsorption of nitrogen which is the limiting step for ammonia synthesis. It is likely that the same effect would be beneficial to recombinative nitrogen desorption which is rate limiting in the ammonia decomposition reaction.

Garcia-Garcia *et al.* [77] found that carbon nanotubes supporting ruthenium nanoparticles performed better when they were graphitized to improve the conductivity and also doped with nitrogen which is thought to increase the positive charge density of the MW CNTs.

Li *et al.* [79] experimented with a variety of acid and alkaline promoters for ruthenium supported on CMK-3 and found that the catalyst modified with alkali groups were far more productive than those with acidic groups. They expressed the catalytic order as $K > Na > Ca > Cl > SO_4 > PO_4 >$ unmodified $> Li$. Given that the performance of the metal promoters follows their electro-negativity trend (with the exception of lithium), it is likely that cesium and barium would be more active than potassium. The presence of electron withdrawing halogens should be avoided from all precursors as this is known to reduce activity. Cesium has been used successfully as a promoter by a number of researchers for ammonia synthesis [36] and the performance of the catalyst was found to have increased for ratios up to 10:1 cesium to ruthenium [64].

The promoter is commonly thought to act electronically. Its effect upon the catalyst activity by donation of electrons into the anti-bonding electronic states of the absorbate weakening the metal - adsorbate interaction strength and increasing it's likelihood to dissociate [83]. From this it can be concluded that the transition metals tend to bond too strongly with the reacting substrate and activity of the catalyst is enhanced by partially deactivating the metal via the transfer of electrons.

Superbasic supports have been used as an alternative to high conductivity supports. This type of support comprises basic species and can donate electrons to the active site which promotes nitrogen recombination. Yin *et al.* [42] claimed that there is a

strong correlation between turnover frequency (TOF) and support basicity. In effect the support takes on a similar role to the alkali promoters that are commonly used for ammonia decomposition catalysts. Yin *et al.* [84] found that a nano-composite of MgO-CNT support had a beneficial effect in which the MgO acted as electron donor. Later, the same group [81] considered a $ZrO_2 - KOH$ support for ruthenium and found it to be more active than promoted CNTs and MgO-CNTs. Klerke *et al.* [85] supported ruthenium nanoparticles upon sodium titanate nanotubes and potassium and cesium titanate nano-wires. The cesium support was most effective but all three decomposed following thermal cycling which limits their practical application.

The desirable attributes of a heterogeneous catalyst support for ammonia decomposition are high surface area, promotion of nanoparticle dispersion and either high conductivity or the presence of intrinsic electron donors within the support structure. The most successful supports found so far feature highly basic properties or highly conductive graphitic carbons such as carbon nanotubes. Strong electron donors make the best promoters with group 1 metals dominating.

### 2.4.5 Catalyst Synthesis and Characterisation Techniques

Many techniques have been investigated to attempt to selectively produce nanoparticles that possess higher intrinsic activity as discussed above. The most important factors are high dispersion, control of nanoparticle size, control of the surface structure, chemical composition and control of bi-metallic nanoparticle conformation. Also considered in this section are characterisation techniques so that the properties of the nanoparticle catalysts can be better understood.

#### Synthesis of Metal Nanoparticles

Most single metal nanoparticle heterogeneous catalysts for ammonia decomposition are synthesised by incipient wetness impregnation. The support is impregnated with a metal salt solution to fill the pore volume exactly. Under evaporation of the solvent, the solution super-saturates as the solvent volume reduces leading to nucleation and growth of numerous small particles. Alternative techniques include wet impregnation in which an excess of solvent is used and subsequently removed by filtration and drying, in this technique the ions adsorb to the support [86]. Finally deposition precipitation is used in which the nanoparticles precipitate from a precursor solution normally following the addition of a reducing agent.

Synthesis of bi-metallic (core-shell or alloy) nanoparticles generally requires a more controlled sequential approach. There are two predominant techniques: *i* - Physical

vapour deposition (PVD) under ultra-high vacuum where the metal to be deposited is wrapped as a wire around a tungsten filament until it evaporates and deposits upon the nanoparticle (this is usually a single crystal); if the nanoparticle is held at room temperature then the metal deposits as a surface shell and if it is heated then the metals diffuse into each other to form an alloy (the temperature varies depending upon the metals in question) [63, 59]; *ii* - liquid-phase multi-step reduction techniques are used in which the metal is introduced in the form of a salt that is dissolved in solution, a reducing agent is added to precipitate the solid metal as suspended nanoparticles. Multiple metal layers can be generated through sequential reduciton steps [44].

The physical vapour deposition method can create a number of different surface layer growth patterns, examples being Frank van der Merwe layer by layer mechanism of the Volmer-Weber 3D island mechanism [63] (see Figure 2.10). The liquid phase in-situ synthesis method does not allow for this growth pattern but it presents other opportunities such as the dendritic Pt shells on Au formulated by Kim *et al.* [87].

Deposition precipitation is often used to create bi-metallic nanoparticle catalysts [86]. In this technique, a reducing agent is added to the metal precursor solution to force the precipitation of nanoparticles. In this way, Duvenhage and Coville [88] created a core-shell structure in which iron encased cobalt nanoparticles so that the cobalt activity was masked by a surface iron layer.

The bi-metallic catalyst synthesis techniques discussed above are more complex compared to the mono-metallic catalyst synthesis methods. This could make them more challenging to scale-up for commercial applications but some results in literature suggest that it may be possible to create structured bi-metallic catalysts using simple wetness impregnation techniques. Huang *et al.* [48] synthesised a bi-metallic ruthenium-platinum core-shell catalyst by incipient wetness impregnation supported on carbon. It was found that ruthenium migrated to the shell during reduction at 620 $K$ but it would migrate to the surface during oxidation above 520 $K$. Although this catalyst would be of limited use for ammonia decomposition (the reaction occurs in a reducing environment in which the ruthenium would be expected to migrate to the core where it would not be accessible), but it suggests that it would be possible to synthesize a bi-metallic catalyst in which the more active metal would migrate to the shell under reaction conditions.

Of the techniques discussed above, the simpler techniques such as incipient wetness impregnation and wet impregnation have greater commercial possibilities than the more complex methods because they are more readily scaleable. Given that the objective of this thesis is the development of an ammonia-PEM fuel cell technology,

it is logical to focus on these simpler synthesis methods as they can be more readily applied to commercial applications.

### 2.4.6 Characterisation Techniques for Heterogeneous Catalysts

This section considers the merits of characterisation techniques for heterogeneous catalysts including examples of their use. Important properties to discern range from the support surface area and chemical structure to the dispersion and size of metal nanoparticles. The techniques described here include some commonly applied methods and some that have been applied to gain significant insight into ammonia decomposition catalysts.

Transmission electron microscopy (TEM) is widely used in heterogeneous catalysis to infer the properties of the support material and the supported nanoparticle. In Figure 2.13, Zheng *et al.* [89] use high resolution TEM to clearly show the structure of the multi-walled carbon nanotube support but also of the supported ruthenium nanoparticle. The difference in the characteristic lattice structures are clearly visible. Frequently in literature, researchers make estimates of the distribution of nanoparticle size from TEM images, Figure 2.14 shows an example of this approach for ruthenium nanoparticles supported on alumina [90]. In the case of bi-metallic catalysts, TEM is commonly combined with X-ray energy dispersive spectroscopy (EDS), an example of which is shown in Figure 2.15. In this case, the stronger gold signal from the nanoparticles is taken as evidence that the gold predominates in the outer layer and suggests a core-shell nanoparticle structure.

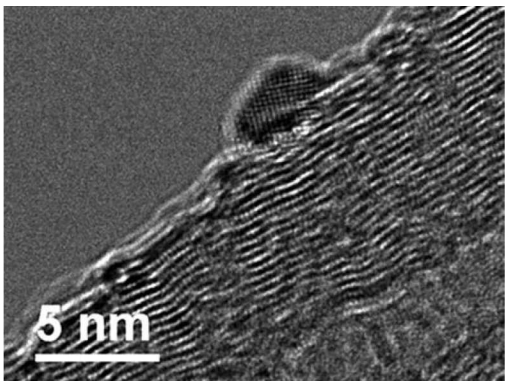


**Figure 2.13:** TEM image of ruthenium nanoparticles supported on multi-walled carbon nanotubes. Directly reproduced from Zheng *et al.* [89].

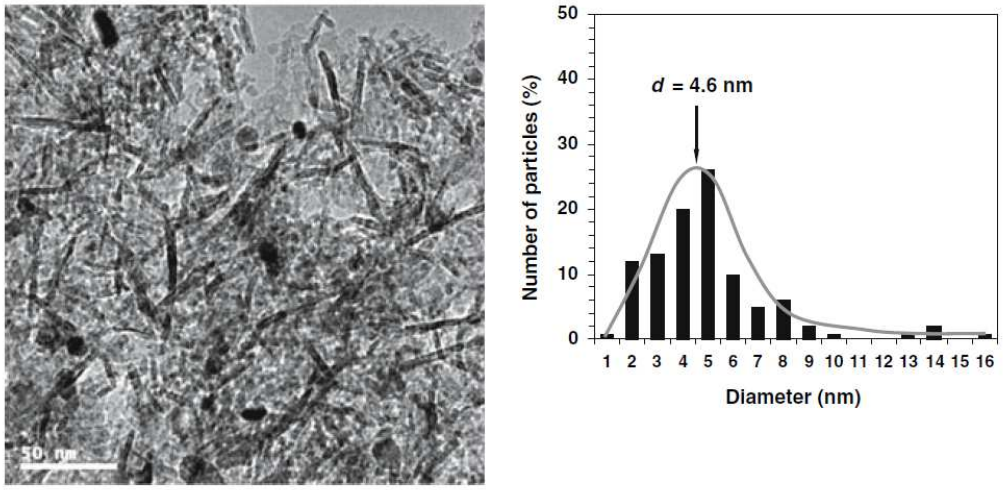


**Figure 2.14:** TEM image and histograms of ruthenium nanoparticles supported on alumina. Directly reproduced with permission from Zheng *et al.* [90].

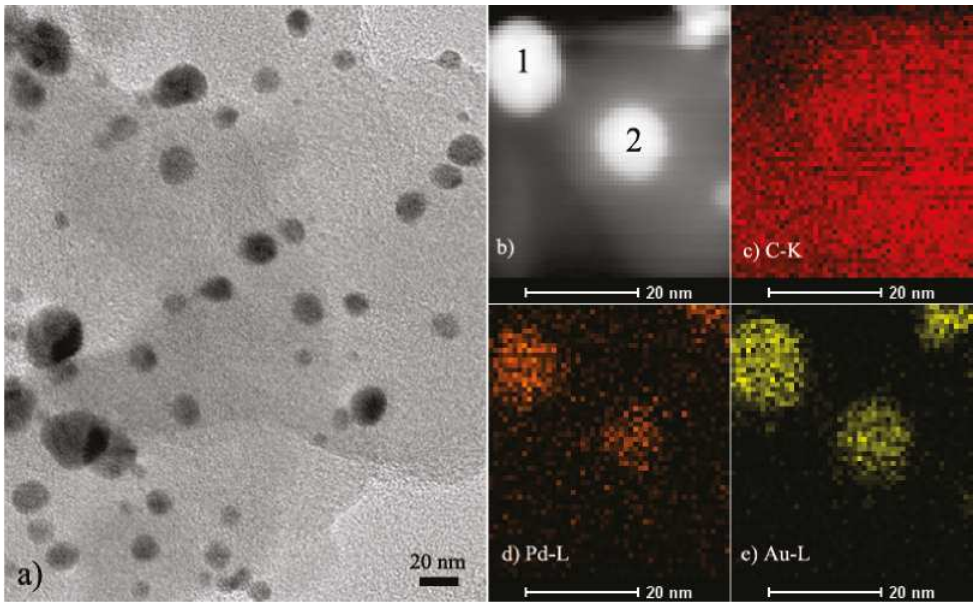


**Figure 2.15:** TEM and EDS images of PdAu@Au nanoparticles on carbon support. Directly reproduced from Zheng *et al.* [61].

Metal nanoparticle particle size and dispersion can also be estimated using pulse chemisorption measurements. In this technique the metallic surface area is estimated by the quantity of gaseous absorbent that is chemically absorbed to the metal surface; the supported metal nanoparticle diameter can be calculated given a metallic density and assuming a hemispherical geometry. This technique typically uses carbon monoxide or hydrogen as the absorbent; care must be taken to use the correct metal - absorbent stoichiometry and also that full surface saturation will occur under the experimental conditions [91].

In Figure 2.16, Zhang *et al.* [92] have used hydrogen chemisorption to estimate the nickel surface area and dispersion as a function of nickel loading on the alumina support (dispersion is calculated as the percentage of theoretical maximum dispersion where all of the metal is present on the surface).

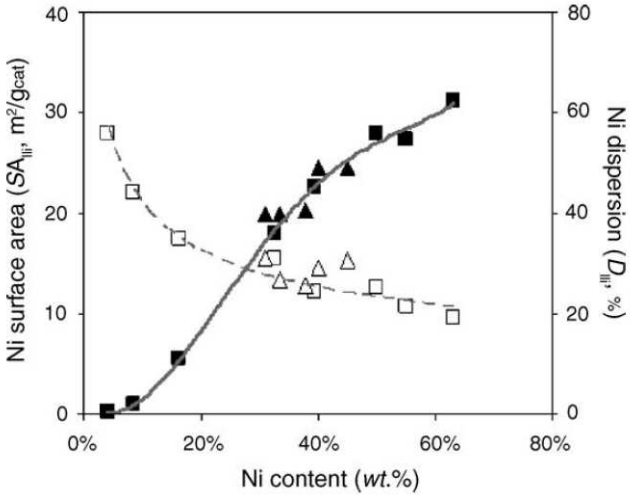


**Figure 2.16:** Results of $H_2$ chemisorption of nickel nanoparticles supported on alumina. Open symbols show dispersion and solid show surface area; triangles indicate where the alumina was modified with lanthanum. Directly reproduced from Zhang *et al.* [92].

An indication of metal nanoparticle dispersion can also be determined via X-ray diffraction (XRD). The diffraction angle of a known wavelength of electromagnetic radiation gives a characteristic diffraction spectra with peaks for different materials occurring at characteristic diffraction angles depending on the crystal structure (known as the Bragg angle, $2\theta$ ). When the diffraction peaks are well defined, the Scherrer equation (2.15) can be utilised to give an estimate of nanoparticle linear dimension, where $\beta$ is the half value breadth of the diffracted beam, $\lambda$ is the x-ray wavelength, $2\theta$ is the Bragg angle and $K$ is a constant of value 0.93 [93].

$$L = \frac{K\lambda}{\beta cos\theta} \tag{2.15}$$

Figure 2.17 shows the diffraction spectra of a range of a range of metal nanoparticles supported on MW CNTs [74]. The broad peak at around $26^o$ and $43 - 44^o$ is present in all cases and likely represents the diffraction spectra from the MW CNTs. Results for spectra **c** nickel and spectra **d** iron both display a clear sharp peak at $44^o$ representative of each metal. In the case of ruthenium (spectra **a**) the broad peak at $43 - 44^o$ appears broader and taller than with other metals. The metal dispersion was also estimated by CO chemisorption for each of these catalysts: Ru, Rh, Pt and Pd had a high dispersion of between 21 and 29 %. Ni and Fe were

lower at 14% and 9.8% respectively, this means that these two catalysts would have larger nanoparticle sizes with more defined crystal structure that produces clear peaks in the XRD spectra in Figure 2.17. In contrast, the catalysts with smaller nanoparticles (greater dispersion) do not produce clear peaks because of the poorly defined lattice structure.

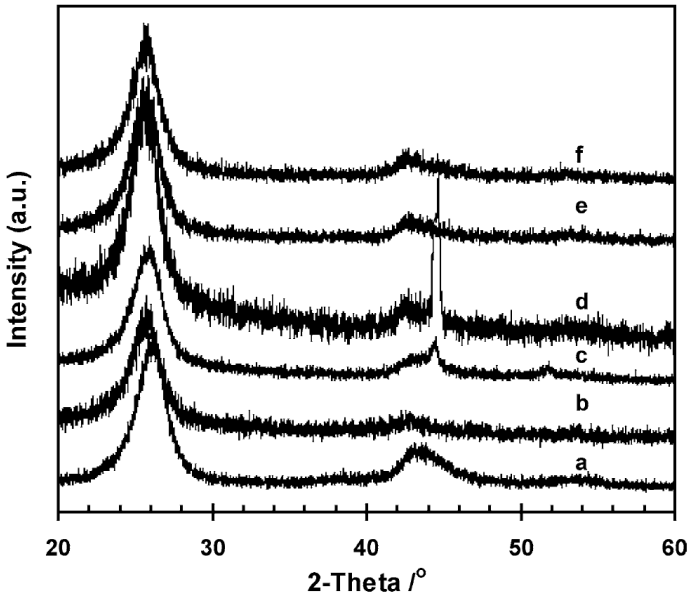


**Figure 2.17:** XRD spectra of metal nanoparticles on CNTs. Directly reproduced with permission from Yin *et al.* [74], **(a)** - Ru, **(b)** - Rh, **(c)** - Ni, **(d)** - Fe, **(e)** - Pt and **(f)** - Pd.

Temperature programmed desorption is a technique used to measure the interaction energies of the catalytic surface with a gas, typically carbon dioxide, ammonia or hydrogen. The $CO_2$-TPD profile was used by Yin *et al.* [74] to approximate the basicity of the support as a more basic support would interact more strongly with the $CO_2$ and the desorption would happen at a higher temperature. Heemeier *et al.* used temperature programmed desorption of CO from Co-Pd surfaces to determine the percentage of surface Co [94].

Temperature programmed desorption of nitrogen was used by a number of researchers to attempt to quantify the interaction energy with nitrogen by measuring the quantity of nitrogen surface coverage and the temperature at which it desorbs. Analysis of results from this technique is challenging: it is easy to conflate chemisorption with physisorption and the ease of which nitrogen desorption will occur does not necessarily correlate with the rate of ammonia decomposition because nitrogen desorption is not the limiting step in the reaction. Rarog-Pilecka *et al.* [95] used this technique to compare a supported ruthenium catalyst promoted with barium or cesium. They found that the more effective cesium doped catalyst had a greater

surface coverage of nitrogen and a lower desorption temperature although they attribute both of these factors to the barium doped catalyst not having achieved nitrogen saturation.

Temperature programmed reduction (TPR) is a widely used technique to determine the reduction characteristics of supported metal nanoparticles. It can be used to measure the temperature of reduction and also the quantity of hydrogen consumed. When multiple metal precursors are present in the un-reduced catalyst then TPR can be combined with mass spectrometry so that the temperature at which reduction events occur can be related to specific chemical interactions. In Figure 2.18, Rarog Pilecka *et al.* [96] use mass spectrometry to identify the evolution of water, ammonia and carbon monoxide during the TPR of ruthenium carbonyl precursor supported on carbon with cesium promoter.

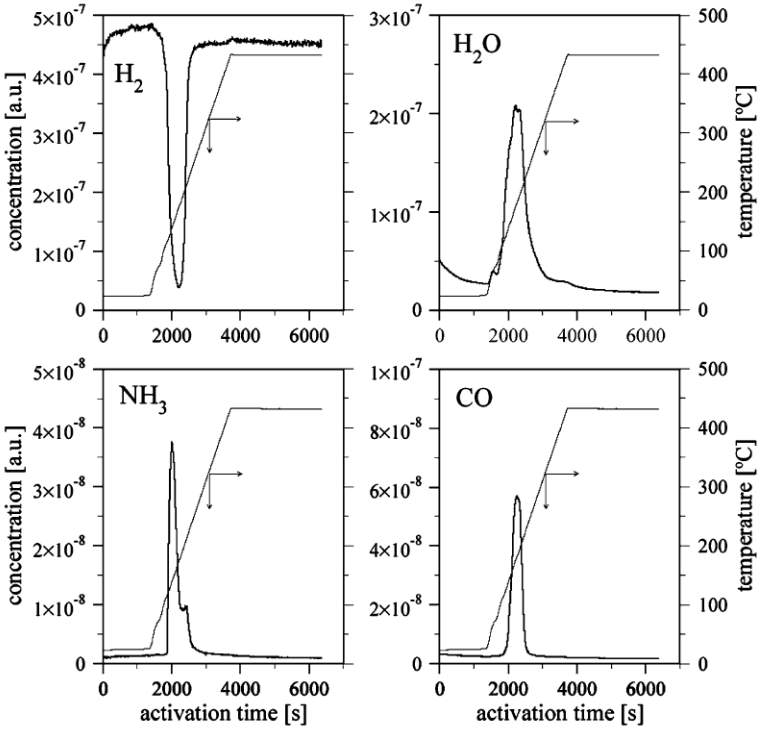


**Figure 2.18:** Analysis of cesium promoted ruthenium carbonyl precursor supported on carbon by TPR and mass spectrometry. Directly reproduced with permission from Rarog Pilecka *et al.* [96].

In conclusion, ammonia decomposition is both thermodynamically and kinetically limited at low temperature. The limiting step at low temperature is the recombination of nitrogen adatoms and the catalyst should be designed to facilitate this step. Ruthenium is the most active metal and its optimum nanoparticle size is between 1 - 3 nm due to the presence of $B_5$ sites rising to 2 - 5 nm for supported nanoparticles.

Bi-metallic systems have been shown to be more active than ruthenium in limited cases and show great promise. Metal selection for bi-metallic catalysts should be made with reference to the volcano curves produced by Ganley *et al.* [30] and Hansgen *et al.* [23] and the tendency for surface separation from density functional theory results. Mono-metallic catalysts can be synthesised by incipient wetness impregnation, core-shell catalysts are typically synthesised using in-situ reduction techniques although some success has been had using incipient wetness impregnation. Metal salts should be selected so that there is no risk of halogen contamination of the catalyst as this inhibits the reaction by electron withdrawal.

Multi-wall carbon nanotubes doped with electron donating promoters such as potassium and cesium are an effective support material as they facilitate electron transfer to the active site. Integrated basic supports comprising electron donating metals such as cesium nano-titanates and zirconia-potassium hydroxide have also been shown to be very active. The key property of a catalytic system for ammonia decomposition is the ability to transfer electrons to the active site. Carbon nanotube conductivity can be improved by graphitising which should improve activity.

## 2.5 Membrane Reactors & Fuel Cell Applications

The application of urea PEM fuel cells and ammonia PEM fuel cells is currently limited by ammonia poisoning of the Nafion™ membrane, the slow rate of the ammonia decomposition reaction and thermodynamic equilibrium at low temperatures. These problems could be overcome if a hydrogen selective membrane is used to improve conversion by reducing the partial pressure of hydrogen in the reactor and to ensure that only pure hydrogen is fed to the PEM fuel cell (see Figure 2.19). This would prevent fuel cell deactivation whilst also enabling overall conversion to exceed thermodynamic equilibrium. Accumulation of nitrogen in a membrane reactor will not have an inhibiting effect because the order of reaction is zero with respect to nitrogen (previously shown in Table 2.2).

This section considers the hydrogen perm-selective membrane technologies available. It includes examples where they have been applied to the ammonia decomposition reaction and considers their suitability to this application.

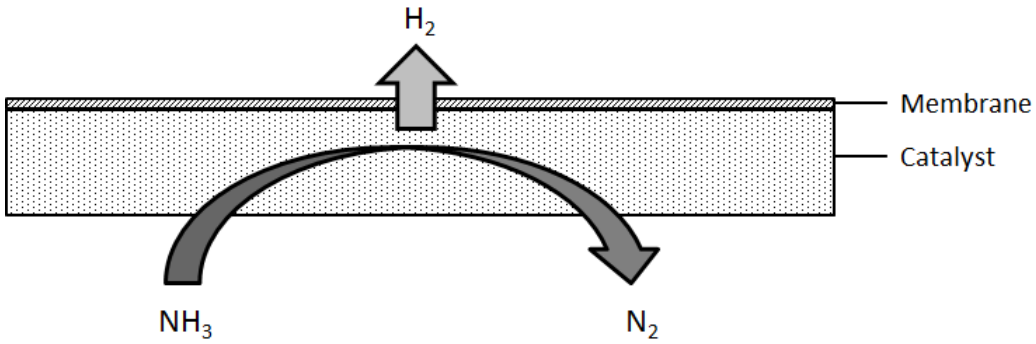


**Figure 2.19:** Schematic of the ammonia decomposition membrane reactor.

### 2.5.1 Transition Metal Membranes

Hydrogen permeation membranes are typically made from transition metals, transition metal alloys or transition metal composites. The metal is selected based on its ability to pass hydrogen by the solution-diffusion mechanism. In this mechanism, hydrogen dissociates on the metal surface and the protons and electrons permeate through the membrane before recombining to form molecular hydrogen on the other side (see Figure 2.20). Membranes of this nature achieve extremely high selectivity to hydrogen by virtue of the chemisorption mechanism, contaminants pass only by physical defects in the membrane such as micro-cracks and pinholes. Amorphous alloys have greater hydrogen transport capacity than pure metal membranes due to the greater number of lattice defects which increases the ease with which hydrogen can be incorporated and thus migrate through the membrane [97].

Palladium membranes are commonly used for hydrogen separation because of a combination of relatively high permeability and 100 % selectivity for hydrogen as well as resistance to high temperatures, solvents and corrosion [98]. Palladium catalyses the dissociation and recombination of hydrogen [97], step 2 in Figure 2.20. Palladium membranes are known to operate best above 670 $K$; below this, Pd-H phase transition occurs which leads to embrittlement and degradation [99]. Basile [100] stated that hydrogen embrittlement can be avoided by alloying the palladium with silver or copper; this also significantly reduces the cost. Palladium membranes are generally used between 670 - 1250 $K$ to enable high hydrogen flux rates [99].

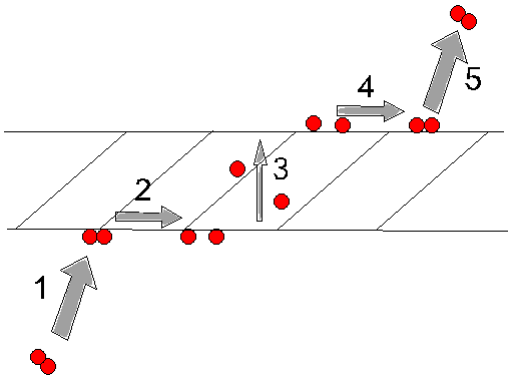


**Figure 2.20:** Solution diffusion mechanism for hydrogen permeation through a dense transition metal membrane. **1.** Adsorption; **2.** Dissolution; **3.** Diffusion; **4.** Recombination; **5.** Desorption.

There are a number of other metal membranes that can operate at lower temperatures with greater hydrogen flux than palladium (see Figure 2.21). Non-palladium metallic membranes tend to feature a body-centred cubic arrangement (BCC) which has one a single atom at the centre of a unit cell consisting of a cube of six atoms; this compares to the face centred cubic structure of palladium (FCC) which has an atom in the centre of each face and non at the centre of the unit cell (refer to Figure 2.8 for the relationship between metals and lattice structure). BCC structures are known to be formed by tungsten, vanadium, chromium, rubidium, niobium, molybdenum and tantalum. BCC membranes tend to allow for faster permeation than Pd-FCC structures although they are more susceptible to hydrogen embrittlement due to the precipitation of metal hydrides, caused by formation of gaseous hydrogen in lattice discontinuities. The embrittlement can lead to pinholes, cracking and total disintegration of the membrane [101]. Embrittlement is known to increase with decreasing temperature [102]. The resistance to embrittlement of Pd-Ag membranes is one of the primary reason that they are favoured above BCC metals.

Palladium FCC structures exhibit increasing permeability with increasing temperature but for BCC membranes the trend is reversed which makes them attractive for the low temperature PEM ammonia fuel cell application. BCC metal membranes are also not as effective in catalysing the hydrogen dissociation and recombination reactions [97] and are often coated with a 100 - 500 $nm$ palladium coating to catalyse hydrogen dissociation and recombination reactions [101].

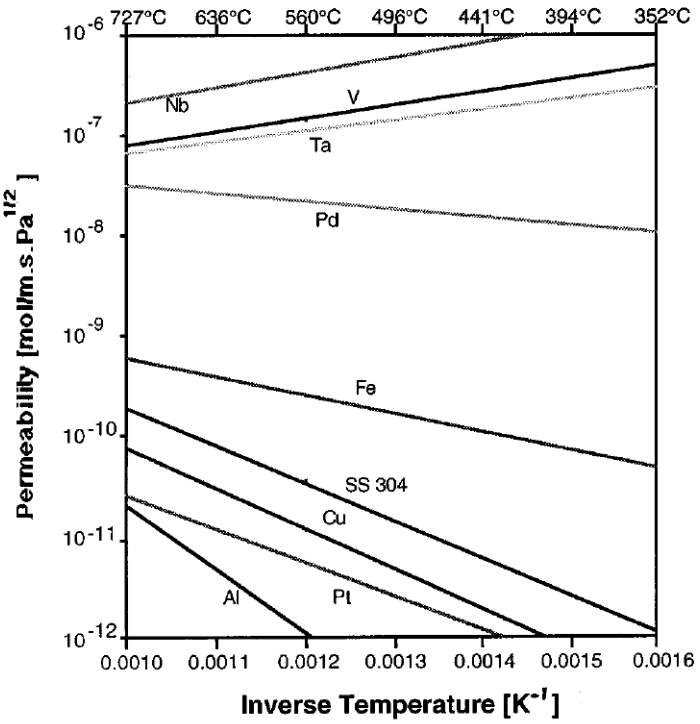


**Figure 2.21:** Hydrogen permeability of transition metals as a function of temperature. Directly reproduced from Buxbaum & Kinney [98].

Palladium membranes are vulnerable to inhibition and poisoning if exposed to $CO_2$ and $CO$. Mejdell *et al.* [103] noted a 27 % permeability inhibition effect of $CO_2$ upon a Pd-Ag alloy membrane caused by the adsorption of $CO_2$ onto the palladium surface. The impairment was greatest at reduced temperature. A similar competitive adsorption has been observed for $H_2O$ in which a reversible inhibition was observed for a Pd-Ag (80:20) membrane. $CO$ inhibition is an order of magnitude more severe upon a palladium membrane than $CO_2$ [104].

### 2.5.2 Inorganic Membranes

There are a number of non-metals that can be used to make hydrogen selective membranes including silica, zeolite, carbon and polymer [99]. Rather than the perm-selective mechanism of the metallic membranes, the inorganic membranes work by competitive diffusion and hence cannot achieve 100 % selectivity. Silica membranes consist of a network of 0.5 $nm$ pores which can achieve $H_2/N_2$ separation values of 10,000:1. Zeolite membranes can achieve separation efficiency of $H_2/N_2$ of 110-120:1 [99]. Carbon based membranes are also not suitable due to high cost and difficulty in handling. Polymer membranes also cannot achieve the high selectivity that is require for this application [99].

The selectivity of $H_2/NH_3$ is not reported in literature but it can be roughly approximated to the widely reported $H_2/N_2$ selectivity: ammonia is a smaller molecule than nitrogen and hence it might be expected that the separation efficiency of $H_2/NH_3$ would be less than $H_2/N_2$ given the competitive diffusion mechanism. In any case, the selectivity would have to be improved by around 3 - 4 order of magnitude for these membranes to achieve the maximum ammonia concentration of 0.1 *ppm*, this is almost certainly not achievable and so this class of membrane are not suitable for this application in the current state of the art.

### 2.5.3 Membrane Applications for Ammonia Decomposition

This section considers examples where researchers have used membrane reactor systems to enhance the ammonia decomposition reaction. Focus is paid to the overall yield of hydrogen and the suitability of the membranes to operate at PEM fuel cell operating temperatures. Some examples of ammonia decomposition membrane reactor applications are shown in Figure 2.5.

Israni *et al.* [105] utilised a palladium nano-porous membrane for the ammonia decomposition reaction upon a 2 mm thick $\alpha - Al_2O_3$ hollow fibre at 3 - 5 *bar* and 770 - 870 $K$ with a packed bed of nickel catalyst. They found that the use of the membrane reactor improved the hydrogen yield by 10 %. Li *et al.* [106] used a bifunctional catalytic membrane reactor with ruthenium on alumina as catalyst and a silica membrane to remove hydrogen. Ammonia conversion was improved from 45 % to 95 % at 723 $K$ but the $H_2/NH_3$ selectivity was only 200:1 which is many orders of magnitude too low for a PEM fuel cell application.

Brunetti *et al.* [107] combined a Pd-Ag membrane ammonia decomposition reactor with a PEM fuel cell and tested it between 573 - 723 $K$. They found that there was no deterioration in performance when the fuel cell was fed from the membrane reactor compared to commercially supplied hydrogen. Peak electrical yield was achieved with the membrane reactor operating at 250 kPa and 723 $K$.

These studies show that it is feasible to utilise Pd-Ag membrane reactors for ammonia decomposition. So far the lowest temperature considered is 573 $K$ which is 100 $K$ higher than the target temperature for a PEM fuel cell application. The membrane reactors were operated at enhanced pressure to facilitate the hydrogen permeation, typically between 2.5 - 5.0 *bar*. This could be problematic for an ammonia decomposition reactor at low temperature as the higher pressure will artificially modify the effective conversion beyond the limits of thermodynamic equilibrium.

**Table 2.5: Example membrane applications for ammonia decomposition**

| **Membrane** | **Temperature** / $K$ | $H_2$ Selectivity | |
|---|---|---|---|
| 3 $\mu m$ Pd on ceramic support | 623 - 773 | 5000 - 12,500 | [108] |
| 4 $\mu m$ Pd on $\gamma - Al_2O_3$ | 773 - 873 | 6600 | [105] |
| 40 $\mu m$ Pd on porous stainless steel | 523-673 | not measured | [109] |
| Silica | 723 | 100-700 | [106] |

In summary, hydrogen perm-selective Pd-Ag membranes have been shown experimentally to simultaneously improve the conversion of ammonia to hydrogen beyond the thermodynamic limitation and to purify hydrogen so as to be suitable for a PEM fuel cell. Although low cost inorganic membranes can be used to separate hydrogen, their inferior hydrogen selectivity to palladium membranes is inadequate for PEM fuel cell applications. Further investigation must be undertaken into the performance of Pd-Ag membranes at low temperatures.

Alternative metal membranes such as vanadium are likely to perform better at low temperature than palladium. They are known to be susceptible to hydrogen embrittlement and require the addition of an active metal for the hydrogen dissociation reaction and significant further development of this technology is required.

## 2.6 Literature Review Conclusions

This review has considered previous work on the suitability of ammonia to be used as a widespread hydrogen storage vector including safety and energy efficiency aspects. Fuel cell and hydrogen permeation membrane technologies have been studied to understand the practicalities of developing a point of use ammonia decomposition and purification integrated reactor. Finally, the state of the art in catalyst design for ammonia decomposition has been considered with the view to achieving low temperature activity. A number of gaps in the current state of the art with regard to the feasibility of the ammonia decomposition fuel cells are:

1. On the question of the suitability of ammonia for widespread use as a hydrogen storage vector there are some clear issues to be addressed. The toxicity of ammonia is an obvious hazard and the smell would detract from widespread uptake. These detractions can be potentially mitigated by storage of ammonia within metal ammine tablets however this also requires further development on the practicalities of doing this. Ammonia may also be considered more palatable in a carbon free future as the number of competitive technologies

would be much reduced. Very little has been done on the question of energy efficiency with most studies that have considered it assuming that the ammonia is obtained from methane and incurs substantial carbon dioxide emissions in the process.

2. While both alkali and solid oxide direct ammonia fuel cells have the advantage of not requiring any pre-conversion or purification of ammonia, they also exhibit significant drawbacks compared to the PEM fuel cell. The alkali fuel cell suffers from a very low power density and the solid oxide fuel cell raises potential issues regarding the very high operating temperature and operability questions. Both technologies are worthy of further development but priority should be given to development of the ammonia - PEM fuel cell in accordance with advice from the US DoE.

3. On the potential for an ammonia decomposition application for portable use, there is much remaining to be done. Palladium - silver membrane reactors have been shown to produce pure hydrogen however it is not clear whether the flux rates are sufficient to render the application cost effective. Experiments with silica membranes have demonstrated enhanced conversion of ammonia, this is encouraging because the application would have to operate in the thermodynamically limited regime and the use of the membrane will make this more viable. As yet there has been no example of a Pd-Ag catalytic membrane reactor for ammonia decomposition operating below 500 $K$ which must be done if the application is shown to be feasible.

4. There is a large body of literature on catalysts for ammonia decomposition however most work is focused on higher temperatures around 600 $K$. Few studies have attempted to explore low temperature activity that would be required for an integrated PEM fuel cell application. In general, it is known that ruthenium nanoparticles on high conductivity supports and highly basic promoters (or supports with a highly basic nature) are most active. Insights have also been gleaned from ammonia synthesis catalysts as the reversible nature of this reaction means that these catalysts will have similar properties to those for ammonia decomposition. Opportunities for future work should focus around understanding low temperature activity, particularly the promoter-support-nanoparticle interaction, and replacing ruthenium with cheaper and more abundant transition metals. Some studies have suggested that bi-metallics such as cobalt-molybdenum can perform better than ruthenium in certain conditions, but there has been little success to date in applying bi-metallics to enhance ammonia decomposition activity. Bi-metallic catalysts present interesting opportunities, while a lot has been done with regard to step-wise

in-solution reduction precipitation techniques, often with the use of colloids or surfactants as stabilisers, these techniques require many steps to prepare a heterogeneous catalyst that would present a challenge for scale-up to commercial application. Studies on the tendency of metals to migrate to the surface of a nanoparticle in different environments suggest that it may be possible to generate effective bi-metallic heterogeneous catalysts using simpler impregnation techniques.

The areas of focus for the experimental work in this thesis are: firstly, the development of low temperature catalysts and the replacement of ruthenium with more abundant metals; Secondly, to develop the understanding of the feasibility of the ammonia-PEM fuel cell concept with particular regard to energy efficiency and to quantify the use of scarce catalytic metals such as ruthenium and palladium.

# Chapter 3

# Experimental Methodology

Experimental techniques that have been applied widely in this study are described in this chapter. This includes techniques used for catalyst synthesis, kinetic testing of catalysts for ammonia decomposition and catalyst characterisation.

## 3.1 Synthesis of Catalysts

Catalysts were prepared by incipient wetness impregnation where the metal precursors were dissolved in solvent before deposition onto the support material filling the pore volume. The pore volume of the support material was found by applying successive drops of the solvent to be used via a Gilson pipette and observing when the support material failed to absorb additional solvent. The volume reported was that to achieve total pore saturation. Solvents used were water and acetone. Solutions of the metal salts to be deposited were made up to the exact wetness volume of the support and applied drop wise. The solvent used was removed by drying for 3 hours at 350 $K$ under vacuum. Active metals and promoters were either applied simultaneously or sequentially depending upon the desired catalyst and solubilities of precursors. Solid precursors were measured using an AND GH-252 balance with +/- 1 $mg$ error.

Catalysts were reduced under 38.8 $NmL\,min^{-1}$ of flowing hydrogen for three hours using the ammonia decomposition rig in its alternate capacity. The reduction temperature was varied depending upon the metal species present.

## 3.2 Characterisation of catalysts

### 3.2.1 Transmission Electron Microscopy

Transmission electron microscopy (TEM) experiments were undertaken using a Jeol TEM-2100 200 kV ultra-high resolution electron microscope at the Research Complex at Harwell facility (RCaH). Samples were prepared by depositing a suspension of the catalyst in ethanol upon a lacey carbon copper grid, the ethanol was removed by drying under vacuum. Energy dispersive x-ray sectroscopy (EDS) measurements were taken using an Oxford Instruments silicon drift detector (SDD) X-Max with 80 $mm^2$ detector size and a high angle annular dark field detector.

### 3.2.2 X-Ray Diffraction

Powder X-ray diffraction experiments (XRD) were undertaken using a Bruker AXS D8 Advance with monochromatised Cu-K$\alpha$ radiation ($\lambda = 0.15406\ nm$), 40 $kV$ and 40 $mA$. Powder samples were prepared in a 0.7 $mm$ diameter glass capillary tube using ultrasound. Non-powder samples were crushed prior to analysis.

### 3.2.3 CO Pulse Chemisorption

Metallic surface area of the supported nanoparticle catalysts was measured using a Micromeritics Autochem II 2920 apparatus equipped with a mass flow controlled gas manifold. Catalysts were tested in a quartz flow reactor located within a programmable furnace with outlet gas measurement by a thermal conductivity detector (TCD). 60 - 100 $mg$ of pre-reduced powder catalyst was prepared in flowing 5 % hydrogen in argon at the catalyst reduction temperature (ruthenium catalysts were treated at 513 $K$), the sample was then heated to 673 $K$ in 10 $mL\,min^{-1}$ of flowing helium to ensure removal of impurities. For the chemisorption experiments, the sample was cooled to 308 $K$ and the metal surface area was measured by sequential pulsing of 5 $mL$ of 5 % carbon monoxide in helium with 50 $mL\,min^{-1}$ of helium carrier gas.

The metal surface area can be estimated by the measurement of the total carbon monoxide that is chemically absorbed to the sample. This method assumes that the saturation consists of complete coverage of the metal at a known carbon monoxide to metal stoichiometry and metallic density.

### 3.2.4 Temperature Programmed Reduction

Temperature programmed reduction (TPR) experiments were conducted using the Micromeritics Autochem II 2920. To ensure the consistency of experimental results, the catalysts were subjected to a preparatory step to remove any absorbed material that might affect the results. 60 to 100 $mg$ of dried un-reduced catalyst was pre-treated at 773 K in 20 $mL\,min^{-1}$ of flowing argon before cooling to 323 $K$. For the TPR experiment and the gas flow was changed to 30 $mL\,min^{-1}$ of 5 % hydrogen in argon mixture, the reactor temperature was increased from 323 to 1173 $K$ at 10 $K\,min^{-1}$. The reactor exit gas was routed to a TCD via a cold trap maintained at 184 $K$ which was intended to remove water or other condensables that may be present.

### 3.2.5 Raman Spectroscopy

Samples were analysed using a Renishaw inVia Raman microscope with a 532 $nm$ diode laser.

### 3.2.6 Nitrogen Adsorption / Desorption Analysis

The surface area and structure of the catalyst supports was determined by nitrogen adsorption / desorption analysis conducted at 77 K using an ASAP 2020 from Micromeritics. Samples of approximately 100 $mg$ were degassed first by heating to 523 $K$ under ultra-high vacuum before undertaking the adsorption / desorption analysis. Surface area was calculated according to the Brunauer, Emmett and Teller (BET) method, pore size and volume was measured according to the Barrett, Joyner and Halenda (BJH) method with the Halsey-Faas correction.

## 3.3 Ammonia Decomposition Catalyst Testing Rig

### 3.3.1 Design and Construction of the Catalyst Testing Rig

The objective of this experimental method is to determine the rate of reaction for ammonia decomposition as a function of temperature for powder catalyst in a flow system. This requires an accurate measurement of the mass balance and determination of the change in composition before and after the catalyst bed. The temperature of the bed must be known to reasonable precision and the control of that temperature must be appropriate to the rate of temperature increase.

In a typical experiment, 2.7 $NmL\,min^{-1}$of anhydrous ammonia (99.999 % purity with maximum 1 $ppm$ water) and 6.1 $NmL\,min^{-1}$of helium were flowed over a packed bed with 25.0 $mg$ of catalyst dispersed in 450 $mg$ of average 360 $\mu m$ diameter, silicon carbide (SiC). Before the inlet of the catalyst bed, a bed of 175 $mg$ of fine SiC powder of average diameter 53 $\mu m$ ensures that plug flow conditions exist. All reagents were measured using an ADS GH-252 balance accurate to +/- 1 $mg$.

The inlet flowrates were controlled using Bronkhorst mass flow controllers (MFCs), catalyst temperature was measured using an in-situ type K thermocouple located at the exit of the bed. Reactor exit composition was measured using a GC with a Porapak Q column and thermal conductivity detector (TCD). During each experiment, the temperature was ramped from around 450 $K$ to 850 $K$ at 2.6 $K\,min^{-1}$ using a Carbolyte ™ tubular furnace with PID control.

These experiments were conducted using a bespoke catalyst testing rig which was designed, constructed and commissioned as part of this project. As well as testing for activity for ammonia decomposition, the rig was also used to undertake in-situ reduction in flowing hydrogen and to provide known composition gas mixtures for calibration of the GC. The rig design is shown in the P&ID in Figure 3.1 which displays all of the key equipment items and control methods. The rig consists of three distinct sections: gas inlet, reactor and analysis.

The gas inlet section is a manifold with flow control and measurement that enables known mixtures to be made of ammonia, helium, hydrogen and nitrogen gases. Gas flows from pressurised bottles via pressure control regulators and enters the rig enclosure via bulkhead fittings. Each gas apart from ammonia passes through a 3A molecular sieve drying bed to remove any entrained moisture. Finally, all gases pass through an in-line filter, high accuracy mass flow controller (MFC), a non-return valve to prevent back flow and contamination of gas sources and a ball valve to provide isolation from the gas mixing manifold. The ammonia system is lagged and heated with electrical heating wire to 323 - 333 $K$ (this heating system covers all areas of flowing ammonia after it enters the rig enclosure).

The reactor section takes flow through 1/8" stainless steel tubing from the gas mixing manifold, via a pressure transducer and to the 4 mm inside diameter (ID) quartz tube reactor. The fitting from stainless steel to quartz tube uses a PTFE ferrule. The reactor is a U-bend configuration with vertical alignment within the tubular furnace, the catalyst and silicon carbide is in the second half of the reactor held in place with quartz wool. At the immediate exit of the catalytic bed and within the reactor, an in-situ type K thermocouple measures the temperature at the exit of the catalytic bed. The flow passes back to 1/8" stainless steel tubing via a fitting with graphite ferrule to handle the elevated temperature, the pressure is measured

by pressure transducer and flow passes outside of the rig enclosure via a bulkhead fitting.

In the analysis section, the reaction gas flows directly to the agilent 7820A GC fitted with a Porapak Q column and thermal conductivity detector. The flowing gas exiting the GC is routed via an empty knockout pot and then bubbled through dilute acid to remove residual ammonia before discharge to the laboratory ventilation system. The knockout pot serves to prevent backflow of dilute acid to the GC in the event of a pressure irregularity in the system.

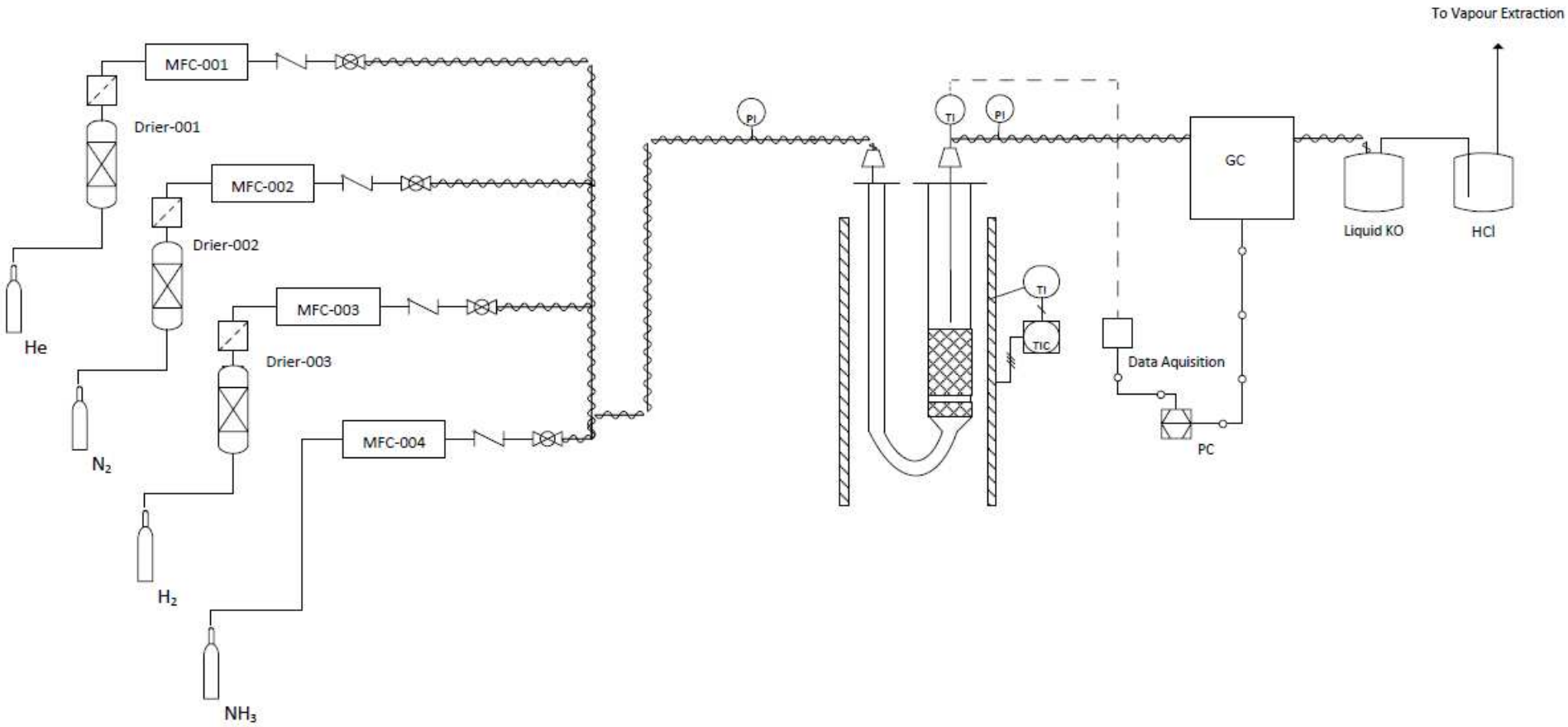


**Figure 3.1:** P&ID of the ammonia decomposition catalyst testing rig

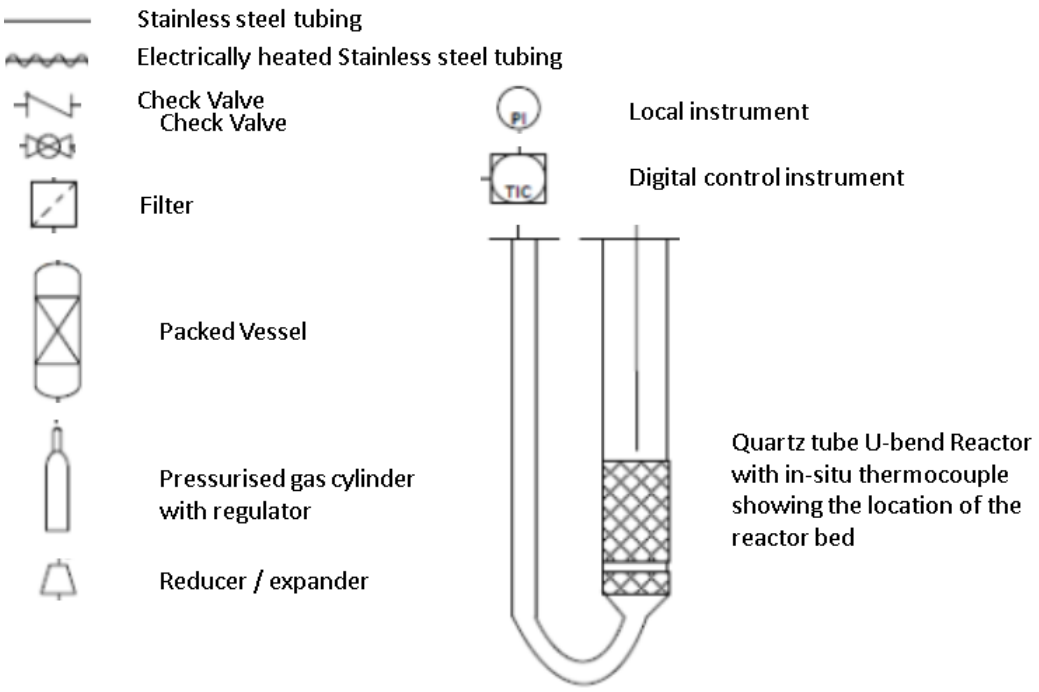


**Figure 3.2:** P&ID Legend

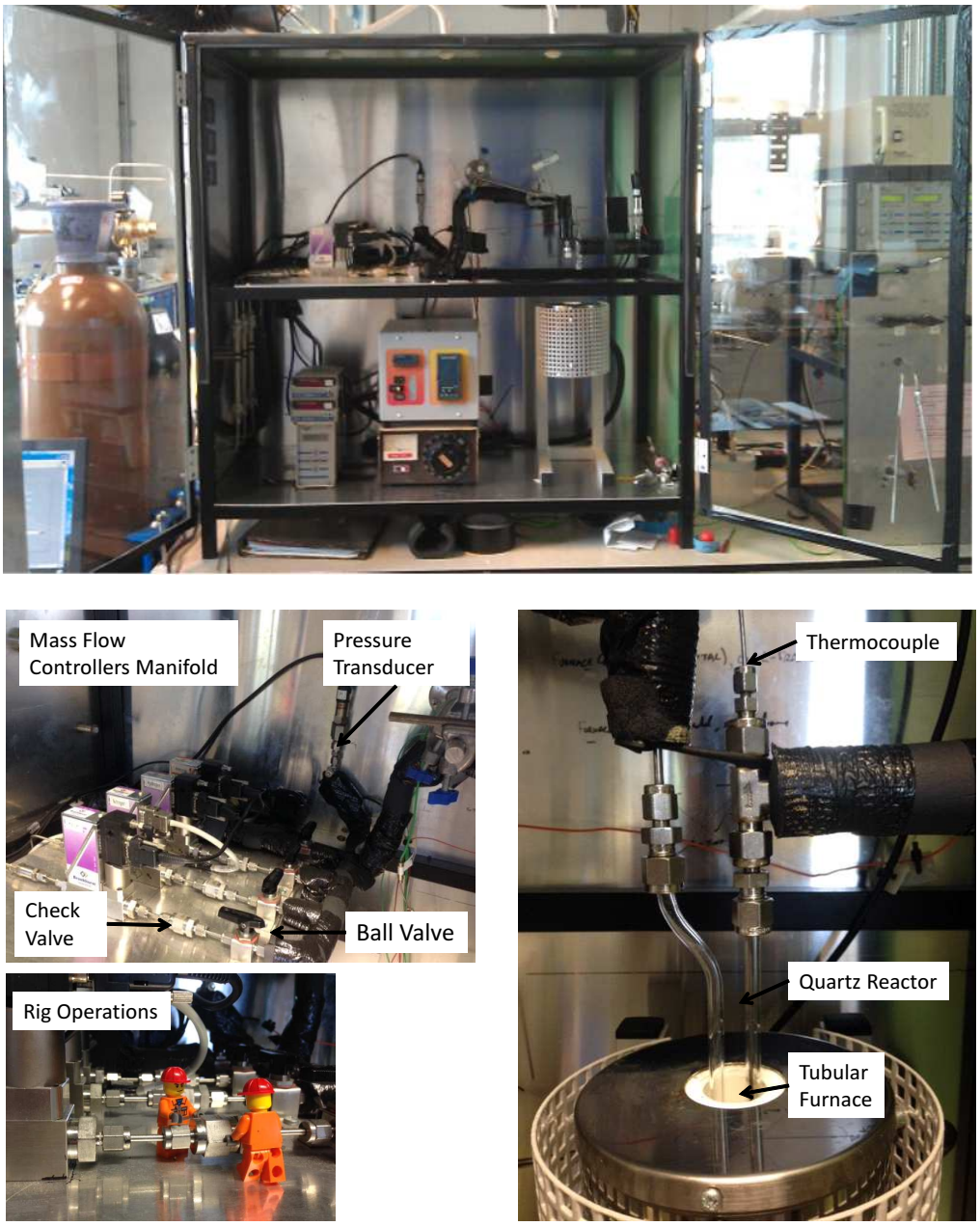


**Figure 3.3:** Images of the catalyst testing rig. Clockwise from top: entire apparatus showing perspex doors; close up of quartz reactor and furnace showing thermocouple location; example of rig operation and layout of the gas manifold showing mass flow controller and valve arrangements.

In addition to providing the required experimental accuracy for kinetic testing of catalyst, the rig also had to satisfy a number of safety and reliability concerns. Ammonia when combined with even trace water presents a risk of either metallic corrosion or degradation of other materials such as elastomers that are widely used as seals in equipment. Many commonly used metals, elastomers and plastics such as brass, copper, nitrile rubber and chlorofluorocarbons are not compatible for use with ammonia and great care has been taken to specify only ammonia compatible

materials. All metals and joints used in the rig are stainless steel apart from the quartz reactor fittings which are PTFE (polytetrafluoroethylene), all plastics are either PTFE or PVC (polyvinylchloride). Elastomers used in gaskets are EPDM (ethylene propylene diene terpolymer). All material compatibility was checked using the Cole Palmer chemical compatibility database [110] and the Air Liquide Gas Encyclopedia [111]. These considerations were applied to equipment purchased and constructed locally as well as for third party deliverables such as mass flow controllers. As a further precaution, all of the flow lines with ammonia were heated to 323 - 333 $K$ and insulated to reduce the risk of the condensation of water during testing. The length of all dead legs has been minimised as much as practicable and pressure instruments have been installed in the correct vertical orientation.

The most important aspect of the design was safety, this reflects both the toxic nature of ammonia and also its potential to create an explosive atmosphere. The most likely initiating event would be a leak of ammonia; to minimise this risk, all fittings were rigorously leak tested and additionally the connections to the quartz reactor were proven to be leak free before commencing every experiment. As back-up to this, the ammonia rig was kept in a semi-enclosed space along with an ammonia alarm to provide warning of any leak. To prevent the risk of flammable gas concentrations accumulating inside the apparatus, the system was purged with helium before any flammable gas was introduced. This was done at the beginning and at the end of all experiments. Effluent gas from the system was routed to a fixed extraction point via a knock-out pot and an HCl gas scrubber to remove effluent ammonia.

### 3.3.2 Demonstration of Experimental Validity

#### Evaluation of Mass Transfer and Kinetic Limitations

To understand the kinetic activity of a catalyst, it is important that the experimental data is representative of this kinetic activity and not of other factors that can become rate limiting such as mass transfer. In this section, a number of experimental and analytical assessments are made of the experimental method to ensure that the results gathered are truly reflective of the catalyst performance. This validity study assesses the closeness to ideal plug flow conditions in the catalyst bed; it considers how closely the experimental results conform to known kinetic and mass transfer relationships and finally it assesses the control and measurement of temperature variation throughout the catalytic bed.

The reactor geometry, packed bed design and reagent flowrates have been designed to achieve ideal plug flow conditions (see Figure 3.4). The quartz tubular reactor has an internal diameter of 4 mm and is aligned vertically to promote radial uniformity

in the catalyst bed. A 10 $mm$ long, 0.3 $mL$ volume, inert bed of 53 $\mu m$ inert SiC particles located before the catalytic bed is designed to promote plug flow at the entrance to the catalytic bed to ensure even gas distribution. The powder catalyst is diluted with silicon carbide (SiC) which is inert with respect to the reactions considered here. It is used to promote consistent packed bed catalyst distribution and to promote equithermal conditions. The catalyst bed is 33 $mm$ long, 0.41 $mL$ volume, and consists of powder catalyst and 360 $\mu m$ SiC inert particles giving a reactor diameter to particle size ratio of 10, significantly greater than generally accepted ratio of 4 for packed bed design. The superficial gas velocity varies from 1.6 – 3.1 $cm\,s^{-1}$ for temperatures between 400 – 800 $K$ giving residence times of 0.6 to 1.2 $s$ (assuming bed voidage of 0.4). The particle Reynolds number in the catalyst bed is 40 meaning that flow in the interstitial channels would be laminar as is characteristic of plug flow in packed beds. These values are such that plug flow can be expected to occur.

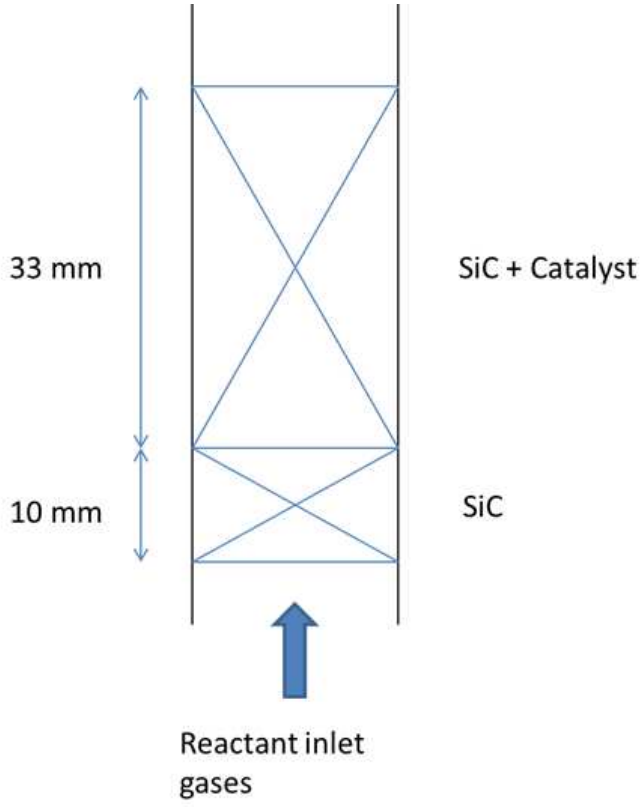


**Figure 3.4:** Schematic showing the catalyst bed geometry

The relationship between the experimental rate of reaction and temperature can be compared to theoretical kinetic and mass transfer relationships to infer whether the rate of reaction was limited by mass transfer or reaction kinetics. Should the rate of reaction be limited by surface kinetics, the relationship between the rate of reaction

and temperature will be described by the Arrhenius equation (3.1) where $k$ is the rate constant, $A$ is the pre-exponential constant, $E_a$ is the activation energy of the reaction, $R$ is the universal gas constant and $T$ is the temperature of reaction. This will be true if the concentration of reagents does not vary as a function of either reactor bed radius or a location inside or outside the catalyst pores.

$$k = A\, e^{\frac{-E_a}{RT}} \tag{3.1}$$

The nature of mass transfer within the catalyst bed can be approximated by the particle Reynolds number, calculated to be 40 under experimental conditions, which suggests that flow through the bed channels will be laminar. This means that Fickian diffusion will govern mass transfer, both within the interstitial channels between particles and in the boundary layer around catalyst particles. Within the catalyst particle, mass transfer through large pores will be governed by Fickian diffusion and through small pores by Knudsen diffusion. To better understand this effect, published correlations that describe the relationship between the diffusion coefficient and temperature for both Fickian and Knudsen diffusion can be used (3.2 and 3.3) [112]. $D_{AB}$ is the relative diffusivity of component A relative to component B in Fickian diffusion, $D_A$ is the diffusivity of component A in Knudsen diffusion and the equations allow the diffusivity constants to be estimated for at $T_2$ & $P_2$ from a known diffusivity at $T_1$ & $P_1$. Thus it can be ascertained whether the rate of reaction is limited by Fickian or Knudsen diffusion or kinetically limited by comparing the change in the experimental data rate of reaction as a function of temperature with these theoretical predictions. If the rate of reaction is limited by Fickian diffusion then the rate of reaction should increase by the ratio of temperature increase to the power of 1.75 (see Equation 3.2). If the rate of reaction is limited by Knudsen diffusion then the power would be 0.5 (see Equation 3.3).

$$D_{AB}(T_2,\, P_2) = D_{AB}(T_1\, P_1)\, \frac{P_1}{P_2} \left(\frac{T_2}{T_1}\right)^{1.75} \tag{3.2}$$

$$D_A(T_2) = D_A(T_1) \left(\frac{T_2}{T_1}\right)^{0.5} \tag{3.3}$$

The relationship between the experimental data for the rate of reaction and temperature has been used to gain further insight into the rate limiting mechanism. Figure 3.5 shows the Arrhenius plot of experimental data for 7.0 wt.% Ru, 4 wt.% Cs on graphitised carbon nanotubes. If the rate of reaction were mass transfer limited, then the relationship between the rate of reaction and temperature would be governed by equations 3.2 or 3.3 depending on the mass transfer mechanism. To

simulate this, the predicted increase in rate of reaction calculated by these equations from a starting point at 5 % conversion has been plotted alongside the actual experimental data. 5 % conversion was chosen as the starting point because the relative experimental error is too significant below this. The gradient of the straight line section of the experimental data is far steeper than that predicted by either Fickian or Knudsen diffusion suggesting that the rate of reaction is not limited by these forms of mass transfer.

The experimental data plotted as an Arrhenius plot in Figure 3.5 shows a threshold conversion at which the straight line relationship no longer holds. When conversion is below 30 %, it appears that the rate of reaction follows Arrhenius kinetics and consists of a straight line relationship. When conversion reaches 30 %, the relationship with temperature changes as mass transfer limitations from the bulk to the catalyst surface become dominant. From this analysis it can be concluded that the experimental data is kinetically limited up to approximately 30% conversion.

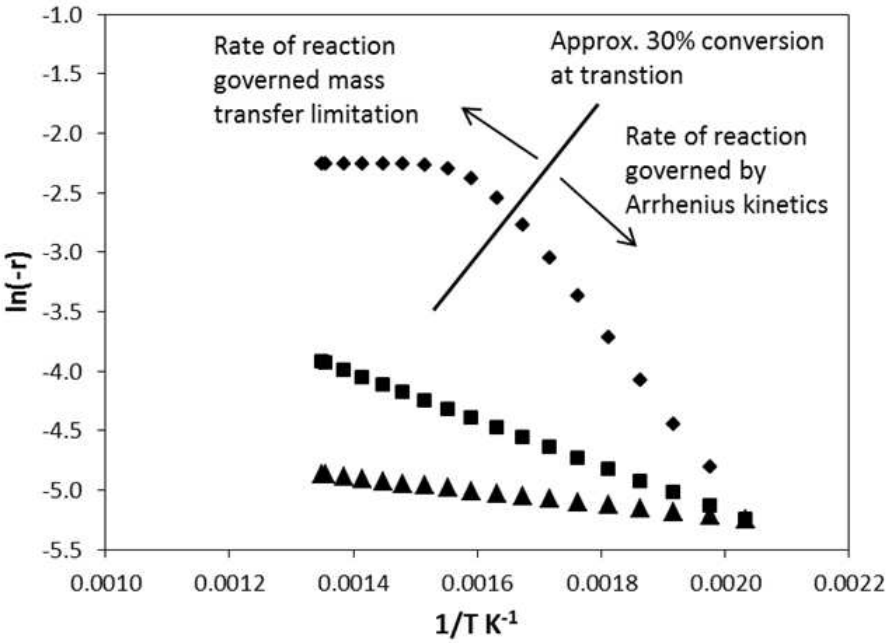


**Figure 3.5:** Arrhenius drawing of experimental Data (◆) showing the transition from kinetic to mass transfer limited regions and contrasted against the predicted results for Fickian (■) and Knudsen (▲) limited scenarios. Experimental results are for 7 wt.% Ru, 4 wt.% Cs on graphitised CNTs.

To examine further the influence of any mass transfer limitation upon the validity of experimental results, a catalyst with 7.0 *wt.*% ruthenium on graphitised CNTs was tested using three different inlet gas flowrates and compositions. Although there is some variation in the Arrhenius curves presented in Figure 3.5, this could be due to

experimental error and it seems that the change in mass transfer resulting from the variation in flowrates through the bed does not significantly affect the experimental results for rate of reaction.

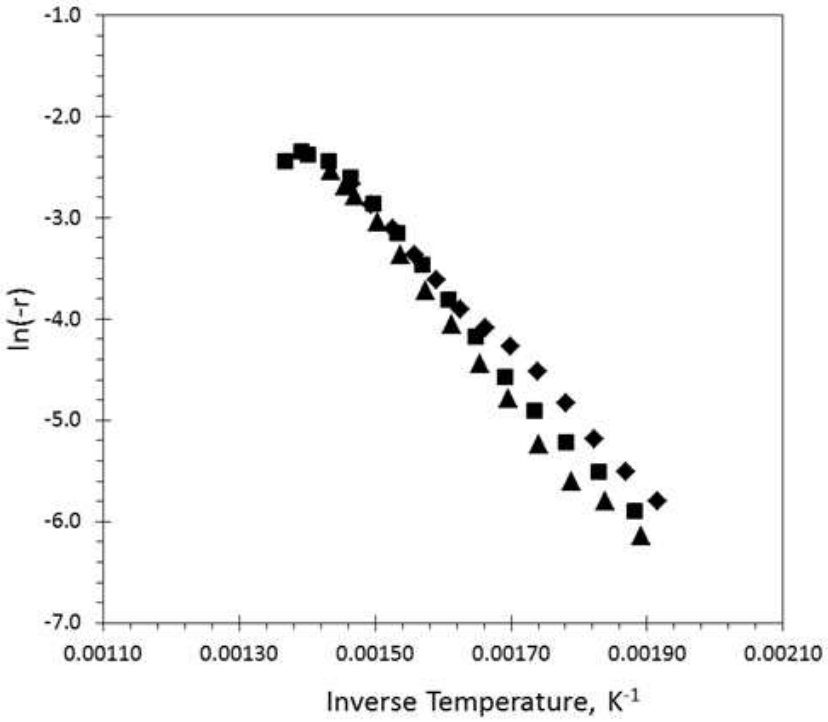


**Figure 3.6:** Comparison of different superficial gas velocities upon the rate of reaction for 7 $wt.\%$ Ru on graphitised CNTs. Each run has 2.6 $NmLmin^{-1}$ of ammonia diluted with 2.8 $NmLmin^{-1}$ of He (◆), 6.1 $NmLmin^{-1}$ of He (▲) and 9.1 $NmLmin^{-1}$ of He (■) giving overall gas hourly space velocity of 12400, 20800, 27100 $NmL\,h^{-1}\,g_{cat}^{-1}$ respectively. Ammonia WHSV was 5,200 $mL_{NH_3}\,h^{-1}\,g_{cat}^{-1}$ in all cases.

The repeatability of the testing procedure was examined in Figure 3.7 which shows the same batch of catalyst tested on three separate occasions. The three curves for conversion as a function of temperature are a close match suggesting that the testing procedure produces consistent and comparable data.

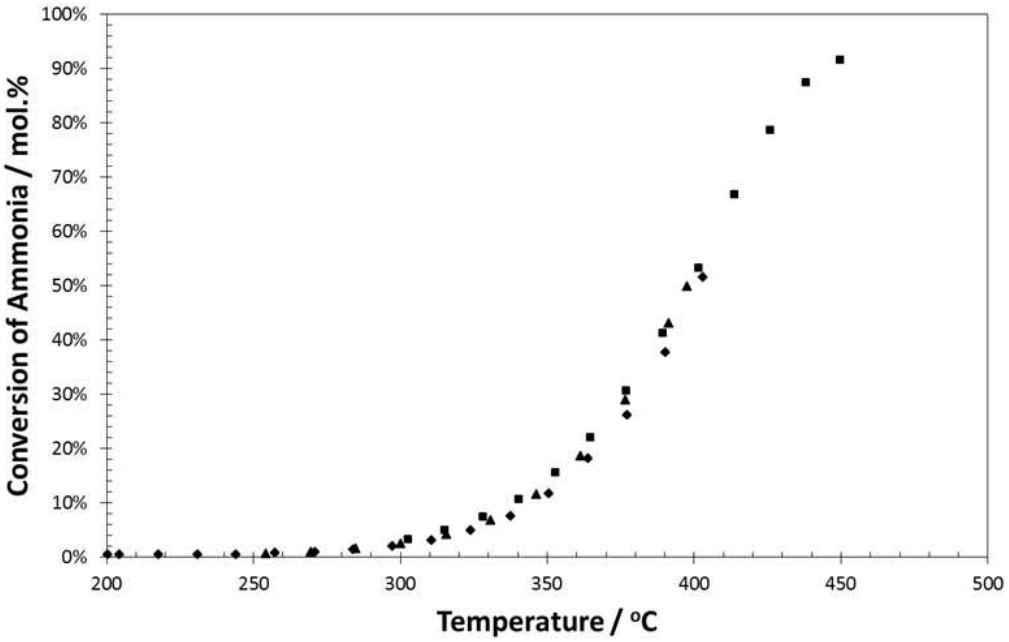


**Figure 3.7:** Repeatability test of catalyst synthesis and kinetic experiments for a 7.0 wt.% ruthenium on carbon nanotube catalyst. ▲ and ◆ show results from different tests on the same catalyst batch. , ■ shows the results from a different catalyst batch.

A blank test was conducted to ensure that all reported activity for ammonia decomposition experiments relates solely to the activity of the catalyst. A reactor was loaded using the normal procedure and tested under the conditions detailed in section 3.3.1 but without the addition of catalyst. Materials present that had the potential to be active were the quartz reactor, the quartz wool, both grades of silicon carbide diluent and the in-situ thermocouple. The experiment studied temperatures up to 800 $K$ and found that no detectable hydrogen was produced. From this it can be concluded that all measured activity by this apparatus under these flow conditions and up to 800 $K$ can be attributed to the activity of the catalyst.

### 3.3.3 Equipment Calibration

#### Mass Flow Controllers

A rising meniscus flow meter (bubble meter) was used to calibrate the four mass flow controllers (MFCs). The duty gas was used for hydrogen, nitrogen and helium. Nitrogen was used to test the ammonia MFC because the solubility of ammonia in water made use of the rising meniscus flow meter impractical. Instead, nitrogen was used and the manufacturers conversion factor was applied. The calibration conditions were 295 $K$ and atmospheric pressure. The calibration curves for each MFC are shown in Figure 3.8

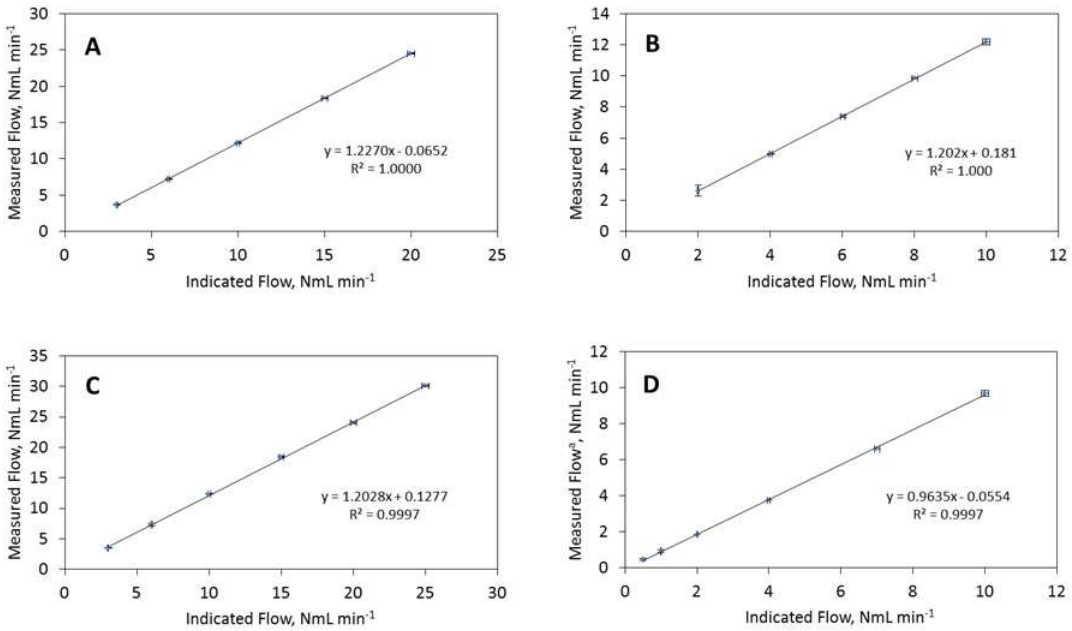


**Figure 3.8:** Calibration results for mass flow controllers. **A** - Helium, **B** - Nitrogen, **C** - Hydrogen, **D** - Helium. The ammonia MFC was calibrated using nitrogen then converted for ammonia using the manufacturers recommended conversion factor.

### Thermocouples

Three type K thermocouples were used in the experimental apparatus. Two sit below the tubing insulation upstream and downstream from the reactor to confirm the efficacy of the electrical heat tracing. The third thermocouple measures the temperature within the reactor immediately after the catalyst bed and can measure temperatures up to 1523 $K$. Type K thermocouples have an accuracy of +/- 0.75 % above 273 $K$, they have been calibrated against a platinum resistance thermometer which has an accuracy of +/- 0.1 $K$ using a Jupiter 650S dry block calibrator which has a thermal stability of +/- 0.02 $K$ up to 523 $K$ and +/- 0.03 $K$ up to 923 $K$. The calibration results are shown in Figure 3.9, the thermocouples were within the quoted error tolerance.

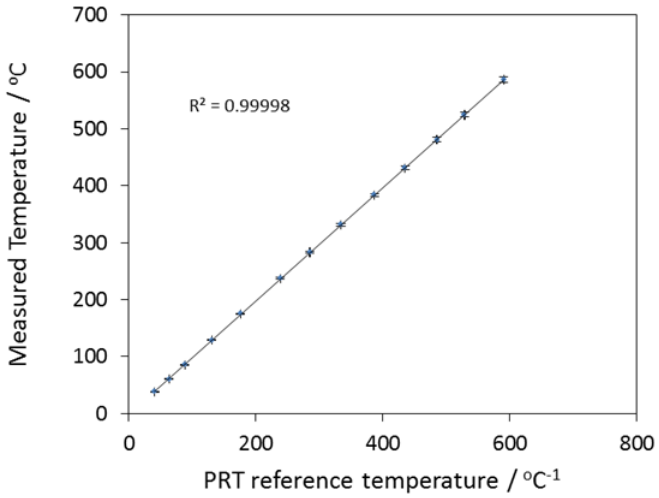


**Figure 3.9:** Calibration results for Type K thermocouples against a platinum resistance thermometer using a Jupiter 650S dry block calibrator.

### Gas Chromatography

GC experiments were undertaken using an Agilent 7820A with on-line sampling. The oven temperature was 333 $K$, the helium carrier gas flow was 10 $mL\,min^{-1}$, the thermal conductivity detector (TCD) was operated at 423 $K$ and the helium reference gas flow was 15 $mL\,min^{-1}$. The hydrogen and nitrogen peaks elute within the first two minutes, after this the oven temperature was ramped to 403 $K$ so as to speed the passage of ammonia through the column. The mass balance was resolved using the hydrogen concentration and hence the temperature ramp did not affect the experimental error.

The chromatographic separation of ammonia, nitrogen and hydrogen is made challenging by the strongly disparate nature of nitrogen and hydrogen to the more polar ammonia. This means that a column for separation of nitrogen and hydrogen is likely to require a long time to elute ammonia and a column good for resolution of ammonia from nitrogen would tend to elute nitrogen and hydrogen simultaneously. The Porapak Q column selected belongs to the first category and gives excellent resolution of hydrogen and nitrogen peaks enabling closure of the experimental mass balance.

The GC was calibrated at frequent intervals, the relationship between TCD output and hydrogen concentration was best represented by a quadratic relationship which achieves a high $R^2$ value. A review of the literature on this subject revealed that hydrogen gives a non-linear response with a TCD and thus it is appropriate to use a non-linear relationship to describe it. The TCD measurements of hydrogen by

Snavely and Subramaniam [113] have been reproduced in Figure 3.10, the calibration for this current work corresponds roughly with regions one and two which explains why a quadratic fit is required for the calibration curve.

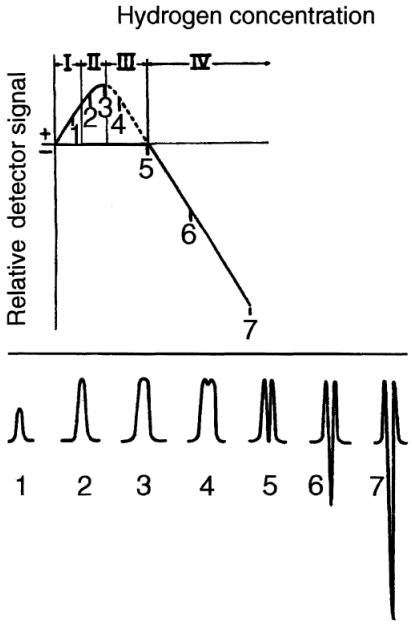


**Figure 3.10:** Response of a thermal conductivity detector to hydrogen concentration. Numbers one to seven show the different peak shapes, directly reproduced with permission from Snavely *et al.* [113].

### 3.3.4 Calculation of Reaction Rate and Error Analysis

The degree of reaction conversion was calculated by the following protocol. Known quantities are the inlet molar flowrate and composition of ammonia ($F_{NH_{3-in}}$) and helium ($F_{He}$) measured by mass flow controllers, the outlet mole fraction of hydrogen ($x_{H_2-out}$) measured by the GC, mole fraction of nitrogen ($x_{N_2-out}$) calculated from reaction stoichiometry and the outlet molar flowrate of helium which is unchanged. The other known quantity used in the calculation is the reaction stoichiometry where one mole of ammonia is converted to $^3/_2$ moles of hydrogen and $^1/_2$ moles of nitrogen. The mass balance was solved to give overall conversion of ammonia ($X_{NH_3}$) by an iterative technique that consisted of the following steps:

1. Assume a value for the outlet mole fraction of ammonia $x_{NH_3}$
2. Calculate total outlet flowrate: $F_{tot-out} = \frac{F_{He}}{\left(1-x_{H_2-out}-x_{N_2-out}-x_{NH_3-out}\right)}$
3. Calculate outlet molar flowrate of ammonia: $F_{NH_3-out} = F_{tot-out}\, x_{NH_3-out}$
4. Calculate overall conversion of ammonia: $X_{NH_3} = \frac{F_{NH_3-in}-F_{NH_3-out}}{F_{NH_3-in}}$

5. Calculate the outlet mole fraction of hydrogen: $x_{H_2-out} = \frac{F_{NH_3-in} X_{NH_3} {}^{3}/_{2}}{F_{tot-out}}$

6. Compare the value calculated of the outlet mole fraction of hydrogen to the measured value. Change the value of $x_{NH_3}$ until the values are the same (this was executed using the goal seek function in Microsoft Excel® using VBA code).

The turnover frequency (TOF) calculated at exit conversion with a ruthenium catalyst was calculated by multiplying the conversion by the ammonia flowrate and dividing my the moles of ruthenium, $N_{Ru}$ (see equation 3.4):

$$TOF = \frac{X_{NH_3} F_{NH_3-in}}{N_{Ru}} \tag{3.4}$$

Uncertainty in mass balance closure arises from error in the MFC that affects the measured ammonia inlet concentration and error in the GC peak area measurement that affects the calculation of ammonia outlet concentration. The accuracy of mass flow controllers is +/- 1 % of full scale and the GC claims a repeatability of peak area measurement of +/- 2 %. From this, the relative uncertainty of ammonia inlet flowrate is +/- 3.8 % and the relative uncertainty in measurement of helium flowrate is +/- 3.3 %. From the GC, the relative uncertainty of hydrogen outlet concentration is +/- 2 %. For a typical 7 $wt.$% ruthenium catalyst, the error in ruthenium loading is +/- 6.7 %. Uncertainty of temperature measurement is taken from the manufacturers quoted precision of +/- 5 $K$ which is approximately +/- 1.25 % at typical testing temperature.

All error is estimated using the standard techniques for estimating error propagation.

- For addition or subtraction: If $Q = a+b-c$, then $\delta Q = \sqrt{(\delta a)^2 + (\delta b)^2 - (\delta c)^2}$ where Q, a, b and c are any real variables [114].
- For multiplication of division: If $Q = \frac{a\,b}{c}$, then $\frac{\delta Q}{Q} = \sqrt{\left(\frac{\delta a}{a}\right)^2 + \left(\frac{\delta b}{b}\right)^2 + \left(\frac{\delta c}{c}\right)^2}$ where Q, a and b are any real variable [114].

These equations to estimate the propagation of experimental uncertainty were applied to the experimental steps 1-5 outlined above. The error estimate given here is for 20 % conversion at which the turnover frequency and activation energy was evaluated. From propagation of uncertainty, the error in total outlet molar flowrate $F_{tot-out}$ is +/- 4.3 % (error in the denominator arises from the measured mole fraction of hydrogen and nitrogen only). Error in the calculated conversion of ammonia $X_{NH_3}$is +/- 4.8 %. Error for the calculated turnover frequency (TOF) and activation energy $E_A$ are +/- 9.1 % given the additional error from the measurement

of the ruthenium loading. This error is shown visually over experimental data for the conversion of ammonia (Figure 3.11); the repeatability of the three datasets of different batches of catalyst each with 7.0 $wt.\%$ ruthenium is within the predicted maximum range.

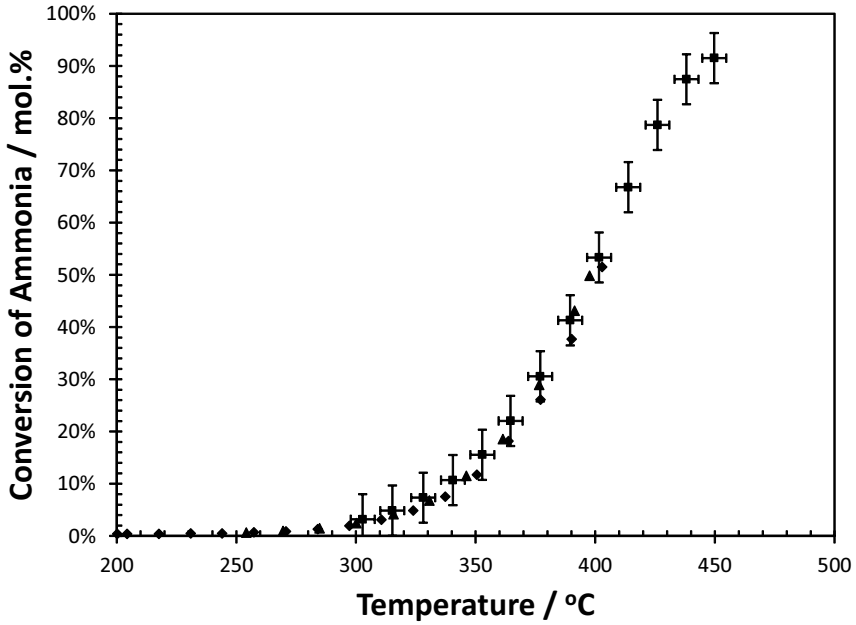


**Figure 3.11:** Error analysis on kinetic data for ammonia decomposition for a 7.0 wt.% ruthenium on CNT catalyst. Data from Figure 3.7 with error bars showing the uncertainty in mass balance reconciliation and temperature measurement.

# Chapter 4

# Development of Ruthenium Catalysts for Low Temperature Generation of Hydrogen from Ammonia

## 4.1 Introduction

Of the challenges encountered in the development of an ammonia-PEM fuel cell, one of the most important -is the development of catalytic systems that can decompose ammonia to hydrogen at temperatures more closely aligned with that of the PEM fuel cell of around 370 $K$. While a great deal of research has been conducted on catalysts for ammonia decomposition, most of this work has considered temperatures around 600 $K$ and relatively little has been done at lower temperatures.

Previous studies have shown that for a catalyst to be active for ammonia decomposition, ruthenium is the most active metal, cesium is the most potent promoter and the best support is one that embodies properties of high conductivity such as CNTs or one that has superbasic properties that has intrinsic electron donating species incorporated within the structure or zirconia or nano-titanates such as $ZrO_2 - KOH$ or $Cs_2Ti_6O_{13}$ [74, 81, 85]. The active metal surface is also very important. For ruthenium, the $B_5$ site (Ru(0001) see Figure 2.9) consisting of a specific five atom step is known to be most active, the tendency for this structure to occur is known to be a function of nanoparticle size. Small nanoparticles are more active in general, but with ruthenium the increase in particle size might put the nanoparticle into the optimum activity range of 3-5 $nm$ which is thought to produce the maximum occurrence of $B_5$ step sites [71].

The other selection criteria is the choice of promoter. The best performing promoters for ammonia decomposition are Group 1 or Group 2 metals with cesium known to be the most active [115, 116]; furthermore the higher the electronegativity of the promoter produces lower activity in the catalyst [42]. However, there is some disagreement in literature about whether this activity is gained by electronic or structural means. Most published studies suggest that the promoter functions by donating electrons to the active site [42] but there is some disagreement and others propose that the promoter produces the enhanced activity by increasing the size of the ruthenium nanoparticle and that these larger nanoparticles are more active [95, 89].

While most studies have considered temperatures above 670 $K$, a small number have looked at catalysts at lower reaction temperatures. Klerke *et al.* synthesised ruthenium nanoparticles on super-basic cesium-titanate nanowires which were active at 593 $K$ [85]. The cesium within the support structure was thought to donate electrons to the active nanoparticle. Sorensen *et al.* found that ruthenium nanoparticles supported on graphitic carbon with cesium promoter were active from around 473 $K$ [117].

From these beginnings, this chapter seeks to further understand the nature of this low temperature activity. For CNT supported catalysts, areas of investigation include the effect of ruthenium loading, the effect of cesium loading and the effect of CNT modification by graphitisation.

## 4.2 The Effect of Ruthenium Loading on Activity for Ammonia Decomposition

A series of promoted ruthenium catalysts were synthesised to investigate low temperature activity for ammonia decomposition. To understand the effect of ruthenium loading, catalysts were prepared on unmodified CNTs used as received (length 5 $\mu m$, diameter 6 - 9 $nm$) with a fixed cesium loading and a range of ruthenium concentrations. Ruthenium and cesium precursors were ruthenium nitrosyl nitrate $Ru(NO)(NO_3)_3$ and cesium hydroxide $CsOH.xH_2O$ where x was 0.17.

The results showing the effect of changing the ruthenium loading are presented in Figure 4.1 and Table 4.1. Figure 4.1 A shows that the activity of the catalyst increases as the ruthenium loading is increased. Activity begins at around 550 $K$ for the catalyst with 3.0 $wt.\%$ ruthenium and at 520 $K$ for the catalyst with 13.2 $wt.\%$ ruthenium.

Although the change in activity might suggest that the surface of ruthenium becomes more active at higher loading, this is contradicted by the Arrhenius drawing (Figure 4.1 B) that shows that the rate of reaction per mole of ruthenium is the same in all cases. From this it can be concluded that the activity of ruthenium stays the same at all loadings and the increase in activity relates to increased number of ruthenium surface sites caused by the higher loading of ruthenium.

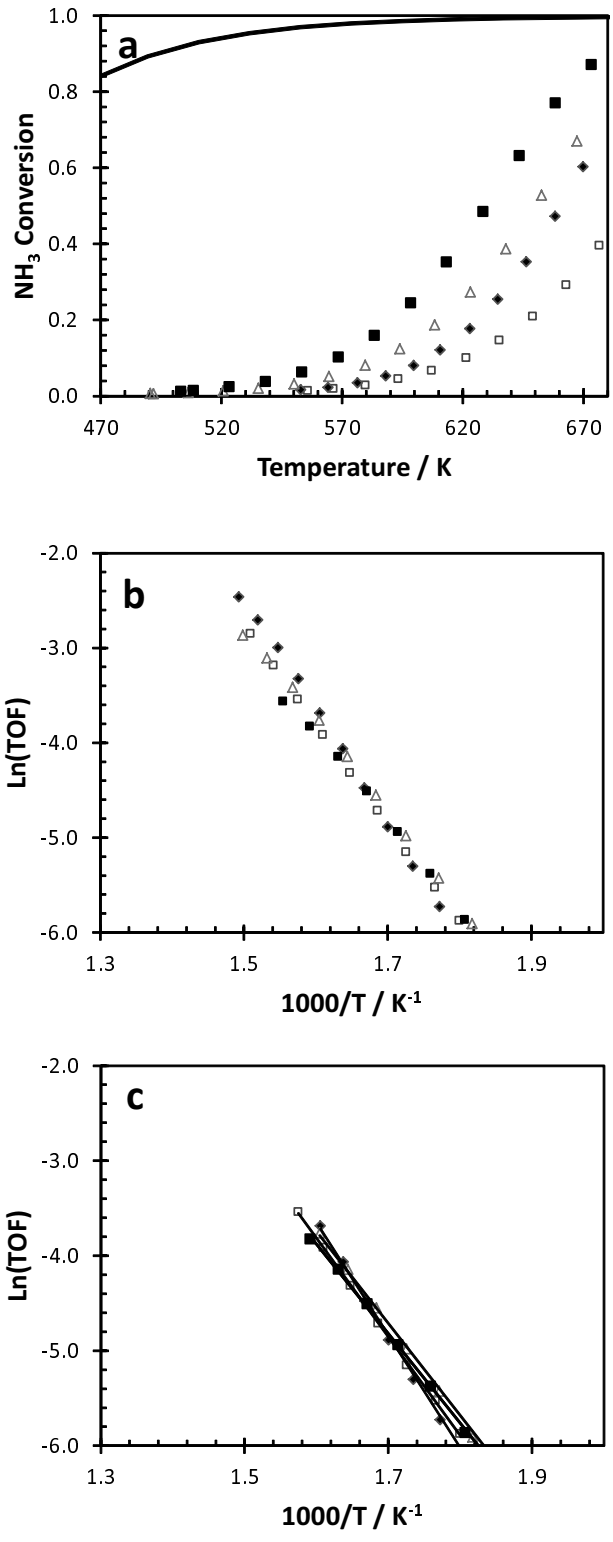


**Figure 4.1:** Effect of ruthenium loading on the rate of ammonia decomposition. (**a**) - Extent of ammonia decomposition reaction as a function of temperature, (**b**) - Arrhenius plot of the same results and (**c**) - Arrhenius plot with data below 20 % conversion for calculation of activation energy. (□) 3.0 *wt.*% Ru, (◆) 4.2 *wt.*% Ru, (△) 10.0 *wt.*% Ru and ■ 13.2 *wt.*% Ru. Figure reproduced from Hill & Torrente [118]. The solid line represents thermodynamic equilibrium conversion, reaction conditions were 5,200 $mL_{NH_3}\,h^{-1}\,g_{cat}^{-1}$ WHSV and 25.0 *mg* of catalyst. TOF has units of $mol_{NH_3}\,mol_{Ru}^{-1}\,s^{-1}$ and was evaluated at exit conversion.

**Table 4.1:** Effect of ruthenium loading upon the catalytic activity for ammonia decomposition [118].

| **Ru loading** | **Ru Particle Size**[a] | **TOF at 600** $K$ [b] | **Activation Energy** | **Regression Fitting Coefficient** $R^2$ |
|---|---|---|---|---|
| $wt.\%$ | $nm$ | $mol_{NH_3}\, mol_{Ru}^{-1}\, s^{-1}$ | $kJ\, mol^{-1}$ | |
| 3.0 | 1.5 | 0.011 | 86.3 | 0.9996 |
| 4.2 | 2.3 | 0.014 | 98.4 | 0.9965 |
| 7.0 | 1.6 | 0.012 | 80.6 | 0.9987 |
| 13.2 | 2.3 | 0.012 | 78.4 | 0.9994 |

[a] Average particle size determined by TEM.
[b] Ru catalysts on CNTs with 4 $wt.\%$ cesium. TOF calculated at exit conversion.

Transmission electron microscopy experiments were used to understand the effect of support modification and promoter loading upon the size and morphology of ruthenium nanoparticles. Figure 4.2 shows the effect of changing the ruthenium loading on un-modified CNTs with 4 $wt.\%$ cesium. At the highest loading of 13.2 $wt.\%$ ruthenium, some elongation of the nanoparticles can be discerned but in all cases the catalyst features well dispersed nanoparticles in a range of 1 - 4 $nm$. Determination of particle size by TEM presents some limitations due to the inherently small sample size of the technique. To partially address this problem, histogram data presented here is taken from a sample size of at least 3 different images taken from diverse locations.

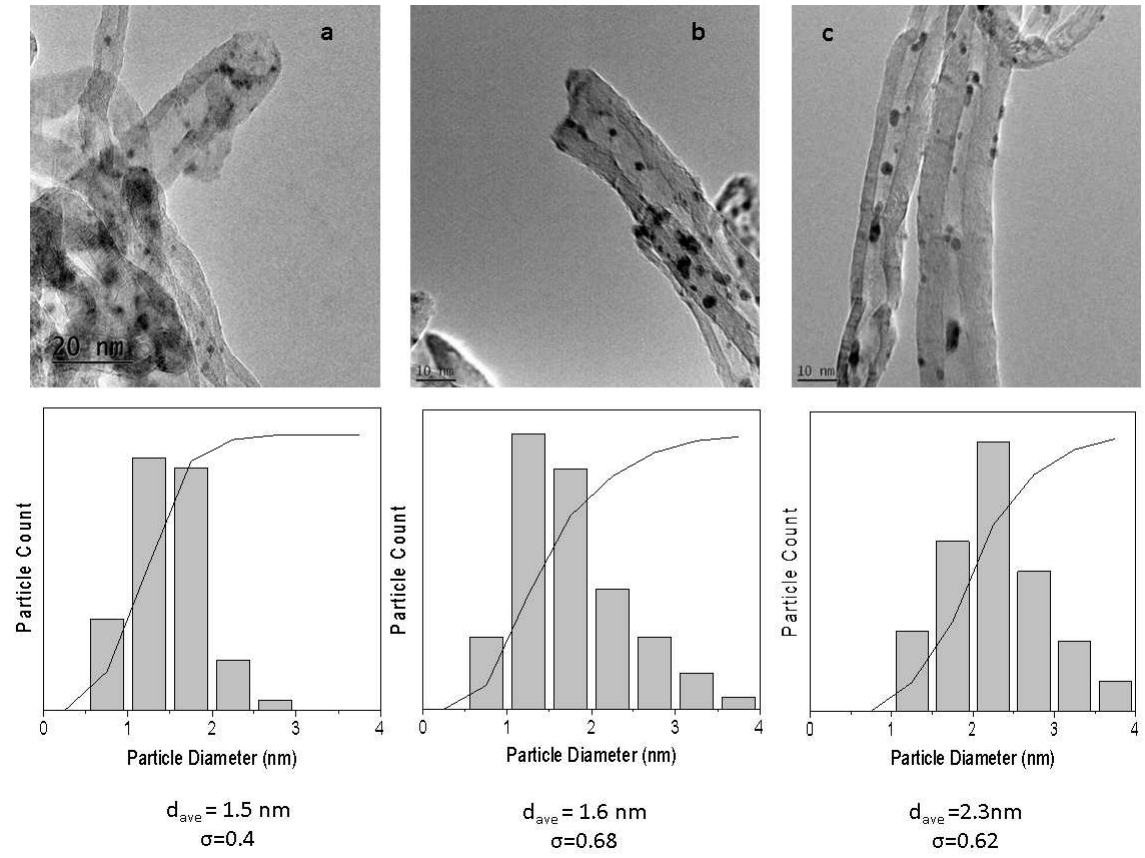


**Figure 4.2:** Representative TEM images and particle size histograms of Ru catalysts with 4 *wt.*% Cs/CNT. (**a**) 3 *wt.*% Ru, (**b**) 7 *wt.*% Ru, (**c**) 13.2 *wt.*% Ru.

CO pulse chemisorption and X-ray diffraction (XRD) experiments can both be used to estimate the distribution of metal particles in catalysts. CO chemisorption measures the surface saturation of carbon monoxide which can be used to estimate metal surface area if the ratio of stoichiometric interaction between CO and metal is known. The average particle size can be calculated assuming that the particles conform to hemispherical geometry. XRD can be used to estimate the size of metal particles by analysing the diffraction of X-rays through their crystal lattice. As the particle size reduces, the width of the X-ray diffraction spectra increases as the lattice structure becomes less clearly defined enabling the particle size to be calculated by the Scherrer equation (see equation 2.15).

Three XRD spectra are shown in Figure 4.3 featuring unmodified CNTs, 4.0 *wt.*% ruthenium with 4 *wt.*% cesium and 13.2 *wt.*% ruthenium with 4 *wt.*% cesium. Characteristic ruthenium peaks should appear at $2\theta$ diffraction angles of $39^o$ and $44^o$ representing the Ru(100) and Ru(101) crystal structures respectively [119]. The unmodified CNTs produce a broad peak between $2\theta$ diffraction angles of $20^o$ and $30^o$ and then a smaller broad peak at $44^o$, the latter of which coincides closely

with the characteristic Ru(101) peak potentially obscuring it. The samples featuring ruthenium differ only slightly from the un-modified CNTs which also shows a broad peak at around 44 degrees. These spectra in which ruthenium peaks cannot be clearly discerned are similar to those published by Yin *et al.* for well dispersed ruthenium on CNTs (see Figure 2.17) [120]. Although an estimate of particle size cannot be made in this case because of the poorly defined peaks, it can be claimed that the ruthenium is highly dispersed on the CNT surface.

Further data on metal nanoparticle size has been estimated by CO chemisorption experiments in which the particle size is estimated from experiments that measure the quantity of carbon monoxide irreversibly bound to the metal surface. The stoichiometric ratio between carbon monoxide and ruthenium is known to be either 1 or 2 [91]; the figure of 2 was used as this gave the best agreement with TEM measurements. These results are presented alongside estimated particle size from TEM experiments in Figure 4.4.

The CO chemisorption technique consistently estimates a larger particle size than the TEM method. Both methods show an increase in particle size with ruthenium loading, but the change in particle size measured by TEM is much smaller than the chemisorption results and within the margin of uncertainty. There are two explanations that can explain this difference in particle size estimation. At higher loadings of cesium, it is likely that the cesium partially covers the surface of ruthenium preventing access of carbon monoxide to the ruthenium active sites. It is also possible that the electronic effect of cesium upon the ruthenium active sites reduces the strength of interaction with carbon monoxide resulting in a reduction in the quantity chemisorbed.

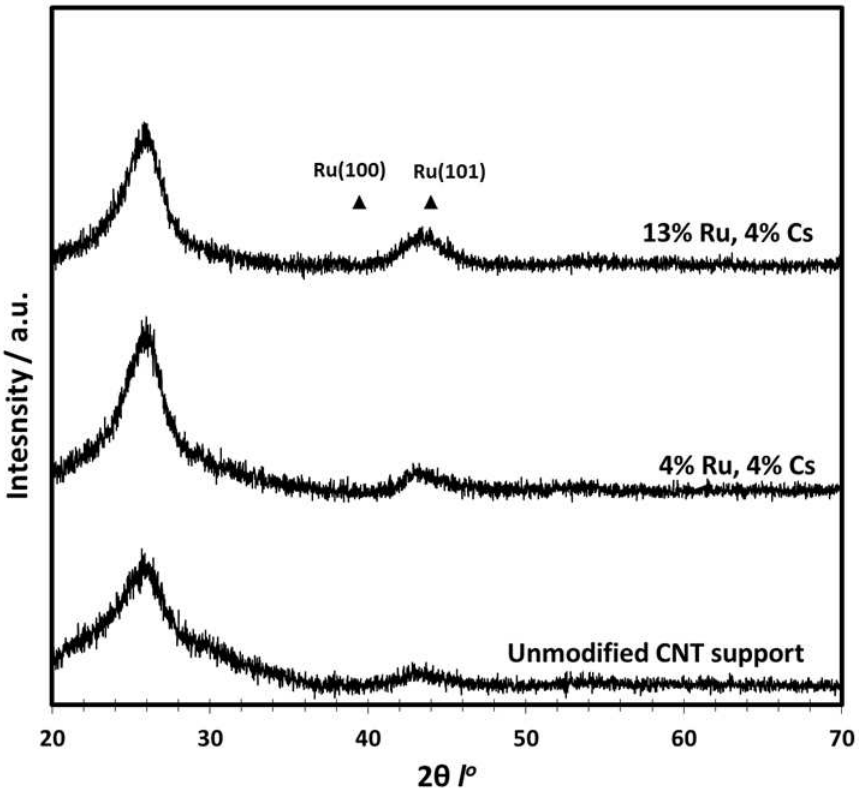


**Figure 4.3:** XRD spectra of ruthenium nanoparticles on CNTs. Directly reproduced from Hill & Torrente-Murciano [118].

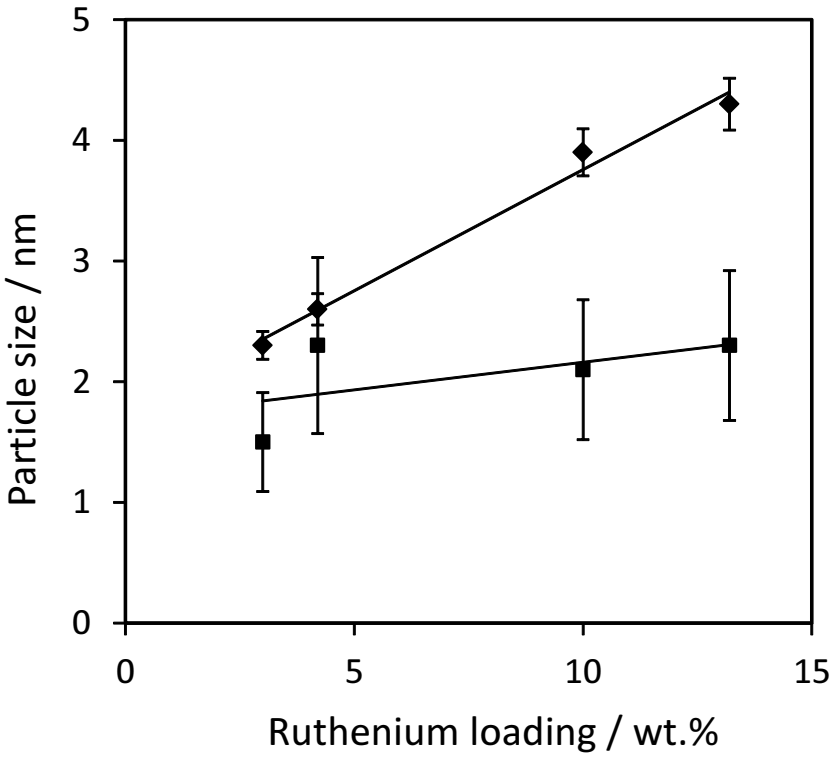


**Figure 4.4:** Ruthenium particle size vs ruthenium loading by CO chemisorption (◆) and TEM (■). Error bars for TEM measurements show one standard deviation, error bars for CO chemisorption are estimated from instrument signal variance [118].

It can be concluded that changing ruthenium loading has limited impact upon activity, the ruthenium surface retains similar activity at all concentrations of ruthenium on the CNT support even up to high loadings above 13 $wt.\%$. Some data suggests an increase in particle size as the ruthenium concentration increases, but CO chemisorption and TEM measurements to not agree well and this finding is inconclusive. It is clear that adjusting ruthenium loading will not produce the low temperature activity required for an ammonia-PEM fuel cell and other factors must be consid\ered instead.

## 4.3 The Effect of Cesium Loading on Activity for Ammonia Decomposition

To understand the effect of cesium to ruthenium ratio, catalysts were prepared on unmodified CNTs with 7.0 $wt.\%$ ruthenium and between 0 - 50 $wt.\%$ cesium.

The effect of varying the loading of cesium promoter upon the activity of catalysts with 7.0 $wt.\%$ ruthenium supported on unmodified CNTs is shown in Figure 4.5.

By increasing the loading of promoter from 0 to 20 $wt.\%$, the temperature at which the catalyst becomes active is reduced from around 600 $K$ to below 500 $K$. This enhancement in activity far exceeds that achieved by altering of ruthenium loading and suggests that the promoter is of prime importance to achieve low temperature activity.

Insights into how the cesium achieves such a remarkable reduction in the minimum reaction temperature can be gleaned by inspection of the Arrhenius plot in Figure 4.5 B. Not only is the activity per mole of ruthenium increased through greater promoter loading, there is also a discernible change in gradient of the straight lines. The gradient of the catalyst with 20 $wt.\%$ cesium is indicative of a reduction in activation energy which is reduced from 91.6 $kJ\,mol^{-1}$ to 57.4 $kJ\,mol^{-1}$ from 0 - 20 $wt.\%$ cesium loading (see Table 4.2).

Results for metal nanoparticle surface area estimated CO chemisorption and particle size measured by TEM have been presented alongside kinetic results in Table 4.2. While the rate of reaction increases and activation energy decreases with cesium loading, the particle size measured by TEM and the metal surface area measured by CO chemisorption do not show a clear relationship with cesium loading. The changes in particle size measured by TEM is within the experimental uncertainty of this technique and the results for CO chemisorption show large variability at higher cesium loadings. These findings generally support the hypothesis that the enhancement of activity by the promoter is an electronic effect through donation of electrons and not a structural effect by changing the active particle size of which no clear change could be measured.

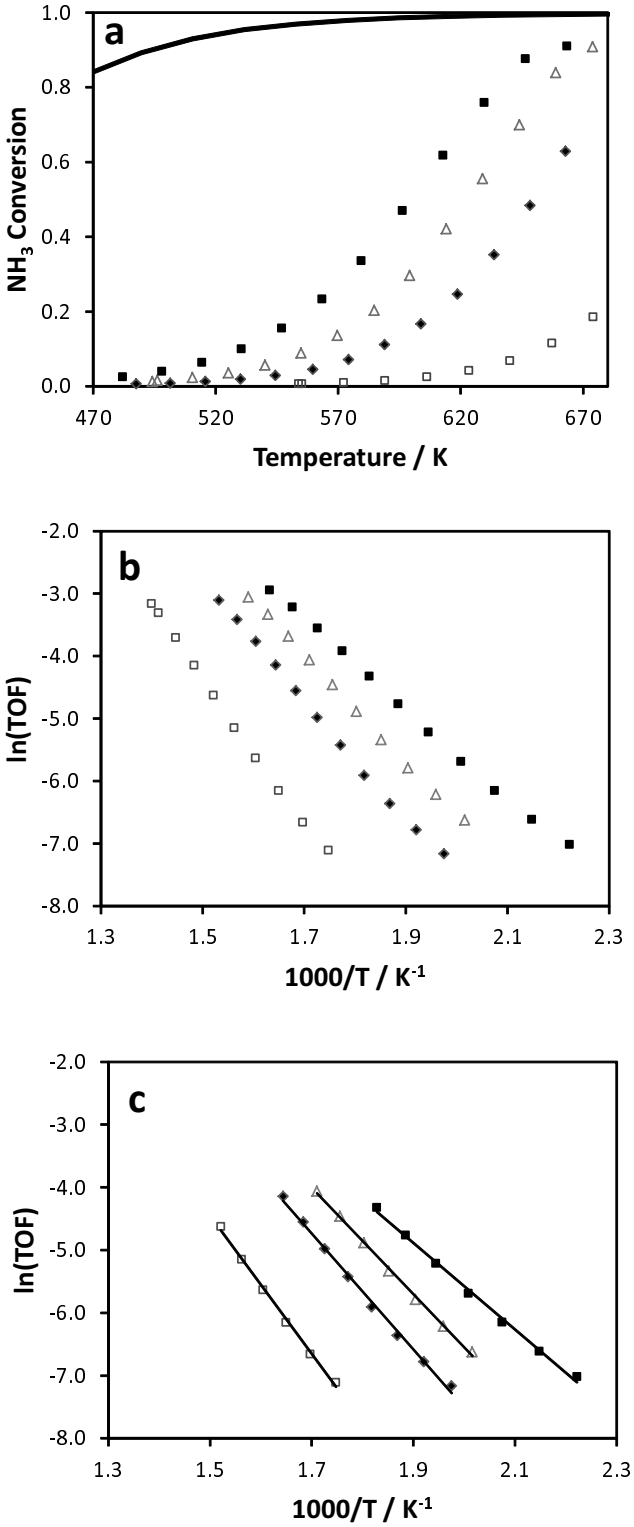


**Figure 4.5:** Effect of cesium loading on the rate of ammonia decomposition for 7.0 wt.% Ru on CNT catalysts. **a** - Extent of ammonia decomposition reaction as a function of temperature, **b** - Arrhenius drawing of the same results and **c** - Arrhenius plot with data below 20 % conversion for calculation of activation energy. (□) 0 wt.% Cs, (◆) 4 wt.% Cs, (△) 10 wt.% Cs and (■) 20 wt.% Ru. Figure directly reproduced from Hill & Torrente-Murciano [118]. The solid line represents thermodynamic equilibrium conversion, reaction conditions were 5,200 $mL_{NH_3}\,h^{-1}\,g_{cat}^{-1}$ WHSV and 25.0 $mg$ of catalyst. TOF has units of $mol_{NH_3}\,mol_{Ru}^{-1}\,s^{-1}$ and was evaluated at exit conversion.

**Table 4.2:** Effect of cesium loading upon the catalytic activity for ammonia decomposition.

| **Cs Loading** | **Ru Particle Size**[a] | **CO absorbed**[b] | **TOF at 600 $K$** [c] | **Activation Energy** | **Regression Fitting Coefficient $R^2$** |
|---|---|---|---|---|---|
| $wt.\%$ | $nm$ | $nm$ | $mol_{NH_3}\, mol_{Ru}^{-1}\, h^{-1}$ | $kJ\, mol^{-1}$ | |
| 0 | 1.6 | 2.6 | 6.5 | 91.6 | 0.9968 |
| 4 | 1.6 | 2.7 | 41.4 | 76.9 | 0.9959 |
| 10 | 2.4 | 3.9 | 92.2 | 70.5 | 0.9980 |
| 20 | 2.0 | 2.9 | 154 | 57.4 | 0.9964 |
| 30 | 2.4 | 4.4 | 134 | 64.5 | 0.9997 |

[a] - Estimated from TEM images
[b] - Estimated from CO chemisorption measurements assuming hemispherical particles
[c] - TOF calculated at exit conversion

While the results in Figure 4.5 show that cesium exhibits a strong effect on catalyst activity up to 20 $wt.\%$ loading, the activity of the catalyst steadily reduces when the cesium concentration exceeds this value. This maxima in activity is illustrated in Figure 4.6 and occurs at a Cs/Ru mass ratio of around 3. This effect has been seen previously in literature for ruthenium nanoparticles on carbon support with cesium promoter [121] but it is not clear why the maxima occurs at a 3:1 ratio, it is possible that cesium blocks access to active sites as its loading increases.

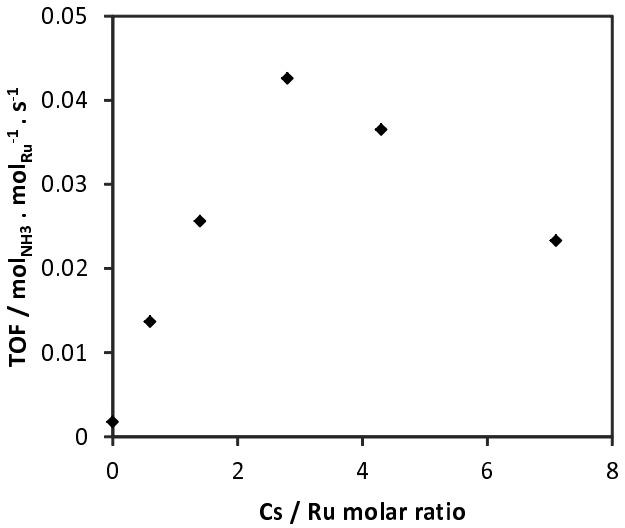


**Figure 4.6:** Effect of cesium to ruthenium ratio on the turnover frequency at 600 $K$. Catalysts had 7.0 $wt.\%$ ruthenium on CNTs. Reaction conditions were 5,200 $mL_{NH_3}\, h^{-1}\, g_{cat}^{-1}$ WHSV and 25.0 $mg$ of catalyst. TOF was calculated at exit conversion.

Further experiments were undertaken to attempt to improve the understanding of the electronic and structural interaction between the CNT support, cesium promoter and ruthenium nanoparticle. Of particular interest was the location of cesium across the surface of the catalyst, the oxidation state of cesium and whether changes in cesium concentration led to any changes to the size, shape and distribution of the ruthenium nanoparticles.

Figure 4.7 shows TEM images of 7.0 wt.% ruthenium with varying cesium loadings upon the unmodified support. Similar particle size distribution is observed with all cesium loadings and the catalyst contains well dispersed ruthenium nanoparticles with typical particle size between 1 and 4 $nm$.

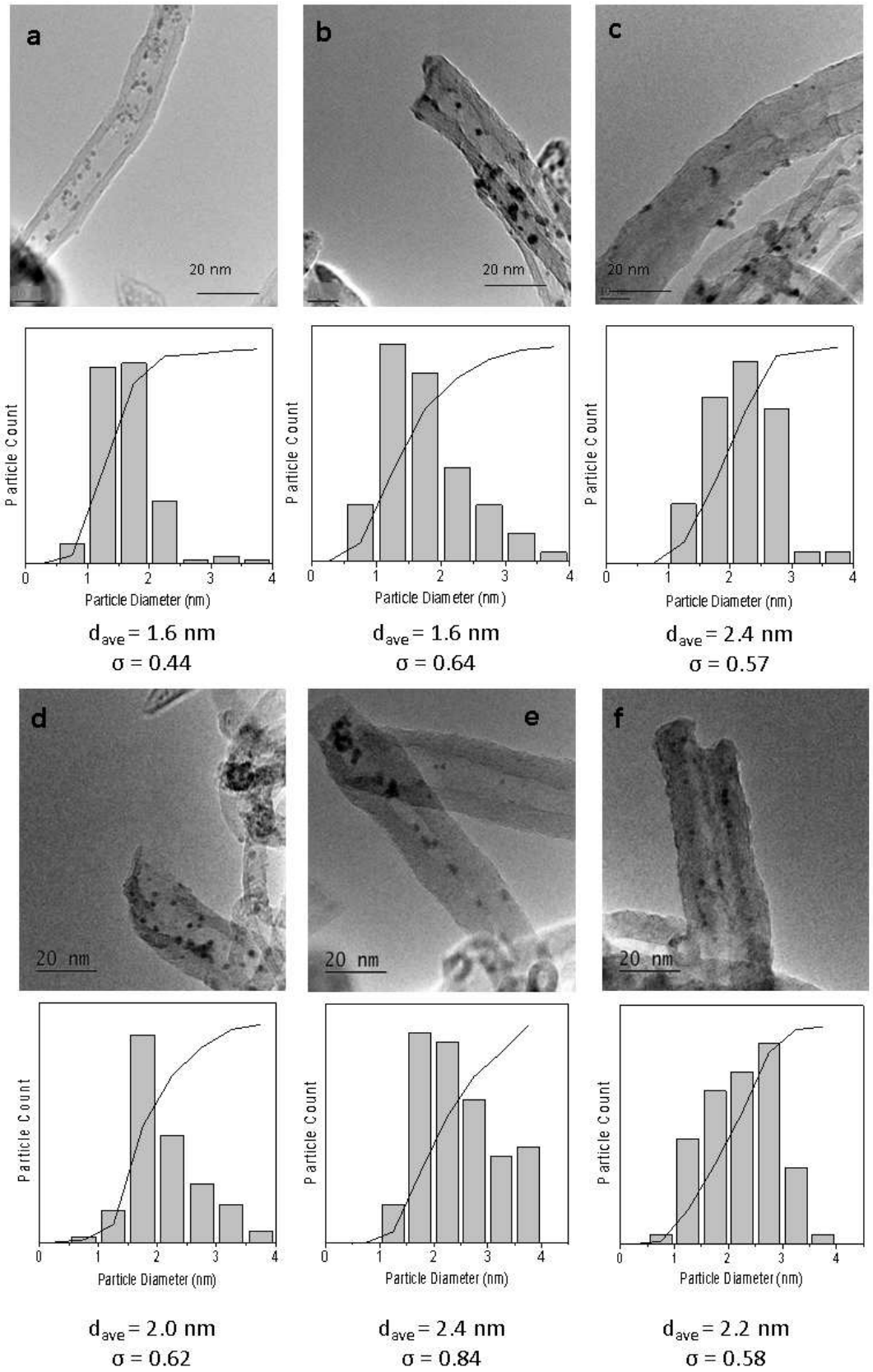


**Figure 4.7:** Representative TEM images and particle size histograms of 7 *wt.*% Ru/CNT catalysts. (**a**) 0 *wt.*% Cs, (**b**) 4 *wt.*% Cs, (**c**) 10 *wt.*% Cs, (**d**) 20 *wt.*% Cs, (**e**) 30 *wt.*% Cs and (**f**) 50 *wt.*% Cs.

The results of pulse chemisorption experiments for catalysts on un-modified CNTs are presented in Figure 4.8 showing estimated ruthenium nanoparticle size along with the corresponding measurement taken from TEM experiments. As before, a stoichiometric ratio of two was used for the ruthenium and carbon monoxide interaction. When the ruthenium loading was kept constant at 7.0 $wt.\%$ and the cesium loading was varied between 0 and 50 $wt.\%$, the variance in the quantity of CO absorbed increased significantly and it is difficult to claim a clear trend in results which varied between 2.5 to 8.0 $nm$; this may be due to cesium covering the surface of the ruthenium or modifying the interaction between ruthenium and carbon monoxide. The TEM estimates of nanoparticle size were consistently less than those estimated by the CO chemisorption method, this was the case even for catalysts without cesium promoter.

The comparison between nanoparticle size measured by both XRD and CO chemisorption are shown in Figure 4.8. The measured particle size by chemisorption consistently exceeds that measured by TEM with the discrepancy increasing at higher cesium loading. Given these variations in results, it is possible to claim that the average size of ruthenium nanoparticles generally lies between 1 - 4 $nm$. This discrepancy can be explained both by the incremental presence of cesium on the ruthenium surface preventing access to CO molecules and by the electronic deactivation of the ruthenium.

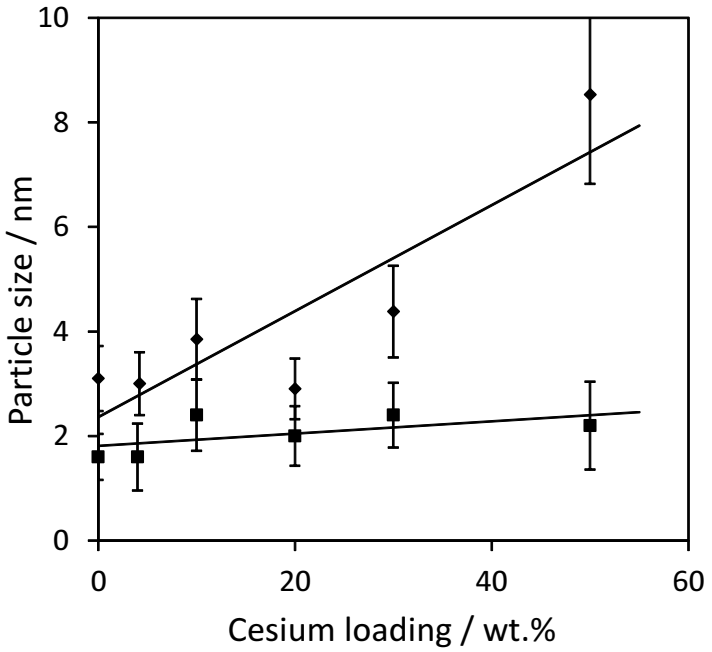


**Figure 4.8:** Ruthenium nanoparticle size estimated by CO Chemisorption (◆) and TEM (■). Error bars for TEM measurements show one standard deviation, error bars for CO chemisorption are estimated from instrument signal variance [118].

Further understanding of the interactions between cesium, ruthenium and the CNT support can be gained through examination of the TPR results presented in Figures 4.9 and 4.10. During the analysis, samples were placed in flowing 5 % hydrogen in argon and heated from ambient temperature to 1173 $K$ with the exit gas being measured for thermal conductivity using the inlet gas as reference. In the resultant spectra, positive peaks potentially represent the consumption of hydrogen from the flowing gas but care must be taken because evolution of gases by other chemical interactions can also alter the measurement of the TCD. All samples were heated to 773 $K$ in an inert atmosphere prior to experiment to ensure that the sample is free of water and other impurities.

The TPR spectra in Figure 4.9 show the effect of varying the cesium loading upon catalysts featuring $Ru(NO)(NO_3)_3$ precursor on CNTs to give 7.0 $wt.\%$ ruthenium loading. The unmodified CNT material exhibits a broad peak at 778 $K$. When ruthenium is added, there are initial negative peaks at low temperature, a small positive peak at 434 $K$ and the broad peak increases in magnitude but the peak temperature falls to around 730 $K$ where it stays constant for all loadings of ruthenium and cesium loading. When cesium is added, the small positive peak at 434 $K$ becomes substantially larger and the peak temperature increases as a function of cesium loading up to 20 $wt.\%$ (508 $K$ for 10 $wt.\%$ cesium and then 593 $K$, 569 $K$ and 575 $K$ for 20, 30 and 50 $wt.\%$ cesium respectively). At cesium loadings of 30 $wt.\%$ and above, a negative peak appears at approximately 950 $K$.

The quantified hydrogen uptake by the catalyst for each of these results is shown in Table 4.3 with hydrogen consumed increasing from 0.001 to 0.014 $mmol\, g_{cat}^{-1}$ when cesium loading is increased from 0 - 20 $wt.\%$. This increased apparent consumption of hydrogen can be caused either by increased conversion of $Ru^{2+}$ to $Ru^0$, or as has been suggested in literature, the increased hydrogen uptake could be caused by the partial reduction of cesium to a substoichiometric cesium oxide ($Cs_2O$) [96]. The presence of $Cs^0$on the surface of the catalyst would act as a powerful electron donor, helping to explain the dramatic effect that cesium loading has upon catalyst activity.

If cesium is undergoing reduction between 500 - 600 $K$, this only occurs when ruthenium is present. The spectra in Figure 4.10 show that cesium on CNTs has no interaction with hydrogen in this temperature range, from this it can be concluded that cesium is present upon the surface and in close proximity to ruthenium as cesium located remotely from any ruthenium would have no interaction. The cesium reduction mechanism may proceed by the dissociation of hydrogen by ruthenium to dissociate hydrogen [122].

TPR results in Figure 4.10 show the effect of 20 and 50 $wt.\%$ cesium loading on CNTs with no ruthenium. These results do not show peaks between 430 - 600 $K$

which suggests that this partial reduction of cesium only occurs in the presence of ruthenium providing more evidence that the cesium is located on the surface and in close proximity to ruthenium nanoparticles. Catalysts with high cesium loading (30 and 50 $wt.\%$) present a negative peak at 950 $K$.

The Autochem II, which was used for this analysis, was not equipped to detect species by mass spectrometry and thus care must be taken when assigning the peaks to reduction events. The broad peak present in the blank CNT spectra at 778 $K$ results from the interaction of hydrogen with the CNT support, it has been suggested in literature that this could be the formation of methyl groups [115] or the reduction of surface oxide groups [123]. For the samples containing ruthenium, the negative peaks around approximately 380 $K$ are likely to be nitric acid or nitrous oxides evolved from the interaction of the ruthenium nitrosyl nitrate precursor and hydrogen. The small positive peak at 434 $K$ for the ruthenium catalyst with no cesium is almost certain to be ruthenium which is known to have a characteristic reduction peak at this temperature [74]. The phenomena that are more challenging to explain are the increased hydrogen uptake by the support following addition of ruthenium and the increased hydrogen consumed by the reduction of ruthenium following addition of cesium.

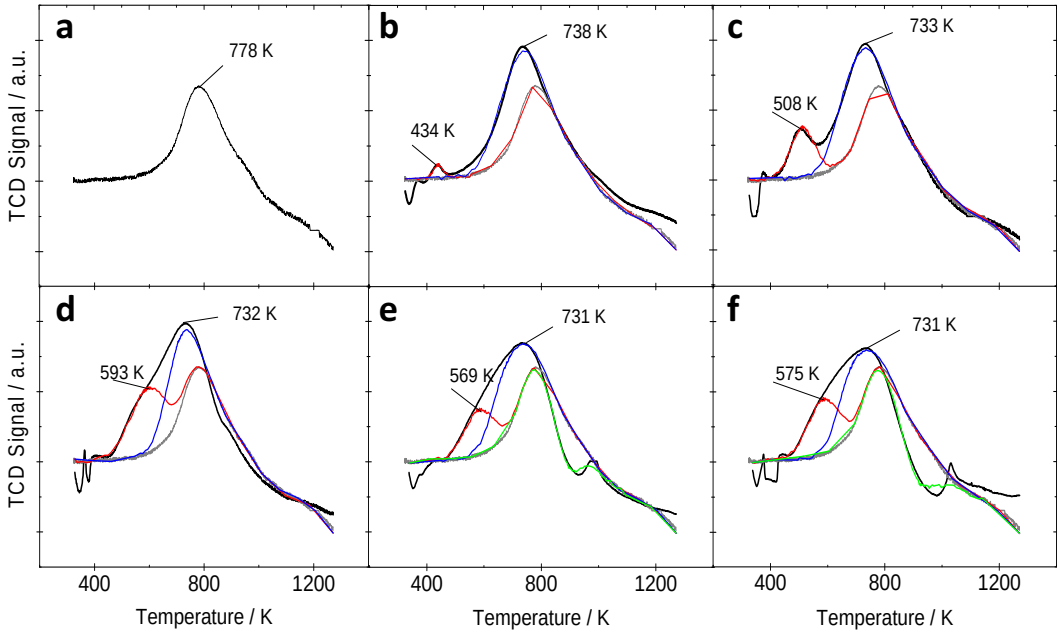


**Figure 4.9:** TPR results showing the effect of cesium loading on 7 *wt.*% Ru/CNT catalysts. (**a**) Blank CNTs; (**b**) 7 *wt.*% Ru/CNT; (**c**) 7 *wt.*% Ru, 10 *wt.*% Cs / CNT; (**d**) 7 *wt.*% Ru, 20 *wt.*% Cs / CNT; (**e**) 7 *wt.*% Ru, 30 *wt.*% Cs / CNT; and (**f**) 7 *wt.*% Ru, 50 *wt.*% Cs / CNT. Curve fitting was performed using Origin Pro 9.0 with the blank CNT TPR result as the baseline. The blank result is shown as a grey line on plots **b** to **f** and serves as a baseline for curve fitting, the black line is the TPR results for the sample, the red, blue and green curves show the fitted results that may relate to the presence of ruthenium, CNTs and cesium respectively. All fitted curves account for the difference in hydrogen uptake compared to the blank CNTs.

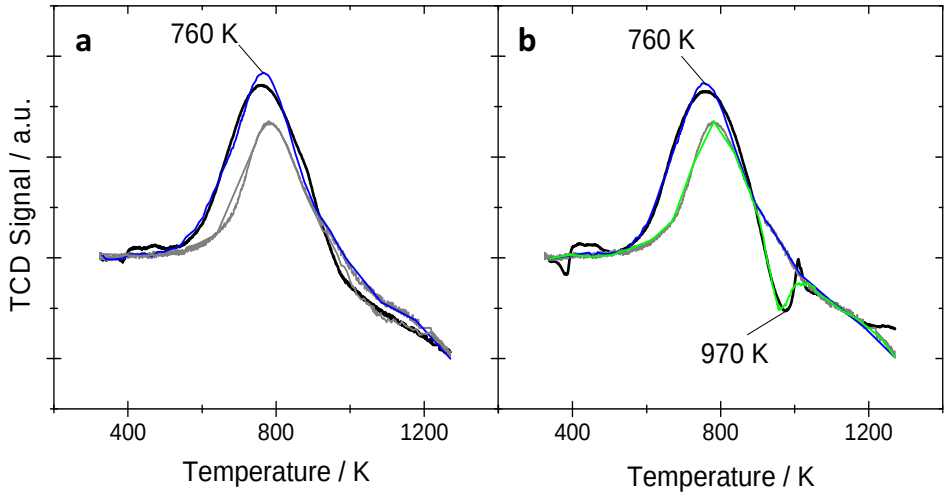


**Figure 4.10:** TPR results showing the effect of cesium loading with 0 *wt.*% Ru/CNT catalysts. (**a**) 20*wt.*% Cs; (**b**) 50*wt.*% Cs. Curve fitting was performed using Origin Pro 9.0 with the blank CNT TPR result as the baseline. The blank result is shown as a grey line and serves as a baseline for curve fitting, the black line is the TPR results for the sample and the intermediate coloured lines are the fitted curves that account for the difference in hydrogen uptake compared to the blank CNTs.

**Table 4.3:** Integration of peaks from TPR experiments by curve fitting showing the impact of cesium loading.

| **Catalyst** | **Peak Temperature** $K$ | $H_2$ **Consumed (apparent)** [a] $mmol\ g_{cat}^{-1}$ |
|---|---|---|
| 7 *wt.*% Ru, 0 *wt.*% Cs / CNTs | 443 | 0.001 |
| 7 *wt.*% Ru, 4 *wt.*% Cs / CNTs | 488 | 0.003 |
| 7 *wt.*% Ru, 10 *wt.*% Cs / CNTs | 517 | 0.008 |
| 7 *wt.*% Ru, 20 *wt.*% Cs / CNTs | 583 | 0.014 |

[a] - Calculated from thermal conductivity measurements.

There are a number of conclusions that can be drawn from the study into the effect of cesium on ruthenium catalysts supported on CNTs. Changes to the loading of cesium has a far greater effect on the catalytic activity than changes in loading of ruthenium. Cesium has been shown to be located on the ruthenium nanoparticle

surface or in close proximity and this study supports the findings in literature that cesium exists as a partially reduced substoichiometric oxide.

## 4.4 The Effect of Graphitisation of the CNT Support on Activity For Ammonia Decomposition

The focus on this section is to explore how the process of graphitisation of CNTs produces enhanced activity in ruthenium nanoparticle catalysts for ammonia decomposition. Graphitisation of CNTs is known to reduce the interlayer spacing, remove residual metal catalyst from the chemical vapour deposition synthesis and to "heal" the graphene like surface of the nanotubes by removing surface functionalised groups and defects [123]. This could make a catalyst less active for ammonia decomposition by reducing the number of surface anchoring points on which metal nanoparticles can form reducing dispersion. Despite the decrease in nanoparticle dispersion, graphitisation of CNTs has previously been shown to increase the activity of supported ruthenium catalysts [89]. The increase in activity was attributed to a 30 - 50 % increase in ruthenium nanoparticle size to around 3 $nm$ resulting from fewer surface defects. Graphitisation is known to increase the electrical conductivity of CNTs [124] and a comparison of the effect of cesium on graphitised and non-graphitised CNT catalysts might shed light onto the mechanism by which cesium enhances the catalytic activity.

To this end, catalysts were prepared with 7.0 $wt.\%$ ruthenium loading by incipient wetness impregnation on CNTs (as received from Sigma-Aldrich) which had been annealed using a J.D Webb ultra-high vacuum (UHV) furnace at 2070 or 2270 $K$. The concentration of cesium was varied between 0 - 30 $wt.\%$. For catalysts with up to 20 $wt.\%$ cesium, the two precursors were simultaneously impregnated, for catalysts with cesium loading greater than 20 $wt.\%$, the cesium was deposited in a second operation due to limits of ruthenium solubility. Ruthenium and cesium precursors were $Ru(NO)(NO_3)_3$ r and $CsOH.xH_2O$ where x was 0.17.

The degree of graphitisation of the CNTs was inferred by Raman spectroscopy, nitrogen adsorption / desorption and TPR experiments on the unmodified CNTs and CNTs annealed at 2073 and 2273 $K$ respectively (see Figures 4.11 and 4.12 and Table 4.4). From Raman spectroscopy, the degree of graphitisation can be estimated by the relative intensity of the D band at 1350 $cm^{-1}$ which is representative of the disorder in graphitic carbon to the G and G' bands at 1580 $cm^{-1}$ and 2700 $cm^{-1}$ respectively which represent the in-plane vibrations from $sp^2$ bonded carbon and 2D vibrations respectively [125]. The ratio of the quantity $I_D/I_G$ is widely used in

literature to signify the degree of graphitisation, a smaller value suggests a greater extent of graphitisation [124, 89].

Results from Raman spectra show that the $I_D/I_G$ ratio decreases from 2.6 for the un-modified CNTs to 1.9 for the CNTs annealed at 2073 $K$ and then 1.5 for CNTs annealed at 2273 $K$. This suggests that there has been a significant increase in the degree of graphitisation after annealing. TPR experiments show that the uptake of hydrogen by the graphitised CNT material is greatly reduced compared to the un-modified material. This uptake by carbon supports in TPR experiments is thought to be caused by methanation [115] or the reduction of surface oxide groups [123]. This has not previously been reported for graphitisation of CNTs but might be expected to occur because the graphene like surface would be more chemically inert with the defects removed and thus interacts less strongly with hydrogen.

The nitrogen adsorption desorption isotherms and pore size distribution calculated by the Barrett-Joyner-Halenda (BJH) method and the Halsey-Faas correction are shown in Figure 4.12 and Table 4.4 showing the effect of annealing CNTs at 2073 and 2273 $K$. All of the CNT samples produced Type IV isotherms with hysteresis that is characteristic of mesoporous materials. The surface area of the material, measured by nitrogen desorption and the Brunauer–Emmett–Teller (BET) method, reduced from 253 $m^2\,g^{-1}$ for the commercial CNTs to 220 $m^2\,g^{-1}$ and 207 $m^2\,g^{-1}$ for the CNTs annealed at 2073 $K$ and to 2273 $K$ respectively. Although the pore volume does not change significantly as a result of annealing, the pore volume distribution shows significantly reduced pore volume in the 2 - 3 $nm$ range. These findings are commensurate with improved ordering of the CNT walls and healing of the graphitic surface that is characteristic of graphitisation [123].

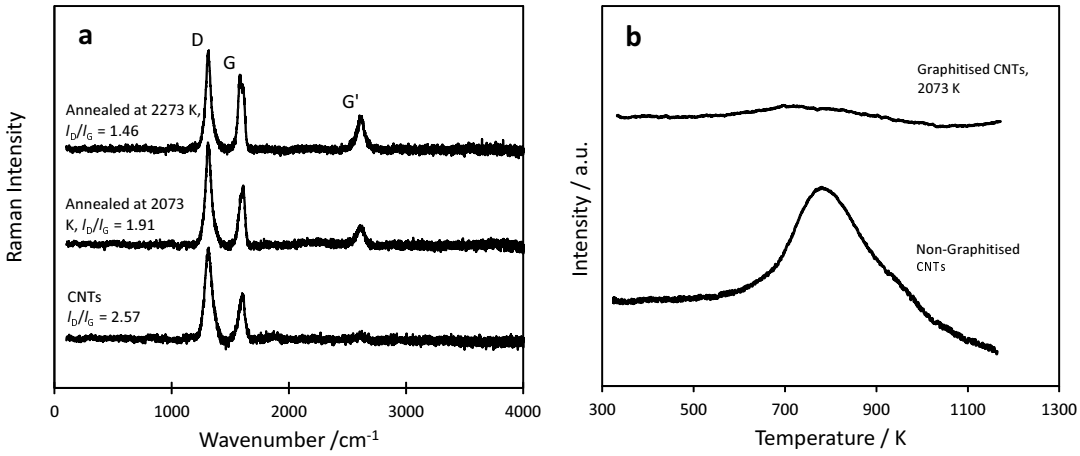


**Figure 4.11:** Investigation of the degree of graphitisation of CNTs. **a** - Raman spectra and **b** - TPR results for non-graphitised CNTs and CNTs graphitised at 2073 $K$.

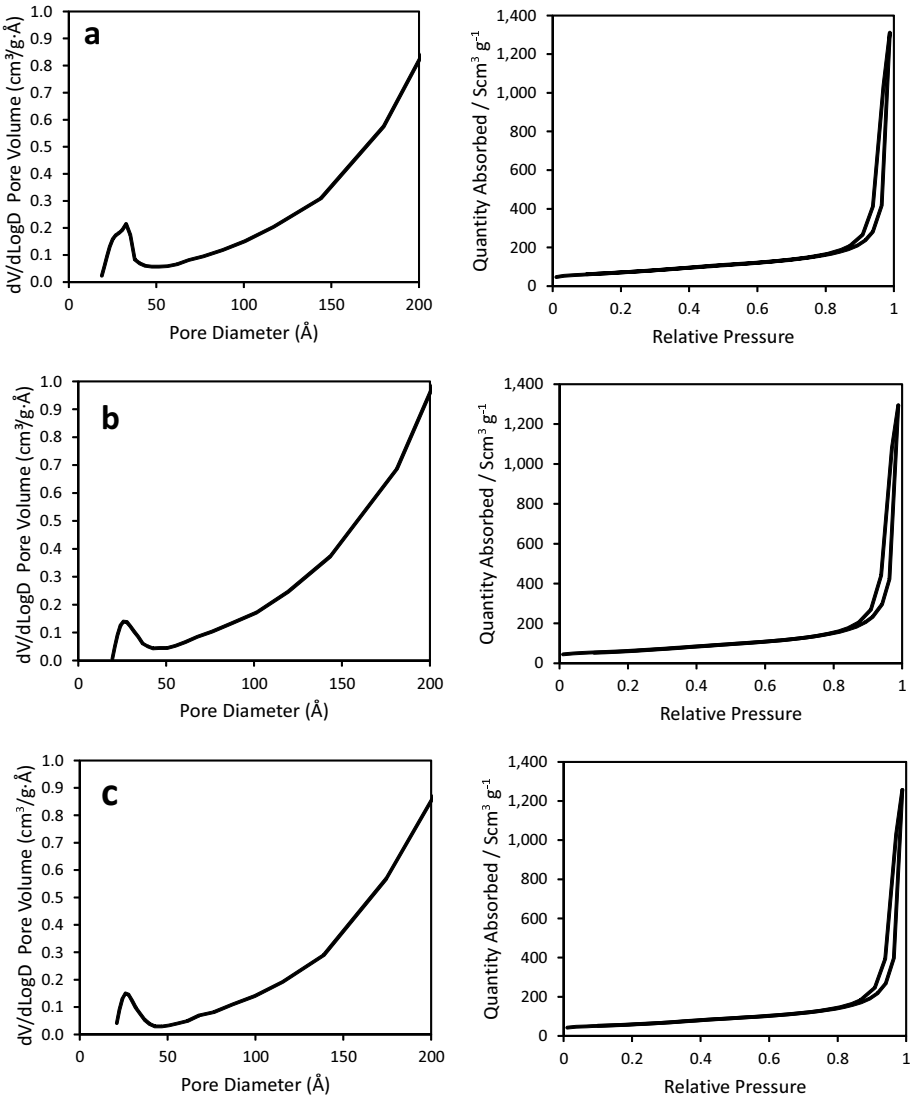


**Figure 4.12:** Nitrogen adsorption / desorption isotherms and pore size distribution for CNTs. Nitrogen adsorption / desorption at 77 $K$, pore size distribution shown for desorption by the BJH method with Halsey-Faas correction. From left to right: dV/dD pore volume, dV/dLogD pore (**a**) - CNTs, (**b**) - CNTs annealed at 2073 $K$ and (**c**) - CNTs annealed at 2273 $K$.

**Table 4.4:** CNT surface area and pore size distribution results from nitrogen desorption.

| **CNT annealing temperature** $K$ | **Surface Area** [a] $m^2\,g^{-1}$ | **Cumulative Pore Volume** [b] $cm^3\,g^{-1}$ | **Average Pore Size** [b] $nm$ |
|---|---|---|---|
| Not annealed | 253 | 2.03 | 27.6 |
| 2073 | 222 | 2.00 | 28.4 |
| 2273 | 207 | 2.95 | 29.6 |

[a] BET method
[b] BJT method with Halsey-Faas correction

Results in Figure 4.13 and Table 4.5 show the effect of changing the loading of cesium upon a catalyst with 7.0 $wt.\%$ ruthenium on CNTs annealed under ultra-high vacuum at 2073 $K$. The activity for the graphitised CNTs with low cesium loadings (0 and 4 $wt.\%$) greatly exceeds that of the non-graphitised support and initial activity is exhibited from 450 $K$ in the more highly promoted case. At cesium loadings of 20 $wt.\%$ and above, the activities of catalysts with graphitised and non-graphitised CNTs were similar with the graphitised support slightly more active.

To understand how catalytic activity is improved at low temperature, this work focuses upon the activation energy as a key factor. The Arrhenius equation defines the activation energy as the factor that governs how the catalytic activity varies with temperature. Thus, reducing the activation energy will significantly lower the temperature at which the catalyst is active (see equation 3.1). The improvement in the rate of reaction for catalysts with graphitised CNTs is reflected in a reduction in activation energy from 91.6 $kJ\,mol^{-1}$ to 63.6 $kJ\,mol^{-1}$ for the 7.0 $wt.\%$ ruthenium catalyst without cesium. When the catalysts are prepared with 4 $wt.\%$ cesium, the catalyst on graphitised CNTs has an activation energy of 48.1 $kJ\,mol^{-1}$ compared to 76.9 $kJ\,mol^{-1}$ for the unmodified support with the same ruthenium and cesium loading. In accordance with the decrease in activation energy, both the degree of conversion and rate of reaction also increased following graphitisation. Catalysts prepared with 7.0 $wt.\%$ ruthenium without cesium on CNTs annealed at a higher temperature of 2273 $K$ showed no measureable difference in activity to the CNTs annealed at 2073 $K$ (see Figure 4.14). With 20 $wt.\%$ cesium, the catalyst with CNTs annealed at 2273 $K$ show similar activity but lower activation energy.

In Table 4.5, the kinetic results and calculated activation energies are presented alongside particle size measured by TEM and absorption of CO to the metal surface.

In the absence of cesium, the measured ruthenium nanoparticle size by TEM is 1.6 $nm$, this is the same as on the catalyst with the non-graphitised support (see Table 4.2). CO absorption upon the catalyst with the graphitised support is less than upon the non-graphitised one by 2.3 compared to 3.0 $mol\, g_{cat}^{-1}$ suggesting that there is a larger average ruthenium particle size on the graphitised support (4.1 $nm$ hemispherical particle size for the graphitised catalyst compared to 2.6 $nm$ for the non-graphitised support. When cesium is added to the catalyst on graphitised CNTs, the particle size measured by TEM increases from 1.6 to 2.6 $nm$ and the CO absorption diminishes. Both effects are in similar proportions to that seen with the non-graphitised CNT supported catalysts and both are within the range of experimental uncertainty for the two respective techniques. The finding that graphitisation of the CNT support causes a small increase in ruthenium particle size is not dissimilar to the work of Zheng *et al.* who found an increase in ruthenium nanoparticle size supported on the outside of CNTs from 2.5 to 3.7 $nm$ when the annealing temperature for graphitisation was increased from 723 to 1773 $K$ [89]. Given the inherent innaccuracies of the TEM method, it seems that the electronic effects of the promoter and support would be far more significant than the change in nanoparticle size.

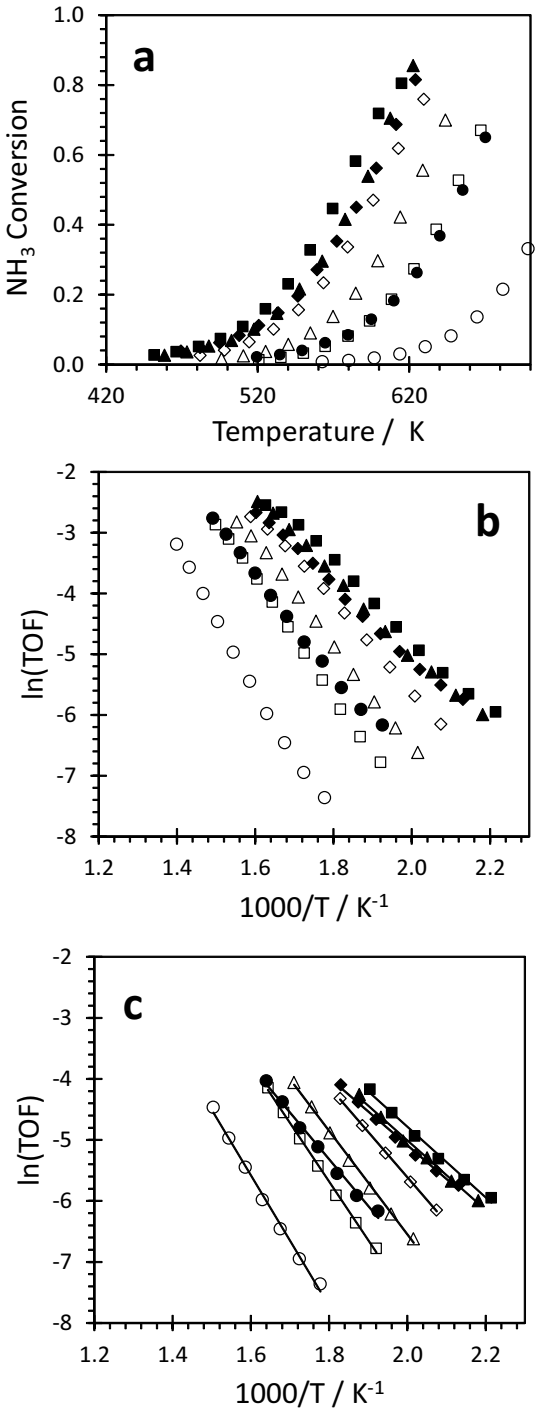


**Figure 4.13:** Effect of graphitisation of CNT support on the rate of ammonia decomposition for catalysts with 7.0 *wt.*% Ru loading. **a** - Extent of ammonia decomposition reaction as a function of temperature, **b** - Arrhenius plot of the same results and **c** - Arrhenius plot for conversion $< 20$ % for measurement of activation energy. (○) 0 *wt.*% Cs on non-graphitised CNTs, (□) 4 *wt.*% Cs on non-graphitised CNTs, (△) 10 *wt.*% Cs on non-graphitised CNTs, (◇) 20 *wt.*% Cs on non-graphitised CNTs, (●) 0 *wt.*% Cs on graphitised CNTs, (■) 4 *wt.*% Cs on graphitised CNTs, (▲) 10 *wt.*% Cs on graphitised CNTs and (◆) 20 *wt.*% Cs on graphitised CNTs. WHSV was 5,200 $mL_{NH_3}\,h^{-1}\,g_{cat}^{-1}$, catalyst mass was 25.0 *mg*. TOF has units of $mol_{NH_3}\,mol_{Ru}^{-1}\,s^{-1}$ and was evaluated at exit conversion.

**Table 4.5:** Effect of cesium loading on catalytic activity for graphitised CNT catalysts with 7.0 $wt.\%$ Ru .

| Cs Loading | Ru Particle Size[a] | Ru particle size[b] | TOF at 600 $K$ [c] | Activation Energy | Regression Fitting Coefficient $R^2$ |
|---|---|---|---|---|---|
| $wt.\%$ | $nm$ | $nm$ | $mol_{NH_3}\, mol_{Ru}^{-1}\, h^{-1}$ | $kJ\, mol^{-1}$ | |
| 0 | 1.6 | 4.1 | 48.9 | 63.6 | 0.9926 |
| 4 | 1.7 | 4.2 | 242 | 48.1 | 0.9926 |
| 10 | 2.1 | 3.0 | 207 | 47.3 | 0.9952 |
| 20 | 2.4 | 7.3 | 176 | 46.0 | 0.9948 |
| 30 | 2.6 | 5.5 | 122 | 55.9 | 0.9913 |

[a] Average particle size determined by TEM
[b] CO chemisorption at 308 $K$
[c] TOF calculated at exit conversion

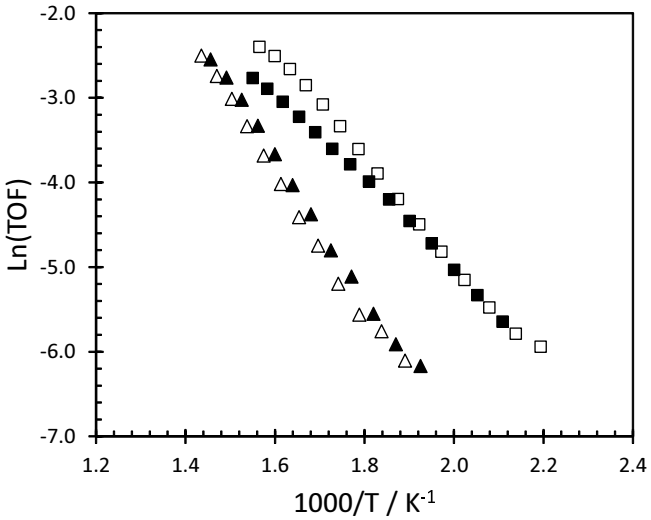


**Figure 4.14:** Effect of the degree of graphitisation of CNTs for a catalyst with 7.0 $wt.\%$ ruthenium. (▲) - CNTs annealed at 2073 $K$, (△) - CNTs annealed at 2273 $K$, ■ - annealed at 2073 $K$ with 20 $wt.\%$ Cs and (□) - annealed at 2273 $K$ with 20 $wt.\%$ Cs. WHSV was 5,200 $mL_{NH_3}\, h^{-1}\, g_{cat}^{-1}$, catalyst mass was 25.0 $mg$. TOF has units of $mol_{NH_3}\, mol_{Ru}^{-1}\, s^{-1}$ and was evaluated at exit conversion.

The results for the change in activity as a function of cesium loading on graphitised CNT supports are presented in Figure 4.15 showing the rate of reaction at 600 $K$ for catalysts with 7.0 wt.% ruthenium alongside the equivalent results for non-graphitised CNTs. Data sets for CNTs graphitised at 2073 $K$ and non-graphitised CNTs follow volcano curve shapes: at lower loadings, the presence of cesium has a beneficial effect upon activity and at higher loadings it has a detrimental effect. The greatest activity for catalysts prepared with graphitised CNTs is achieved

with around 4 $wt.\%$ cesium loading, substantially less than the 20 $wt.\%$ required to achieve maximum activity with the non-graphitised CNTs. This finding clearly shows that by graphitising the CNT support, the activity for ammonia decomposition can be enhanced while also reducing the use of cesium.

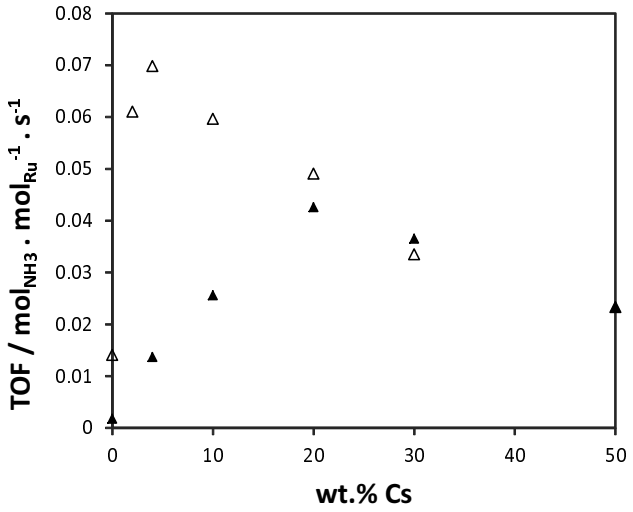


**Figure 4.15:** Rate of reaction for ammonia decomposition as a function of cesium loading at 600 $K$. (▲) - non-graphitised; (△) - graphitised. WHSV was 5,200 $mL_{NH_3}\, h^{-1}\, g_{cat}^{-1}$, catalyst mass was 25.0 $mg$ and TOF has units of $mol_{NH_3}\, mol_{Ru}^{-1}\, s^{-1}$ and was evaluated at exit conversion. Figure from paper (publication pending).

CO chemisorption and TEM experiments have been undertaken to understand the effect on the distribution of ruthenium nanoparticle supported on graphitised CNTs by changing the loading of cesium promoter. Representative TEM images of the different catalysts are shown in Figure 4.16. Similarly to ruthenium particles supported on non-graphitised CNTs, the ruthenium particles on graphitised CNTs are well dispersed with particle size between 1 - 4 $nm$.

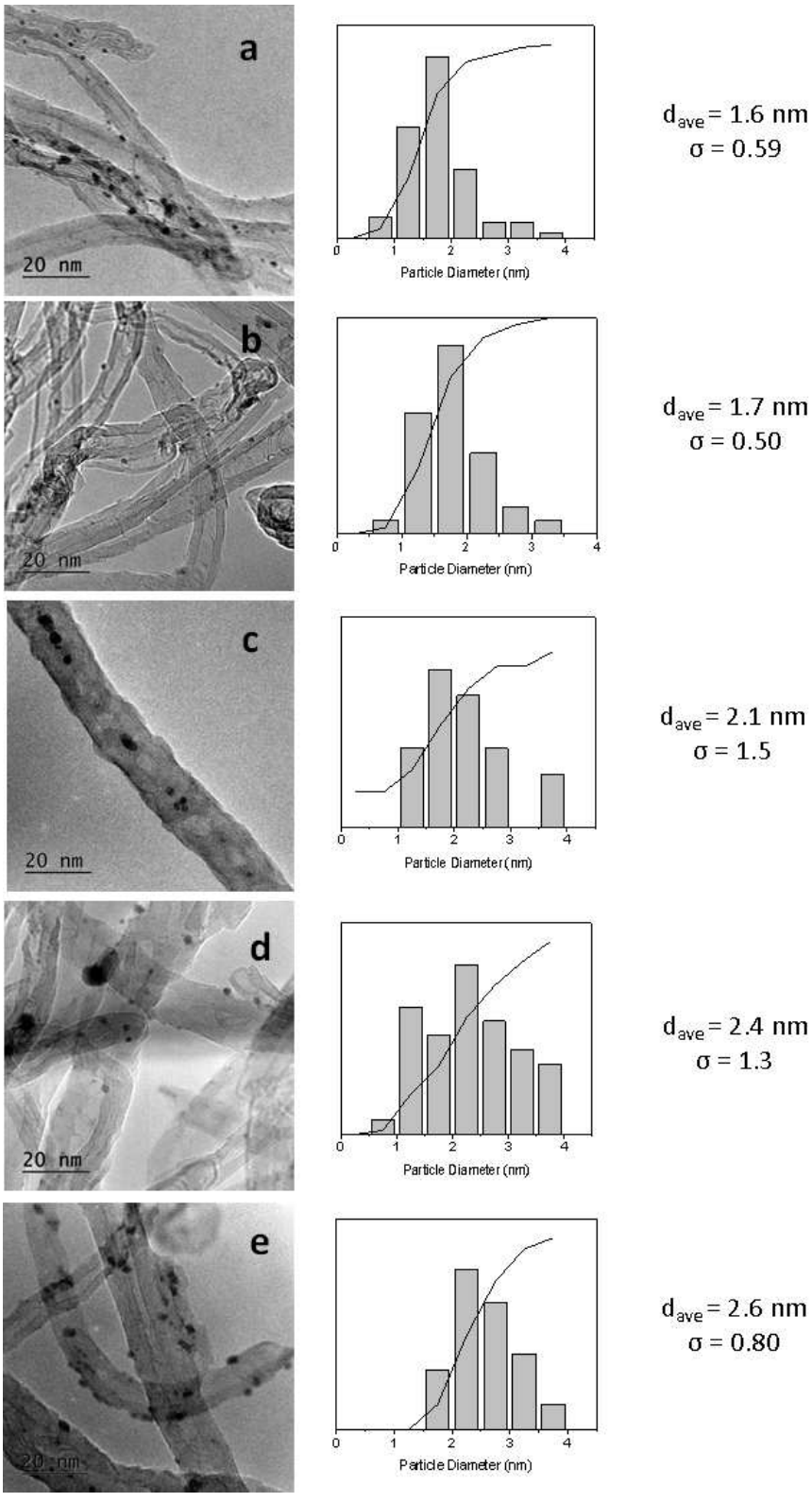


**Figure 4.16:** Representative TEM images showing the effect of cesium loading on Ru nanoparticles supported on CNTs annealed at 2073 $K$, histogram data taken from multiple images. (**a**) 7.0 *wt.*% Ru, 0 *wt.*% Cs; **b**) 7.0 *wt.*% Ru, 4 *wt.*% Cs; **c**) 7.0 *wt.*% Ru, 10 *wt.*% Cs; **d**) 7.0 *wt.*% Ru, 10 *wt.*% Cs; **e**) 7.0 *wt.*% Ru, 20 *wt.*% Cs.

Results of TPR experiments for ruthenium catalysts with varying cesium loading

supported on graphitised CNTs compared to non-graphitised CNTs are presented in Figure 4.17 and Table 4.6. Figure 4.17 a and d show catalysts with no cesium, Figure 4.17 b and e show catalysts with 4 $wt.\%$ Cs and Figure 4.17 c and f show catalysts with 10 $wt.\%$ cesium. All of the catalysts exhibit an initial negative peak caused by the interaction with the ruthenium precursor as discussed previously. In the absence of cesium, ruthenium reduces at around 440 $K$, this is similar to the findings for non-graphitised CNTs. This similarity suggests that there are equivalences in both the particle size and metal support interactions for both the graphitised and non-graphitised case. The temperature of reduction is aligned with published work on the reduction of ruthenium on CNTs [74]. Graphitisation of the CNTs has two effects upon the TPR result for the broad carbon peak, firstly the amplitude of the broad carbon peak is lessoned and secondly, the peak temperature occurs at higher temperature between 750 - 800 $K$ compared to around 700 $K$ in the non-graphitised case.

The introduction of cesium to the catalyst produces remarkable changes to the TPR spectra. Figure 4.17 b and e show the effect of loading 4 $wt.\%$ Cs upon the catalyst with 7.0 $wt.\%$ ruthenium. Both the graphitised and non-graphitised cases show a small positive peak at around 380 $K$. The non-graphitised CNT supported catalyst has a ruthenium reduction peak at 488 $K$ and a broader carbon peak at 707 $K$, but in the graphitised case, the ruthenium peak is larger and occurs at 516 $K$ with the broader carbon peak at 745 $K$. Figure 4.17 c and f show the effect of 10 $wt.\%$ Cs to catalysts with 7.0 $wt.\%$ ruthenium: the non-graphitised catalyst has a small positive peak at 380 $K$, a ruthenium peak at 517 $K$ and carbon peak 693 $K$. In contrast, the graphitised catalyst has a very tall peak at 380 $K$ and two converged peaks that have been deconvoluted with peaks at 516 and 745 $K$. Cesium has the same broad effect on ruthenium supported on both graphitised and non-graphitised CNTs: in both cases the reduction temperature and the magnitude and width of the reduction peak increase as a function of cesium loading. Graphitisation of the CNTs allows the same degree of interaction of ruthenium and cesium to occur but at much lower loadings of the promoter.

The reduction peak for ruthenium increases from 433 $K$ with no promoter, and increases to 517 and 600 $K$ for 4 and 10 $wt.\%$ cesium respectively and hydrogen consumption increasing from 0.001 to 0.008 $mmol\, g_{cat}^{-1}$ (see Table 4.6).

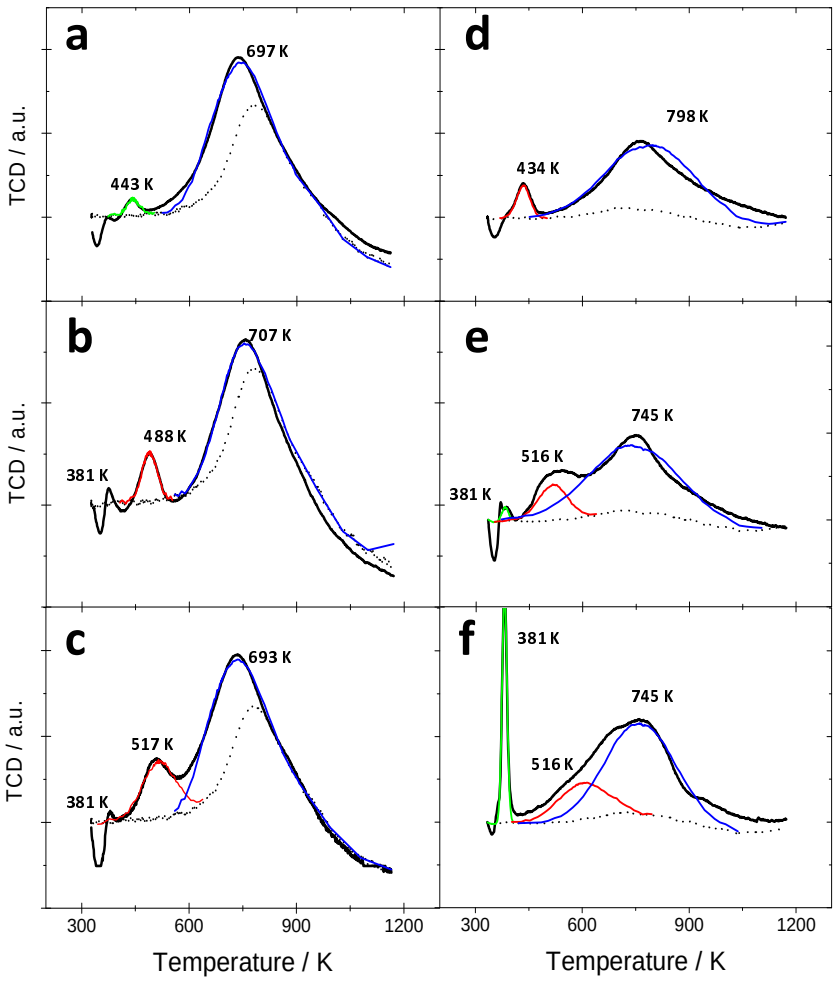


**Figure 4.17:** TPR results showing the effect of CNT graphitisation and Cs loading with 7 *wt.*% Ru/CNT catalysts. (**a**) 7 *wt.*% Ru/CNT; (**b**) 7 *wt.*% Ru, 4 *wt.*% Cs / CNT; (**c**) 7 *wt.*% Ru, 10 *wt.*% Cs / CNT; (**d**) 7 *wt.*% Ru / graphitised CNT; (**e**) 7 *wt.*% Ru, 4 *wt.*% Cs / graphitised CNT; and (**f**) 7 *wt.*% Ru, 10 *wt.*% Cs / graphitised CNT. The blank result is shown as a dotted line and serves as a baseline for curve fitting, the black line is the TPR results for the sample and the intermediate coloured lines are the fitted curves that account for the difference in hydrogen uptake compared to the blank graphitised CNTs.

**Table 4.6:** Integration of peaks from TPR experiments by curve fitting showing the effect of graphitisation.

| **Catalyst** | **Peak Temperature** $K$ | $H_2$**Consumed**) $mmol\, g_{cat}^{-1}$ | **Peak Temperature** $K$ | $H_2$ **Consumed** $mmol\, g_{cat}^{-1}$ |
|---|---|---|---|---|
| 7 $wt.\%$ Ru, 0 $wt.\%$ Cs / graphitised CNT | | | 433 | 0.002 |
| 7 $wt.\%$ Ru, 4 $wt.\%$ Cs / graphitised CNT | 378 | 0.0005 | 487 | 0.005 |
| 7 $wt.\%$ Ru, 10 $wt.\%$ Cs / graphitised CNT | 382 | 0.0050 | 517 | 0.008 |

It is clear that graphitisation of CNTs increases the effectiveness of the promoter in its interaction with ruthenium. This effect could be explained by the increase in electrical conductivity of the graphitised CNTs enabling the more efficient transfer of electrons from promoter to active nanoparticle. This work has found little evidence of a change in ruthenium nanoparticle size resulting from graphitisation of the CNT support and thus the electronic modification would appear to be the more likely cause of the increase in activity.

## 4.5 Test of Catalyst Stability

So far in this study, CNT supported ruthenium catalysts have been shown to possess excellent activity for the ammonia decomposition reaction but there are other important properties that influence its practical potential. In this case, a catalyst for an automotive application must operate for thousands of hours and still maintain a reasonable level of activity. While it was not possible to conduct a thousand hour experiment, an experiment was conducted in which the most active catalyst developed here with 7.0 $wt.\%$ ruthenium, 4 $wt.\%$ cesium on CNTs graphitised at 2073 $K$ was tested at elevated temperature (670 $K$), 200 $K$ above the intended operating temperature for an ammonia-PEM fuel cell, for over 100 hours. The results of this experiment are presented in Figure 4.18, conversion of ammonia started at 60 %, fell to 50 % after 50 hours and after 100 hours the activity was approaching 45 %. It is not clear whether this loss of activity was related to the effect of temperature or a poisoning of the catalyst caused by contaminants in the reactor feed gases.

The rate of loss of activity is not linear and could be considered to be exponential decay. If true, then the half-life can be calculated as 241 hours using equation 4.1 below

where $t_{1/2}$is the time to lose half of the catalyst's activity and $c$ is the decay constant [126]. The decay constant $c$ was evaluated to be 0.0029 from the experimental results where the time to reach 3/4 activity was 100 hours (the value 3/4 was substituted for 1/2). Although the rate of decay in activity would be significantly less at lower operating temperatures (assuming that the decay is temperature related), this loss of activity suggests that this catalyst system requires further development in this regard before it could be considered for practical applications.

$$t_{1/2} = \frac{1}{c} ln \left( \frac{1}{2} \right) \tag{4.1}$$

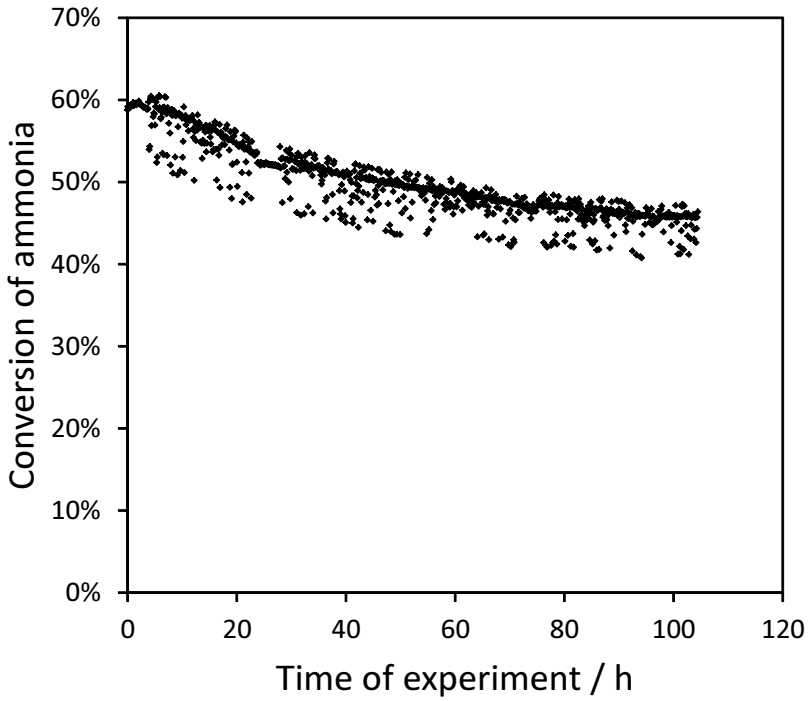


**Figure 4.18:** 100 hour longevity test of catalyst with 7.0 $wt.\%$ ruthenium, 4 $wt.\%$ Cs on graphitised CNTs. The experiment was conducted at 670 $K$, WHSV of ammonia was 10,350 $mL_{NH_3}\, h^{-1}\, g_{cat}^{-1}$ and the reactor contained 6.8 $mg$ of catalyst with the standard quantity of $SiC$ diluent used throughout this work.

## 4.6 Conclusions

The presence of high loadings of cesium promoter, up to 20 $wt.\%$, to CNT supported ruthenium catalysts is shown to achieve activity for ammonia decomposition below 470 $K$. Characterisation by TPR shows that the cesium is located on the surface of or in close proximity to the active ruthenium nanoparticles where it probably

modifies the ruthenium nanoparticles electronically producing a remarkable decrease in activation energy for ammonia decomposition. At high cesium loadings, the cesium on the surface of the ruthenium nanoparticle seems to block access to the active site causing a reduction in activity.

Modification of ruthenium nanoparticle size by changing the ruthenium loading had a much more modest effect on activity and made little change to the measured activation energy for ammonia decomposition, this suggests that a similar ruthenium active surface was present at all loadings from 3.0 to 13.2 $wt.\%$. TPR results show that the degree of apparent hydrogen consumption by ruthenium increases greatly following the addition of cesium, suggesting that partial reduction of cesium occurs in proximity to ruthenium. This substoichiometric cesium oxide would act as a powerful electron donor explaining its effectiveness as promoter and further supporting the claim that the cesium promoter primarily acts electronically.

Modification of the CNT support by graphitisation produced catalysts for ammonia decomposition that were active from 450 $K$. The enhanced conductivity of the graphitised CNTs had a strong effect on the impact of the cesium promoter by enabling the promoter to effectively donate electrons from greater distance on the catalyst surface. The result was substantially enhanced catalytic activity to be achieved at lower promoter loadings.

The activity of the catalyst was shown to decay during operation at 670 $K$ with a half-life of 241 hours. The cause of this decay is not well understood and further development is required to improve this stability before this catalyst can be considered for a practical application.

The reduction in active temperature to 450 $K$ represents good progress toward the goal of an integrated ammonia-PEM fuel cell operating around 373 $K$ but significant further enhancements are required before a successful catalyst can be produced for this process. Future catalyst development should build upon the success shown here with modification of the electrical conductivity of support material and develop new supports to allow tailoring of nanoparticle size and electronic interaction with the promoter. Bi-metallic active nanoparticles present an interesting possibility to increase the activity over ruthenium by the modification of the surface metal by a second metal through the pseudo-ligand effect, this is explored further in chapter 5. Furthermore, the application of bi-metallics could enable more abundant and more commercially viable catalytic metals such as cobalt or nickel to be utilised for this application. Despite being less active, catalysts designed with these metals can compensate by using much greater quantities and therefore can achieve similar performance at lower cost. This mirrors the ammonia synthesis industry in which

iron based catalysts are almost exclusively used despite the much greater activity of ruthenium.

# Chapter 5

# Development of Sustainable Catalysts for the Decomposition of Ammonia

## 5.1 Introduction

The ultimate goal of this project is the development of an ammonia-PEM fuel cell that delivers renewable low-carbon energy to mobile applications such as road transport. This requires not just a highly active catalyst but also the sustainable aspects of this application means that the sustainability of the catalyst design should also be considered. In the previous chapter, carbon nanotube (CNT) supported ruthenium and cesium catalysts were developed with excellent low temperature activity for ammonia decomposition. However, the use of ruthenium as an active metal raises questions around the sustainability of this design of catalyst. In an analysis of endangered elements, Davies found that the supply of ruthenium was under rising threat due to increased use [127].

The sustainability of a metal is difficult to quantify clearly because of the many different aspects that contribute to its sustainability. In Table 5.1 recent findings on sustainable aspects of catalytic metals of interest for the ammonia decomposition reaction are quantified. The most highly active metals (see Figures 2.6 and 2.7) ruthenium, iridium and rhodium have low abundance, high global warming potential (GWP) and high human toxicity. For these reasons, despite their high activity, they cannot be considered as a sustainable choice of catalytic metal. The second tier of active metals are cobalt and nickel, they have much greater abundance and lower GWP and toxicity. Next most active is iron which has the best scores here, the other metals, copper, molybdenum and silver have significantly less or no activity.

It can be concluded that cobalt, nickel and iron can be considered as significantly more sustainable alternatives to ruthenium.

**Table 5.1:** Sustainability Assessment of Catalytic Metals

| Catalytic Metal | Abundance [128] *ppm* | Supply Risk Rating [a] [128] | GWP [b] $kg_{CO_2-eq}\,kg^{-1}$ [129] | Human Toxicity $MCTUh\,kg^{-1}$ [c] [129] |
|---|---|---|---|---|
| Cobalt | 26.6 | 7.6 | 8.3 | 3.8 |
| Copper | 27 | 4.3 | 2.8 | 270 |
| Iridium | 0.000037 | 7.6 | 8,860 | 50,000 |
| Iron | 52,157 | 5.2 | 1.5 | 0.4 |
| Molybdenum | 0.8 | 8.6 | 5.7 | 900 |
| Nickel | 26.6 | 6.2 | 6.5 | 23 |
| Rhodium | | | 35,100 | 270,000 |
| Ruthenium | 0.00057 | 7.6 | 2,110 | 16,000 |
| Silver | 0.055 | 6.2 | 196 | 690 |

[a] - Includes abundance, consumption rate, recycling rate, location of reserves and other factors.
[b] - Global warming potential.
[c] - Comparative toxic units.

From a commercial perspective, the price of these metals differs substantially from 30 - 40 US dollars per gram ($USD\,g^{-1}$) for rhodium and iridium, around 3 $USD\,g^{-1}$ for ruthenium and 0.02 - 0.03 $USD\,g^{-1}$ for nickel and cobalt respectively [130]. Thus, the development of catalysts featuring nickel and cobalt can be considered as sustainable both from a perspective of depleting global resources and also commercial viability.

In this chapter, sustainable active metals such as nickel and cobalt, are investigated as catalysts for the ammonia decomposition reaction. The relationship between the carbon support structure and catalyst activity is investigated and a study of supported bi-metallic catalysts is also presented.

## 5.2 Sustainable Single Metal Catalysts on Porous Carbons

The objective of this section is to examine the combination of a single active metal and porous carbon support for the ammonia decomposition reaction. The best starting point for finding alternative metals to ruthenium are the volcano curves that show activity for ammonia decomposition for active metals as a function of

key interaction energies with reacting species (see Figures 2.6 and 2.7 in Chapter 2). In these curves, the most active metals for the ammonia decomposition reaction other than ruthenium are generally iridium, nickel, cobalt and rhodium. Given the previous discussion on the sustainability of these metals, this study focuses on the use of cobalt and nickel as both active and sustainable catalytic metals.

In changing the active metal from ruthenium to nickel or cobalt, the choice of support should be reconsidered as the best support for one metal may not be the optimum for others. The support can alter the properties of the active nanoparticle both structurally and electronically. The particle size of nanoparticles confined within pores is a function of the support pore size. For nanoparticles outside of pores, the dispersion of nanoparticles and the resultant particle size depends upon the surface area and surface defects [123]. Aspects of the surface structure such as the degree of graphitic quality can also have a strong influence upon nanoparticle activity [131]. The relative importance of these factors was investigated for ruthenium on porous carbon supports by Li *et al.* who found the most important factor to be the degree of surface graphitic alignment [131]. After graphite, the order of activity was CNT > carbon black > CMK3 > activated carbon. It is not known whether this tendency also applies to other metals such as nickel and cobalt.

Before proceeding, the concept of a volcano curve to represent the relationship between the optimum active surface to the interaction of that surface with characteristic reacting species was tested by constructing a volcano curve based upon two different published studies (Figure 5.1). The activity for ammonia decomposition (taken from a screening of metals for ammonia decomposition by Yin *et al.* [120]) was plotted as a function of the theoretical metal surface to molecular nitrogen bonding energy. For a reaction such as ammonia decomposition that is limited by surface recombination of nitrogen adatoms, the interaction energy with nitrogen could be considered to be an important factor. This data was taken from a published DFT volumetric analysis of surface properties (VASP) analysis by Hansgen *et al.* who calculated the zero coverage binding energy of nitrogen on the metal surface for each metal (lattice structures were FCC(111) for Pt, Pd, Ni & Rh, HCP(0001) for Ru and BCC(110) for Fe) [23]. The figure does not contain activity data for cobalt as this was omitted in the study by Yin *et al.* but the binding energy of cobalt with $N_2$ is indicated.

The results in Figure 5.1 conform to the volcano curve shape with the optimum activity for active metal occurring with a nitrogen interaction energy of 570 - 620 $kJ\,mol^{-1}$. The binding energy of cobalt would suggest that it possesses similar activity to nickel and rhenium. These results give further evidence to support using nickel and cobalt as sustainable active metals for the ammonia decomposition

reaction.

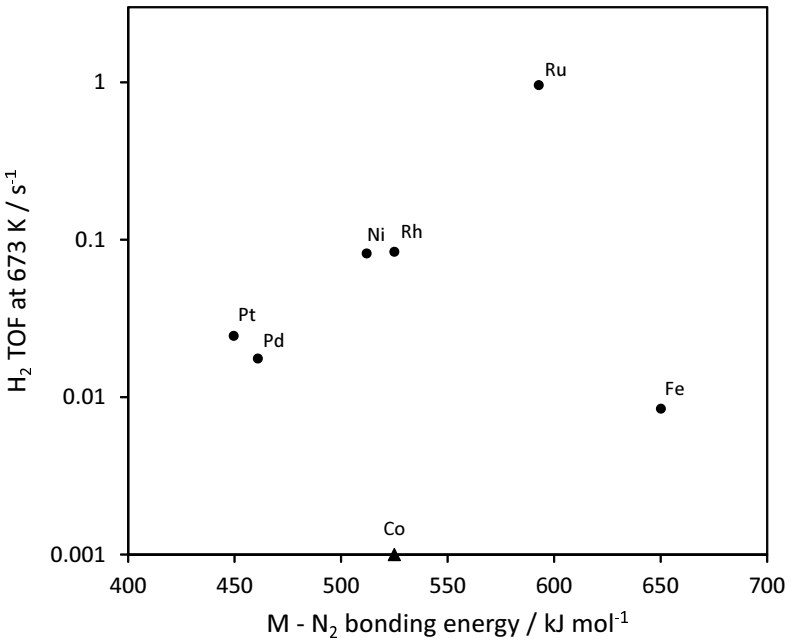


**Figure 5.1:** Ammonia decomposition vs metal to $N_2$ bonding energy volcano curve and indication of $N_2$ bonding energy for cobalt. Constructed from published data for decomposition of ammonia at 673 $K$ [120] and published zero coverage metal - nitrogen binding energy calculated from DFT VASP. The metal surface (M) was FCC(111) for Pt, Pd, Ni & Rh; HCP(0001) for Ru & Co and BCC(110) for Fe [23, 59].

Although the relative activity of ruthenium, cobalt and nickel is well known, there is much less information on the properties of catalyst support required to maximise the activity of these metals. In a preliminary look at this relationship, mono-metallic catalysts with 7.0 $wt.\%$ ruthenium, cobalt and nickel supported on CNT and a microporous carbon (Ax21) were tested for activity for ammonia decomposition, the results are presented in Figure 5.2. Metal precursors were $Ru(NO)(NO_3)_3$, $NiNO_3$ and $CoNO_3.6H_2O$; solvents were water for ruthenium and acetone for nickel and cobalt. Acetone was used in preference to water where the solubility of the precursors permitted because its lower surface tension allows for greater pore filling of the support [58]. The results show that the ruthenium catalyst becomes less active when supported on Ax21 than CNTs. This is a similar finding to that of Li *et al.* who found that CNTs were more active than porous carbons as supports for ruthenium [131]. However, the opposite is true for cobalt which becomes substantially more active when supported on Ax21 compared to CNTs and almost reaches the same activity as ruthenium on this support. The nickel catalyst was less active than both the ruthenium and cobalt catalysts. These findings suggests that the order of activity for carbon supports will not be the same for cobalt as it is for ruthenium. They

also suggest that tailoring of key support properties is a vital factor in maximising cobalt activity for this reaction.

The porous carbons studies here vary in a number of different aspects relating to the material origin and synthesis method. The Ax21 support was prepared by an alkali activation technique and is likely to have significant residual potassium which could be expected to behave as a promoter given its location in group 1 of the periodic table. Also, the use of different solvents: water for ruthenium and acetone for nickel and cobalt may change the relative activities of the metals. These aspects do not undermine the finding that cobalt is proportionally more active on Ax21 than CNTs compared to ruthenium. The effect of residual potassium would be expected to enhance ruthenium activity as much as cobalt, the fact that it doesn't means that this effect is unlikely to be significant. While the change in solvent is likely to be significant, the same solvent was used for the same metal across both supports and hence the comparison between supports is valid for each metal .

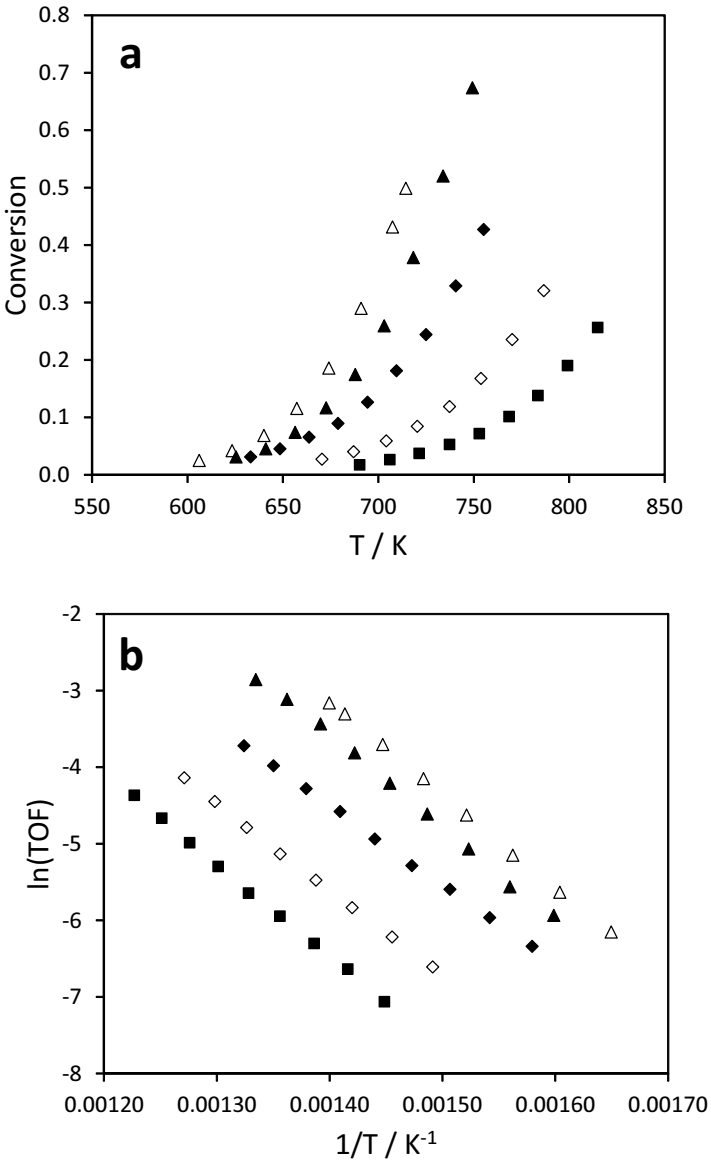


**Figure 5.2:** Conversion vs Temperature and Arrhenius drawing showing the activity of metal M on carbon supports for ammonia decomposition where M is either Co, Ru or Ni. ◇ - 7 *wt.*% Co on CNTs, ◆ - 7 *wt.*% Co on Ax21, △ - 7 *wt.*% Ru on CNTs, ▲ - 7 *wt.*% Ru on Ax21 and ■ - 7 *wt.*% Ni on Ax21. **a** - conversion vs temperature and **b** - Arrhenius plot. Reaction conditions were 5,200 $mL_{NH_3}\,h^{-1}\,g_{cat}^{-1}$ WHSV and 25.0 $mg$ of catalyst. TOF has units of $mol_{NH_3}\,mol_{Ru}^{-1}\,s^{-1}$ and was evaluated at exit conversion.

Given the enhancement in cobalt activity by microporous Ax21 compared to CNTs, the study was widened to consider a broader variation of carbon supports. A range of carbon supports were prepared, each with 7.0 *wt.*% cobalt. The carbons were Ax21, MSC-30 and activated charcoal that have microporosity as well as CMK-1, mesoporous carbon, and CNTs that exhibit mesoporosity. The activity for ammonia decomposition is shown in Figure 5.3, the most active catalyst was Ax21 followed by CMK-1, MSC-30, mesoporous carbon and then CNTs. The activated charcoal

support was found to have negligible activity. It is significant that the cobalt catalyst supported on different porous carbons exceed the activity of cobalt on CNTs and it is a clear change to the order of activity for ruthenium in which Li *et al.* showed that the activity of ruthenium on CNTs exceeded all porous carbons except for graphitic carbon [131].

To better understand why porous carbons produced more active cobalt catalysts, the supports were characterised by nitrogen adsorption / desorption and Raman spectroscopy. These techniques enable estimates to be made of key properties of the support such as surface area, pore size distribution, degree of graphitisation (inferred from the $I_D/I_G$ ratio which reflects the ratio of amorphous carbon to graphitically ordered carbon) and incipient wetness pore volume. Results from these characterisation experiments are shown in Table 5.2 alongside kinetic results for ammonia decomposition. The activity for ammonia decomposition does not correlate to the $I_D/I_G$ ratio: the most graphitic support, mesoporous carbon, is less active than CNTs, Ax21 and CMK-1. This is a departure from the results presented in Chapter 4 and also the findings of Li *et al.* [131] for ruthenium on carbon where the activity strongly correlated with the degree of surface graphitisation. The three most active catalysts have the smallest support pore size and the greatest support surface area of all the catalysts tested. This factor appears to have a strong impact upon the rate of reaction compared to activation energy which is largely constant across the supports, despite significant variations in the degree of surface graphitisation.

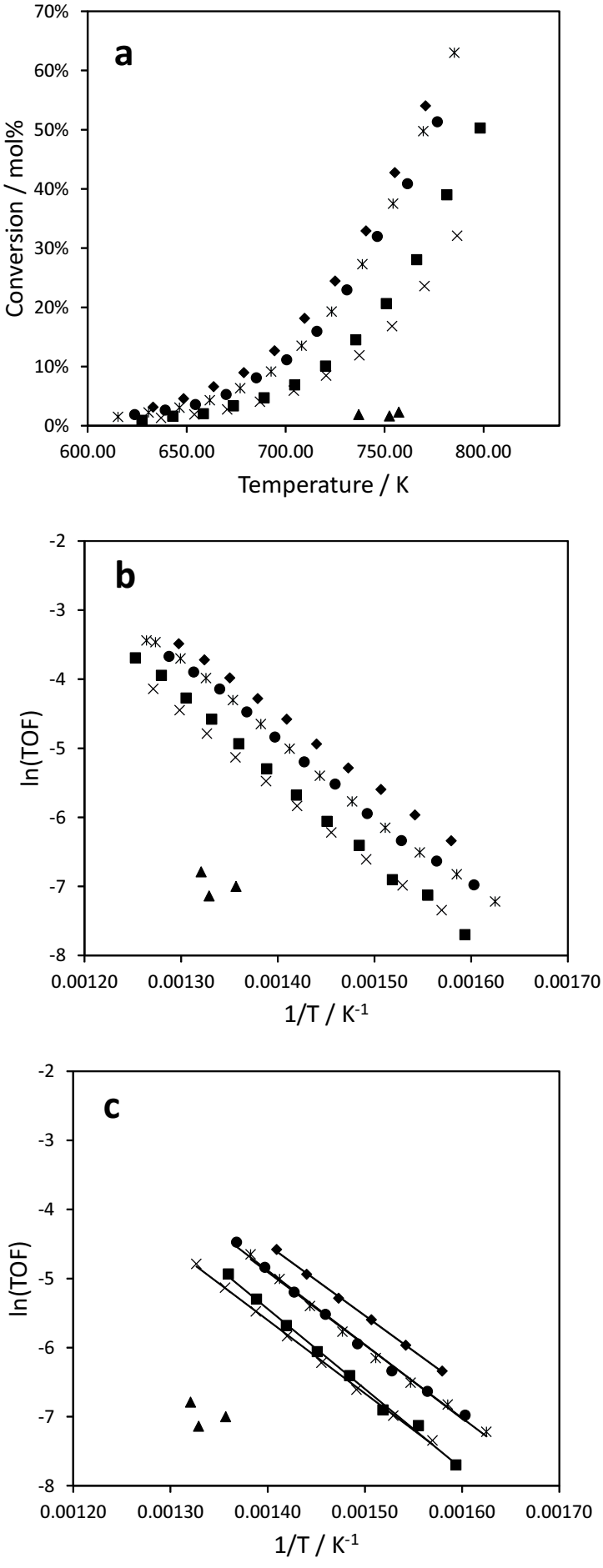




**Figure 5.3:** Conversion vs Temperature and Arrhenius drawing showing the activity of Co on various carbon supports for ammonia decomposition: **a** - conversion vs temperature, **b** - Arrhenius plot and **c** - Arrhenius plot with conversion $< 20$ % for evaluation of the

**Table 5.2:** Summary of characterisation data and activity for ammonia decomposition at 700 $K$ for catalysts with 7.0 $wt.\%$ cobalt supported on porous carbons.

| Carbon Support | BET Surface Area[a] $m^2\,g^{-1}$ | BJH Pore Size[b] $nm$ | Raman Intensity $I_D/I_G$ | Incipient Wetness Volume[c] $mL\,g^{-1}$ | TOF at 700 $K$ (x1000) $s^{-1}$ | Activation Energy $kJ\,mol^{-1}$ |
|---|---|---|---|---|---|---|
| Ax-21 | 2257 | 2.3 | 3.2 | 3.0 | 8.0 | 85.1 |
| CMK-1 | 776 | 3.3 | 2.4 | 2.5 | 5.2 | 89.2 |
| MSC-30 | 2662 | 2.3 | 2.2 | 2.8 | 4.8 | 87.8 |
| Mesoporous Carbon | 217 | 6.9 | 0.8 | 1.7 | 3.0 | 96.3 |
| CNTs | 253 | 27.5 | 2.6 | 10.0 | 2.8 | 88.2 |
| Activated Charcoal | 483 | 5.7 | 1.6 | 1.9 | $< 0.1$ | - |

[a] - Measured by $N_2$ desorption using the BET method from desorption data.
[b] - Measured by $N_2$ desorption using the BJH method with Halsey Faas correction.
[c] - Incipient wetness volume measured with acetone.

The results of nitrogen physisorption experiments at 77 $K$ are shown in Figure 5.4. Results presented for each support include the BJH dV/dlog(D) pore volume distribution alongside the isotherm. Data is presented up to a pore size of 20 $nm$, most of the data shows the sharp characteristic nitrogen peak at around 4 $nm$ that is caused by the instability of the hemispherical meniscus for nitrogen desorption in pores of this specific size [132]. CNTs show average pore size of 27.5 $nm$ by BJH desorption method that is representative of the tubular structure and a smaller peak at 3 - 4 $nm$ that may be related to defects. Mesoporous carbon has average pore size of 6.9 $nm$ , Ax21 and MSC-30 have 2.3 $nm$ , activated charcoal at 5.7 $nm$ and CMK-1 at 3.3 $nm$ by the same method. Ax21 and MSC-30 show type I isotherms typical of microporous material, the other supports show variations of type IV isotherms that are indicative of mesoporosity, with CMK-1 and activated charcoal showing some significant adsorption and desorption at low relative pressure indicating a greater degree of microporosity. The surface area of the carbons is in accordance with the isotherms, the microporous Ax21 and MSC-30 show very high surface area of 2257 and 2662 $m^2\,g^{-1}$, the more mesoporous CMK-1 and activated charcoal have surface area of 776 and 483 $m^2\,g^{-1}$ respectively and the fully mesoporous supports of CNTs and mesoporous carbon have a surface area of 253 and 217 $m^2\,g^{-1}$ respectively.

In general it can be said that the CNTs and mesoporous carbon show only mesoporosity, CMK-1 and activated charcoal show both meso and microporosity and the Ax21 and MSC-30 are microporous.

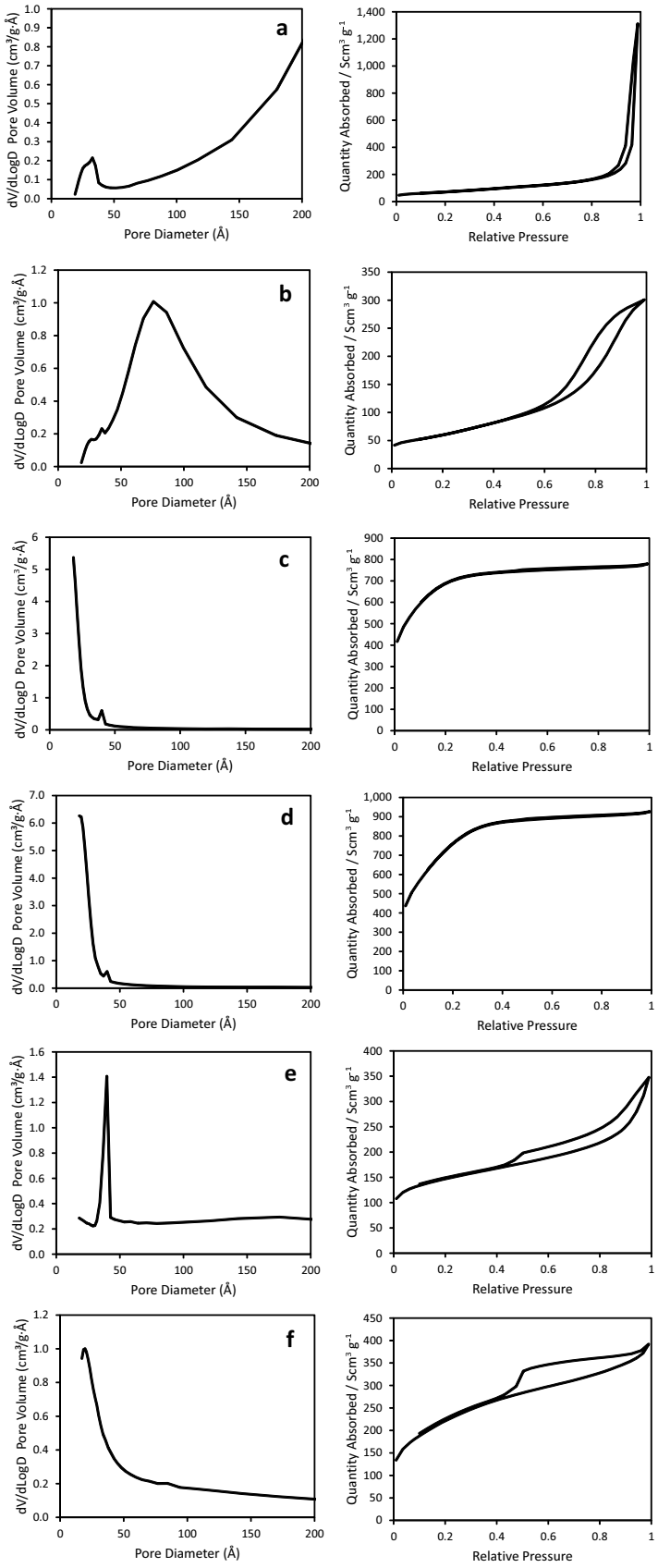


**Figure 5.4:** Nitrogen desorption results for porous carbons at 77 $K$. **a** - CNTs, **b** - mesoporous carbon, **c** - Ax21, **d** - MSC-30, **e** - activated charcoal, **f** - CMK1.

Further information on the structure of the carbons can be gathered by analysing the Raman spectra shown in Figure 5.5. Three significant peaks are exhibited by the carbon supports. The D band, which reflects the degree of disorder in the carbon structure, appears at approximately 1350 $cm^{-1}$. The other peaks of significance are the G band and the G' band that occur at approximately 1600 and 2750 $cm^{-1}$ respectively and reflect the graphitic ordering and alignment of the carbon structure. The degree of graphitisation of carbon materials is often described using the ratio of the intensity of D and G bands [131], these ratios are shown here in Table 5.2. The most graphitic support is mesoporous carbon, then activated charcoal, MSC-30, CMK-1, CNTs and Ax21.

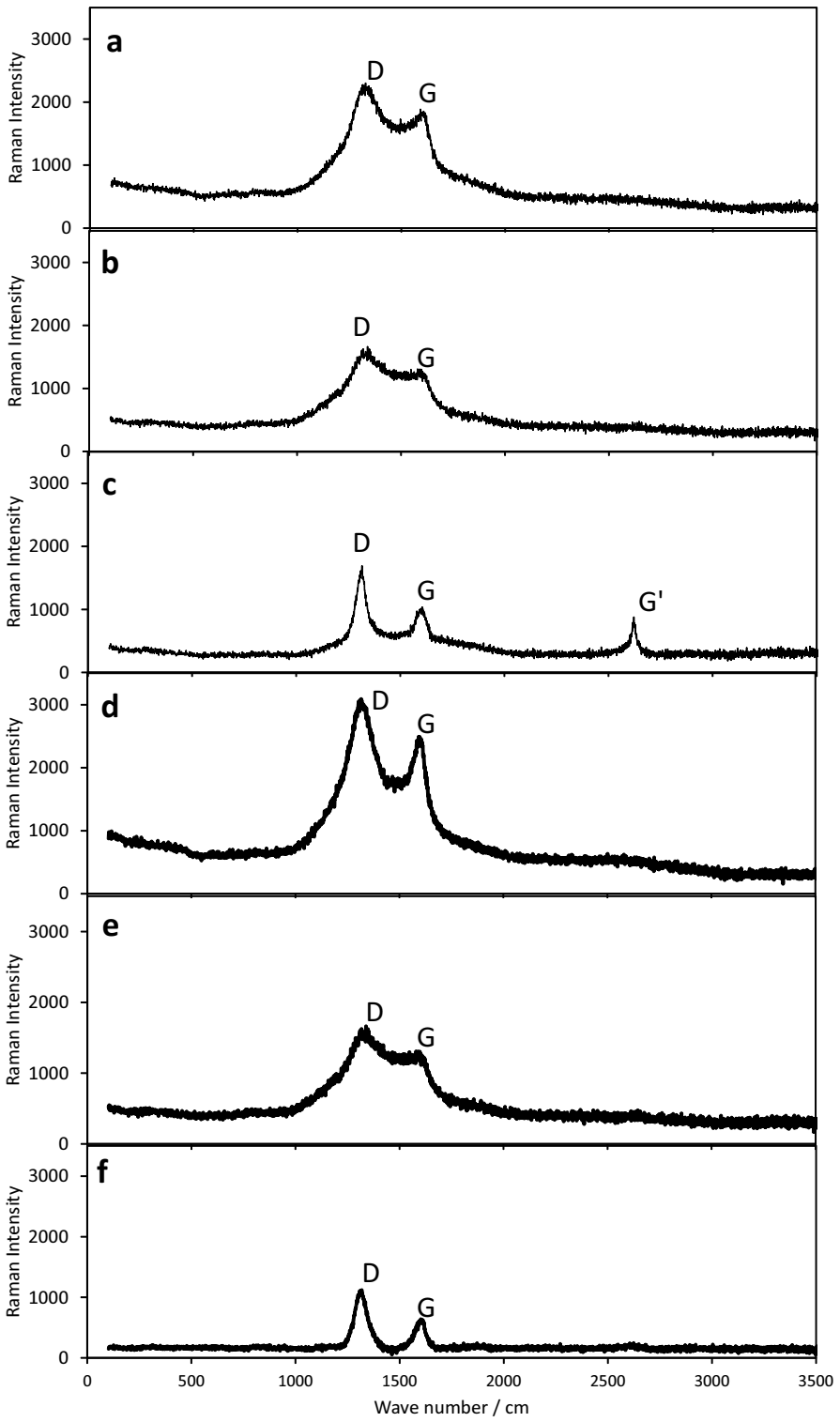


**Figure 5.5:** Raman spectra of porous carbons with characteristic D, G and G' bands identified. **a** - Ax21, **b** - MSC-30, **c** - Mesoporous carbon, **d** - CMK-1, **e** - CNTs and **f** - Activated Charcoal.

TEM images of catalysts with cobalt supported on the various carbon supports are shown in Figures 5.6 and 5.7. Figure 5.6 shows the images of Ax21 and MSC-30

microporous carbon supports with and without 7.0 *wt.*% cobalt. Figure 5.7 shows the cobalt nanoparticles supported on mesoporous carbon, activated carbon and CMK-3. In all cases there is a great deal of variability in the size of nanoparticles which range between 2 - 20 *nm*. Larger agglomerates appear on the microporous supports activated charcoal, Ax21 and MSC-30 that are not present on the mesoporous carbon or CMK-1. It must also be noted that any cobalt particles with a diameter of approximately 1 *nm* or less would not be visible in these images, this would include particles confined within micropores. It is for this reason that no histograms have been constructed for particle size distribution as they are unlikely to be representative.

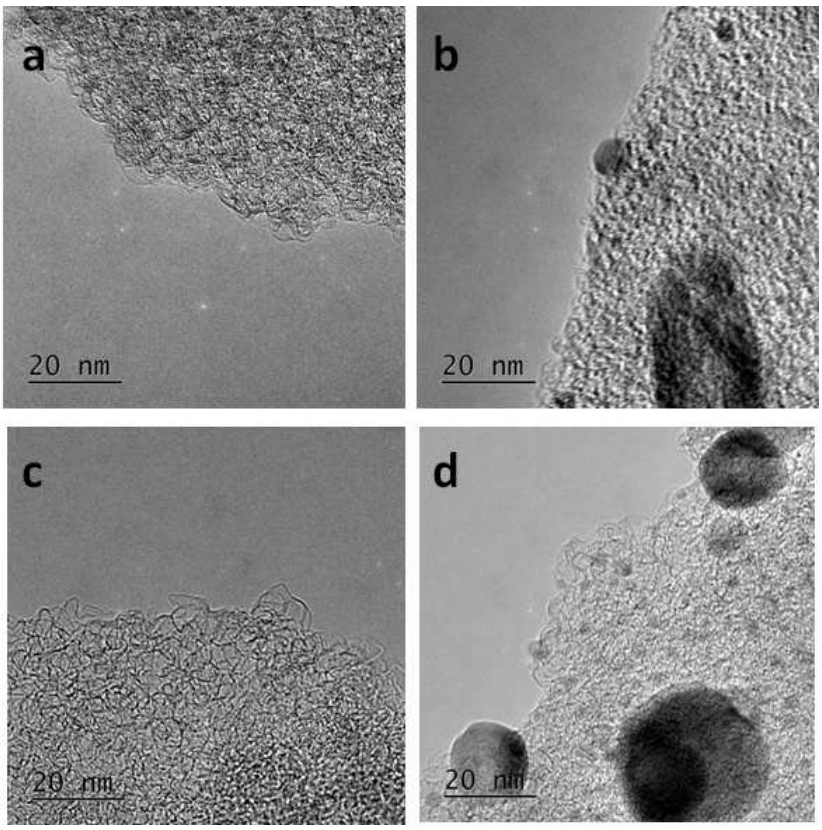


**Figure 5.6:** Representative TEM images of porous carbons with and without cobalt. **a** - Ax21, **b** - Ax21 with 7.0 *wt.*% Co, **c** - MSC-30 and **d** - MSC-30 with 7.0 *wt.*% Co.

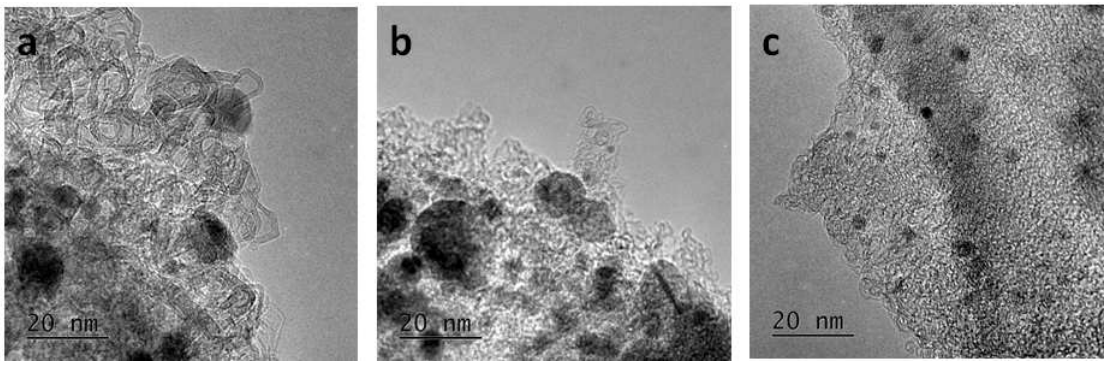


**Figure 5.7:** Representative TEM images of porous carbons with with 7.0 *wt.*% Co. **a** - mesoporous carbon, **b** - activated carbon and **c** - CMK-3.

To better understand the distribution of cobalt on MSC-30, an EDS experiment was undertaken on the catalyst with 7.0 *wt.*% cobalt. The results of which are presented in Figure 5.8 alongside the TEM image of the same site. The TEM image shows a number of dark areas on the catalyst surface that could be cobalt particles ranging here from 5 - 20 *nm*. The EDS spectra shows that while there may be slightly more cobalt density in these regions, the cobalt is generally very well dispersed on the catalyst surface and pore structure. Any cobalt present within the carbon micropores would be too small to be resolved from the TEM image and this may account for a significant proportion of the total cobalt. Of the species analysed, the spectra analysis measured 77.1 *wt.*% carbon, 22.4 *wt.*% cobalt, 0.5 *wt.*% oxygen and 0 *wt.*% potassium. The high concentration of cobalt compared to the overall loading of 7.0 *wt.*% suggests that the incipient wetness impregnation method employed here produced substantial localised variations in metal loading. The small quantity of oxygen suggests that the cobalt was largely in its reduced state and not oxidised, the zero results for potassium suggests that residual material from the alkali activation method was not a significant factor.

From the microscopy experiments, it can be concluded that for microporous supports, there is a large range of cobalt particle sizes from being confined within micropores through to larger agglomerations of 20 *nm* or more. The mesoporous supports tended to produce a more consistent particle size. It was not possible to accurately quantify the particle size and distribution of particle size.

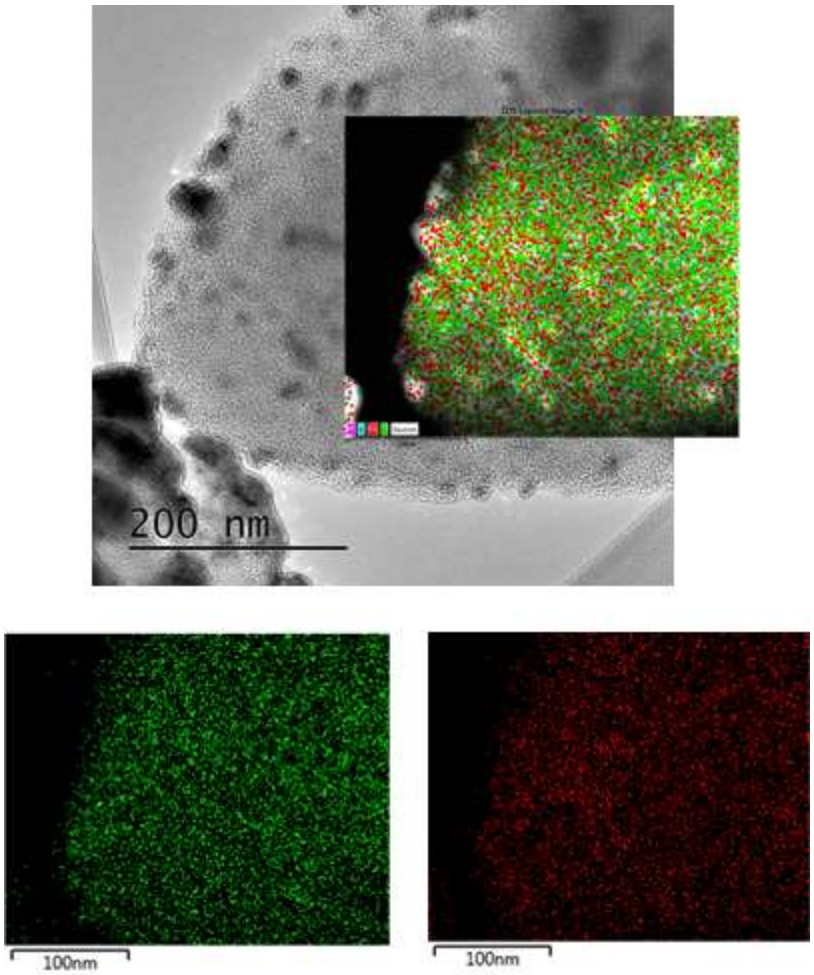


**Figure 5.8:** EDS analysis of 7 *wt.*% Co on MSC-30. EDS spectra inset from main TEM image where green is carbon, red is cobalt, blue is potassium and purple is oxygen.

Temperature programmed reduction analyses (TPR) were undertaken for cobalt supported on six different carbons: Ax21, MSC-30, CMK-1, mesoporous carbon, activated charcoal and CNTs. The normalised results are presented in Figure 5.9, the fainter line is the TPR spectra of the support material and the darker line is the support after impregnation with cobalt. In the absence of cobalt, each of the carbons except the mesoporous carbon exhibit a broad peak between 800 and 1000 $K$; the mesoporous carbon showed very little consumption of hydrogen at all presenting a negligible peak compared to the other supports. When 7.0 *wt.*% cobalt is added, a broad peak is expressed at around 720 to 754 $K$ and the peak at higher temperature is no longer present. Exceptions are activated charcoal where the cobalt peak is expressed at 560 $K$ and on CNTs where two peaks are expressed at 400 and 750 $K$. Published studies on cobalt reduction suggest reducing the catalyst at 773 $K$ [25] although some studies also suggest a partial reduction of cobalt oxide at 483 $K$ [133].

Each of the catalysts that showed activity for ammonia decomposition exhibit a reduction peak maxima within the narrow range of 720 to 754 $K$. It is likely that this feature relates to the active state of cobalt supported on the carbon. The activated charcoal supported catalyst showed an apparent cobalt reduction peak at 560 $K$ but this did not produce an active catalyst.

Information about the dispersion of cobalt on the catalyst can be gained by comparing the change in TPR spectra following addition of cobalt. With the exception of the graphitic mesoporous carbon that showed no consumption of hydrogen, each of the other carbon supports exhibited a significant consumption of hydrogen at around 800 - 1000 $K$. The consumption of hydrogen by the support could be caused by a methanation reaction occurring at surface defects [115], or it could be a reaction with surface oxygen complexes such as those present on acid treated CNTs [134]. Both surface defects and surface oxygen complexes are known to act as anchoring points for metal nanoparticles [80], so the hydrogen consumption measured by TPR experiments has a direct implication to the performance of the material as a catalyst support by altering the dispersion of metal nanoparticles.

The loading of cobalt decreases the temperature of interaction with hydrogen by over 100 $K$, leaving little interaction at the higher temperature. The presence of cobalt either changes the interaction between the support and hydrogen or prevents interaction by coverage. The disappearance of the original peak from most of the spectra is a good indication that the cobalt is highly distributed upon the support.

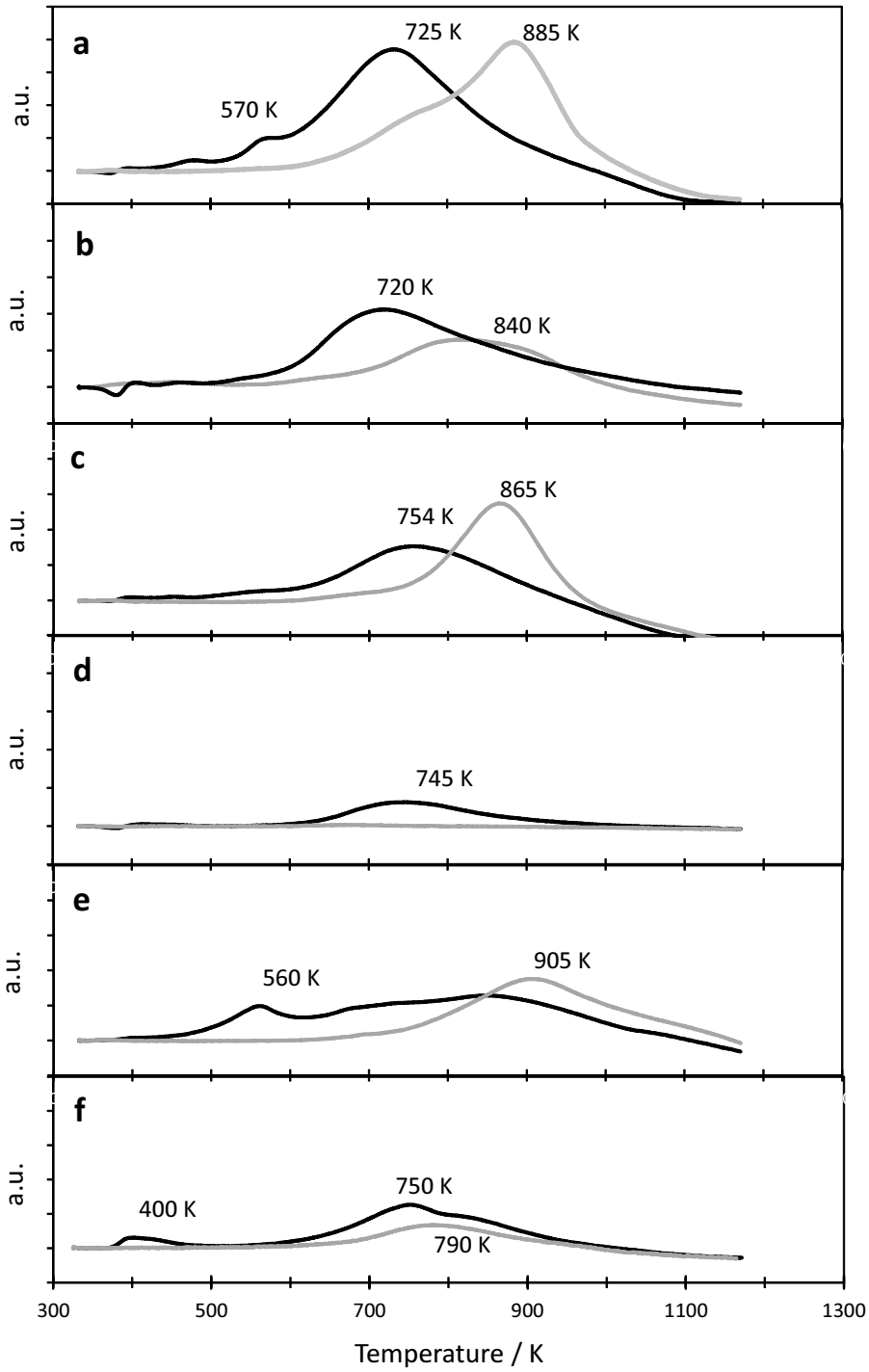


**Figure 5.9:** TPR Spectra of Co particles supported on porous carbons. Catalysts consisted of 7 *wt.*% Co supported on **a** - Ax21, **b** - MSC-30, **c** - CMK-1, **d** - Mesoporous carbon, **e** - Activated Charcoal and **f** - CNTs.

XRD spectra for the carbon supports with and without 7.0 *wt.*% cobalt are presented in Figure 5.10. All of the carbon supports display a broad peak at a diffraction angle ($2\theta$) between 10 - 18$^o$ and a smaller broad peak at 43$^o$. In addition to this, the mesoporous carbon displays a broad peak at 26$^o$; the mesoporous carbon, Ax21,

MSC-30 and CMK-3 display a sharp peak at 29°. The addition of cobalt does not produce a clear change in spectra on any of the supports other than a reduction in amplitude of existing peaks, there are no new peaks that correspond with standard cobalt FCC crystal diffraction spectra (See Figure 5.10 b). This might suggest either that the cobalt is well distributed or that it is not in ordered crystalline form and could be partially oxidised (although CoO peaks are also not exhibited in the spectra).

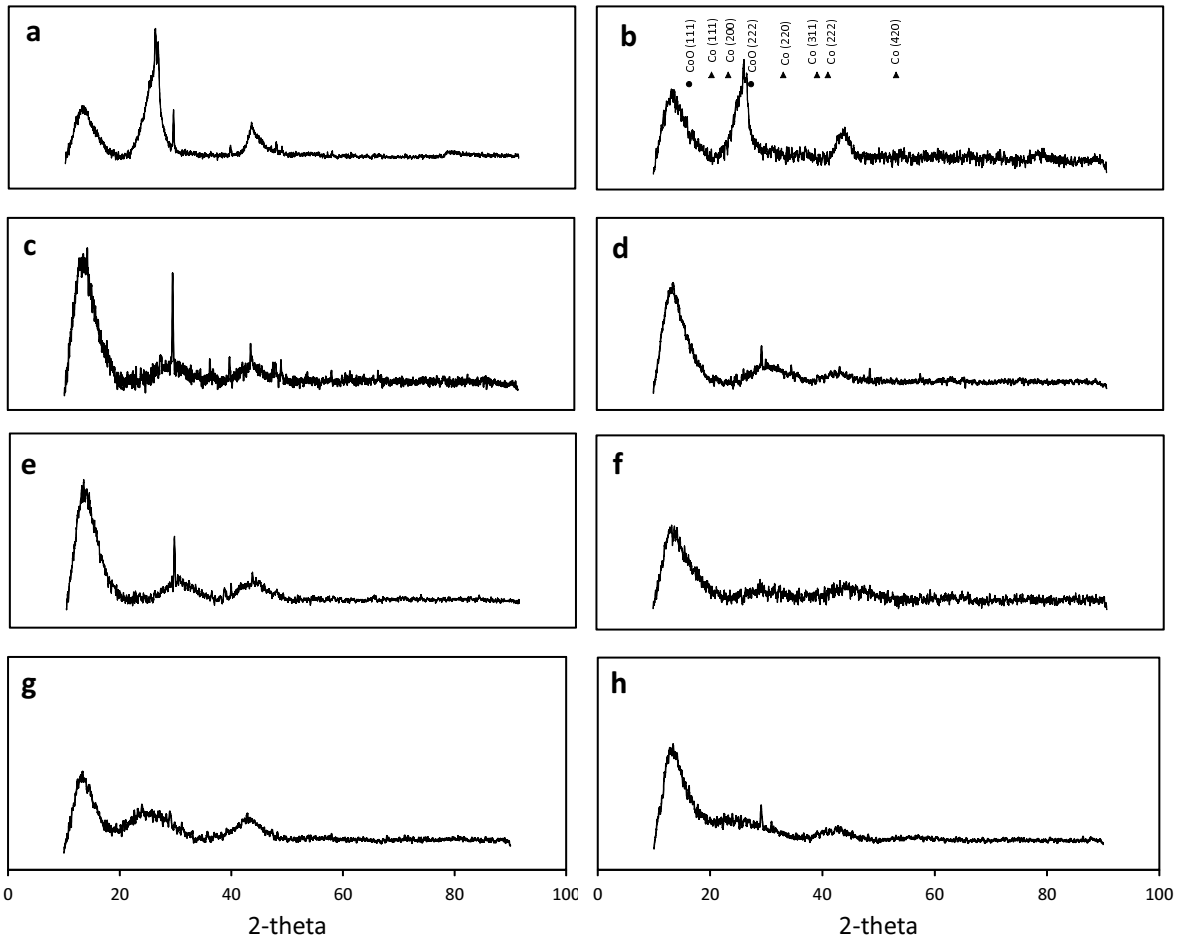


**Figure 5.10:** XRD spectra of porous carbons and cobalt. **a** - mesoporous carbon, **b** - 7 *wt.*% Co on mesoporous carbon, **c** - Ax21, **d** - 7 *wt.*% Co on Ax21, **e** - MSC-30, **f** - 7 *wt.*% Co on MSC-30, **g** - CMK1, **h** - CMK3. 2 theta diffraction angles shown for cobalt FCC crystal structure and cobalt oxide [135].

The catalyst supports presented here possess a great range of pore size, surface area and degree of graphitic alignment. Similarly the cobalt catalysts that have been prepared with them show a great range in activity. The microporous supports and CMK-1 which exhibits some microporosity produced the most active catalysts. The mesoporous carbon and the CNTs (also mesoporous) were less active despite these possessing the greater degree of graphitisation of all of the supports tested. In

previous chapters, the activity of ruthenium, which increased greatly with the degree of graphitisation, also showed a fall in activation energy with that graphitisation. In the case of cobalt, the activation energy does not vary significantly, despite large variations in the degree of surface graphitic structure.

This tendency of cobalt to be more active upon a microporous support rather than a support with a greater degree of graphitic structure clearly distinguishes it from ruthenium which has activities in the reverse order. The temperature programmed reduction results show that cobalt reduced within a narrow range of 720 - 750 $K$ for each of the four supports that showed some microporosity and CNTs. This peak could therefore be characteristic of the reduction of cobalt confined within carbon micropores. The presence of cobalt within micropores was also supported by TEM-EDS (energy dispersive x-ray spectroscopy) results that showed strong cobalt traces across a wide area of microporous carbon (MSC-30) in which no cobalt particles were visible implying that they might be present within the pores.

The notable outlier to this trend is the activated charcoal which possesses some microporosity but no activity. There could be a number explanations for the lack of activity in this case as it is not just pore structure that defines activity. For example, the presence of many contaminants such as sulphur or residual metals from the wood origin could be detrimental to activity.

The finding that cobalt appears to be more suited to microporous supports than mesoporous ones has a number of implications. Any metals present in the micropores would have a much smaller particle size than for a mesoporous supported catalyst and this suggests that cobalt is more active at smaller particle sizes compared to ruthenium. Results from Raman spectroscopy suggest that cobalt does not require such a high degree of graphitic alignment as for ruthenium. This suggests either that electrical interactions with the support are less important for cobalt compared to ruthenium or that the absence of a graphitic surface presents many more anchoring points for cobalt nanoparticles, this would increase dispersion and reduce cobalt particle size. Both findings suggest that reduction in cobalt particle size is more important than the electrical interactions with the support.

## 5.3 Sustainable Bimetallic Catalysts for Ammonia Decomposition

There is potential to enhance the activity of supported nanoparticle catalysts by combining two active metals to create an active surface with activity greater than

the two constituent components. Jacobsen *et al.* proposed that their cobalt-molybdenum nitride catalyst for ammonia synthesis presented active sites with both high and low nitrogen interaction energy, this allowed for optimum conditions for different reaction steps to occur [43]. An alternative approach utilises the second metal to act as a "pseudo-ligand" that alters the absorption properties of gaseous species upon the surface metal by shifting the d-band relative to the fermi level [136].

This chapter explores the potential of active metal combinations to act as successful bi-metallic catalysts for the ammonia decomposition reaction. The design of a bi-metallic catalyst presents an additional challenge to that of mono-metallic catalysts because the addition of a second metal increases the number of possible permutations many times over. To make this complexity manageable, a number of design criteria have been formulated. Building upon the work presented earlier in this chapter, each catalyst features cobalt and the selection of support and promoter is kept constant for each study. The selection of the second metal is to be based upon two principles: either it acts as a an alternative catalytic surface with a different interaction energy with nitrogen to facilitate recombinative desorption or it acts as a pseudo-ligand that is located away from the nanoparticle surface and modifies the active surface either structurally or electronically.

All catalysts were synthesised by simultaneous or sequential incipient wetness impregnation. Precursors impregnated in aqueous solution were $Ru(NO)(NO_3)_3$, $CsOH.xH_2O$ (where x is 0.17) and $(NH_4)_2MoO_4$ as they were insoluble in acetone. Precursors impregnated with acetone as solvent were $CoNO_3.6H_2O$ , $CuNO_3$, and $AgNO_3$.

In an attempt to optimise the interaction energy between the active surface and nitrogen adatoms, cobalt-ruthenium catalysts were synthesised by sequential impregnation onto CNTs with 20 $wt.\%$ cesium. Cobalt was impregnated first with acetone as solvent and reduced at 673 $K$ under flowing hydrogen followed by simultaneous impregnation of ruthenium and cesium with water as solvent and reduction at 510 $K$ under flowing hydrogen. The results are shown in Figure 5.11, presented in Arrhenius form in which the rate of reaction is presented as moles of ammonia converted per mole of ruthenium (the catalyst with only cobalt is presented as rate per mole of cobalt and is included as a reference) and conversion plotted as a function of cobalt to ruthenium mole fraction. It can be observed that the addition of ruthenium to cobalt greatly enhances the activity and also that the addition of cobalt to ruthenium diminishes the activity. Thus, it can be claimed that the combination of the two metals has produced a bi-metallic catalyst as the presence of one metal clearly influences the activity of the other. This shows that an active

metal-alloy catalyst can be synthesised by a consecutive wetness impregnation and reduction technique; from here the objective is to find a combination of metals to alloy where the overall activity is greater than either of the constituent metals.

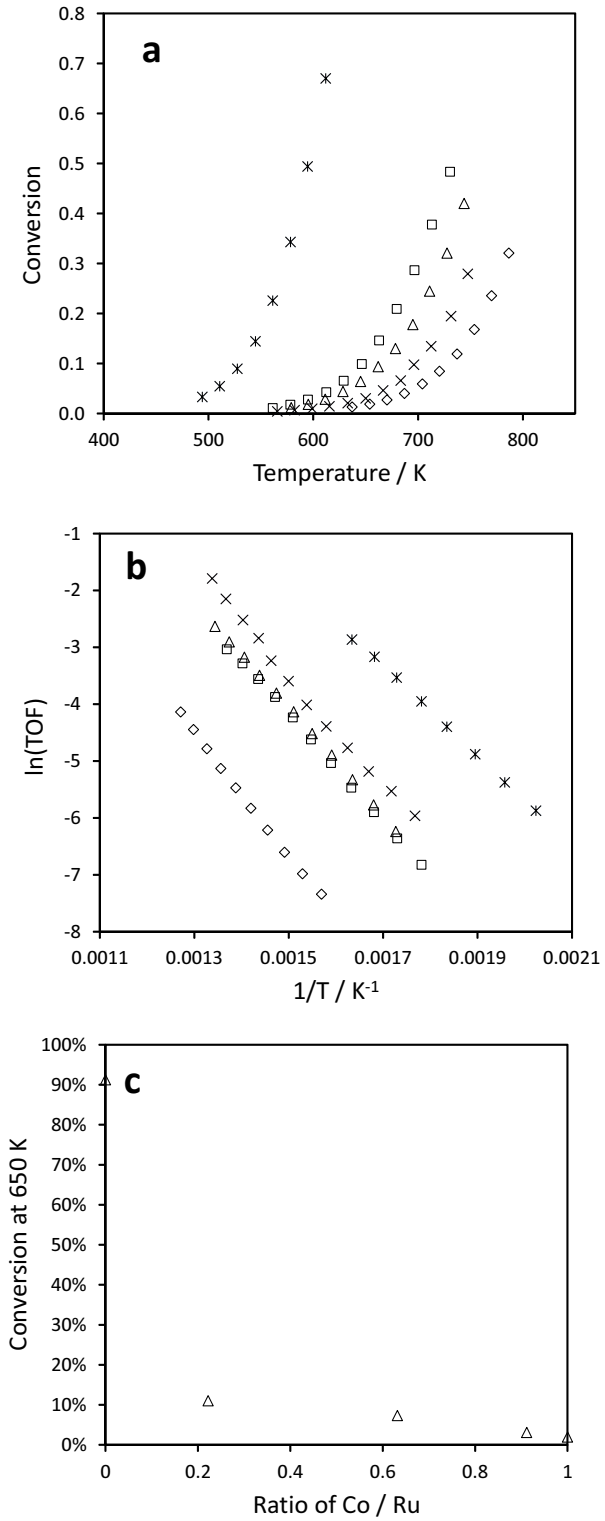


**Figure 5.11:** Conversion vs Temperature and Arrhenius drawing showing the activity per mole of ruthenium of bimetallic catalysts of ruthenium and cobalt with 20 $wt.\%$ cesium on CNTs. **a** - Conversion of ammonia vs temperature, **b** - Arrhenius plot and **c** - Conversion at 650 $K$ as a function of the molar ratio of Co to Ru + Co. $\diamond$ - 7.0 $wt.\%$ Co (activity is per mole of Co), $\times$ - 1.0 $wt.\%$ Ru and 6.0 $wt.\%$ Co, $\triangle$ - 3.5 $wt.\%$ Ru and 3.5 $wt.\%$ Co, $\square$ - 6.0 $wt.\%$ Ru and 1.0 $wt.\%$ Co, $*$ - 7.0 $wt.\%$ Ru. Reaction conditions were 5,200 $mL_{NH_3}\, h^{-1}\, g_{cat}^{-1}$ WHSV and 25.0 $mg$ of catalyst. TOF has units of $mol_{NH_3}\, mol_{Ru}^{-1}\, s^{-1}$ and was evaluated at exit conversion.

The next approach to the development of bi-metallic nanoparticle catalysts was to examine the hypothesis of the second metal acting as a pseudo-ligand. The choice of the second metal should be one therefore that either electronically enhances the activity of the first metal, in this case by changing the d-band level of the surface metal [136], or alters the structure of the surface metal. The less active metal should not be present on the nanoparticle surface during the reaction and so the catalyst must be designed with a core-shell structure.

Metals that might act as electron donors would be those with relatively high Fermi level relative to the more active metal. The nanoparticle catalyst can be engineered with one metal in the core and the other in the shell either by sequential impregnation of the metals or, in-line with the work of Ma *et al.* [49], by selecting the two metals so that the more active one would tend to migrate to the surface (see Table 2.4). According to this work, a metal will tend to migrate to the surface if it has a smaller surface segregation energy, a larger atomic radius, a less dense packing structure or a stronger energy of interaction with the surrounding atmosphere. Based on these criteria, the first (active) metal for this study was selected as cobalt based on work presented earlier in this chapter. The second metals selected are copper, which combines small atomic radius with a higher fermi level than cobalt and weak interaction with ammonia. With these properties, copper might be expected to migrate to the core of a core-shell nanoparticle under reaction conditions. Silver was also selected as it is in the same periodic group as copper and it had been shown in literature to enhance the activity of ammonia synthesis catalysts [137]. The support used for these experiments was Ax21 as it had shown excellent activity for single metal cobalt catalysts earlier in this chapter.

The results of activity tests for these bi-metallic catalysts are presented in Figure 5.12. The addition of 3.5 *wt.*% silver and copper to 3.5 *wt.*% cobalt produce no change in activity compared to just 3.5 *wt.*% cobalt on its own, all three of which are less active per mole of cobalt than the catalyst with 7.0 *wt.*% cobalt. The gradient of the Arrhenius curves is not altered by cobalt loading or by the addition of a second metal. From these results, it is not clear whether a genuine bi-metallic catalyst has been made as separately supported nanoparticles might achieve similar results.

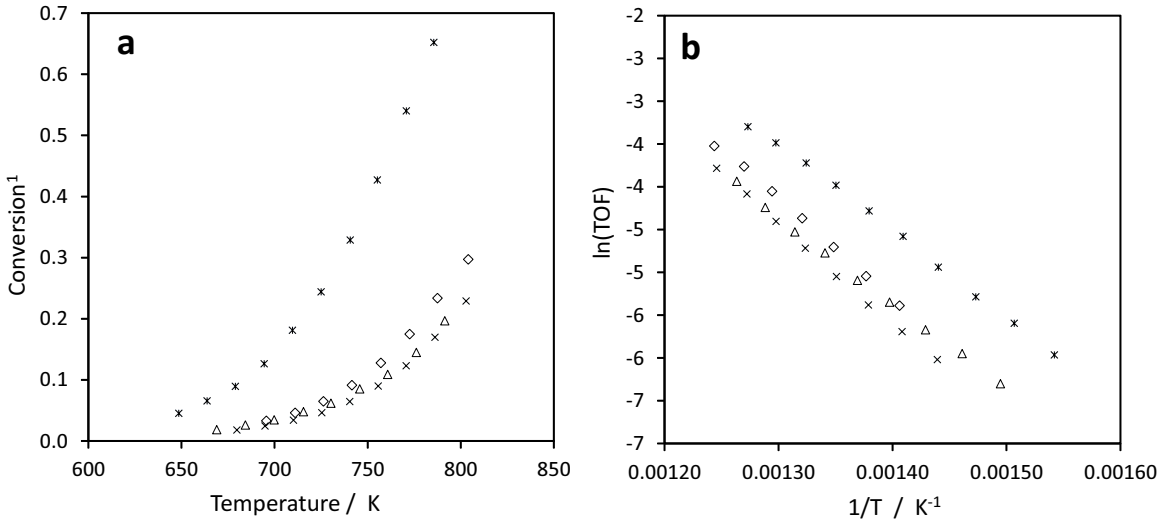


**Figure 5.12:** Conversion vs Temperature and Arrhenius drawing showing the activity of bimetallic catalysts of cobalt on Ax21. **a** - Conversion of ammonia vs temperature and **b** - Arrhenius plot with activity per mole of cobalt. ◇ - 3.5 $wt.\%$ Co and 3.5 $wt.\%$ Ag, △ - 3.5 $wt.\%$ Co and 3.5 $wt.\%$ Cu, × - 3.5 $wt.\%$ Co, ∗ - 7.0 $wt.\%$ Co. Reaction conditions were 5,200 $mL_{NH_3}\, h^{-1}\, g_{cat}^{-1}$ WHSV and 25.0 $mg$ of catalyst. TOF has units of $mol_{NH_3}\, mol_{Ru}^{-1}\, s^{-1}$ and was evaluated at exit conversion.

A similar study using nickel as the active metal in a bi-metallic catalyst was undertaken by Masters undergraduate students under the direct supervision of this author and their results are presented here. The active metal precursor was $NiNO_3$, and the secondary metals were copper and silver as before, plus molybdenum. The less active metal was impregnated and reduced first prior to addition of cobalt to promote a core-shell structure. The support used was MSC-30 microporous carbon. The results are presented in Figure 5.13. The exact loading of molybdenum is not known as some of the ammonium molybdate solution had precipitated as molybdenum oxide prior to impregnation, molybdenum loading on the catalyst is appropriately expressed as a range. Whereas copper and cobalt both diminish the activity of the catalyst compared to just nickel, the addition of molybdenum enhances the activity.

The enhanced activity of the cobalt - molybdenum catalyst compared to the cobalt only catalyst is significant as it presents the opportunity to enhance the activity of cobalt catalysts further for ammonia decomposition.

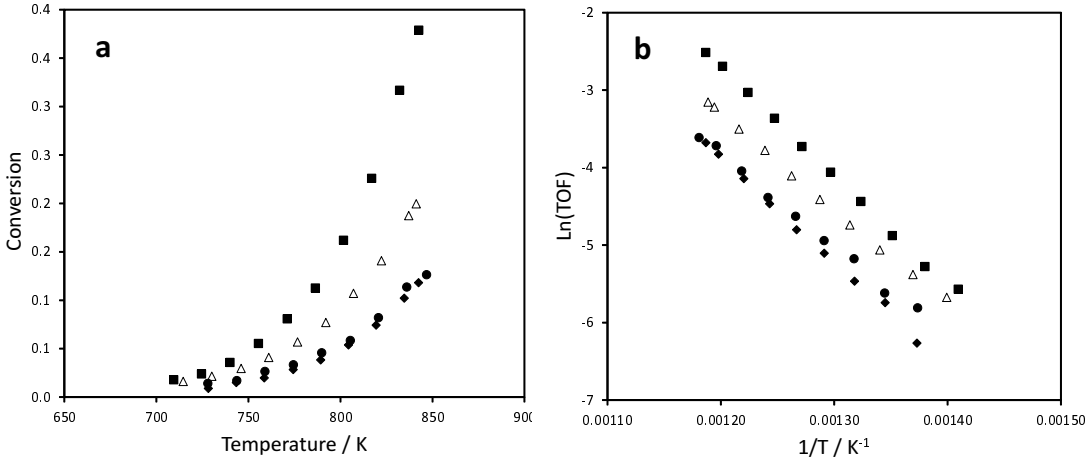


**Figure 5.13:** Conversion vs Temperature and Arrhenius drawing showing the activity of bimetallic catalysts of cobalt on Ax21. **a** - Conversion of ammonia vs temperature and **b** - Arrhenius plot with activity per mole of nickel. △ - 2.0 $wt.\%$ Ni, ◆ - 2.0 $wt.\%$ Ni and 2.0 $wt.\%$ Cu, ● - 2.0 $wt.\%$ Ni and 2.0 $wt.\%$ Ag and ■ 2.0 $wt.\%$ Ni and $<$ 2.0 $wt.\%$ Mo. The data presented here is the work of Masters students working under the direct supervision of this author. Reaction conditions were 5,200 $mL_{NH_3}\, h^{-1}\, g_{cat}^{-1}$ WHSV and 25.0 $mg$ of catalyst. TOF has units of $mol_{NH_3}\, mol_{Ru}^{-1}\, s^{-1}$ and was evaluated at exit conversion.

## 5.4 Conclusions

It was found that changing support from mesoporous CNTs to microporous AX21 decreased the activity of the ruthenium catalyst for ammonia decomposition and increased the activity of the cobalt catalyst. On Ax21, the activity of cobalt approached that of ruthenium, especially at low temperature. On the assumption that the cobalt is dispersed within the pore structure, this might suggest that activity of cobalt for ammonia decomposition favours a smaller particle size. Unlike the finding for the graphitisation of CNTs earlier in this thesis and the findings of Li *et al.* for ruthenium on porous carbons [131], there was no correlation in activity for ammonia decomposition and surface graphitic nature as inferred from the Raman spectra.

In contrast to ruthenium, cobalt catalysts were more active when the support had high surface area and a microporous structure. It can be concluded that the cobalt particles confined within the micropores were more active. All of the catalysts that showed activity had ruthenium reduction occurring between 720 - 754 $K$, this suggests similarities in the metal - support interaction in all of the active catalysts.

A number of bimetallic nanoparticle catalysts were synthesised on MSC-30, CNT and Ax21 supports. The addition of molybdenum was shown to increase the activity of nickel catalysts supported on MSC-30. Cobalt was shown to reduce the activity of ruthenium catalysts on CNTs and the activity of the Ru-Co catalyst was the

same per mole of ruthenium in all formulations. On Ax21, Co-Cu was more active than Co-Ag. These findings are preliminary explorations into the potential of bi-metallic catalysts have for ammonia decomposition on carbon supports. They show significant potential and are worthy of further investigation. The results for nickel catalysts on Ax21 showed a similar relationship with copper and silver however the combination with molybdenum was more active than cobalt on its own. This is an interesting finding and further studies should be undertaken to explore this result more thoroughly.

The results presented here suggest that there is potential to replace ruthenium with more sustainable metals by utilising microporous supports and bi-metallic effects. Much more development is required however these findings suggest that the concerns around the sustainability of an ammonia PEM fuel cell can be addressed. In the next chapter, the other questions around sustainability of an ammonia PEM fuel cell will be explored in more depth.

# Chapter 6

# The Sustainable Case for Ammonia as a Chemical Storage Vector for Hydrogen

## 6.1 Motivation

Ammonia manufacture is among the most energy intensive industrial processes and is responsible for 0.93 % of global carbon dioxide emissions [138]. This would suggest that using ammonia as a sustainable hydrogen storage vector would involve substantial energy losses and would not be a suitable storage vector for sustainable hydrogen. However, it has often been proposed as a sustainable hydrogen storage medium [12]. If ammonia is to be used in this way, then it is important to evaluate the energy efficiency associated with the processes of storing and then releasing hydrogen from ammonia is energetically efficient.

In this case study, three aspects relating to the use of ammonia for storage of energy are investigated. The energy losses incurred by using ammonia to store hydrogen are estimated and compared to key benchmarks set by the US Department of Energy (DoE). The study also considers the energy loss implications of storing ammonia as $Mg(NH_3)_6Cl_2$ which has been proposed as a safer storage alternative to liquid ammonia as a way of reducing its toxicity [11]. To better understand the impact of ammonia as a hydrogen storage medium upon anthropogenic climate change, the incremental carbon footprint for storage and release of hydrogen from ammonia has been calculated and compared to benchmark publications from the UK Department for Transport (DfT).

There has been much progress in literature on catalyst-reactor systems for ammonia decomposition to provide hydrogen for PEM fuel cell applications [139]. These

have generally been lab scale applications, often operating at high temperature and are not yet ready for low temperature applications. This study builds upon this work to make a design and sensitivity analysis of a low temperature ammonia decomposition membrane reactor; key focuses are the quantity of precious metals required, emissions management and operating temperature and energy efficiency.

## 6.2 Definitions

Before embarking upon this study into the sustainable justification of an integrated ammonia-PEM fuel cell, it is essential to attempt to define sustainability in this context. The term sustainability is defined by the Brundtland commission as "development that meets the needs of the present without compromising the ability of future generations to meet their own needs" [140]. In practice, sustainability is very difficult to quantify because is possesses many different aspects. Among many other aspects, sustainable technologies must reduce the demand placed upon finite resources such as fossil fuels, land and water, they should make efficient use of energy and they shouldn't diminish the biosphere by pollution. As this application is intended to provide energy for mobile transport applications, the sustainability assessment will focus on energy related sustainability factors such as reduction in fossil fuel consumption, minimisation of carbon footprint and the minimisation of energy losses.

The following terminology are used throughout this study to attempt to clarify the sustainable qualities of hydrogen storage as ammonia.

- Renewable Electricity is defined as electrical energy from renewable energy sources such as wind, solar and so forth.
- Renewable hydrogen is defined as hydrogen that has not incurred the consumption of fossil fuels or the emission of significant carbon emissions in its manufacture. A good example is hydrogen synthesised by electrolysis using renewable electricity.
- The conventional Haber-Bosch process is defined as the production of ammonia in the conventional manner from fossil fuels such as methane or coal.
- The sustainable Haber-Bosch process is defined as the production of ammonia from renewable hydrogen.
- Total energy requirement for a process is defined as the total energy of all material and energy inputs to the process.

- Energy loss is defined as the energy required for a process that is in addition to the minimum thermodynamic energy requirement for the conversion of material inputs to outputs.

## 6.3 Introduction

The case for ammonia as a sustainable road transport fuel has been proposed by a number of researchers, based on a series of sustainable justifications. Most publications on the production of hydrogen by ammonia decomposition follow the example of Yin *et al.* and justify the research based on the high hydrogen storage capacity of ammonia [42]. Some studies have attempted to quantify the sustainability question with regards to energy use, flammability and toxicity [11, 12, 10]. Most of these energy assessments quote energy losses for the conventional methane fed Haber-Bosch process, rather than a renewable hydrogen fed process and without considering the system energy losses. This case study attempts to goes a step further to quantify the energy efficiencies for the full hydrogen-ammonia-hydrogen system.

Data for the energy losses for the conventional Haber-Bosch process for ammonia production have been widely published. In 2007, the US DoE claimed that the modern process with methane feedstock typically requires a total energy input of 28.5 $GJ\ t_{NH_3}^{-1}$ and that 60 - 65 % of the energy input (including the lower heating value of methane) is stored within the ammonia product [9]. In 2012, Schuth *et al.* stated the figures as 27 $GJ\ t_{NH_3}^{-1}$ and 75 % efficiency [12] which suggests that there have been some further improvements in the process. These figures are for energy consumption, the greater part of which is chemically stored in the product ammonia.

It is not unreasonable to make a sustainable justification for hydrogen storage in ammonia synthesised from methane despite the fact that it is a fossil fuel. Methane has the lowest carbon footprint of all fossil fuels and the conversion to ammonia uses very well understood technology. The Haber-Bosch process is among the very oldest of all industrial technologies and has undergone many generations of efficiency improvements. Figure 6.1 shows how the energy losses associated with the ammonia synthesis have been reduced since the 1950s, taken from the IPCC Climate Change 2007 report [141]. The global consumption of hydrogen is dominated by the manufacture of ammonia and this hydrogen is overwhelmingly sourced from fossil fuels as shown in Figure 6.2. Despite the improvements to energy efficiency, the energy consumption by the modern Haber-Bosch process from methane remain significant and potentially undermine the feasibility of using ammonia for hydrogen storage if that ammonia is synthesised from methane.

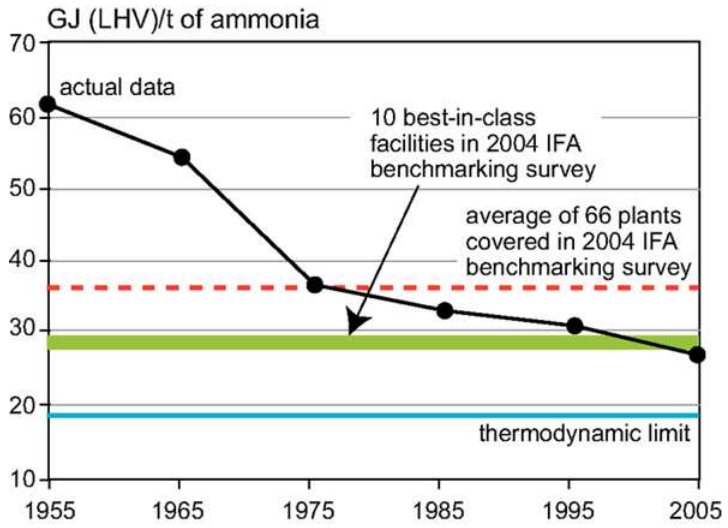


**Figure 6.1:** Efficiency Improvements in the Haber Bosch Process [141]. *IFA is the International Fertilizer Industry Association, LHV is the lower heating value which is the heat of combustion of the fuel not include the heat of condensation of the combustion products.*

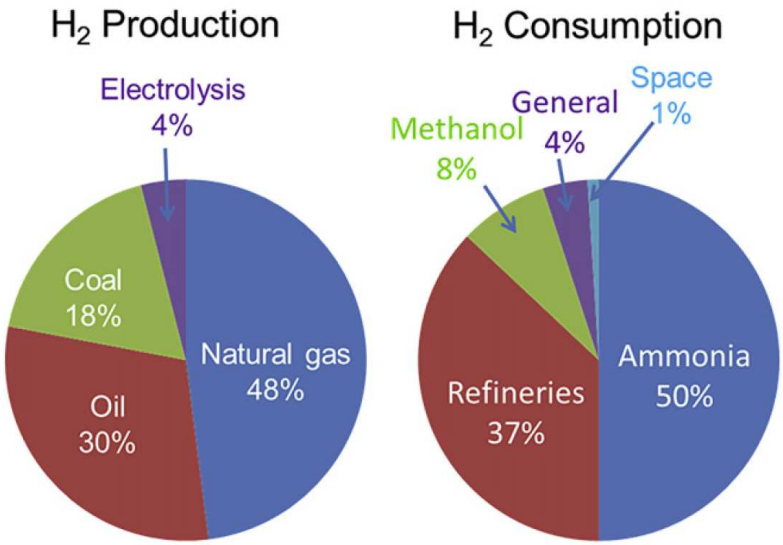


**Figure 6.2:** Global production and consumption of hydrogen [10, 142].

This high consumption of fossil fuels and generation of carbon dioxide potentially undermines the use of ammonia as a sustainable hydrogen storage medium. To overcome this, it is necessary to move away from the conventional fossil fuel driven Haber-Bosch process and to consider a sustainable Haber-Bosch process instead. One of the key aspects that affects the Haber-Bosch process sustainability is the source of hydrogen. In the conventional process, hydrogen is produced by steam methane reforming or coal gasification depending upon local availability of these

fuels. A typical Haber-Bosch process converts the methane to hydrogen by steam methane reforming and water-gas shift reactions which account for the bulk of energy losses from the process [1].

For ammonia synthesis to be sustainable, the requisite hydrogen must be obtained from a renewable source. This sustainable ammonia plant would be smaller and less complex than current plants: the three main steps are the production of hydrogen by electrolysis, the production of nitrogen by air separation and the conversion to ammonia using a conventional high pressure synthesis loop. This approach would only be sustainable if the hydrogen production by electrolysis uses renewable electricity which in turn is produced from a renewable source such as wind or solar.

The high energy cost of ammonia synthesis has led researchers to investigate alternative approaches to the Haber-Bosch process with the goal of reducing carbon dioxide emissions. Lan *et al.* have produced ammonia directly from either $H_2$ or $H_2O$ and $N_2$ or air reacted via a proton exchange membrane fuel cell operating at ambient temperature and pressure [143]. Although it is a promising approach, the proposal needs much more development before commercialisation could be realised as the conversion of electrical energy to ammonia formation was around 2 % (with the balance forming hydrogen) and improving this ratio is the main challenge. Lichte *et al.* have shown how ammonia can be synthesised directly from $N_2$ and steam using electrolysis in molten hydroxide with $Fe_2O_3$ catalyst [144]. 35 % conversion of electrical energy to ammonia formation was achieved operating at 473 $K$ and 25 $bar$. Both of these technologies allow for the direct conversion of electrical energy to ammonia which breaks the link between fossil fuels and ammonia, further improvements must be made to the efficiency and capacity of these technologies before they could be considered for applications for sustainable ammonia production.

The final stage of the hydrogen-ammonia-hydrogen system is the decomposition of ammonia to hydrogen at the point of use. A number of researchers have investigated membrane reactor systems for decomposition of ammonia to hydrogen for PEM fuel cell applications. A selection of these are presented in Figure 2.5, the best selectivity for ammonia is achieved with palladium membranes due to the nature of the solution diffusion mechanism. The examples in literature only consider membrane reactor temperatures above 523 $K$ and more must be done to understand the performance of these membranes at PEM fuel cell temperatures of around 370 $K$. This objective will be challenging to meet, both the permeability of hydrogen in palladium and the catalytic hydrogen dissociation and re-combination reactions all slow down as temperature decreases (see Figures 2.20 and 2.21 and Table 2.5).

## 6.4 Feasibility Assessment of an On-Board Ammonia-PEM Fuel Cell

### 6.4.1 Objectives & Design Criteria

An ammonia-PEM fuel cell providing high purity hydrogen at the point of use for an automotive application must satisfy the following criteria:

- The hydrogen produced must be of sufficient quality for the fuel cell or the ammonia impurity will poison the Nafion™ membrane. The US DoE have set a target for hydrogen purity for PEM fuel cells of at least 99.99 % [105].
- All effluent streams must have an ammonia concentration low enough for direct discharge to atmosphere. The smell of ammonia is detectable at very low concentrations and although the maximum personal exposure limit is 25 *ppm* [145], the acceptable limit would be very much smaller than this in practice given the distinctive aroma of ammonia.
- Particular care should be paid to ensure that likely failure modes do not create a hazardous environment or event.
- The ammonia decomposition reaction should occur at a temperature in-line with the operating temperature of a PEM fuel cell of up to around 370 $K$ [9].

The following criteria that are specific to this study have been applied to enable sizing of the design aspects:

- The system should be sized to provide power to a Nissan Leaf™, a 100 % electric small family car which has an 80 $kW$ electric motor [146]. This does not include the energy for peripheral equipment such as lights but it remains a sensible initial target for the system. Assuming that the PEM fuel cell is operating at 50 % efficiency, the ammonia decomposition system must produce 0.56 $mol\,s^{-1}$ of high purity hydrogen.
- The ammonia decomposition membrane reactor should be designed to achieve $>$ 99 % conversion of ammonia.

Figure 6.3 is a schematic showing a potential design including the most important functional aspects and significant heat inputs. Pressurised ammonia stored at around 10 *bar* and ambient temperature can be easily vaporised using a pressure regulating valve to produce pure gaseous ammonia; the heat of vaporisation is required

at ambient temperature and thus it can be drawn from surroundings. Ammonia is decomposed to hydrogen in a catalytic membrane reactor, the reaction is endothermic and requires heat input of 2.7 $GJ\ t_{NH_3}^{-1}$. There is also sensible heat input to raise the temperature of the feed ammonia to the reaction temperature, a portion of this can be recovered by system heat integration. The membrane has a thin layer of palladium or palladium-silver alloy which can produce pure hydrogen permeate to react in a PEM fuel cell operating at around 370 $K$. The retentate stream consists of nitrogen with some unreacted ammonia and hydrogen, this is passed through an ammonia removal system before being routed to atmosphere at a safe location. A sweep gas has not been shown although one would probably be necessary to improve trans-membrane flux, its use is problematic because it would reduce the partial pressure of hydrogen at the PEM fuel cell. A great deal of refinement is required to this system, in particular the design of the membrane reactor which must achieve high overall conversion of ammonia, but it serves to illustrate the major functional requirements and the significant energy inputs that are required.

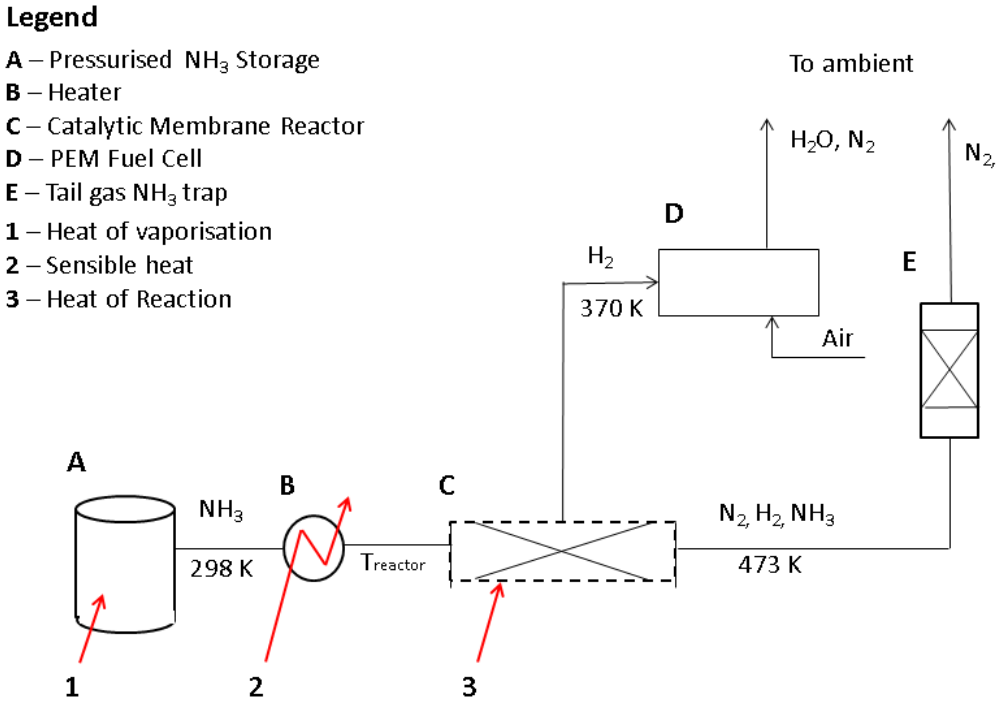


**Figure 6.3:** Schematic of the proposed on-board hydrogen production application. Heat integration is not shown. Two heat exchangers would need to be employed to recover heat from the two membrane reactor discharge streams, in particular to reduce temperature to 370 $K$ for the fuel cell, and use it to raise the temperature of the ammonia feed stream.

The choice of operating pressure and temperature for the membrane reactor is of critical importance. High pressure lessens the extent of equilibrium conversion but

increases the trans-membrane flux which enhances the overall conversion. Higher temperature has a generally positive effect as it speeds the reaction kinetics, increases the degree of equilibrium conversion and increases the membrane permeability (in the case of palladium) which further improves overall conversion. Higher temperature requires a heat exchanger to cool the hydrogen before the PEM fuel cell and incurs the waste of energy through impererfect heat transfer. Thus the choice of operating pressure and temperature is a compromise and depends upon the performance of both catalyst and membrane.

### 6.4.2 Modelling Methodology

#### Membrane

The membrane reactor is designed as a simple plug-flow model incorporating the rate of decomposition of ammonia limited by either reaction kinetics or thermodynamic equilibrium and the rate of hydrogen permeation through the membrane. A differential model was used in which the cylindrical membrane was separated into 300 radial slices each containing a proportional mass of catalyst and membrane surface area. For each slice, equations were solved for the extent of ammonia decomposition reaction (governed either by reactions kinetics or thermodynamic equilibrium) and the rate of hydrogen permeation through the membrane to give the exit gas composition for that slice. By dividing the reactor into 300 slices, this method approaches a differential model.

The membrane was selected to be a 4 $\mu m$ palladium membrane on porous ceramic tubes developed by Zhang *et al.* [108], this membrane possesses the advantages of high permeability and minimises the use of palladium. Permeation of hydrogen through the membrane proceeds by solution diffusion, the key steps are the dissociation of hydrogen on the membrane surface, transport through the palladium and recombination (see Figure 2.20). Transport is governed by the following equation adapted from Zhang *et al.* [108]:

$$J_{H_2} = \frac{D_0}{l} e^{-E_a/RT} \Delta P_{H_2}^n \tag{6.1}$$

$J_{H_2}$ is the rate of hydrogen flux in $m^3\, m^{-2}\, h^{-1}\, bar^{-n}$, $D_0$ is the hydrogen permeability coefficient, $l$ is the membrane thickness, $E_a$ is the activation energy, $R$ is the universal gas constant, $T$ is the operating temperature, $\Delta P_{H_2}$ is the transmembrane partial pressure difference of hydrogen and $n$ defines the relationship with hydrogen pressure and was shown to be equal to one. The membrane hydrogen permeability coefficients for the temperatures used in this study were extrapolated from the

published data (see Figure 6.4). Extrapolation of data in this way is not ideal and could introduce significant error into the analysis. To address this error, permeability data was compared to published data by Garcia-Garcia *et al.* who had made a lower temperature study of a 40 $\mu m$ palladium membrane (see Figure 6.4) [109]. The permeability of the 4 $\mu m$ membrane was found to be approximately 2 to 4 times that of the 40 $\mu m$ membrane over the 450 to 550 $K$ temperature range of this study.

The membrane used for this study was pure palladium as it achieved high flux with small thickness. In practice a palladium-silver membrane might be selected to take advantage of the reduced susceptibility of membrane cracking. The use of the membrane from Zhang *et al.* [108] is sufficient for the purposes of a feasibility study as the difference from using a palladium-silver membrane would not have a significant bearing upon the results.

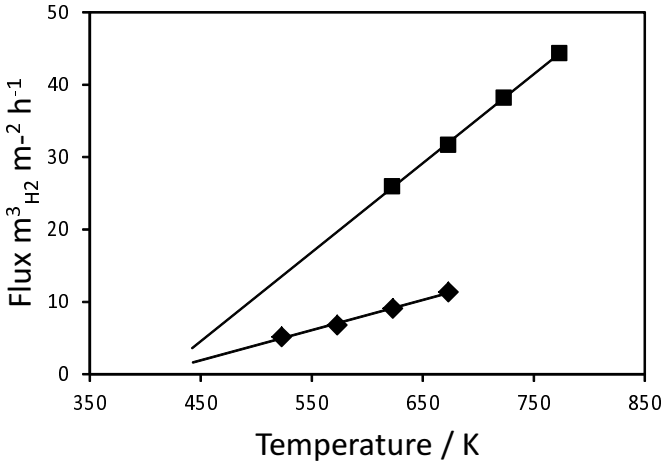


**Figure 6.4:** Comparison of the rate of hydrogen flux through palladium membranes as a function of temperature. ◆ - data from Garcia-Garcia *et al.* [109], ■ - data from Zhang *et al.* [108]. The lines show the extrapolation toward lower temperatures.

### Rate of Reaction and Equilibrium

Data for the rate of reaction was taken for catalyst 7 $wt.\%$ ruthenium on graphitised carbon nanotubes with 4 $wt.\%$ cesium promoter based upon the progress achieved in this thesis as it has the best activity of those studied for ammonia decomposition (the apparent rate of reaction evaluated at exit conversion is given in equations 6.2, 6.3 and 6.4 for temperatures of 550, 500 and 450 $K$).

$$-r_{550K} = 0.0229\ mol_{NH_3}\, g_{cat}^{-1}\, s^{-1} \tag{6.2}$$

$$-r_{500K} = 0.0060\ mol_{NH_3}\ g_{cat}^{-1}\ s^{-1} \tag{6.3}$$

$$-r_{450K} = 0.0022\ mol_{NH_3}\ g_{cat}^{-1}\ s^{-1} \tag{6.4}$$

Equations 6.2, 6.3 and 6.4 can be applied to describe the initial rate of reaction, they do not necessarily apply at different reaction conversions when the ammonia partial pressure is lower and the hydrogen and nitrogen partial pressures are elevated. To account for this effect, a Langmuir-Hinshelwood approach was used to describe how the rate of reaction on a solid catalysis surface relates to the partial pressures of gaseous feed and product components as has been widely used in literature for this reaction [147, 22, 55]. The ammonia decomposition reaction was described earlier as a six step reversible mechanism (see equations 2.2 to 2.13) and the full Langmuir-Hinshelwood representation of these steps would be unwieldy. This larger equation is simplified by defining one reaction step as rate limiting, in this case the recombination of surface nitrogen adatoms (equation 2.10), and the most abundant reaction intermediate (MARI) on the catalyst surface which is nitrogen adatoms for low temperature ammonia decomposition on ruthenium [29]. The six step reaction mechanism can now be abbreviated to the two step approach shown in equations 6.5 and 6.6 taken from Bradford *et al.* [22]. The first step is equilibrium limited and governed by the equilibrium constant $K_1$ and the second step is slow and governed by kinetic constant $k_2$.

$$2\left[NH_3 + * \overset{K_1}{\rightleftharpoons} \frac{3}{2}H_2 + N*\right] \tag{6.5}$$

$$2N* \overset{k_2}{\rightarrow} N_2 + 2* \tag{6.6}$$

This simplification reduces the Langmuir-Hinshelwood rate of reaction expression to that shown in equation 6.7 below. It gives the rate as a function of partial pressure of ammonia and hydrogen along with kinetic constant for slow recombination of nitrogen adatoms. Examination of this equation shows that at low hydrogen partial pressure (ie. at low conversion), the denominator becomes equal to $(K_1 P_{NH_3})^2$and the rate of reaction $(-r_{NH_3})$ is zero order with respect to ammonia and the initial rate of reaction is equal to $k_2$ under these conditions. Equations 6.2, 6.3 and 6.4 give the apparent rate of reaction at known temperatures and conversion of 24 %, 7 % and 2.5 % respectively. If it is assumed that $P_{H_2}^{3/2} << K_1 P_{NH_3}$ at this low conversion, these values for the rate of reaction are equal to $k_2$ for the specified temperatures.

The error inherent in using the results from an integral reactor to approximate the initial rate of reaction is discussed later in this section.

$$-r_{NH_3} = \frac{k_2 K_1^2 P_{NH_3}^2}{(P_{H_2}^{3/2} + K_1 P_{NH_3})^2} \tag{6.7}$$

While $k_2$ can be approximated for the ruthenium-cesium on graphitised carbon nanotube catalyst presented earlier in this thesis, the value of $K_1$ is not known. There are results presented in literaature for this equilibrium constant, for example, Armenise *et al.* found $K_1$ to be 2.37 $atm^{1/2}$ to fit the kinetic results between 773 to 973 $K$ [147]. It would not be appropriate to use the same value of $K_1$ here because the equilibrium coefficient would be a strong function of reaction temperature; the equations used by Armenise *et al.* suggest that $K_1$ would have a significantly smaller value between the 450 to 550 $K$ temperature range that is of interest to this study. The solution applied was to manually adjust the value of $K_1$ until the predicted conversion aligned with the thermodynamic equilibrium at that temperature. The extent of equilibrium of the ammonia decomposition reaction as a function of temperature was calculated using the ideal thermodynamic model in Aspen™(see Figure 2.4).

Nitrogen partial pressure has no significant impact upon the reverse rate of reaction and so it is not included in the equilibrium calculation. This was validated experimentally in which partial pressures of hydrogen and nitrogen were introduced in the reactor feed during the ammonia decomposition reaction. It was found that small quantities of hydrogen slow the rate of reaction significantly but that nitrogen had no measureable effect. This approach is also supported by the modelling study of Abashar *et al.* whose modelling equations show that the forward reaction is only retarded by high partial pressures of hydrogen and the reverse reaction will only proceed at extremely high nitrogen partial pressure [148].

To approximate a differential model, the membrane reactor was divided into 300 cells as shown in Figure 6.5. The model is solved for continuity of all species. For hydrogen, hydrogen molar flowrate at *i+1* is equated to the hydrogen molar flowrate at *i+1* less the transmembrane flux and plus the hydrogen generated by the ammonia decomposition reaction. The rate of membrane flux is calculated by solving equation 6.1. When the rate of reaction is kinetically limited, the rate of hydrogen generation is calculated using equation 6.7 with the value of $k_1$ taken from equations 6.2, 6.3 or 6.4 depending upon the temperature.

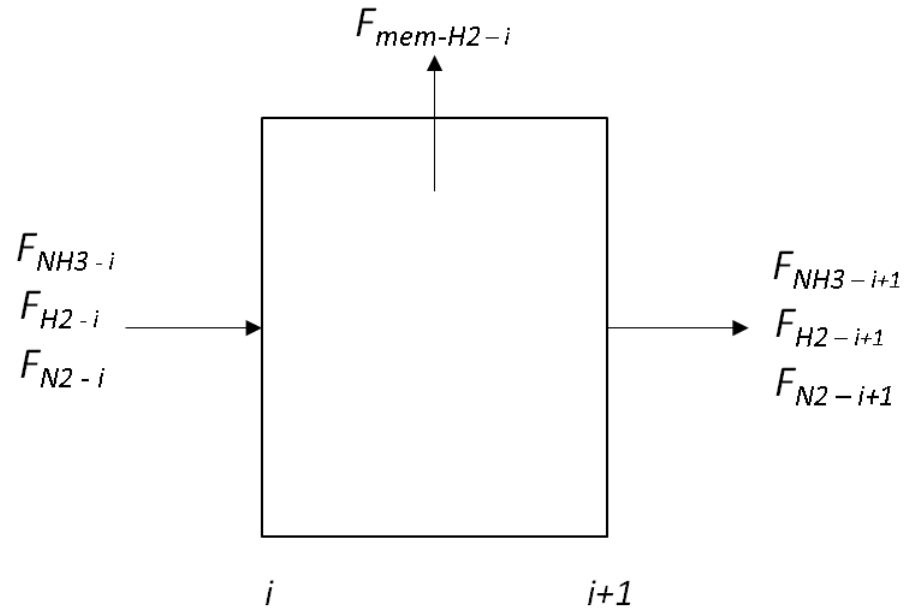


**Figure 6.5:** Membrane reactor model schematic.

The model solves in Microsoft Excel™and resolves each of the equations for the extent of reaction, trans-membrane flux and continuity (see equations 6.8, 6.9 and 6.10). $F_x$ is the molar flowrate of component x, $m_{cat}$ is the incremental mass of catalyst, $A_m$ is the membrane surface area for the reactor increment and $\Delta P_{H_2}$ is the transmembrane hydrogen partial pressure difference. Although there is error from using non-differential equations in this manner, the division of the reactor into 300 theoretical sections that are solved sequentially minimises this error and the model approaches a differential model. The values asigned to key variables are shown in Table 6.1.

$$F_{H_2\,i+1} = F_{H_2\,i} + \frac{3}{2}\,m_{cat}\left[\frac{k_2 K_1^2 P_{NH_3}^2}{\left(P_{H_2}^{3/2} + K_1 P_{NH_3}\right)^2}\right] - J_{H_2,i} A_{m\,i} \Delta P_{H_2\,i} \tag{6.8}$$

$$F_{N_2\,i+1} = F_{N_2\,i} + \frac{1}{2}\,m_{cat}\left[\frac{k_2 K_1^2 P_{NH_3}^2}{\left(P_{H_2}^{3/2} + K_1 P_{NH_3}\right)^2}\right] \tag{6.9}$$

$$F_{NH_3\,i+1} = F_{NH_3\,i} - m_{cat}\left[\frac{k_2 K_1^2 P_{NH_3}^2}{\left(P_{H_2}^{3/2} + K_1 P_{NH_3}\right)^2}\right] \tag{6.10}$$

**Table 6.1:** Values Assigned to Key Model Variables

| **Reactor temperature** $K$ | **Kinetic Constant, $k_2$.** [a] $mol\, g_{cat}^{-1}\, s^{-1}$ | **Equilibrium Constant, $K_1$.** [b] $bar^{0.5}$ | **Membrane Flux, $J_{H_2}$.** [c] $m^3\, m^{-2}\, h^{-1}\, bar^{-1}$ |
|---|---|---|---|
| 450 | 0.0022 | 0.022 | 5.4 |
| 500 | 0.0060 | 0.42 | 11.5 |
| 550 | 0.0229 | 0.80 | 17.7 |

[a] Data taken from this thesis for catalyst with 7.0 *wt.*% Ru, 4 *wt.*%Cs on graphitised CNTs.
[b] Tuned to agree with thermodynamic equilibrium.
[c] Data taken from Figure 6.4.

Of the many sources of error in this modelling approach. Potentially the most significant is the assumption that the rate of reaction in equations 6.2, 6.3 and 6.4 represent the initial rate of reaction that is important for the calculation of the kinetic term $k_2$. The error arises from the fact that the data is produced from an integral reactor that approximates a differential reactor, this assumption is only true at low conversions and may not be appropriate in this case. According to equation 6.7, for this assumption to be true, the value of $P_{H_2}^{3/2}$ in the denominator term $P_{H_2}^{3/2} + K_1\, P_{NH_3}$ must be very small compared to the rest of the term (generally true for low conversion). To assess the magnitude of this error, the values of $P_{H_2}^{3/2}$ and $K_1\, P_{NH_3}$ were calculated using the known conversion at which the rate of reaction was measured experimentally. The calculated error is shown in Table 6.2; althought the error is significant, it does not exceed 25 % in any of the cases and thus it does not undermine the results that are presented to give only an approximate sizing for the membrane reactor.

In general, this simple approach to modelling to the reactor ignores many of the complexities of the reacting system and it is designed to produce results to provide confidence of around +/- 50 %. While not a precise approach, the results are sufficient to answer key questions around the feasibility of the low temperature ammonia decomposition reactor and also to highlight the aspects in most need of further development.

**Table 6.2:** Assessment of the error in the kinetic data arising from the assumption that the kinetic experimental results represent the initial rate of reaction.

| **Reactor temperature** $K$ | **Conversion for measured kinetic data, X.** | $P_{H_2}^{3/2}$ $bar^{3/2}$ | $K_1 P_{NH_3}$ $bar^{3/2}$ | Error[a] |
|---|---|---|---|---|
| 450 | 0.025 | 0.007 | 0.0209 | 25 % |
| 500 | 0.07 | 0.031 | 0.365 | 8 % |
| 550 | 0.24 | 0.16 | 0.490 | 24 % |

[a] - Error calculated as the proportion of $P_{H_2}^{3/2}$ to the denominator term $P_{H_2}^{3/2} + K_1 P_{NH_3}$

### 6.4.3 Results of the Membrane Reactor Model

The model was solved in each case to give the minimum surface area of membrane with sufficient catalyst to achieve $>$ 99 % conversion and produce 0.56 $mol\,s^{-1}$ of hydrogen. The results are shown in Figure 6.6 and Table 6.3. In Figure 6.6, the reactor composition versus membrane area results are shown. Concentration of hydrogen in the reactor reaches a peak of around 50 - 60 % at 550 $K$, however at 450 $K$, the less favourable thermodynamic equilibrium means that hydrogen concentration doesn't reach 25 %. The reaction is initially kinetically limited before transitioning to equilibrium limited at which point the conversion of ammonia is effectively controlled by the rate of trans-membrane hydrogen flux. The equilibrium concentrations are a function of temperature: at 550 $K$, equilibrium conversion is 97 %, at 500 $K$ this changes to 91 % and at 450 $K$ this falls further to 77 %. Thus the performance of the membrane becomes more important at lower temperature compared to the performance of the catalyst as it is only by removal of hydrogen that the reaction can proceed.

The modelling results showing predicted membrane size and catalyst loading are presented in Table 6.3. As the operating temperature is reduced from 550 to 450 $K$, the required membrane surface area increases from 9.5 to 50.0 $m^2$ and the required mass of catalyst from 300 to 3,400 $g$. The demand for the precious metals of palladium and ruthenium increase from 457 $g$ and 19 $g$ to 2404 $g$ and 218 $g$ respectively. The requirement for such large quantities of precious metals for an automotive application is clearly not viable and this finding shows that membrane performance is the most important area for improvement.

There is some potential for improvements to membrane performance. Firstly, the membrane thickness can be reduced further below the current 4 $\mu m$ while still maintaining a continuous barrier. Secondly, metals that have body centred cubic (BCC) lattice structures such as vanadium have a greater permeability to hydrogen than

palladium. As a further benefit to low temperature application, the permeability of these BCC metals increases as temperature falls (see Figure 2.21). For these metals to be applied for this application, two problems must be addressed. They are known to suffer from cracking caused by hydrogen embrittlement and they would also require additional surface metals to catalyse the hydrogen dissociation and recombination steps (see Figure 2.20).

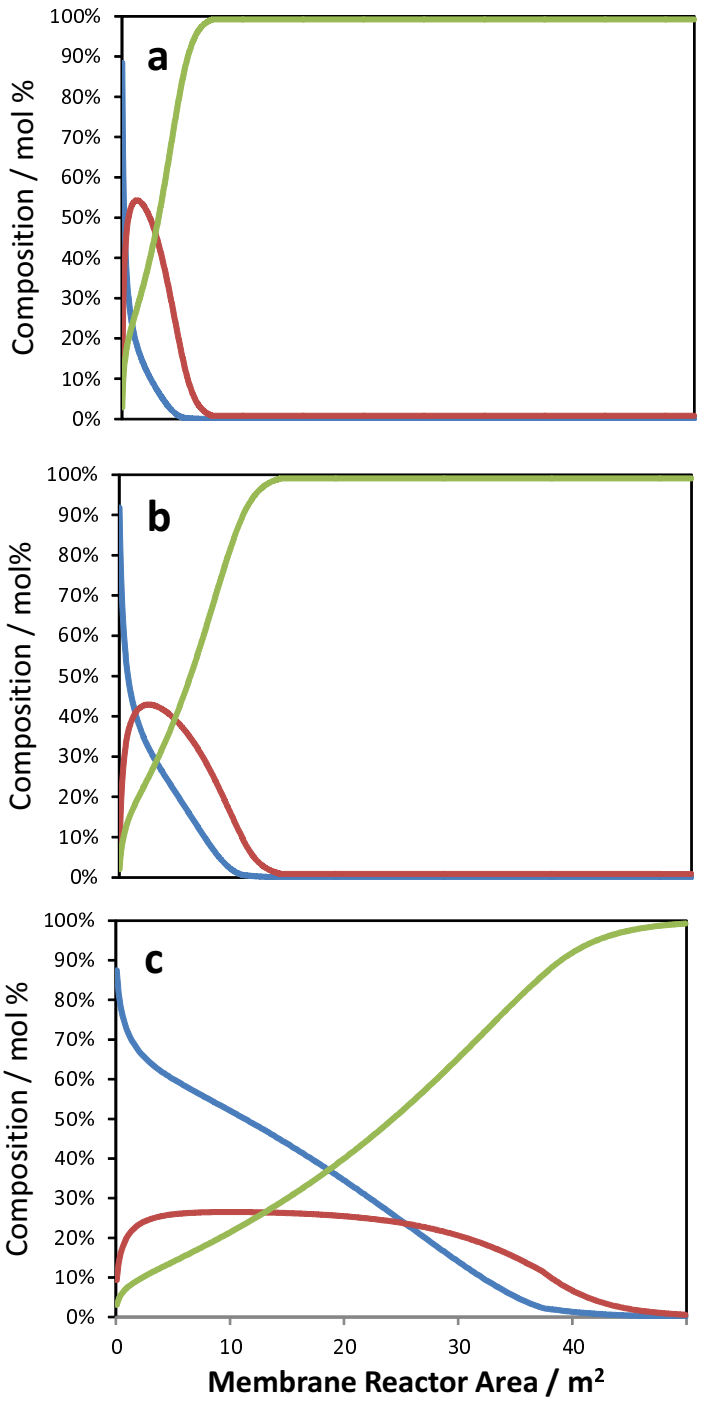


**Figure 6.6:** Model of an ammonia decomposition palladium membrane reactor showing composition of ammonia (blue), hydrogen (red) and nitrogen (green) as a function of membrane surface area (x axis) for a given catalyst loading. **a** is at 550 $K$, **b** is at 500 $K$ and **c** is at 450 $K$. Membrane permeability data is taken from Zhang *et al.* for a 4 $\mu m$ Pd membrane [108], catalyst data is taken for a 7 wt.% Ru, 4 wt.% Cs on graphitised CNT support taken from this work.

**Table 6.3:** Results from the ammonia decomposition membrane reactor model

| **Reactor temperature** $K$ | **Membrane surface area to achieve > 99 % conversion** $m^2$ | **Mass of catalyst** $g$ | **Mass of Pd** $g$ | **Mass of Ru** $g$ |
|---|---|---|---|---|
| 450 | 56 | 3400 | 2405 | 218 |
| 500 | 17 | 800 | 818 | 51 |
| 550 | 9.5 | 300 | 457 | 19 |

There are a number of limitations and inherent inaccuracies in this modelling approach that must be acknowledged.

- It is assumed that the partial pressure of hydrogen on the permeate side of the membrane is zero and consequently the rate of hydrogen flux is likely to be overstated. Although a sweep gas is often employed to increase flux by reducing the hydrogen partial pressure on the permeate side, this inherently reduces the permeate hydrogen partial pressure and correspondingly reduce the effectiveness of the PEM fuel cell [139]. To overcome this limitation in the optimised design, hydrogen should be consumed directly by the catalyst at the PEM fuel cell anode; in effect the membrane would act as the anode. This would have to be assessed experimentally and the rate of hydrogen transmembrane flux would probably be somewhat lower than that shown here.

- No attempt has been made to account for mass transfer, flow regime or heat transfer within the reactor. In particular, mass transfer of hydrogen from the catalyst surface to the membrane will of prime importance in determining the reactor efficiency and the design must focus upon obtaining the optimum flow and mass transfer characteristics. In general, these aspects could be addressed by employing micro-reactor strategies as has been suggested in literature [139].

- The reactor geometry and aspect ratio have not been defined. The model makes the simplistic assumption that all combinations of catalyst quantity and membrane surface area can be accommodated. The next step would be to consider membrane reactor geometries such as micro-channel or tubular configurations to make a further assessment.

The final aspect for the design to address is the removal of residual ammonia from the membrane reactor retentate stream. There are examples in literature of carbon adsorbents being used for similar purposes [139]. Alternatively, materials that absorb the ammonia chemically such as $MgCl_2$ could be employed [11]. In both

cases the ammonia trapped could be subsequently recovered and recycled, for this to work the sorbent material would be in the form of a cartridge that would be periodically replaced with fresh or regenerated material. To protect against failure of the absorbent material, release of ammonia to atmosphere would be prevented by a sensor monitoring the exhaust stream linked to an automatic shutdown of the flow of ammonia. It is likely that a system like this would be effective but substantial development and refinement is required. Improvement of membrane performance remains as the primary challenge.

An alternative solution to the problem of high use of palladium in the membrane would be to switch from the perm-selective palladium membrane for a competitive diffusion membrane such as silica. In this event, the membrane expense would be substantially reduced, the risk of poisoning of the PEM fuel cell could be offset by employing a similar ammonia trap as would exist in the exhaust stream.

## 6.5 Assessment of the Use of Ammonia as a Road Transport Fuel Versus the US DoE Hydrogen Storage Targets

### 6.5.1 Introduction

The objective of this assessment is to understand how the use of ammonia as a hydrogen storage vector meets with the energy efficiency targets established by the US DoE for hydrogen storage technologies. Accordingly, the energy cost incurred by the process steps required to utilise ammonia to store hydrogen have been estimated and compared with the US DoE benchmarks.

The key steps included in this assessment are hydrogen production by electrolysis, nitrogen separation, ammonia synthesis, optional storage as $Mg(NH_3)_6Cl_2$ and subsequent thermal decomposition, ammonia decomposition and hydrogen purification. All energy data is presented in units of $GJ\ t^{-1}$ of hydrogen or ammonia. The analysis assumes 100 % conversion of hydrogen to ammonia and ammonia to hydrogen, this could be considered to be optimistic and will need to be amended as the technology develops. Only energy costs incurred during normal operation are included, this excludes energy costs from equipment manufacture and decommissioning. It also does not incorporate ancillary energy losses such as transportation of materials. This study is a feasibility assessment and not a life cycle analysis (LCA); it is designed to advance the understanding of the feasibility and sustainability of this

application, a full LCA will eventually be required to support the implementation of this technology.

The storage of ammonia in the form of solid metal ammine salts such as $Mg(NH_3)_6Cl_2$ is included because this material has been proposed as a solution to the toxicity hazard presented by the storage of ammonia. Klerke *et al.* showed that while the explosion and flammability risks presented by ammonia are similar to conventional fossil fuels, the toxicity of ammonia is many times greater [11].

### 6.5.2 Case Study Definitions and Terms of Reference

The systems to be compared are illustrated in Figure 6.7 showing *i)* the conventional Haber-Bosch process from natural gas, *ii* a sustainable Haber-Bosch process in which hydrogen from electrolysis and renewable electricity replaces natural gas and *iii)* the use of $MgCl_2$ for safer storage of ammonia. The case study boundaries are defined in accordance with the US DoE targets for "well to power-plant" scenarios. For the hydrogen storage system proposed here, the case-study boundaries are as follows: for the conventional Haber-Bosch process this study extends from methane supply at the point of ammonia synthesis to hydrogen delivered at the point of use; for the sustainable Haber-Bosch process, the boundaries are from supply of renewable electricity to the delivery of hydrogen at the point of use.

a) Conventional Haber-Bosch process and ammonia decomposition

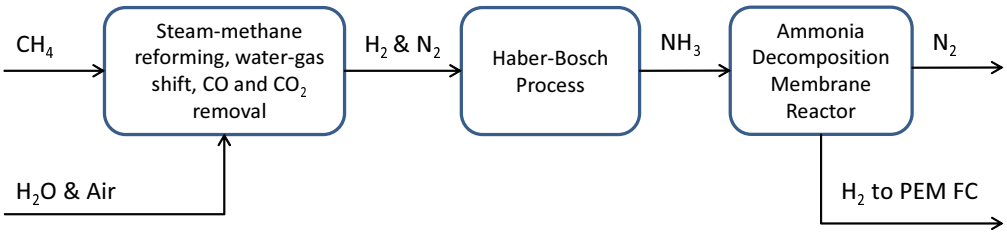


b) Sustainable energy Haber-Bosch process and ammonia decomposition

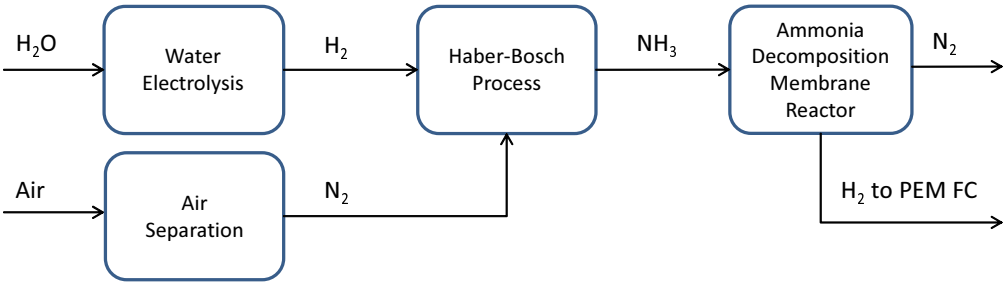


c) Sustainable energy Haber-Bosch process and ammonia decomposition incorporating $Mg(NH_3)_6Cl_2$ safe storage

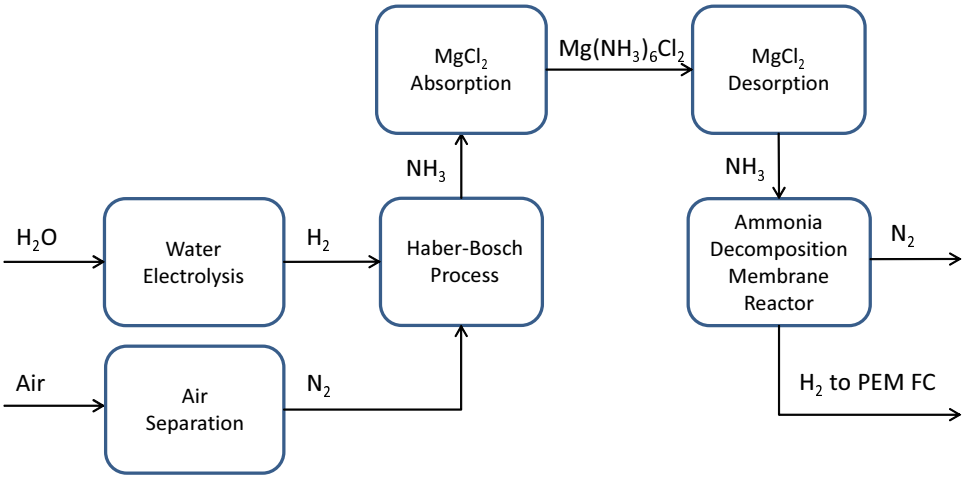


**Figure 6.7:** Schematic of the case-study system boundaries for both the conventional and sustainable Haber-Bosch Processes with ammonia decomposition to supply hydrogen at the point of use.

To evaluate and compare the energy costs associated with the production and decomposition of ammonia, it is essential to set clear system boundaries. The US DoE have set two energy criteria for hydrogen storage systems for road transport applications. The first is that on-board energy efficiency should exceed 90 %, the

second is that "well to power-plant efficiency", defined as the energy costs from initial production through to final delivery of hydrogen, should exceed 60 % [149]. These two targets effectively define the system boundaries for this study. At one end, the US DoE definition of "well" applies to methane extraction or supplied electricity; at the other end, "power-plant" would refer to the delivery of hydrogen to a PEM fuel cell at the point of use. On-board efficiency in this case comprises all energy inputs from stored ammonia at the point of use to delivery of pure hydrogen to the PEM fuel cell.

A study of this nature is only as good as the quality of input data. In this case data from academic or industrial publications has been used where possible. Where no data exists, best estimates by the author have been used. This particularly applies to the ammonia decomposition reactor which has not yet been commercialised; data for ammonia decomposition and hydrogen purification is taken from work in this thesis.

### 6.5.3 Quantification of Energy Losses

To enable an assessment to be made of the energy costs for converting hydrogen to ammonia, a detailed understanding of the conventional Haber-Bosch process accompanied with energy inputs is necessary. Data taken from the ICI Haber-Bosch process is shown in Figure 6.8 [1]. The conventional Haber-Bosch process consists of the following steps: methane feed is desulphurised followed by steam methane reforming and water gas shift reactions, then $CO_2$ removal and methanation to remove residual oxygenated carbons takes place before finally undertaking ammonia synthesis. Energy losses quoted are incremental to the thermodynamic minimum energy requirement for this process; in literature this has been taken as 20.9 $GJ\ t_{NH_3}^{-1}$ [12] using the higher heating value of ammonia (HHV) or 18.9 $GJ\ t_{NH_3}^{-1}$ using the lower heating value of ammonia (LHV) (see Figure 6.1). The LHV will be used in this study. The energy required for this older ICI process is substantially greater than the modern processes and losses total 15.3 $GJ\ t_{NH_3}^{-1}$ compared to 8.0 $GJ\ t_{NH_3}^{-1}$ for the modern plant [12]. Despite this, the detailed energy breakdown provided for the ICI process gives a unique insight showing which steps contribute a greater share of energy losses.

The energy losses for the ICI process in Figure 6.8 are dominated by desulpherisation and steam methane reforming, ammonia synthesis accounts for only 8 % of the total energy loss. The energy requirement is small because the ammonia synthesis reaction is exothermic, a significant proportion of the hydrogen and nitrogen feed

is introduced as cold quench to prevent reactor temperature increase. These figures suggest that a sustainable Haber-Bosch process employed to chemically store hydrogen as ammonia would incur substantially reduced energy losses compared to the methane fed process. While there is a scarcity of data on energy losses from the Haber-Bosch process, the ICI figure of 1.3 $GJ\ t_{NH_3}^{-1}$ is the same as the more recent figure from KBR [150]; other sources have the figure as 1.4 $GJ\ t_{NH_3}^{-1}$ [151] and 1.5 $GJ\ t_{NH_3}^{-1}$ [11].

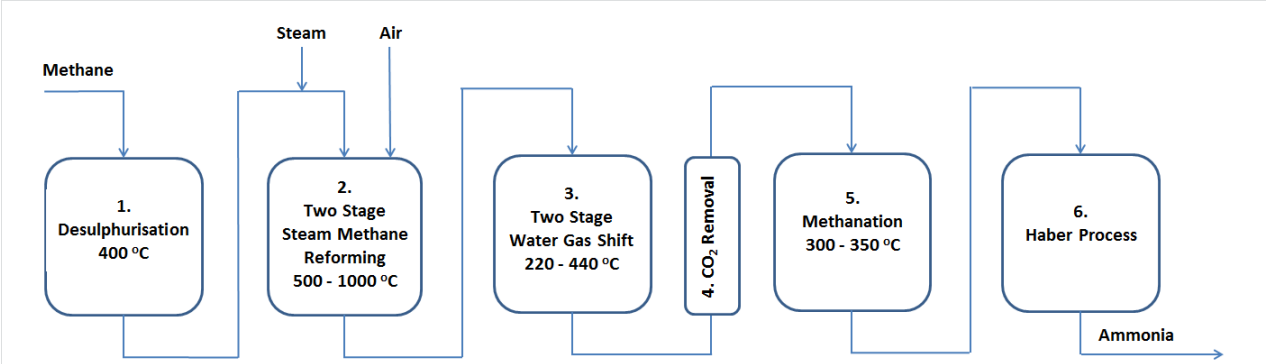


| | Stages 1 & 2 | Stages 3 - 5 | Stage 6 | Refrigeration | Steam System | General Losses | Total |
|---|---|---|---|---|---|---|---|
| Energy Loss, GJ/$t_{NH3}$ | 10.5 | 1.4 | 1.3 | 0.1 | 1.3 | 0.7 | **15.3** |
| Percentage of Total | **69%** | **9%** | **8%** | **1%** | **8%** | **5%** | |

**Figure 6.8:** Energy breakdown for the Conventional Haber-Bosch Process (1983 design), data from ICI [1]. The energy losses are accretive to the minimum thermodyamic energy requirement of 18.9 $GJ\,t_{NH_3}^{-1}$.

It is important to also consider the energy losses associated with the production and purifcation processes of natural gas. Purification of methane requires the removal of $H_2S$ and $CO_2$ and $H_2O$ contaminants and gas liquids including ethane, propane, butane and pentane [152]. PetroChina estimated that the average energy loss from production and purification of natural gas methane to be 10 % [153].

To break the link between ammonia synthesis and fossil fuels, the methane feed should be replaced with renewable hydrogen. In this sustainable Haber-Bosch process, hydrogen is produced by electrolysis of water before being fed with pure nitrogen to a conventional synthesis loop (see Figure 6.7 b). The energy costs of the sustainable Haber-Bosch process has been estimated and compared with the conventional Haber-Bosch process in Table 6.4.

The energy losses for the generation of hydrogen are estimated assuming that the alkali electrolyte water electrolysis process is used. Although there are alternative technologies such as photo-catalytic processes that would be more energy efficient and proton exchange membrane PEM systems, it is appropriate to select electrolysis

because it is a widely used technology and a number of commercial technologies exist at various scales [154]. In a review of five commercial electrolysers, the commercial electrolyte based systems were more energy efficient than PEM [154] even though research has shown the PEM approach to have similar efficiency [155]. For this analysis, data for the best commercial applications will be used, both the Stuart and Norsk Hydro alkali electrolyte systems require energy input of 192 $GJ\ t_{H_2}^{-1}$ (33.9 $GJ\ t_{NH_3}^{-1}$), the system efficiency of 73 % giving an energy loss of 51.8 $GJ\ t_{H_2}^{-1}$.

The other significant energy losses that are incurred by the sustainable Haber-Bosch process arise from air separation and the high pressure synthesis loop for production of ammonia. The nitrogen that is required for the Haber-Bosch process can be obtained by a number of different air separation technologies each of which is capable of providing high purity nitrogen. Cryogenic distillation requires 1.6 $GJ\ t_{NH_3}^{-1}$, pressure swing adsorption requires 1.2 $GJ\ t_{NH_3}^{-1}$ and hollow fibre gas filtration membrane technologies use around 0.6 $GJ\ t_{NH_3}^{-1}$ [156]. Given the importance of energy efficiency in a hydrogen storage application, it is logical that the membrane technology should be selected. Synthesis of ammonia is done by the conventional Haber-Bosch process, as discussed above, modern plants incur energy losses of approximately 1.3 - 1.5 $GJ\ t_{NH_3}^{-1}$.

If ammonia is stored in $MgCl_2$ pellets to form the composite $Mg(NH_3)_6Cl_2$, this creates two additional steps within the hydrogen storage cycle. Ammonia easily absorbs into $MgCl_2$ tablets which are safe to be handled at room temperature and have an ammonia vapour pressure of only 2 $mbar$; the ammonia is released by heating to between 323 and 523 $K$. The enthalpy of desorption of the first ammonia molecule from $Mg(NH_3)_6Cl_2$ is 40 $kJ\,mol_{NH_3}^{-1}$ and this additional energy input must be provided at the point of use [11]. The absorption process is exothermic and occurs at ambient temperature, this would be done at a centralised location away from the point of use and thus the heat released from absorption is unlikely to be recovered and is considered to be lost. Desorption requires 3.2 $GJ\ t_{NH_3}^{-1}$ [11], this energy must be provided at the point of use to release the ammonia from storage and thus it will impair the efficiency of on-board generation of hydrogen.

The energy inputs for the production of hydrogen from ammonia at the point of use consists of sensible heat to raise the temperature of ammonia to the ammonia decomposition reaction temperature and the heat of reaction for the endothermic decomposition reaction (15.4 $GJ\,t_{H_2}^{-1}$ [157]). The reaction temperature chosen for this study is 450 $K$ based upon reactor design work presented earlier in this chapter. The temperature is not the most critical of factors however, results from a sensitivity study presented in Figure 6.9 show that increasing the temperature of reaction from 450 - 550 $K$ reduces the efficiency of onboard generation from 87.7 % to 86.8 %.

The energy costs for the "well to power-plant" scenarios are presented in Table 6.4. Energy efficiency is calculated as the sum of energy losses as a proportion of the heat of combustion of hydrogen. The first scenario shows the production of ammonia from methane using the most efficient conventional Haber-Bosch process and decomposition to hydrogen at the point of use. This gives overall energy efficiency of 51 %, if the breakdown of energy losses is similar to the ICI process (Figure 6.8) then it can be said that the steam-methane reforming (SMR) and water-gas shift reactions (WGS) account for the bulk of the energy losses. The second scenario switches the conventional Haber-Bosch process for a sustainable one in which the hydrogen is sourced by alkali electrolysis from renewable energy. In this scenario, energy efficiency falls to 44 % with the electrolysis step accounting for the majority of the energy losses. The third scenario builds upon the second by including ammonia storage as $Mg(NH_3)_6Cl_2$. In this case, the energy efficiency reduces further to 32 % because of the additional heat input for ammonia desorption. While these predicted efficiencies are below the 60 % target set by the US DoE, there may be energy savings available. Firstly, improvements to the electrolysis process which accounts for the bulk of the energy losses would greatly improve overall efficiency and secondly, thermal integration of the electrolysis, air separation and Haber-Bosch synthesis loop could yield substantial further savings.

The energy costs for 'on-board efficiency' are presented in Table 6.5. For the scheme outlined in Figure 6.3, the energy efficiency is 88 %, close to the 90 % target set by the US DoE. The use of $Mg(NH_3)_6Cl_2$ for ammonia storage reduces the efficiency to 75 %. No account was made of the potential for thermal integration within the on-board hydrogen generation system. Efficiency could be improved by utilising waste heat streams such as heat from the PEM fuel cell and membrane reactor retentate that could be recycled to heat the reactor inlet ammonia .

**Table 6.4:** Case study results for storage of hydrogen as ammonia - Well to Power-plant

A - Conventional Haber-Bosch process

| **Process Step** | **Energy Loss** $GJ\,t_{H_2}^{-1}$ | **Notes** | |
|---|---|---|---|
| Production and purification of methane | 6.4 | *Data from PetroChina* | [153] |
| Ammonia synthesis from methane | 45.9 | *Losses for modern H-B plant from Schuth et al.* | [12] |
| Energy to heat ammonia to reaction temperature | 2.2 | *Heating of ammonia to reaction temperature* | [157] |
| Release of hydrogen from ammonia - heat of reaction | 15.4 | *Heat for endothermic reaction* | [157] |
| **Total** | **69.9** | | |
| **Energy Efficiency** | **51 %** | *Calculated with reference to the hydrogen heat of combustion* | |

B - Sustainable energy Haber-Bosch process

| **Process Step** | **Energy Loss** $GJ\,t_{H_2}^{-1}$ | **Notes** | |
|---|---|---|---|
| Hydrogen production by electrolysis | 51.8 | *Norsk Hydro alkali electrolysis* | [154] |
| Nitrogen purification by air separation | 3.5 | Assumes gas membrane separation | [156] |
| Ammonia synthesis | 7.4 | *ICI* | [1] |
| Energy to heat ammonia to reaction temperature | 2.2 | *Heating of ammonia to reaction temperature* | [157] |
| Release of hydrogen from ammonia - heat of reaction | 15.4 | *Heat for endothermic reaction* | [157] |
| **Total** | **80.3** | | |
| **Energy Efficiency** | **44 %** | *Calculated with reference to the hydrogen heat of combustion* | |

C - Sustainable Haber-Bosch Process plus safe storage as $Mg\,(NH_3)_6\,Cl_2$

| **Process Step** | **Energy Loss** $GJ\,t_{H_2}^{-1}$ | **Notes** | |
|---|---|---|---|
| Hydrogen production by electrolysis | 51.8 | *Norsk Hydro alkali electrolysis* | [154] |
| Nitrogen purification by air separation | 3.5 | Assumes gas membrane separation | [156] |
| Ammonia production from hydrogen | 7.4 | *ICI* | [1] |
| Ammonia storage as $Mg\,(NH_3)_6\,Cl_2$ | 0 | Assumes that the heat of absorption is not recovered | |
| Ammonia release from $Mg\,(NH_3)_6\,Cl_2$ | 18.3 | *Heat of desorption* | [11] |
| Energy to heat ammonia to reaction temperature | 2.2 | *Heating of ammonia to reaction temperature* | [157] |
| Release of hydrogen from ammonia - heat of reaction | 15.4 | *Heat for endothermic reaction* | [157] |
| **Total** | **98.6** | | |
| **Energy Efficiency** | **32 %** | | |

**Table 6.5:** Case study results for storage of hydrogen as ammonia - on-board generation

1 - on-board generation of hydrogen from ammonia

| **Step** | **Energy Loss** $GJ\,t_{H_2}^{-1}$ | **Notes** | |
|---|---|---|---|
| Ammonia vaporisation | 0 | *Assumes that the latent heat is obtained for free from ambient.* | |
| Energy to heat ammonia to reaction temperature | 2.2 | *Heating of ammonia to reaction temperature* | [157] |
| Release of hydrogen from ammonia - heat of reaction | 15.4 | *Heat for endothermic reaction* | [157] |
| **Total** | **17.6** | | |
| **Energy Efficiency** | **88 %** | | |

2 - on-board hydrogen generation from $Mg\,(NH_3)_6\,Cl_2$

| **Step** | **Energy Loss** $GJ\,t_{H_2}^{-1}$ | **Notes** | |
|---|---|---|---|
| Heat of desorption of ammonia from $Mg\,(NH_3)_6\,Cl_2$ | 18.3 | *Heat of desorption* | [11] |
| Energy to heat ammonia to reaction temperature | 2.2 | *Heating of ammonia to reaction temperature* | [157] |
| Release of hydrogen from ammonia - heat of reaction | 15.4 | *Heat for endothermic reaction* | [157] |
| **Total** | **36.0** | | |
| **Energy Efficiency** | **75 %** | | |

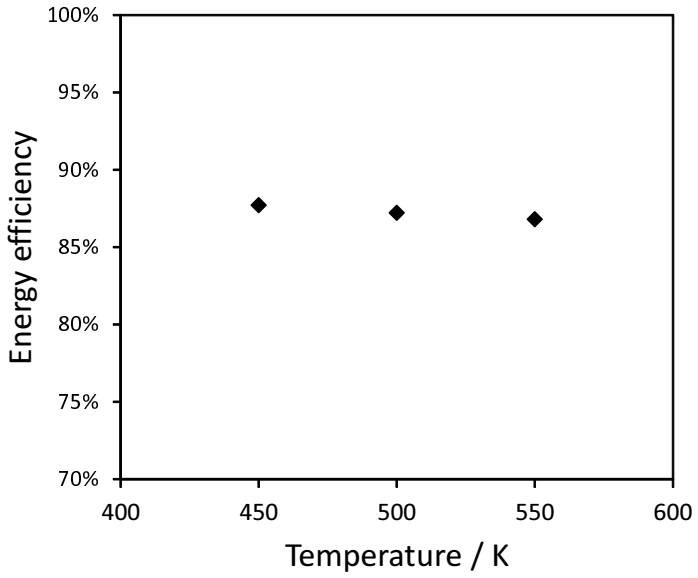


**Figure 6.9:** Sensitivity study on the effect on ammonia decomposition temperature on energy efficiency for on-board hydrogen production

These scenarios assume that that low carbon electricity is used as the input energy. In Q2 of 2013, the UK produced an average 15.5 % of total UK electricity supply with a total installed capacity of 19.5 GW [158]. Gasoline consumption for UK motoring in a typical month is 3,000,000 t which equates to 135,000 TJ of energy [159, 160]. In case B above, the energy efficiency for the conversion of renewable electricity to hydrogen at the point of use was 44 %, thus the UK renewable energy production could deliver equivalent energy to suppy 15 % of the gasoline powered vehicles in the UK on an equal energy basis. If the greater efficiency of the PEM fuel cell of over 80 % [13] compared to maximum 35 % for an internal combustion engine [161] then the maximum proportion of vehicles supplied with renewable hydrogen increases to 34 %. If other low carbon electricity, such as the 18.6 % from nuclear generation in Q2 2013, is considered then the figure rises further to 75 % of current gasoline fueled vehicles. Given the rate of increase of renewable energy generation and energy efficiency in road transport vehicles, there could in the future be sufficient energy to provide for this application.

The system energy losses for the sustainable Haber-Bosch system are dominated by the hydrogen production by electrolysis. This energy loss will be incurred by all hydrogen storage technologies when benchmarked against the US DoE targets and does not reflect the merits of ammonia as a hydrogen storage vector. That being said, the conventional Haber-Bosch process has the best energy efficiency and is the option that gets closest to the US DoE efficiency targets. If we consider the broader sustainability, fugitive emission of methane (a greenhouse gas itself) to atmosphere that have been estimated at between 1 - 9 % of total delviered methane [162]. Methane is also a finite resource with reserves at the end of 2013 sufficient for 55.1 years of production [163]. These aspects must also be considered as part of a sustainability assessment.

## 6.6 Carbon Footprint of Road Transport Fuels

As well as considering overall energy efficiency for using ammonia as a hydrogen vector, it is important to also consider the impact upon greenhouse gas emissions so that the impact on climate change can be understood. To do this, the quantified energy losses associated with hydrogen storage as ammonia for road transport applications are represented as a carbon footprint ($g_{CO_2}\,km^{-1}$). The results of which have been compared to published benchmark data for the carbon footprint of common road transport fuels [164, 165]. The carbon footprint associated with a road transport fuel depends on both energy efficiency and on the origin of the energy

used. Although the energy losses for hydrogen production by electrolysis are large, the carbon footprint is close to zero if the electricity comes from renewable sources.

Figure 6.10 is adapted from the E4Tech report for the Department for Transport into low-carbon vehicles in 2007 [164]. The results compare the carbon footprint of a typical road vehicle with different technology options and also three different carbon intensities of the electrical supply. The baseline case, grid mix A, is the 2007 scenario emits 450 $g_{CO_2}\,kWh^{-1}$, grid mix B is the carbon intensity of a combined gas turbine emits 351 $g_{CO_2}\,kWh^{-1}$ and grid mix C represents full implementation of the UK low carbon energy strategy which would result in carbon intensity of 176 $g_{CO_2}\,kWh^{-1}$.

To understand the effect of using ammonia to store hydrogen on the carbon footprint of the fuel, the incremental $CO_2$ emissions from storage of hydrogen as ammonia using the sustainable Haber-Bosch process outlined earlier in this chapter shown alongside this analysis. The carbon footprint for the sustainable Haber-Bosch process has been estimated assuming that all of the energy input to the process comes from grid mix electricity. This is reasonable as the processing steps in the sustainable Haber-Bosch process would be electrically powered, it is significant because it links the carbon footprint of the sustainable Haber-Bosch process to the electrical grid carbon footprint. The method of comparison incurs error because the two studies are not "like for like". The E4Tech analysis of vehicle carbon footprint was a "well to wheels" analysis based on commercial operating technologies and presents a more complete picture compared to the estimates presented here for the energy losses for the sustainable Haber-Bosch process which is a more limited analysis. If a full LCA was made for the sustainable Haber-Bosch process, it is likely that the $CO_2$ emissions would be greater when aspects like transportation are included. Despite this caveat, this approach puts the $CO_2$ emissions resulting from the use of ammonia to store hydrogen into the broader context of those from other available road transport fuels.

The results displayed in Figure 6.10 show that hydrogen powered fuel cell vehicles (FCV) have less than half the carbon footprint of conventional internal combustion engines when the hydrogen is sourced from natural gas. The carbon footprint is similar to 100 % electric vehicles run on grid mix A, however the carbon footprint of these vehicles decreases substantially as the carbon intensity of the electricity supply reduces. More surprising is the high carbon footprint of hydrogen from electrolysis: it is only when the full set of low carbon electrical policies and the carbon intensity of the electrical supply falls below 176 $g_{CO_2}/kWh$ that the carbon footprint of hydrogen from electricity falls below that of hydrogen from natural gas. The use of ammonia as a hydrogen storage medium produces a relatively modest

increase in carbon footprint accounting for around 22 % of the carbon footprint for hydrogen sourced from natural gas.

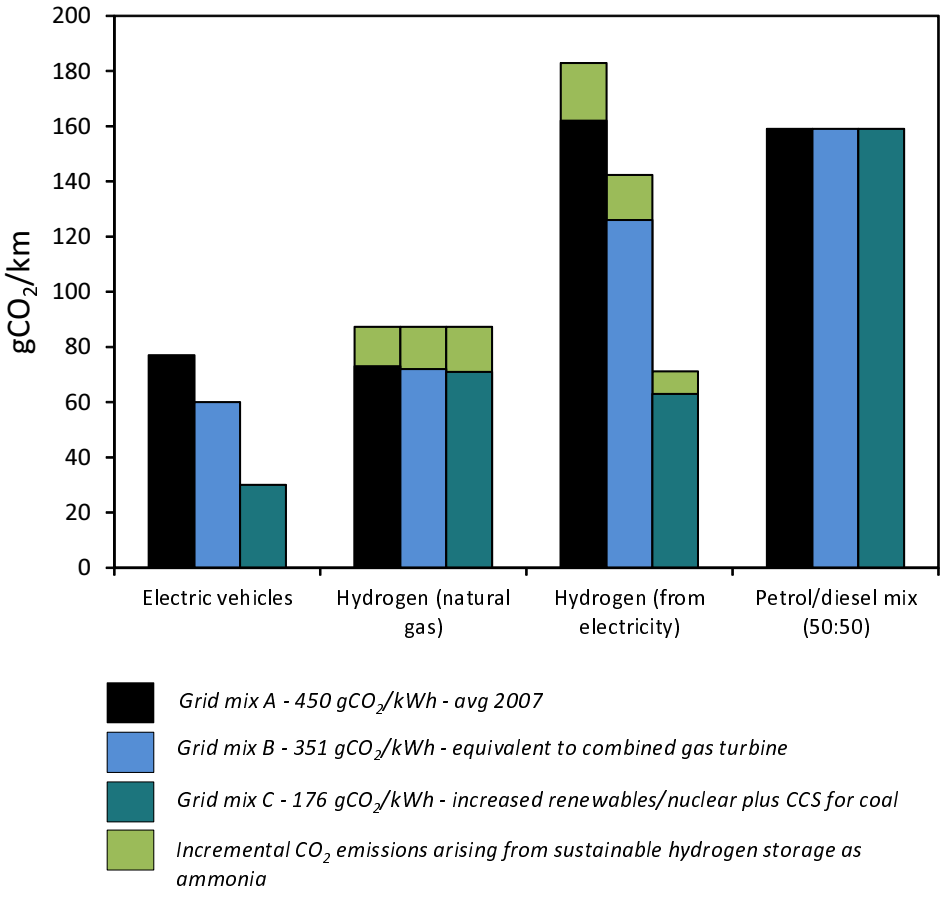


**Figure 6.10:** $CO_2$ emissions from road transport fuels for the UK showing the impact of ammonia as a hydrogen storage medium and the effect of the carbon intensity of the electricity supply [164]. The carbon footprint for sustainable ammonia is estimated using results from this chapter and assumes energy inputs are from the electrical grid, the carbon footprint of the Haber-Bosch process from natural gas is taken from literature [166].

On this evidence, the best technology to be used for low carbon road transport would be the 100 % electric vehicle utilising battery technology in the context of a decarbonised electrical infrastructure. However, this technology suffers from its own difficulties: the high cost of batteries, the inability to store sufficient energy to give a reasonable driving range and the resulting high mass of the vehicle. This energy density dilemma is illustrated in Figure 6.11 taken from Zuttel *et al.* [6]. Hydrogen storage as ammonia achieves a significant reduction in carbon footprint from conventional fossil fuels if the source of electrical energy has been substantially decarbonised, it is thus valid as an alternative option to 100 % electric vehicles.

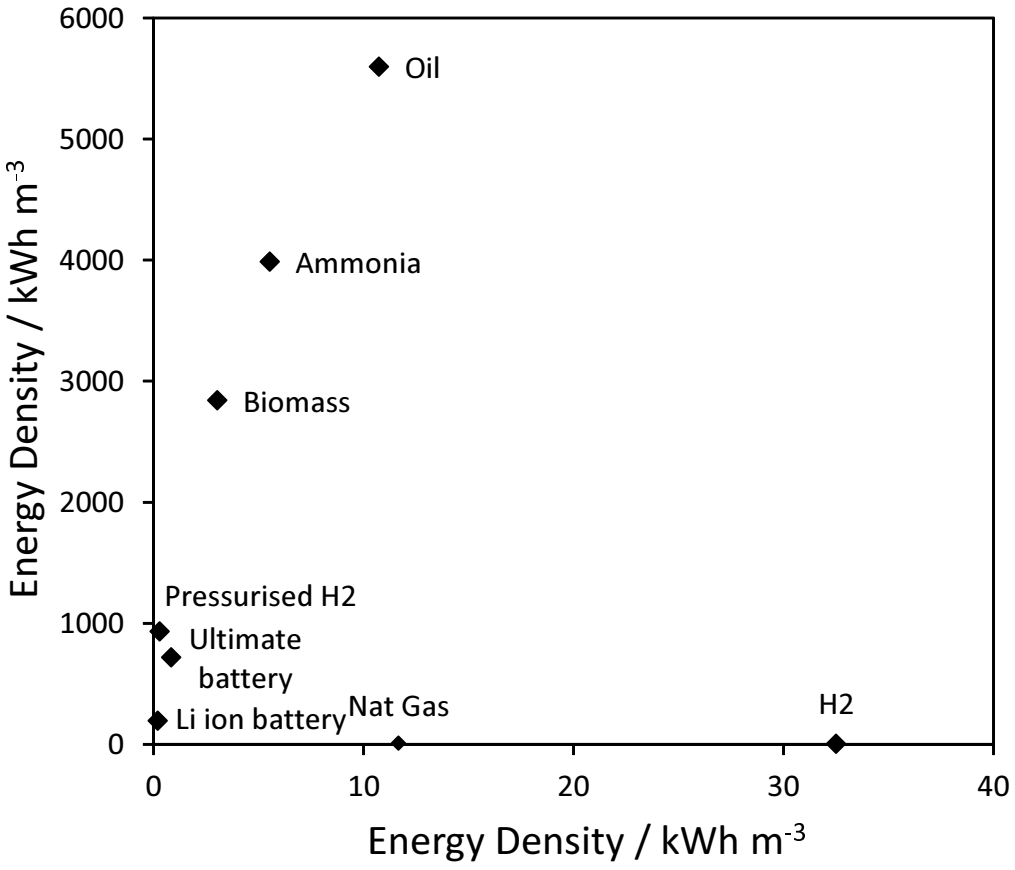


**Figure 6.11:** Volumetric versus Gravimetric Energy Density for selected energy carriers, adapted from Zuttel *et al.* [6].

## 6.7 Conclusions

The energy efficiency and the indicative carbon footprint for the use of ammonia as a hydrogen storage medium have been quantified and compared to key government benchmarks. The energy efficiencies fall somewhat below the targets set by the US DoE for hydrogen storage. The efficiency for on-board generation of hydrogen from ammonia has been estimated as 88 % compared to the target of $>$ 90 %. There is little scope for this efficiency to be improved because it comprises almost entirely of the heat of reaction for ammonia decomposition which cannot be avoided. The "well to power plant" efficiency was calculated as 51 % with the conventional Haber-Bosch process, 44 % with the sustainable Haber-Bosch process and 32 % for the sustainable Haber-Bosch process with safe storage as $Mg(NH_3)_6Cl_2$. These are less than the US DoE target of 60 % but they could be acceptable given the high hydrogen storage density achieved by ammonia. In contrast to on-board generation efficiency of hydrogen from ammonia, there is scope for the "well to power plant" efficiency

to be improved through development and system integration of air separation and ammonia synthesis technologies. Furthermore the bulk of the energy loss (65 %) in the "well to power-plant" scenario is from the electrolysis process and will be incurred by all hydrogen storage technologies.

The use of ammonia as a hydrogen storage medium increases the carbon footprint of the hydrogen fuel cycle and accounts for 22 % of the total when hydrogen is synthesised from methane. The use of hydrogen from electrolysis only reduces the carbon footprint if the electricity supply has a carbon intensity below 176 $g_{CO_2}/kWh$ which will not be achieved in the UK for many years. Compared to the alternatives considered here, ammonia used for hydrogen storage can result in a significantly lower carbon footprint than conventional hydrocarbon fuels but can never outperform a battery electric vehicle in this metric. Future research into high efficiency hydrogen productions such as photo-catalytic processes would have a strong impact on improving these energy efficiency and carbon footprint results.

In summary, these efficiency estimates are close enough to the targets with enough potential for improvement to justify further research and development. Given the very high hydrogen storage capability of ammonia, this study finds that the system can be made efficient enough to produce a viable technology for on-board generation of hydrogen from ammonia that falls within a few percentage points of the US DoE targets and can achieve a low carbon footprint. The "well to power-plant" efficiency for the sustainable Haber-Bosch process is significantly below the US DoE target, this can be improved by making improvements to the production of hydrogen by electrolysis and by thermal integration of the different process steps.

This study is valid as a feasibility exercise and it is recommended that a full life-cycle analysis be conducted to fully understand the system energy costs.

A feasibility conceptual design for on-board decomposition of ammonia to hydrogen was presented with a view to understanding the viability of the technology proposal. A membrane reactor for ammonia decomposition has been shown to be a workable approach with $>$ 99 % conversion achieved at 450 $K$. However, the application will not be commercially viable until substantial improvements are made to the membrane technology, the large quantity of palladium required at present for this application is commercially and practically unsustainable. It is suggested that alternative strategies such as silica membranes in combination with ammonia traps be considered to circumvent this problem. Further improvements to catalyst activity will also improve the commercial viability by reducing the amount of ruthenium required as demonstrated by the use of cobalt catalysts earlier in chapter 5.

# Chapter 7

# Conclusions and Further Work

In this chapter, the project context and objectives are briefly outlined before a summary of the main conclusions from this thesis, presented in the same order as the thesis chapters.

The over-riding goal of this thesis was the development of catalysts that had activity at low temperature for ammonia decomposition for application to an integrated ammonia-PEM fuel cell with a hydrogen permeation membrane reactor. It was proposed that development of this technology would unlock the potential of ammonia to act as a high capacity hydrogen storage vector. Hydrogen generated with electricty from renewable sources can be converted to ammonia, in which form it can easily be stored and transported before conversion back to hydrogen at the point of use to fuel a high efficiency PEM fuel cell. This enables higher effective hydrogen storage densities than even liquefied hydrogen and allows for low carbon energy to be provided effectively for road transport applications.

This overall objective is broken down into three aspects. A key premise for this thesis is that the integrated ammonia-PEM fuel cell must contain a catalyst that can decompose ammonia to hydrogen at a similar temperature to the fuel cell operating temperature of approximately 370 $K$. Given the sustainable nature of the final application, the catalyst developed should itself be sustainable and not comprise aspects like rare elements. The final part of this thesis was dedicated to understanding how this technology performs from the perspective of feasibility and sustainability.

## 7.1 Development of Low Temperature Catalysts for Ammonia Decomposition

A great deal of the work in this thesis focuses upon the development of catalysts for an ammonia PEM fuel cell. Investigation was focused on the factors that produce low temperature catalyst activity for ruthenium on carbon nanotube (CNT) supports with cesium promoter. Ruthenium-cesium based systems are presented in the literature as the most active, and this work focused on understanding the nature of this activity with the goal to enhance it. The variation of ruthenium loading from 3.0 - 13.2 $wt.\%$ (with 4 $wt.\%$ cesium on CNTs) produced no change in the rate of reaction per mole of ruthenium or change in activation energy. The conclusion from this is that the change in loading made no change to the active surface of the ruthenium nanoparticles. The modification to cesium loading produced a dramatic increase in activity for ammonia decomposition, even at very high loadings of cesium. This effect was accompanied by a large reduction in activation energy and activity for ammonia decomposition started from 470 $K$.

Evidence was found to suggest that cesium is partially reduced on the surface of ruthenium particles and in close proximity. The great improvement in activity and the reduction in activation energy following addition of cesium did not produce a discernable change in ruthenium particle size and thus it is probable that the action of cesium is electronic rather than structural. Temperature programmed reduction experiments showed that as cesium loading was increased, the temperature of ruthenium reduction and the quantity of hydrogen consumed also increased. This change can only occur if the cesium was present on the surface or in close proximity to the ruthenium particles. From the increase in hydrogen consumption, it is concluded that the cesium has been partially reduced on the surface of ruthenium nanoparticles.

Further investigation into the optimum activity of ammonia decomposition catalysts was conducted by modification of the CNTs by graphitisation. Graphitisation was found to increase activity and to reduce the cesium loading required for peak activity. In contrast to published literature, graphitisation of the CNT support produced no measureable change in ruthenium particle size. The addition of cesium to the catalyst with ruthenium on graphitised CNTs produced even greater activity for ammonia decomposition and lowered the activation energy of the reaction. This approach produced the most active catalyst in this study, with activity from 450 $K$, and it was achieved at a much lower cesium loading than was required for the catalyst on unmodified CNTs. This effect has not been demonstrated previously and it also supports the assertion that the main mode of action of cesium is electronic.

It is known that graphitisation will have substantially increased the electrical conductivity of the CNT support allowing cesium to donate electrons to the ruthenium nanoparticle from a greater distance.

The study on the stability over time of a ruthenium-cesium-CNT catalyst demonstrated a loss of activity that was quicker than would be suitable for a commercial application. This presents many further avenues for investigation: the mechanism of deactivation is not known and could be caused by thermal degradation or agglomeration of nanoparticles or it could be due to other factors such as poisoning. Further investigations are required to understand this mechanism. Future work could consider prevention of nanoparticle agglomeration by confinement within the CNT structure. If agglomeration of nanoparticles is the cause of deactivation, then other porous supports that can better confine the nanoparticles may provide a solution. The study could be expanded to consider support and electronic properties given the effect that these factors had upon the activity of ruthenium.

## 7.2 Development of Sustainable Catalysts for Ammonia Decomposition

The world supply of ruthenium is limited compared to many other catalytic metals and hence the use of it in this application would detract from the overall sustainable objective. In response to this, a study was made of sustainable metals that would be more appropriate for use in this application. Cobalt catalysts were found to be more active on microporous carbon supports than mesoporous carbon or supports with high degrees of surface graphitic structure. This is directly opposite to ruthenium, and the activity of cobalt almost reached that of ruthenium on the microporous support. By TEM - EDS it was shown that cobalt was distributed evenly over the catalyst surface at a particle size too small to be measured, from this it is possible to conclude that cobalt was distributed within the microporous structure, it was also concluded that cobalt is more active for ammonia decomposition with a smaller particle size (although comparison could be drawn with smaller ruthenium particles in future). This finding is in direct contrast to ruthenium where activity was shown in literature to be a strong function of the support's graphitic nature.

An exploration was made of bi-metallic catalysts based upon cobalt and nickel as sustainable active metals and microporous carbon supports. It was demonstrated by changes in activity that bi-metallic catalysts were formed as the resultant activity was different from both individual metals. The addition of silver and copper to cobalt and nickel catalysts had no effect on the activity compared to the single

metal catalysts. In contrast to this, the addition of molybdenum to a nickel catalyst caused a significant increase in activity. This finding is very promising and suggests that there is scope within bi-metallic catalysts to enhance the activity of more sustainable catalysts for ammonia decomposition.

The work into sustainable catalysts presents the greatest opportunity for further investigation. The study into the optimum particle size of cobalt would be greatly aided by characterisation techniques that could determine the cobalt particle size. Higher resolution microscopy would enable imaging of the micropores with the cobalt confined within them. In combination with electron-dispersive X-ray spectroscopy (EDS), this would help to shed light upon the structure of sustainable bi-metallic catalysts on microporous supports. Further to microscopy, other techniques are required to measure the cobalt metallic surface area.

Bi-metallic nanoparticles supported on microporous carbons have much potential for further study. The use of incipient wetness impregnation to synthesise bi-metallic nanoparticles, as was shown in this work, is a straightforward and commercially scaleable process (compared to in-situ reduction techniques that require many more processing steps). The work presented here on bimetallics of nickel, cobalt and molybdenum needs to be expanded upon and many other combinations tried. Characterisation of these catalysts in combination with measurement of kinetic activity can shed light upon the interactions between metals and help to understand how higher catalytic activity can be produced.

## 7.3 The Sustainability and Feasibility of Ammonia as a Hydrogen Storage Vector

### 7.3.1 Sustainability

A sustainable system that utilises ammonia as a chemical hydrogen storage medium has been proposed, consisting of hydrogen synthesised by electrolysis from renewable energy, ammonia synthesised directly from hydrogen and nitrogen and decomposition to pure hydrogen using a membrane reactor at the point of use. Safer storage of ammonia as metal chloride ammine complexes was also considered. Comparisons were drawn with variants of this scheme including ammonia from methane using the conventional Haber-Bosch process. These processes are referred to here as the sustainable ammonia scheme and the conventional ammonia scheme.

The proposed use of ammonia as a sustainable hydrogen storage vector was benchmarked against the US Department of Energy (US DoE) targets for energy efficiency.

The first target is for 60 % "well to powerplant" energy efficiency. For the sustainable scheme, this comprises all energy losses between supply of renewable electricity for hydrogen production through to delivery of hydrogen for a PEM fuel cell at the point of use. For the conventional scheme, this comprises all energy losses from natural gas extraction through to delivered hydrogen at the point of use. The conventional process achieves estimated "well to powerplant" efficiency of 51 % and the sustainable process achieves 44 %. In the conventional process, the losses are primarily from the steam-methane reforming and water-gas shift reactions. In the sustainable process, the production of hydrogen by electrolysis accounts for 65 % of the total energy losses. The Haber-Bosch process in the sustainable scheme requires very little energy, accounting for only 9.3 % of the total losses. When metal chloride ammine complex $Mg(NH_3)_6Cl_2$ is used for safer storage, the overall energy efficiency falls further to 32 % due to the heat required for ammonia desorption at the point of use. In conclusion, the proposed sustainable process is less energy efficient than the conventional process and falls short of the US DoE target for energy efficiency.

The focus of development to improve performance against this US DoE metric should be on high efficiency hydrogen production technologies from sustainable energy resources. The high onboard energy cost associated with ammonia decomposition from metal chloride ammine complexes throws doubt upon their suitability for this application unless the heat of desorption can be supplied from waste heat via heat integration.

The second US DoE target is that the onboard energy efficiency of all hydrogen storage technologies should be at least 90 %. Against this target, the ammonia decomposition membrane reactor would achieve estimated 88 % energy efficiency in delivering high purity hydrogen to a PEM fuel cell. This efficiency cannot be much improved upon because the greatest energy demand is the heat of reaction for ammonia decomposition which cannot be avoided. Furthermore, it cannot be supplied by heat integration as the membrane reactor is the highest temperature part of the system. The use of metal chloride ammine complex $Mg(NH_3)_6Cl_2$ for safer storage reduces this efficiency to 75 %, the losses arise from the heat of desorption of ammonia from the complex. These results suggest that an on-board hydrogen from ammonia device could succeed as it is within 2 % of the US DoE target and could be considered acceptable given the very high effective hydrogen storage density achieved through chemical storage as ammonia.

The impact of using ammonia as a hydrogen storage vector was compared to work by the UK Department for Transport (DfT) on carbon footprint of road transport technologies. With hydrogen produced from 100 % renewable energy and with all other energy inputs also sourced from renewable energy, the carbon footprint of the

sustainable ammonia scheme can approach zero. However, with the actual carbon intensity of the UK electricity "mix", it would require implementation of the full 2007 UK strategy for increased renewables, nuclear and implementation of carbon capture and storage for coal before. The proposal could be feasible in the short term at locations of abundant renewable energy away from large energy consumers. However, it still requires a substantial decarbonisation of the electricity supply before the carbon footprint of sustainable ammonia becomes low enough to make it a viable option.

In conclusion, the realisation of sustainable ammonia as a hydrogen storage vector requires substantial decarbonisation of the electricity supply and energy efficiency improvements to hydrogen production technologies. It is likely that both of these events will occur in time given the global concern around climate change, but it will be some years before the sustainable case for the use of ammonia as a hydrogen storage vector becomes compelling. There is optimism that it may occur and recently the EU announced the 2030 framework for climate and energy targets that aim to achieve 27 % renewable energy by 2030 [167]. Given the analysis in Chapter 6, it is likely that this framework will need to be fully implemented before the renewable ammonia scheme can be considered for widespread implementation.

### 7.3.2 Feasibility Assessment

The question of practicality is focused upon the ammonia decomposition and hydrogen purification technology that is to be employed at the point of use to supply hydrogen to a PEM fuel cell. The use of sustainable ammonia for hydrogen storage scheme relies upon three main technological processes: hydrogen generation by water splitting, ammonia synthesis by the Haber-Bosch process and ammonia decomposition in a membrane reactor at the point of use. Of these technologies, the ammonia decomposition reactor is the only one that has not been commercially proven, there are also very few examples of this technology being developed in research. Given this lack of operational data, a conceptual design was undertaken of an integrated ammonia decomposition palladium membrane reactor. The design utilised the most effective catalyst developed in this project for ammonia decomposition (ruthenium and cesium on graphitised CNTs) with a palladium membrane, details of which were taken from literature. Palladium was selected due to its ability to separate pure hydrogen with 100 % selectivity by virtue of the perm-selective mechanism.

The results from the conceptual design showed that while the proposal was technically feasible, it required the use of high quantities of palladium and ruthenium to achieve the desired $>$ 99 % conversion of ammonia at temperatures as low as

450 $K$. The design also highlighted the requirement for an ammonia guard bed to remove residual ammonia from exhaust streams. For the design to become practical, either the reaction temperature must be increased significantly to enhance the rate of reaction and membrane flux, or more pragmatically, the palladium membrane should be replaced with a cheaper silica membrane. A silica membrane could be combined with an ammonia trap to remove trace ammonia from the membrane permeate stream to protect the PEM fuel cell.

The investigation into the practicality of an integrated ammonia PEM fuel cell has identified two main areas for further development. The membrane size and quantity of palladium required was excessive and future development should focus upon either reducing the palladium membrane thickness or investigating alternative reactor design approaches such as silica membranes. To make the silica membrane work in practice, the ammonia contamination of the permeate stream must be removed prior to the fuel cell to prevent poisoning of the fuel cell membrane. To accomplish this it is thought that an ammonia trap that would remove ammonia with very high efficiency could be employed, a similar bed would also be required for the reactor retentate to ensure that no ammonia is vented to atmosphere. Using an ammonia trap in combination with the membrane enables the size and weight of the trap to be minimised while delivering high purity hydrogen to the fuel cell.

The study into the sustainability of the use of ammonia as a hydrogen storage vector highlighted the need for decarbonisation of the UK electricity supply and the need to increase the energy efficiency of hydrogen generation technologies. Potential options for more sustainable production of hydrogen include PEM fuel cells (in reverse) and photo-catalysis. Hydrogen can also be produced sustainably through consuming excess electricity to balance fluctuations of supply and demand in electricity distribution systems. Energy inefficiency incurred here would be less problematic as it would consume unwanted energy.

# Bibliography


[1] S A Ward. *ICI Catalysts - Paper 43, A New Low Energy Ammonia Process Concept.* ICI, 1983.

[2] Intergovernmental panel on climate change, 2013: Climate Change 2013: The Physical Science Basis.

[3] Daniel Barrett. Hydrogen london. Personal Communication, January 2014.

[4] Anon. Targets for onboard hydrogen storage systems for light-duty vehicles. Technical report, US Department of Energy, 2009.

[5] Louis Schlapbach and Andreas Zuttel. Hydrogen-storage materials for mobile applications. *Nature*, 414:353–358, 2001.

[6] Andreas Zuttel, Arndt Remhof, Andreas Borgshulte, and Oliver Friedrichs. Hydrogen: the future energy carrier. *Philosophical Transactions of the Royal Society A*, 368:3329–3342, 2010.

[7] Ned Stetson. Hydrogen storage sub-program overview. Technical report, US Department of Energy, 2012.

[8] US Department of Energy. Hydrogen and fuel cells programme, September 2012.

[9] G Thomas and G Parks. Potential roles of ammonia in a hydrogen economy. Technical report, U.S. Department of Energy, 2006.

[10] Rong Lan, John T.S. Irvine, and Shanwen Tao. Ammonia and related chemicals as potential indirect hydrogen storage materials. *International Journal of Hydrogen Energy*, 37:1482 – 1494, 2012.

[11] Asbjorn Klerke, Claus H. Christensen, Jens K. Norskov, and Tejs Vegge. Ammonia for hydrogen storage: challenges and opportunities. *Journal of Materials Chemistry*, 18:2304–2310, 2008.

[12] F Schuth, R Palkovits, R Schogl, and D S Su. Ammonia as a possible element in an energy infrastructure: catalysts for ammonia decomposition. *Energy and Environmental Science*, 5:6278–6289, 2012.

[13] Neil V. Rees and Richard G. Compton. Carbon-free energy: a review of ammonia- and hydrazine-based electrochemical fuel cells. *Energy and Environmental Science*, 4(4):1255–1260, 2011.

[14] James Larminie and Andrew Dicks. *Fuel Cell Systems Explained.* John Wiley & Sons Ltd, the Atrium, Southern Gate, Chichester, West Sussex, PO19 8SQ, England, 2003.

[15] Rong Lan, Shanwen Tao, and John T. S. Irvine. A direct urea fuel cell - power from fertiliser and waste. *Energy Environ. Sci.*, 3:438–441, 2010.

[16] Rong Lan, Xiaoxiang Xu, Shanwen Tao, and John T.S. Irvine. A fuel cell operating between room temperature and 250°C based on a new phosphoric acid based composite electrolyte. *Journal of Power Sources*, 195(20):6983 – 6987, 2010.

[17] Rong Lan and Shanwen Tao. Direct ammonia alkaline anion-exchange membrane fuel cells. *Electrochemical and Solid-State Letters*, 13:B83–B86, 2010.

[18] K. D. Kreuer. Proton-conducting oxides. *Annual Review of Materials Research*, 33(1):333 – 359, 2003.

[19] Meng Ni, Michael K. H. Leung, and Dennis Y. C. Leung. Ammonia-fed solid oxide fuel cells for power generation - a review. *International Journal of Energy Research*, 33:943–959, 2009.

[20] Kui Xie, Ruiqiang Yan, Guangyao Meng, and Xingqin Liu. Direct ammonia proton-conducting solid oxide fuel cells prepared by a modified suspension spray. *Ionics*, 15:115–119, 2009.

[21] S.J.C. Cleghorn, X. Ren, T.E. Springer, M.S. Wilson, C. Zawodzinski, T.A. Zawodzinski, and S. Gottesfeld. PEM fuel cells for transportation and stationary power generation applications. *International Journal of Hydrogen Energy*, 22(12):1137 – 1144, 1997.

[22] Michael C.J. Bradford, Paul E. Fanning, and M.Albert Vannice. Kinetics of NH3 decomposition over well dispersed Ru. *Journal of Catalysis*, 172(2):479 – 484, 1997.

[23] D.A. Hansgen, D.G. Vlachos, and J.G. Chen. Using first principles to predict bimetallic catalysts for the ammonia decomposition reaction. *Nature Chemistry*, 2:484–489, 2009.

[24] Egawa, Nishida T, Naito S, and Tamaro K. Ammonia decomposition on (1 1 10) and (0 0 1) surfaces of ruthenium. *J. Chem. Soc., Faraday Trans.*, 80:1595–1604, 1984.

[25] Astrid Boisen, Soren Dahl, Jens K. Norskov, and Claus Hviid Christensen. Why the optimal ammonia synthesis catalyst is not the optimal ammonia decomposition catalyst. *Journal of Catalysis*, 230(2):309 – 312, 2005.

[26] K Tamaru. Adsorption measurements during the decomposition of ammonia on a tungsten catalyst. *Transactions of the Faraday Society*, 57:1410–1415, 1960.

[27] K Matsushita and R Hansen. Adsorptiopn and decomposition of ammonia on a polycrystalline tungsten filament. *The Journal of Chemical Physics*, 52:4877–4889, 1970.

[28] L.R Danielson, M.J Dresser, E.E Donaldson, and J.T Dickinson. Adsorption and desorption of ammonia, hydrogen, and nitrogen on ruthenium (0001). *Surface Science*, 71(3):599 – 614, 1978.

[29] W. Tsai and W. H. Weinberg. Steady-state decomposition of ammonia on the ruthenium(001) surface. *The Journal of Physical Chemistry*, 91(20):5302–5307, 1987.

[30] J.C. Ganley, F.S. Thomas, E.G. Seebauer, and R.I. Masel. A priori catalytic activity correlations: The difficult case of hydrogen production from ammonia. *Catalysis Letters*, 96:117–122, 2004.

[31] Robert W. McCabe. Kinetics of ammonia decomposition on nickel. *Journal of Catalysis*, 79(2):445 – 450, 1983.

[32] SR Logan and C Kemball. The catalytic decomposition of ammonia on evaporated metal films. *Transactions of the Faraday Society*, 56:144–153, 1960.

[33] Akiro Amano and Hugh Taylor. The decomposition of ammonia on ruthenium, rhodium and palladium catalysts supported on alumina. *Journal of the American Chemical Society*, 76(16):4201–4204, 1954.

[34] T.V. Choudhary, A.K. Santra, C. Sivadinarayana, B.K. Min, C.-W. Yi, K. Davis, and D.W. Goodman. Ammonia decomposition on Ir(100): From ultrahigh vacuum to elevated pressures. *Catalysis Letters*, 77:1–5, 2001.

[35] W.L. Guthrie, J.D. Sokol, and G.A. Somorjai. The decomposition of ammonia on the flat (111) and stepped (557) platinum crystal surfaces. *Surface Science*, 109(2):390 – 418, 1981.

[36] O. Hinrichsen, F. Rosowski, M. Muhler, and G. Ertl. The microkinetics of ammonia synthesis catalyzed by cesium-promoted supported ruthenium. *Chemical Engineering Science*, 51(10):1683 – 1690, 1996.

[37] S. R. Deshmukh, A. B. Mhadeshwar, and D. G. Vlachos. Microreactor modeling for hydrogen production from ammonia decomposition on ruthenium. *Industrial & Engineering Chemistry Research*, 43(12):2986–2999, 2004.

[38] Srinivas Appari, Vinod M. Janardhanan, Sreenivas Jayanti, Lubow Maier, Steffen Tischer, and Olaf Deutschmann. Micro-kinetic modeling of NH3 decomposition on Ni and its application to solid oxide fuel cells. *Chemical Engineering Science*, 66(21):5184 – 5191, 2011.

[39] A. J. B. Robertson. The early history of catalysis. *Platinum Metals Review*, 19:64–69, 1975.

[40] George Papapolymerou and Vasilis Bontozoglou. Decomposition of NH3 on Pd and Ir comparison with Pt and Rh. *Journal of Molecular Catalysis A: Chemical*, 120(1-3):165 – 171, 1997.

[41] T.V. Choudhary, C. Sivadinarayana, and D.W. Goodman. Catalytic ammonia decomposition: COx-free hydrogen production for fuel cell applications. *Catalysis Letters*, 72:197–201, 2001.

[42] S.F. Yin, B.Q. Xu, X.P. Zhou, and C.T. Au. A mini-review on ammonia decomposition catalysts for on-site generation of hydrogen for fuel cell applications. *Applied Catalysis A: General*, 277(1-2):1 – 9, 2004.

[43] Claus J. H. Jacobsen, Soren Dahl, Bjerne S. Clausen, Sune Bahn, Ashildur Logadottir, and Jens K. Norskov. Catalyst design by interpolation in the periodic table: Bimetallic ammonia synthesis catalysts. *Journal of the American Chemical Society*, 123(34):8404–8405, 2001.

[44] Hai-Long Jiang and Qiang Xu. Recent progress in synergistic catalysis over heterometallic nanoparticles. *Journal of Materials Chemistry*, 21:13705–13725, 2011.

[45] Beatriz Roldan Cuenya. Synthesis and catalytic properties of metal nanoparticles: Size, shape, support, composition, and oxidation state effects. *Thin Solid Films*, 518(12):3127 – 3150, 2010.

[46] John H. Sinfelt. *Bimetallic Catalysts*. John Wiley & Sons Ltd, Baffins Lane, Chichester, West Sussex, PO19 1UD, England, 1983.

[47] Riccardo Ferrando, Julias Jellinek, and Roy Johnston. Nanoalloys: From theory to applications of alloy clusters and nanoparticles. *Chemical Reviews*, 108:846–904, 2008.

[48] S. Huang, S. Chang, C. Lin, C. Chen, and C. Yeh. Promotion of the electrochemical activity of a bimetallic platinum-ruthenium catalyst by oxidation-induced segregation. *Journal of Physical Chemistry: B*, 110:23300–23305, 2006.

[49] Yuguang Ma and Perla B. Balbuena. Pt surface segregation in bimetallic Pt3M alloys: A density functional theory study. *Surface Science*, 602(1):107 – 113, 2008.

[50] A. Naitabdi, L. K. Ono, F. Behafarid, and B. Roldan Cuenya. Thermal stability and segregation processes in self-assembled size-selected AuxFe1-x nanoparticles deposited on TiO2(110): composition effects. *The Journal of Physical Chemistry C*, 113(4):1433–1446, 2009.

[51] Guofeng Wang, M.A. Van Hove, P.N. Ross, and M.I. Baskes. Quantitative prediction of surface segregation in bimetallic Pt-M alloy nanoparticles (M=Ni;Re;Mo). *Progress in Surface Science*, 79(1):28 – 45, 2005.

[52] Claus J.H. Jacobsen, Soren Dahl, Astrid Boisen, Bjerne S. Clausen, Henrik Topsoe, Ashildur Logadottir, and Jens K. Norskov. Optimal catalyst curves: Connecting density functional theory calculations with industrial reactor design and catalyst selection. *Journal of Catalysis*, 205(2):382 – 387, 2002.

[53] Jian Ji, Xuezhi Duan, Gang Qian, Xinggui Zhou, Gangsheng Tong, and Weikang Yuan. Towards an efficient como/gamma-alumina catalyst using metal amine metallate as an active phas precursor: enhanced hydrogen production by ammonia decomposition. *International Journal of Hydrogen Energy*, 39:12490–12498, 2014.

[54] Xuezhi Duan, Gang Qian, Xinggui Zhou, De Chen, and Weikang Yuan. MCM-41 supported Co-Mo bimetallic catalysts for enhanced hydrogen production by ammonia decomposition. *Chemical Engineering Journal*, 207-208:103–108, 2012.

[55] A.S Chellappa, C.M Fischer, and W.J Thomson. Ammonia decomposition kinetics over Ni-Pt/Al2O3 for PEM fuel cell applications. *Applied Catalysis A: General*, 227(1-2):231 – 240, 2002.

[56] Changhai Liang, Wenzhen Li, Zhaobin Wei, Qin Xin, and Can Li. Catalytic decomposition of ammonia over nitrided monx/r-al2o3 and nimony/r-al2o3 catalysts. *Industrial & Engineering Chemistry Research*, 39:3694–3697, 2000.

[57] S B Simonsen, D Chakraborty, I Chorkendorff, and S Dahl. Alloyed ni-fe nanoparticles as catalysts for nh3 decomposition. *Applied Catalysis A: General*, 447-448:22–31, 2012.

[58] Jian Zhang, Jens-Oliver MuÌller, Weiqing Zheng, Di Wang, Dangsheng Su, and Robert Schlogl. Individual Fe-Co alloy nanoparticles on carbon nanotubes: structural and catalytic properties. *Nano Letters*, 8(9):2738–2743, 2008.

[59] Danielle A. Hansgen, Lisa M. Thomanek, Jingguang G. Chen, and Dionisios G. Vlachos. Experimental and theoretical studies of ammonia decomposition activity on Fe-Pt, Co-Pt, and Cu-Pt bimetallic surfaces. *The Journal of Chemical Physics*, 134(18):184701, 2011.

[60] K Tedsree, T Li, S Jones, CWA Chan, KMK Yu, PAJ Bagot, EA Marquis, GDW Smith, and SCE Tsang. Hydrogen production from formic acid decomposition at room temperature using a Ag-Pd core-shell nanocatalyst. *Nature Nanotechnology*, 6:302–307, 2011.

[61] Yunjie Huang, Xiaochun Zhou, Min Yin, Changpeng Liu, and Wei Xing. Novel PdAu@Au/C core-shell catalyst: Superior activity and selectivity in formic acid decomposition for hydrogen generation. *Chemistry of Materials*, 22(18):5122–5128, 2010.

[62] Danielle A. Hansgen, Dionisios G. Vlachos, and Jingguang G. Chen. Ammonia decomposition activity on monolayer Ni supported on Ru, Pt and WC substrates. *Surface Science*, 605(23-24):2055 – 2060, 2011.

[63] Jingguang G. Chen, Carl A. Menning, and Michael B. Zellner. Monolayer bimetallic surfaces: Experimental and theoretical studies of trends in electronic and chemical properties. *Surface Science Reports*, 63(5):201 – 254, 2008.

[64] Shuzo Murata and Ken-Ichi Aika. Preparation and characterization of chlorine-free ruthenium catalysts and the promoter effect in ammonia synthesis.: 1. an alumina-supported ruthenium catalyst. *Journal of Catalysis*, 136(1):110 – 117, 1992.

[65] J. R. Hook and H. E. Hall. *Solid State Physics*. John Wiley & Sons Ltd, Baffins Lane, Chichester, West Sussex, PO19 1UD, England, 1991.

[66] D.G Loffler and L.D Schmidt. Kinetics of NH3 decomposition on single crystal planes of Pt. *Surface Science*, 59(1):195 – 204, 1976.

[67] Hans L. Skriver. Crystal structure from one-electron theory. *Phys. Rev. B*, 31:1909–1923, Feb 1985.

[68] T. H. Rod, A. Logadottir, and J. K. Norskov. Ammonia synthesis at low temperatures. *The Journal of Chemical Physics*, 112(12):5343–5347, 2000.

[69] D Rosenthal. Functional surfaces in heterogeneous catalysis: A short review. *Physica Status Solidi A*, 208:1217–1222, 2011.

[70] Claus J.H Jacobsen, Soren Dahl, Poul L Hansen, Eric Tornqvist, Lone Jensen, Henrik Topsoe, Dorthe V Prip, Pernille B Moenshaug, and Ib Chorkendorff. Structure sensitivity of supported ruthenium catalysts for ammonia synthesis. *Journal of Molecular Catalysis A: Chemical*, 163(1-2):19 – 26, 2000.

[71] F. Garcia-Garcia, A. Guerrero-Ruiz, and I. Rodriguez-Ramos. Role of B5-type sites in Ru catalysts used for the NH3 decomposition reaction. *Topics in Catalysis*, 52:758–764, 2009.

[72] Xuezhi Duan, Gang Qian, Yan Liu, Jian Ji, Xinggui Zhou, De Chen, and Weikang Yuan. Structure sensitivity of ammonia decomposition over Ni catalysts: A computational and experimental study. *Fuel Processing Technology*, 108(0):112–117, 2012.

[73] Hongyu Sun, Yanlong Yu, and Mashkoor Ahmad. Shape-controlled synthesis of metal nanocrystals - multiwalled carbon nanotubes hybrid structures via electrodeposition. *Materials Letters*, 65:3482 – 3485, 2011.

[74] Shuang-Feng Yin, Qin-Hui Zhang, Bo-Qing Xu, Wen-Xia Zhu, Ching-Fai Ng, and Chak-Tong Au. Investigation on the catalysis of COx-free hydrogen generation from ammonia. *Journal of Catalysis*, 224(2):384 – 396, 2004.

[75] Weiping Deng, Xuesong Tan, Wenhao Fang, Qinghong Zhang, and Ye Wang. Conversion of cellulose into sorbitol over carbon nanotube-supported ruthenium catalyst. *Catalysis Letters*, 133:167–174, 2009.

[76] Shujing Guo, Xiulian Pan, Haili Gao, Zhiqiang Yang, Jijun Zhao, and Xinhe Bao. Probing the electronic effect of carbon nanotubes in catalysis: NH3 synthesis with Ru nanoparticles. *Chemistry - European Journal*, 16(18):5379–5384, 2010.

[77] F.R. Garcia-Garcia, J. Alvarez-Rodriguez, I. Rodriguez-Ramos, and A. Guerrero-Ruiz. The use of carbon nanotubes with and without nitrogen doping as support for ruthenium catalysts in the ammonia decomposition reaction. *Carbon*, 48(1):267 – 276, 2010.

[78] Xiaomin Yang, Xiuna Wang, and Jieshan Qiu. Aerobic oxidation of alcohols over carbon nanotube-supported Ru catalysts assembled at the interfaces of emulsion droplets. *Applied Catalysis A: General*, pages 131–137, 2010.

[79] L. Li, Z.H. Zhu, G.Q. Lu, Z.F. Yan, and S.Z. Qiao. Catalytic ammonia decomposition over CMK-3 supported Ru catalysts: Effects of surface treatments of supports. *Carbon*, 45(1):11 – 20, 2007.

[80] Philippe Serp, Massimiliano Corrias, and Philippe Kalck. Carbon nanotubes and nanofibers in catalysis. *Applied Catalysis A: General*, 253(2):337 – 358, 2003.

[81] Shuang-Feng Yin, Bo-Qing Xu, Shui-Ju Wang, and Chak-Tong Au. Nanosized Ru on high-surface-area superbasic ZrO2-KOH for efficient generation of hydrogen via ammonia decomposition. *Applied Catalysis A: General*, 301(2):202 – 210, 2006.

[82] Dirk M. Guldi, G. M. A. Rahman, Francesco Zerbetto, and Maurizio Prato. Carbon nanotubes in electron donor-acceptor nanocomposites. *Acc. Chem. Res.*, 38:871–878, 2005.

[83] Kurt K Kolasinski and Kurt W Kolasinski. *Surface Science: Foundations of Catalysis and Nanoscience*. Wiley, 2012.

[84] S.F. Yin, B.Q. Xu, S.J. Wang, C.F. Ng, and C.T. Au. Magnesia-carbon nanotubes (MgO-CNTs) nanocomposite: Novel support of Ru catalyst for the generation of COx-free hydrogen from ammonia. *Catalysis Letters*, 96:113–116, 2004.

[85] Asbjarn Klerke, Saren Klitgaard, and Rasmus Fehrmann. Catalytic ammonia decomposition over ruthenium nanoparticles supported on nano-titanates. *Catalysis Letters*, 130:541–546, 2009.

[86] M Campanati, G Fornasari, and A Vaccari. Fundamentals in the preparation of heterogeneous catalysts. *Catalysis Today*, 77(4):299 – 314, 2003.

[87] Yena Kim, Jong Wook Hong, Young Wook Lee, Minjung Kim, Dongheun Kim, Wan Soo Yun, and Sang Woo Han. Synthesis of AuPt heteronanostructures with enhanced electrocatalytic activity toward oxygen reduction. *Angewandte Chemie International Edition*, 49(52):10197–10201, 2010.

[88] D.J. Duvenhage and N.J. Coville. Fe:Co/TiO2 bimetallic catalysts for the Fischer-Tropsch reaction: Part 4: A study of nitrate and carbonyl derived FT catalysts. *Journal of Molecular Catalysis A: Chemical*, 235:230 – 239, 2005.

[89] Weiqing Zheng, Jian Zhang, Bo Zhu, Raoul Blume, Yonglai Zhang, Klaus Schlichte, Robert Schlogl, Ferdi Schuth, and Dang Sheng Su. Structure-Function Correlations for Ru/CNT in the Catalytic Decomposition of Ammonia. *ChemSusChem*, 3:226–230, 2010.

[90] Weiqing Zheng, Jian Zhang, Hengyong Xu, and Wenzhao Li. NH3 decomposition kinetics on supported Ru clusters: morphology and particle size effect. *Catalysis Letters*, 119:311–318, 2007. 10.1007/s10562-007-9237-z.

[91] Kazujuki Nakai and Kaori Nakamura. Pulse chemisorption measurement cat-app-002. Technical report, Bel-Cat, 2003.

[92] Jian Zhang, Hengyong Xu, and Wenzhao Li. Kinetic study of NH3 decomposition over Ni nanoparticles: The role of La promoter, structure sensitivity and compensation effect. *Applied Catalysis A: General*, 296(2):257 – 267, 2005.

[93] A L Patterson. The Scherrer Formula for X-Ray Particle Size Determination. *Physical Review*, 56:978–982, 1939.

[94] Michael Heemeier, Anders F. Carlsson, Matthias Naschitzki, Martin Schmal, Marcus Baumer, and Hans-Joachim Freund. Preparation and characterization of a model bimetallic catalyst: Co-Pd nanoparticles supported on Al2O3. *Angewandte Chemie International Edition*, 41(21):4073–4076, 2002.

[95] Wioletta Rarog-Pilecka, Dariusz Szmigiel, Zbigniew Kowalczyk, Slawomir Jodzis, and Jerzy Zielinski. Ammonia decomposition over the carbon-based ruthenium catalyst promoted with barium or cesium. *Journal of Catalysis*, 218(2):465 – 469, 2003.

[96] Wioletta Rarog-Pilecka, Elzbieta Miskiewicz, Slawomir Jodzis, Jan Petryk, Dariusz Lomot, Zbigniew Kaszkur, Zbigniew Karpinkski, and Zbigniew Kowalczyk. Carbon-supported ruthenium catalysts for NH3 synthesis doped with caesium nitrate: Activation process, working state of Cs-Ru/C. *Journal of Catalysis*, 239:313–325, 2006.

[97] John W. Phair and Richard Donelson. Developments and design of novel (non-palladium-based) metal membranes for hydrogen separation. *Industrial & Engineering Chemistry Research*, 45(16):5657–5674, 2006.

[98] Robert E. Buxbaum and Andrew B. Kinney. Hydrogen transport through tubular membranes of palladium-coated tantalum and niobium. *Industrial & Engineering Chemistry Research*, 35(2):530–537, 1996.

[99] Nathan W. Ockwig and Tina M. Nenoff. Membranes for hydrogen separation. *Chemical Reviews*, 107(10):4078–4110, 2007.

[100] Angelo Basile. Hydrogen Production Using Pd-based Membrane Reactors for Fuel Cells. *Topics in Catalysis*, 51:107–122, 2008.

[101] M.D. Dolan. Non-Pd BCC alloy membranes for industrial hydrogen separation. *Journal of Membrane Science*, 362(1-2):12 – 28, 2010.

[102] P Cotterill. The hydrogen embrittlement of metals. *Progress in Materials Science*, 9(4):205 – 301, 1961.

[103] A.L. Mejdell, M. Jondahl, T.A. Peters, R. Bredesen, and H.J. Venvik. Effects of CO and CO2 on hydrogen permeation through a 3micron Pd/Ag membrane employed in a microchannel membrane configuration. *Separation and Purification Technology*, 68(2):178 – 184, 2009.

[104] Jacopo Catalano, Marco Giacinti Baschetti, and Giulio C. Sarti. Influence of water vapor on hydrogen permeation through 2.5 micron Pd-Ag membranes. *International Journal of Hydrogen Energy*, 36(14):8658 – 8673, 2011.

[105] Sameer H. Israni, Balamurali Krishna R. Nair, and Michael P. Harold. Hydrogen generation and purification in a composite Pd hollow fiber membrane reactor: Experiments and modeling. *Catalysis Today*, 139:299 – 311, 2009.

[106] Gang Li, Masakoto Kanezashi, and Toshinori Tsuru. Highly enhanced ammonia decomposition in a bimodal catalytic membrane reactor for COx-free hydrogen production. *Catalysis Communications*, 15(1):60 – 63, 2011.

[107] Adele Brunetti, Giuseppe Barbieri, and Enrico Drioli. A PEMFC and H2 membrane purification integrated plant. *Chemical Engineering and Processing*, 47:1081–1089, 2008.

[108] J Zhang, H Xu, and W Li. High-purity COx-free H2 generation from NH3 via the ultra permeable and highly selective Pd membranes. *Journal of Membrane Science*, 277:85–93, 2006.

[109] F R Garcia-Garcia, Yi Hua Ma, I Rodriguez-Ramos, and A Guerrero-Ruiz. High purity hydrogen production by low temperature catalytic ammonia decomposition in a multifunctional membrane reactor. *Catalysis Communications*, 9:482–486, 2008.

[110] Cole palmer chemical compatibility database, [http://www.coleparmer.co.uk/chemical-resistance].

[111] Air liquide gas encyclopedia, [http://encyclopedia.airliquide.com/encyclopedia.asp].

[112] H. Scott Fogler. *Elements of Chemical Reaction Engineering.* Prentice Hall International Series, 1999.

[113] Kirk Snavely and Bala Subramaniam. Thermal conductivity detector analysis of hydrogen using helium carier gas and HayeSep D columns. *Journal of Chromatographic Science*, 36:191–196, 1998.

[114] Joon Pahk. Summary of Rules for Error Propagation.

[115] I Rossetti, F Mangiarini, and L Forni. Promoters state and catalyst activation during ammonia synthesis over ru/c. *Applied Catalysis A: General*, 323:219–225, 2007.

[116] YV Larichev, DA Shlyapin, PG Tsyrul'nikov, and VI Bukhtiyarov. Comparative study of rubidium and cesium as promoters in carbon-supported ruthenium catalysts for ammonia synthesis. *Catalysis Letters*, 120:204–209, 2008.

[117] Rasmus Sorensen, Asbjorn Klerke, Ulrich Quaade, Soren Jensen, Ole Hansen, and Claus Christensen. Promoted Ru on high-surface area graphite for efficient miniaturized production of hydrogen from ammonia. *Catalysis Letters*, 112:77–81, 2006. 10.1007/s10562-006-0167-y.

[118] Alfred K Hill and Laura Torrente-Murciano. In-situ H2 production via low temperature decomposition of ammonia: Insights into the role of cesium as a promoter. *International Journal of Hydrogen Energy*, 39:7646–7654, 2014.

[119] Xin Zhang and Kwong-Yu Chan. Water-in-oil synthesis of platinum-ruthenium nanoparticles, their characterisation and electrocatalytic properties. *Chemistry of Materials*, 15:451–459, 2003.

[120] S.F. Yin, B.Q. Xu, W.X. Zhu, C.F. Ng, X.P. Zhou, and C.T. Au. Carbon nanotubes-supported Ru catalyst for the generation of COx-free hydrogen from ammonia. *Catalysis Today*, 93-95(0):27 – 38, 2004.

[121] De-Chin Huang, Cheng-Hong Jiang, Feng-Jiin Liu, Yu-Chi Cheng, Yen-Cho Chen, and Kan-Lin Hsueh. Preparation of Ru-Cs catalyst and its application on hydrogen production by ammonia decomposition. *International Journal of Hydrogen Energy*, 38:3233–3240, 2013.

[122] B. Fastrup. On the interaction of n2 and h2 with ru catalyst surfaces. *Catalysis Letters*, 48:111–119, 1997.

[123] R Andrews, D Jacques, D Qian, and E C Dickey. Purification and structural annealing of multiwalled carbon nanotubes at graphitization temperatures. *Carbon*, 39:1681–1687, 2001.

[124] D Mattia, M P Rossi, B M Kim, G Korneva, H H Bau, and Y Gogotsi. Effect of graphitization on the wettability and electrical conductivity of cvd-carbon nanotubes and films. *Journal of Physical Chemistry: B*, 110:9850–9855, 2006.

[125] A C Ferrari and J Robertson. Interpretation of raman spectra of disordered and amorphous carbon. *Physical Review B*, 61:14095–14107, 2000.

[126] D W Jordan and P Smith. *Mathematical Techniques*. Oxford University Press, 1999.

[127] Emma Davies. Critical thinking - endangered elements. *Chemistry World*, pages 50–54, Jan 2011.

[128] British Geological Survey. Risk list 2012 - an update to the supply risk index for elements or element groups that are of economic value. 2012.

[129] Philip Nuss and Matthew J Eckelman. Life cycle assessmentof metals: A scientific synthesis. *PLoS One*, 9(7), 2014.

[130] http://mineralprices.com/ [accessed 04-10-2014].

[131] L Li, Z H Zhu, Z F Yan, G Q Lu, and L Rintoul. Catalytic ammonia decomposition over Ru/carbon catalysts: The importance of the structure of carbon support. *Applied Catalysis A: General*, 320:166–172, 2007.

[132] Lei Zhang, Adri N.C. van Laak, Petra E. de Jongh, and Krijn P. de Jong. *Zeolites and Catalysis Synthesis, Reactions and Applications*. Wiley-VCH, 2010.

[133] Z. Lendzion-Bielun, R. Pelka, and W. Arabczyk. Study of the kinetics of ammonia synthesis and decomposition on iron and cobalt catalysts. *Catalysis Letters*, 129:119–123, 2009.

[134] Jinshan Lu. Effect of surface modifications on the decoration of multi-walled carbon nanotubes with ruthenium nanoparticles. *Carbon*, 45:1599–1605, 2007.

[135] A Gorschinkski, G Khelashvili, D Schild, W Habicht, R Brand, M Ghafari, H Bonnemann, E Dinjus, and S Behrens. A simple aminoalkyl siloxane-mediated route to functional magnetic metal nanoparticles and magnetic nanocomposites. *Journal of Materials Chemistry*, 19:8829–8838, 2009.

[136] B Hammer and JK Norskov. Theoretical surface science and catalysis - calculations and concepts. *Advances in Catalysis*, 45:71–129, 2000.

[137] J Lin, L Zhang, Z Wang, J Ni, R Wang, and K Wei. The effect of ag as a promoter for ru/ceo2 catalysts in ammonia synthesis. *Journal of Molecular Catalysis A: Chemical*, 366:375–379, 2013.

[138] IFA. Fertilizers and climate change, July 2009.

[139] S Chiuta, R C Everson, H W J P Neomagus, P van der Gryp, and D G Bessarabov. Reactor technology options for distributed hydrogen generation via ammonia decomposition: a review. *International Journal of Hydrogen Energy*, 38:14968–14991, 2013.

[140] Gro Harlem Brundtland. *Our Common Future: The World Commission on Environment and Development*. Oxford University Press, 1987.

[141] IPCC. Ipcc fourth assessment report: Climate change 2007, 7.4.3.2 fertilizer manufacture, 2007.

[142] Arnold J Bloom. The hydrogen economy, May 2012.

[143] Rong Lan, John T. S. Irvine, and Shanwen Tao. Synthesis of ammonia directly from air and water at ambient temperature and pressure. *Scientific Reports*, 3:1145, 2013.

[144] Stuart Lichte, Baochen Cui, Baohui Wang, Fang-Fang Li, Jason Lau, and Shuzi Liu. Ammonia synthesis by N2 and steam electrolysis in molten hydroxide suspensions of nanoscale Fe2O3. *Science*, 345:637–640, 2014.

[145] J D Pritchard. Hpa compendium of chemical hazards - ammonia version 4. Technical report, Health Protection Agency, 2011.

[146] Nissan Great Britain. Nissan great britain (2014) http://www.nissan.co.uk/gb/en/vehicle/electric-vehicles/leaf.html accessed on 14-09-2014, 2014.

[147] S Armenise, E Garcia-Bordeje, J Valverde, E Romeo, and A Monzon. A Langmuir-Hinshelwood approach to the kinetic modelling of catalytic ammonia decomposition in an integral reactor. *Physical Chemistry Chemical Physics*, 15:12104–12117, 2013.

[148] M.E.E. Abashar, Y.S. Al-Sughair, and I.S. Al-Mutaz. Investigation of low temperature decomposition of ammonia using spatially patterned catalytic membrane reactors. *Applied Catalysis A: General*, 236(1-2):35 – 53, 2002.

[149] US Department of Energy. Technical system targets: Onboard hydrogen storage for light-duty fuel cell vehicles, 2014.

[150] Shashi Singh. New KBR Ammonia Synthesis Loop Revamp Technology Improves Plant Energy Efficiency. Technical report, KBR, 2009.

[151] Jeffrey Ralph Bartels. A feasibility study of implementing an ammonia economy. Master's thesis, Iowa State University, 2008.

[152] Biruh Shimekit and Hilmi Mukhtar. *Advances in Natural Gas Technology. Chapter 9: Natural Gas Purification Technologies - Major Advances for CO2 Separation and Future Directions.* InTech, 2012.

[153] Xunmin Ou and Xiliang Zhang. Life-cycle analyses of energy consumption and ghg emissions of natural gas-based alternative vehicle fuels in china. *Journal of Energy*, 2013:1–8, 2013.

[154] Johanna Ivy. Summary of electrolytic hydrogen production, September 2004.

[155] Marcelo Carmo, David L Fritz, Jurgen Mergel, and Detlef Stolten. A comprehensive review on PEM water electrolysis. *International Journal of Hydrogen Energy*, 38:4901–4934, 2013.

[156] Peter Froehlich. A sustainable approach to the supply of nitrogen. Technical report, Parker Balston (Parker Hannifin Corporation), 2013.

[157] Don W. Green, editor. *Perry's Chemical Engineers' Handbook*. McGraw Hill, 1997.

[158] Department of Energy and Climate Change (DECC). UK Renewable Energy Road Map 2013. 2013.

[159] Sabena Khan and Mary Gregory. Sub-national road transport fuel consumption statistics. *Department of Energy and Climate Change*, 2014.

[160] World Nuclear Association. World nuclear association - heat values of various fuels, March 2010.

[161] John Fyffe. The reports of my death have been greatly exaggerated, an internal combustion engines story. *Stanford Energy Club*, 4, 2014.

[162] Stefan Schwietzke, W. Michael Griffen, H. Scott Matthews, and Lori M. P. Bruhwiler. Global bottom-up fossil fuel fugitive methane and ethane emissions inventory for atmospheric modeling. *ACS Sustainable Chemistry and Engineering*, 2:1992–2001, 2014.

[163] BP Statistical Review of World Energy June 2014 Url: bp.com/statisticalreview.

[164] A review of the UK innovation system for low carbon road transport technologies. A report for the Department of Transport. Technical report, E4Tech, 2007.

[165] Julia King. *The King Review of low-carbon cars.* HM Treasury, 2007.

[166] Luis F Razon. Life cycle analysis of an alternative to the haber-bosch process: Non-renewable energy usage and global warming potential of liquid ammonia from cyanobacteria. *Environmental Progress and Sustainable Energy*, 33:618–624, 2014.

[167] 2030 framework for climate and energy policies. directorate general for climate action, october 2014.

# Appendix I - TEM Images used for Generation of Particle Size Histograms

3.0 wt.% ruthenium, 4 wt.% cesium on commercial CNTs

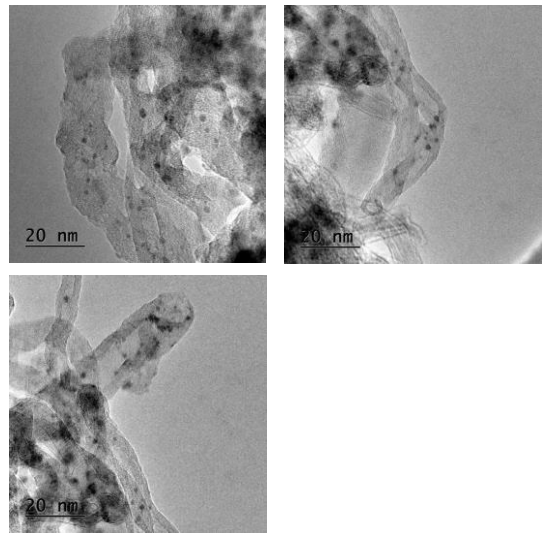


4.2 wt.% ruthenium, 4 wt.% cesium on commercial CNTs

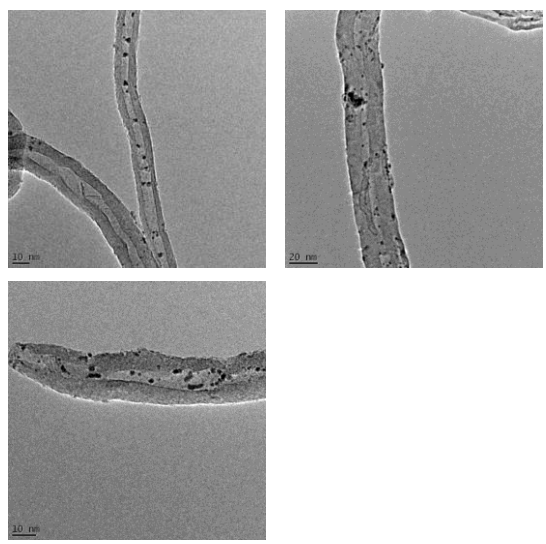

7.0 wt.% ruthenium, 4 wt.% cesium on commercial CNTs

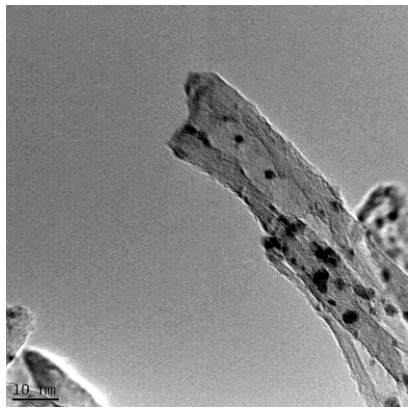


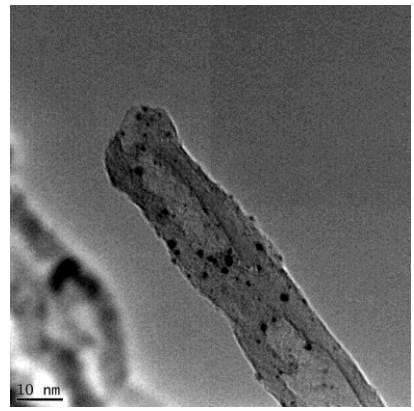


10.0 wt.% ruthenium, 4 wt.% cesium on commercial CNTs

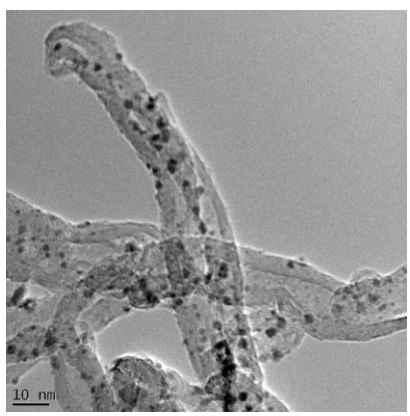


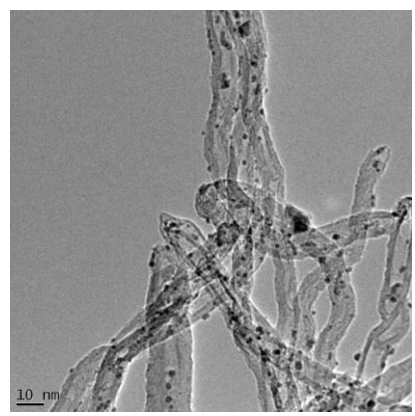

13.2 wt.% ruthenium, 4 wt.% cesium on commercial CNTs

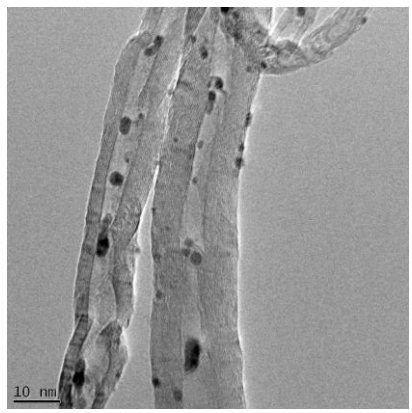


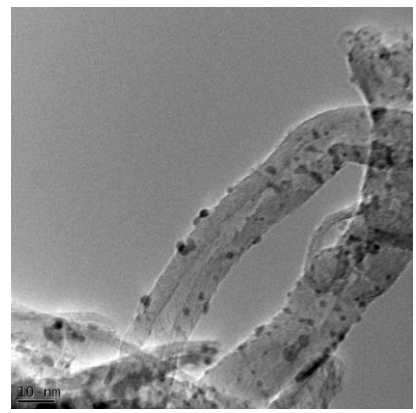


7.0 wt.% ruthenium, 0 wt.% cesium on commercial CNTs

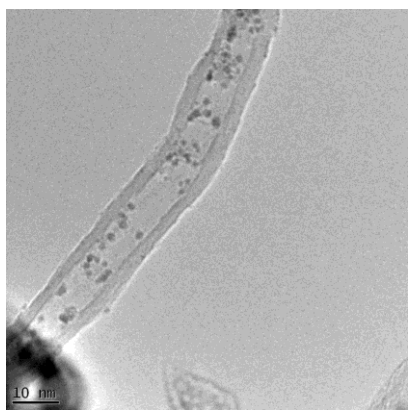


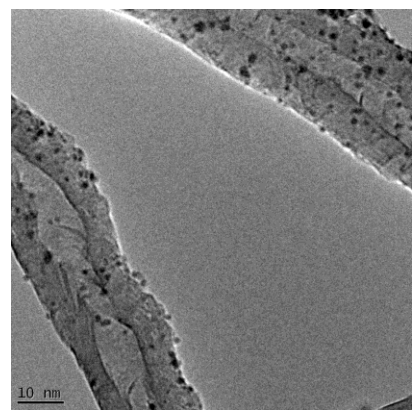

7.0 wt.% ruthenium, 7 wt.% cesium on commercial CNTs

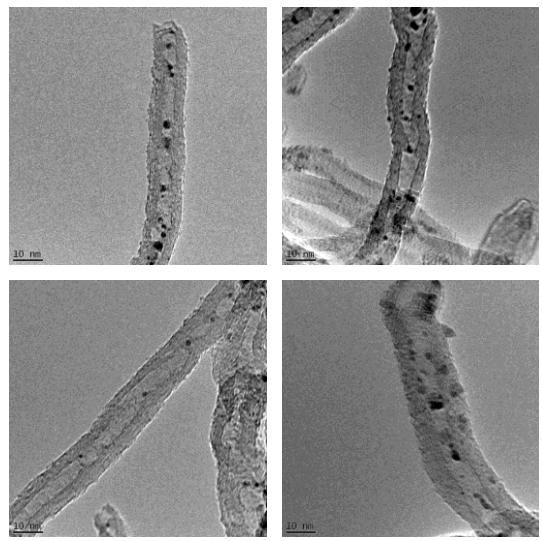

7.0 wt.% ruthenium, 10 wt.% cesium on commercial CNTs

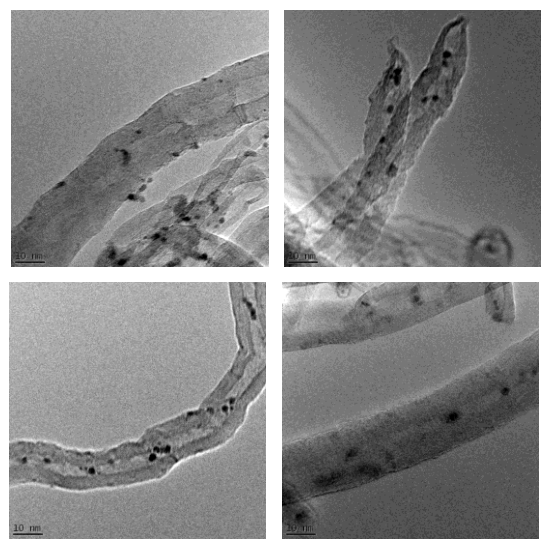

7.0 wt.% ruthenium, 20 wt.% cesium on commercial CNTs

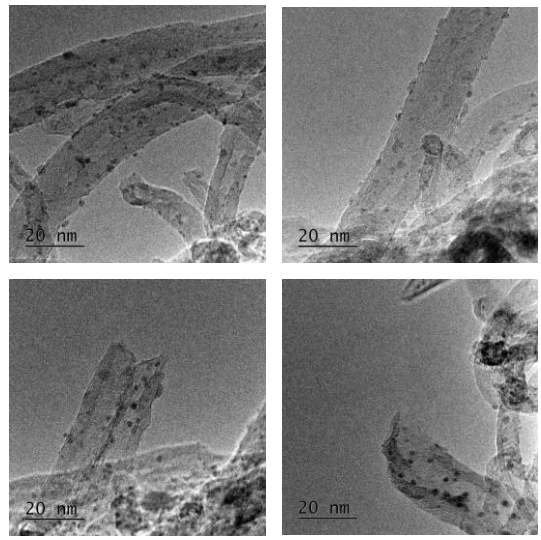


7.0 wt.% ruthenium, 30 wt.% cesium on commercial CNTs

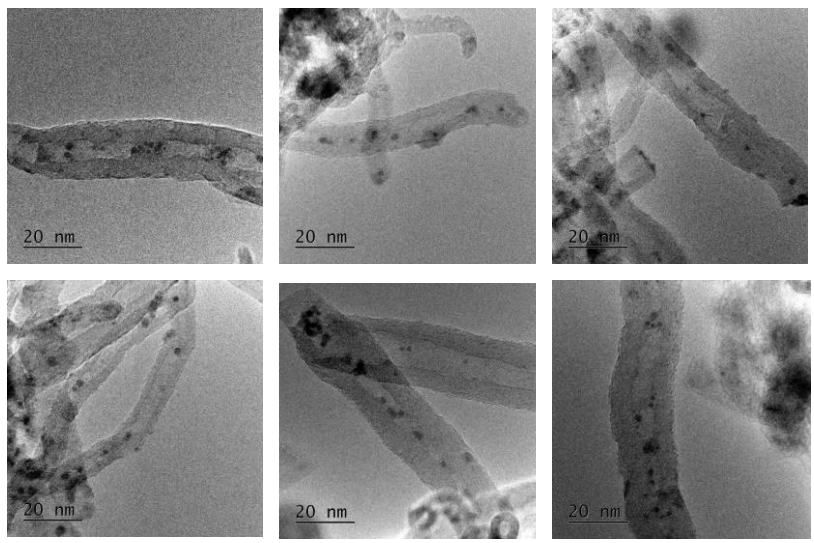

7.0 wt.% ruthenium, 0 wt.% cesium on graphitised CNTs (2073 K)

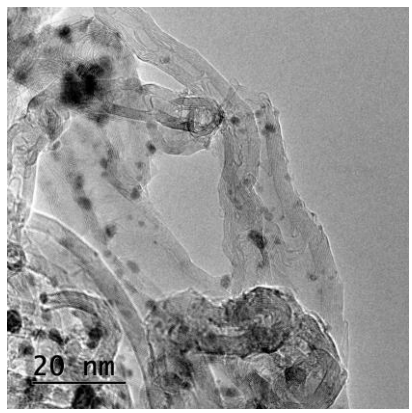


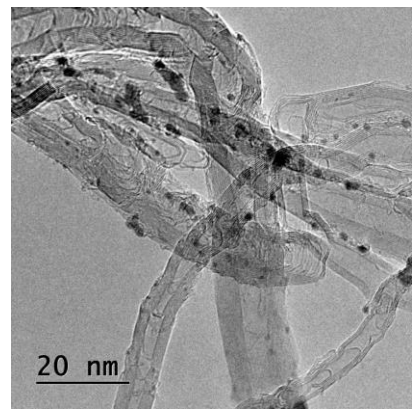


7.0 wt.% ruthenium, 4 wt.% cesium on graphitised CNTs (2073 K)

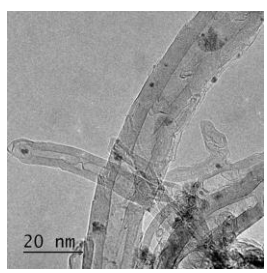


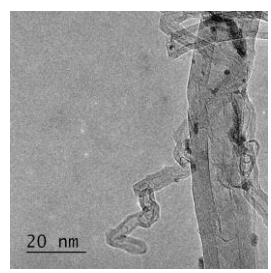


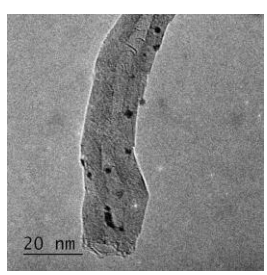


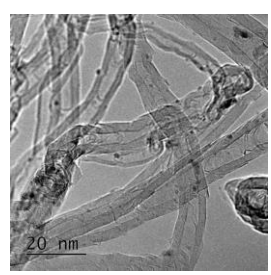

7.0 wt.% ruthenium, 10 wt.% cesium on graphitised CNTs (2073 K)

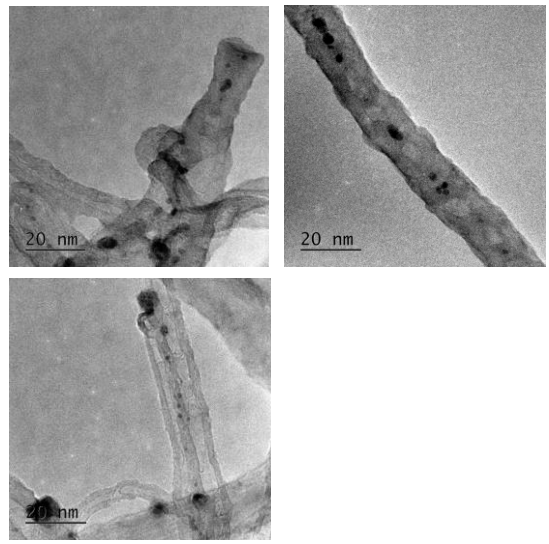


7.0 wt.% ruthenium, 20 wt.% cesium on graphitised CNTs (2073 K)

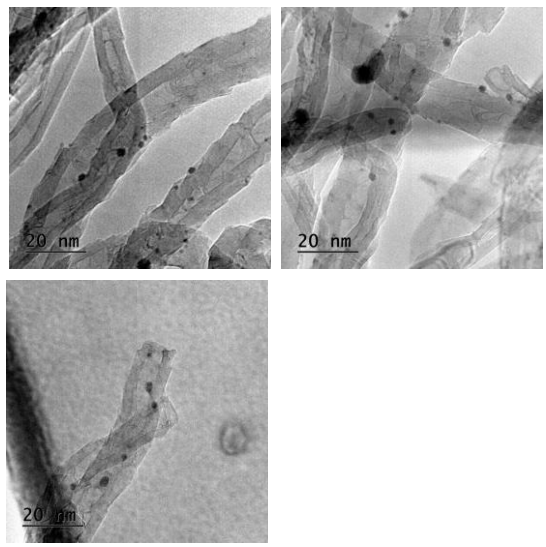

7.0 wt.% ruthenium, 30 wt.% cesium on graphitised CNTs (2073 K)

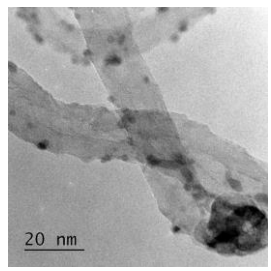


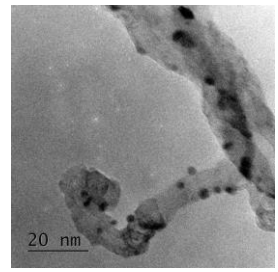


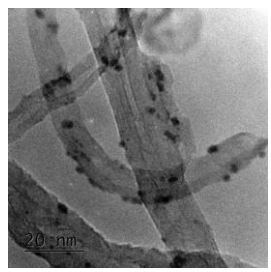

# Appendix II - Work from this Thesis that is Published or Submitted for Publication

## Contents

1. In-situ H2 production via low temperature decomposition of ammonia : Insights into the role of cesium as a promoter. International Journal of Hydrogen Energy, 39 (15). pp. 7646-7654.

2. Low Temperature H2 production from ammonia using ruthenium-based catalysts: synergetic effect of promoter and support. Applied Catalysis B: Environmental, 172-173 (2015), pp129-135.

INTERNATIONAL JOURNAL OF HYDROGEN ENERGY 39 (2014) 7646–7654

Available online at www.sciencedirect.com

ScienceDirect

journal homepage: www.elsevier.com/locate/he

# In-situ $H_2$ production via low temperature decomposition of ammonia: Insights into the role of cesium as a promoter

*Alfred K. Hill* [a,b], *Laura Torrente-Murciano* [a,b,*]

[a] *Department of Chemical Engineering, University of Bath, Bath BA2 7AY, UK*
[b] *Centre of Sustainable Chemical Technologies, University of Bath, Bath BA2 7AY, UK*

ARTICLE INFO

*Article history:*
Received 9 January 2014
Received in revised form
25 February 2014
Accepted 5 March 2014
Available online 13 April 2014

*Keywords:*
Ammonia decomposition
In-situ $H_2$ production
Ruthenium
Cesium
Promoter

ABSTRACT

Cesium-promoted ruthenium nanoparticles supported on multi-walled carbon nanotubes catalysts are shown to be highly active for hydrogen production by ammonia decomposition. Its low temperature activity is significantly improved as the cesium loading increases, reducing the activation energy from 96.7 kJ/mol in the absence of cesium to 59.3 kJ/mol with a cesium/ruthenium molar ratio of 3. Hydrogen production was observed to proceed below 590 K which represents a breakthrough towards the use of ammonia as chemical storage for *in-situ* hydrogen production on fuel cells. The catalytic enhancement is shown to be due to the electronic modification of ruthenium by the electron donating cesium promoter located on the ruthenium surface and in close proximity on the CNT surface. However, higher promoter loadings above a cesium/ruthenium ratio of 3 leads to ammonia inaccessibility to the catalytic active sites.



## Introduction

Hydrogen is widely recognized as an alternative portable energy medium to fossil fuels. It can be utilized for road transport applications presenting high energy efficiencies in combination with a proton exchange membrane fuel cell (PEM-FC) with zero emissions at the point of use [1]. Despite the vast potential of the use of hydrogen as an energy vector in the so-called hydrogen economy, its widespread implementation is currently limited by the capacity limitations of current hydrogen storage technologies and by the safety issues associated with its storage and transportation [1,2]. Hydrogen is a highly flammable gas in the presence of oxygen and, therefore, its storage in cylinders at high pressure makes public acceptance difficult due to safety reasons. During the last two decades, great scientific effort has been made to discover a suitable way of storing hydrogen. Adsorption into a variety of solid porous materials including metal organic frameworks is the most promising approaches [2,3]. Despite this, none of these materials have, to date, successfully fulfilled the 5.5 wt.% hydrogen content target established by the US Department of Energy for a complete storage system [4].

* *Corresponding author*. Department of Chemical Engineering, University of Bath, Bath BA2 7AY, UK. Tel.: +44 1225 38 5857; fax: +44 1225 38 5713.
E-mail address: ltm20@bath.ac.uk (L. Torrente-Murciano).

http://dx.doi.org/10.1016/j.ijhydene.2014.03.043

The use of hydrogen enriched compounds such as hydrates as storage molecules is a viable chemical alternative to the above mentioned physical methods. Amongst such compounds, ammonia is one of the most promising due to its availability and narrow flammability limits. Liquid ammonia has a high hydrogen content of 17.3 wt.%, higher than liquid hydrogen [5] and can be easily stored as a liquid or incorporated within solid salts [6]. In addition, ammonia synthesis is amongst the most energy efficient commercial processes with an overall energy conversion efficiency of 75% [7].

The decomposition of ammonia reaction for hydrogen production has been extensively studied in the literature with most of the efforts focused on the development of active catalytic systems. Despite the reversibility of the reaction, the optimum catalytic system for the synthesis of ammonia from molecular hydrogen and nitrogen differs from the optimum catalyst for ammonia decomposition. Low temperature ammonia decomposition requires a catalyst that is active for the recombinative desorption of nitrogen adatoms [8], which has been shown to be the rate determining step [9]. Iron based ammonia synthesis catalysts tend to bind nitrogen adatoms too strongly and the surface becomes saturated and consequently poisoned at low temperature [10]. Ruthenium-based catalysts present the highest rate of hydrogen production from ammonia to date [11,12]. Highly conductive and basic supports promote nitrogen recombinative desorption while high surface areas lead to high metal dispersion. Consequently, carbon nanotubes and super-basic supports such as potassium-zirconia have the highest reported catalytic performance [7,13]. The ruthenium activity is commonly enhanced by the presence of promoters as electron donors [14–16]. The effectiveness of the promoter is partially related to its basic character and its interaction with both the active species and the support [15,16]. Of all promoters considered to date, cesium is the best performing ahead of barium and potassium which are also highly effective [13,17]. Despite this, the role of the promoter is still debated in the literature with most authors suggesting an electronic modification of the metal particle properties although some have proposed a structural effect upon the metal particle [17].

Despite the extensive investigation and progress in this area, most studies are carried out at high reaction temperatures in excess of 670 K where the equilibrium conversion towards hydrogen formation is above 99%. However, the application of ammonia as a hydrogen vector for a low carbon energy delivery system requires *in-situ* hydrogen production at temperatures suitable for the PEM fuel cell technology (below 470 K). The thermodynamic equilibrium at these conditions can be overcome using engineering approaches such as membrane reactors for in-situ removal of hydrogen [18]. This leaves the development of a catalytic system sufficiently active at low temperature as the foremost challenge.

To date, only a few scattered studies have investigated the decomposition of ammonia at temperatures below 670 K. Klerke et al. [19] found that ruthenium nanoparticles supported on cesium-titanate nanowires become active at 593 K due to the high electron donating character of the super-basic support. Even lower temperature reactivity was observed by Sorensen et al. [20] in a microreactor using ruthenium nanoparticles supported on graphitic carbon with a high loading of cesium promoter. No apparent change in the reaction mechanism at low temperature was observed by either study. Following these preliminary results, this paper demonstrates the reduction of the ammonia decomposition activation energy at low temperature when the Cs/Ru ratio reaches an optimum value (~3 when carbon nanotubes are used as support). Investigations into the interaction between the cesium promoter and the ruthenium species reveal the electronic modification of the ruthenium active sites by partially reduced cesium located on the metal surface or its close surroundings.

## Experimental

### *Synthesis and characterization of catalysts*

All catalysts were prepared by incipient wetness impregnation of multi-walled carbon nanotubes (Sigma Aldrich, OD 6–9 nm, length 5 μm, $S_{BET}$ 253.0 $m^2\ g^{-1}$). $Ru(NO)(NO_3)_3$ (Alfa Aesar) and $CsOH.xH_2O$ (Sigma Aldrich, $x = 0.17$) were used as ruthenium and cesium precursors respectively. On a typical catalyst synthesis, an aqueous solution with a final volume

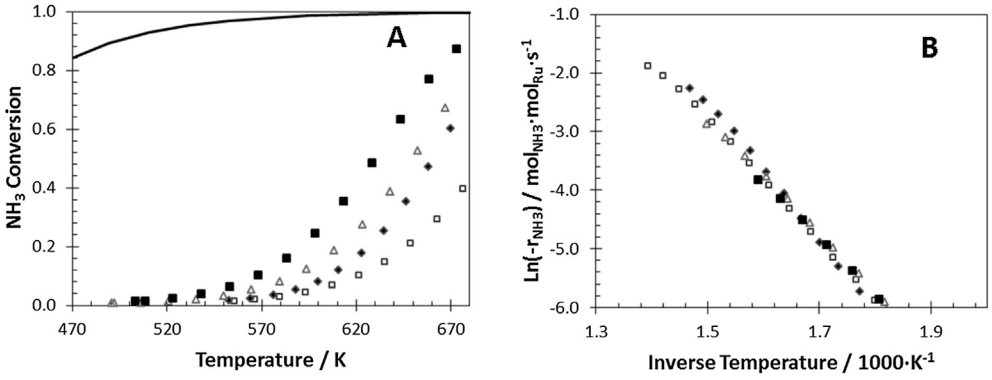


**Fig. 1 – (A) Ammonia decomposition conversion as a function of reaction temperature of 4.2 wt.% Cs promoted Ru/CNT catalysts. The solid line shows the thermodynamic equilibrium. (B) Arrhenius' plot (□) 3.0 wt.% Ru, (◆) 4.2 wt.% Ru, (Δ) 10.0 wt.% Ru and (■) 13.2 wt.% Ru.**

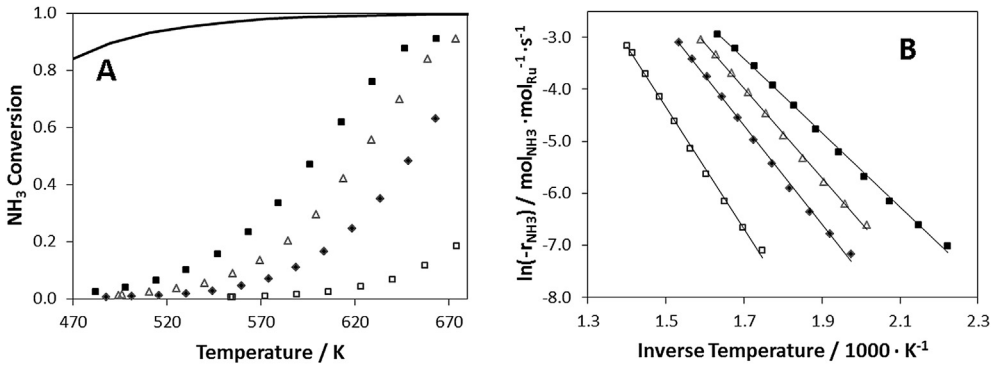


**Fig. 2 – (A) Ammonia decomposition conversion as a function of reaction temperature of promoted 7 wt.% Ru/CNT catalysts. (B) Arrhenius' plot (□) 0 wt.% Cs, (◆) 4 wt.% Cs, (Δ) 10 wt.% Cs and (■) 20 wt.% Cs.**

corresponding to the pore volume of the carbon nanotubes support was prepared containing the desired amount of ruthenium and cesium. This solution was then slowly dropped into the solid support, wetting it homogeneously. After synthesis, the catalysts were dried to remove the water solvent under vacuum at 350 K for 3 h and reduced under hydrogen at 500 K for 1.5 h.

$N_2$ adsorption analyses at 77 K were carried out using a Micromeritics ASAP 2020 and the surface area was calculated using the Brunauer, Emmett and Teller (BET) method. Powder X-ray diffraction was undertaken using a Bruker AXS D8 Advance with monochromatised Cu-$K_\alpha$ radiation ($\lambda = 0.15406$ nm), 40 kV and 40 mA. Ruthenium nanoparticle size distribution was determined with a JEOL TEM-2100 200 kV ultra-high resolution transmission electron microscope. Samples were prepared by depositing a drop of ~0.5 mg/mL of the material suspended in ethanol onto a Lacey carbon coated copper mesh grid and dried under vacuum. CO pulse chemisorption analyses at 308 K were carried out using a Micromeritics Autochem II equipment equipped with a thermal conductivity detector (TCD). Samples were pre-treated at 523 K under helium flow for 1 h to ensure the desorption of water or any other impurity from the catalyst surface. The same equipment was used for the temperature programmed reduction experiments. In this case, catalysts were pre-treated at 773 K under flowing argon for 20 min prior to temperature programmed reduction using 30 mL/min of 5% $H_2$/Ar from 333 to 1273 K with a ramp rate of 10 K/min.

### *Ammonia decomposition*

In a typical reaction, 25.0 mg of catalyst were evenly dispersed in a packed bed with 450 mg of inert silicon carbide acting as a diluent inside a U-shape 1/4″ O.D. quartz reactor. The temperature of the packed bed was regulated by an external tubular furnace (Carbolite) and a type K thermocouple situated at the exit of the catalyst bed. A mixture of $NH_3$ and He was continuously fed into the reactor giving a gas hourly space velocity of 5200 $mL_{NH3}\ g_{cat}^{-1}\ h^{-1}$. During the catalytic test, the temperature was increased from ambient up to 675 K at a rate of 2.6 K/min. Gas analyses were performed using on-line gas chromatography equipped with a HayeSep Q column and thermal conductivity detector and the mass balance was closed to within a ±10% error. A blank test was conducted in a reactor with SiC only showing no conversion within the experimental temperature range.

## Results and discussion

A series of promoted ruthenium-based catalysts supported on multi-walled carbon nanotubes (CNT) were used for the production of hydrogen via decomposition of ammonia at low temperatures (below 650 K). In order to study the effect of ruthenium and cesium loadings, two sets of catalysts were prepared. Firstly, the effect of the ruthenium content on the ammonia decomposition activity was studied by varying the ruthenium loading in the range from 3 to 13.2 wt.%, keeping

**Table 1 – Effect of ruthenium metal loading of Cs promoted (4.2 wt.%) Ru/CNT catalysts on Ru particle size, activity and activation energy for the ammonia decomposition reaction.**

| Ruthenium loading/wt.% | Cs/Ru ratio | Ru average particle size[a]/nm | Metallic Ru surface area[b]/$m^2\ g^{-1}$ | TOF @ 600 K /$mol_{NH3}\ mol_{Ru}^{-1}\ h^{-1}$ | Rate of reaction @ 600 K/$mol_{NH3}\ m^{-2}{}_{Ru}\ h^{-1}$ ($\times 10^{-7}$) | Activation energy/kJ $mol^{-1}$ |
|---|---|---|---|---|---|---|
| 3.0 | 1.4 | 1.5 | 212 | 0.0110 | 5.1 | 79.8 |
| 4.2 | 1.0 | 2.3 | 187 | 0.0136 | 7.2 | 75.1 |
| 10.0 | 0.4 | 2.1 | 122 | 0.0125 | 10.1 | 71.8 |
| 13.2 | 0.3 | 2.3 | 113 | 0.0115 | 10.1 | 70.9 |

[a] Average metal particle size determined by TEM.
[b] Determined by CO pulse chemisorption.

the promoter loading constant at 4.2 wt.% of cesium. Secondly, the role of cesium as a promoter was investigated by preparing a set of catalysts with a constant ruthenium loading (7 wt.%) while varying the cesium content by up to 50 wt.%. All catalysts were prepared by simultaneous incipient wetness impregnation of ruthenium and cesium precursors on multi-walled carbon nanotubes as support. The catalytic activity of both sets of catalysts towards ammonia decomposition as a function of temperature is shown in Figs. 1 and 2 respectively.

Increasing the ruthenium loading on the Ru/CNT catalysts while maintaining the cesium loading (4.2 wt.%) constant increases the ammonia conversion for a given reaction temperature (Fig. 1(a)). Similar turnover frequency activity (TOF, calculated per mole of Ru) is observed in all cases, suggesting not only the presence of the same active sites, but also the same concentration of active sites per mass of ruthenium (Table 1).

The effect of the cesium content has a more remarkable function in determining the Ru/CNT activity, especially at low temperatures. The role of cesium is purely as a promoter, with cesium supported on CNT (20 wt.% Cs/CNT) not showing any ammonia decomposition activity in the range of temperatures studied. The presence of cesium enhances the Ru/CNT ammonia decomposition activity by reducing its activation energy and its incremental effect remains significant even at high Cs to Ru ratios, as shown in Table 2. In these cases, the Cs–Ru/CNT catalysts show activity towards ammonia decompositions at temperatures as low as 500 K (Fig. 2(a)).

Fig. 3 shows the volcano-type effect of cesium loading on the rate of reaction measured at 600 K. As the Cs/Ru ratio in the catalyst increases, the ammonia decomposition rate increases linearly reaching a maximum at Cs/Ru molar ratio of around 3. When the cesium loading is further increased (Cs/Ru >> 3), the rate of reaction decreases; however, the beneficial effect of cesium at low Cs/Ru ratio is greater than its detrimental effect at high Cs/Ru ratios, with similar rates of reaction obtained at Cs/Ru ratios of 1.4 and 7.1. This finding is in agreement with previous observations on the detrimental effect of cesium on the catalytic activity at very high promoter loadings [21]. The presence of an excess of cesium seems to partially block the access to the active ruthenium sites, reducing the hydrogen production rate [22]. This steric effect suggests that cesium decorates not only the CNT support but also the ruthenium surface, at least at high Cs/Ru ratios. The promotional effect of cesium would only be observed if it directly interacts with the ruthenium to ensure the electron donation [16], which not only increases its catalytic activity but consequently also modifies the nature of the ruthenium active species. This catalytic enhancement is observed at all Cs/Ru ratios and it significantly reduces the activation energy of the system from 97 kJ/mol in the absence of cesium to a minimum value of 60 kJ/mol when the Cs/Ru ratio has a value of 3, as shown in Table 2. These findings would suggest that cesium is present upon the surface of the ruthenium nanoparticle for all catalysts investigated.

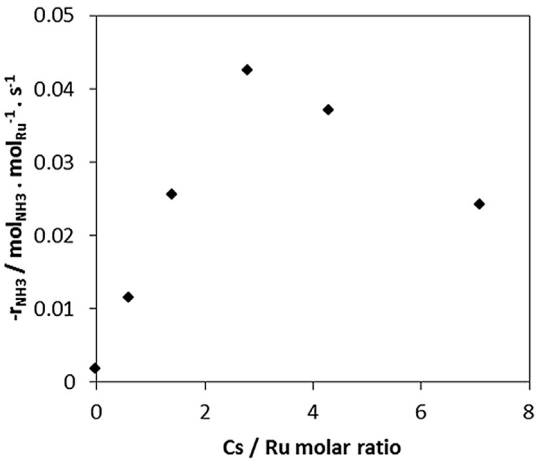


**Fig. 3 – Rate of reaction of ammonia decomposition (at 600 K) as a function of the Cs loading using 7 wt.% Ru/CNT as catalyst.**

The disparity of the promotional effect of cesium at different Cs/Ru ratios is explained by the effect of the cesium loading on its location across the catalyst. The distribution of cesium over the ruthenium surface and the CNT support respectively depends on the relative heat of adsorption [23]. At low promoter loadings, cesium strongly adsorbs on the surface of the CNT, although a small proportion is located on the ruthenium surface and its proximity, with a significant promotional effect. As the heat of adsorption on the carbon support decreases dramatically as the adsorbed cesium content increases [24], the relative amount of cesium adsorbed on the ruthenium surface increases at high cesium loadings. An optimum ruthenium coverage is observed when the Cs/Ru ratio is

**Table 2 – Effect of cesium loading on 7 wt. % Ru/CNT catalysts on Ru particle size, activity and activation energy for the ammonia decomposition reaction.**

| Cesium loading/wt.% | Cs/Ru ratio | Ru average particle size[a]/nm | Metallic Ru surface area[b]/$m^2$ $g^{-1}$ | TOF @ 600 K /$mol_{NH3}$ $mol_{Ru}^{-1}$ $h^{-1}$ | Rate of reaction @ 600 K/$mol_{NH3}$ $m^{-2}{}_{Ru}$ $h^{-1}$ ($\times 10^{-7}$) | Activation energy/kJ $mol^{-1}$ |
|---|---|---|---|---|---|---|
| 0.0 | – | 1.6 | 154 | 0.0018 | 1.2 | 96.7 |
| 4.2 | 0.6 | 1.6 | 160 | 0.0115 | 7.1 | 78.6 |
| 10 | 1.4 | 2.4 | 125 | 0.0256 | 20.0 | 71.48 |
| 20 | 2.8 | 2.0 | 167 | 0.0426 | 25.2 | 59.33 |
| 30 | 4.3 | 2.4 | 110 | 0.0371 | 33.4 | 64.5 |
| 50 | 7.1 | 2.2 | 56 | 0.0242 | 42.7 | 66.1 |

[a] Average metal particle size determined by TEM.
[b] Determined by CO pulse chemisorption.

~3 above which, blockage of the active sites occurs having a detrimental effect on the catalytic activity. This optimum ratio is dependent on the support and the promoter used [22].

In addition to the promoting electronic effect of cesium, transmission electron microscopy (TEM) was used to determined its effect on the size and morphology of ruthenium nanoparticles. Fig. 4 shows representative TEM images of 7 wt.% Ru/CNT with different cesium loadings. The presence of cesium does not seem to have an effect on the distribution of the ruthenium nanoparticles. Similar particle size distributions (histograms in Fig. 4) are observed independently of the cesium content with the majority of ruthenium nanoparticles in sizes between 1 and 4 nm and mostly between 1.5 and 2.5 nm. The observed variance between TEM nanoparticle

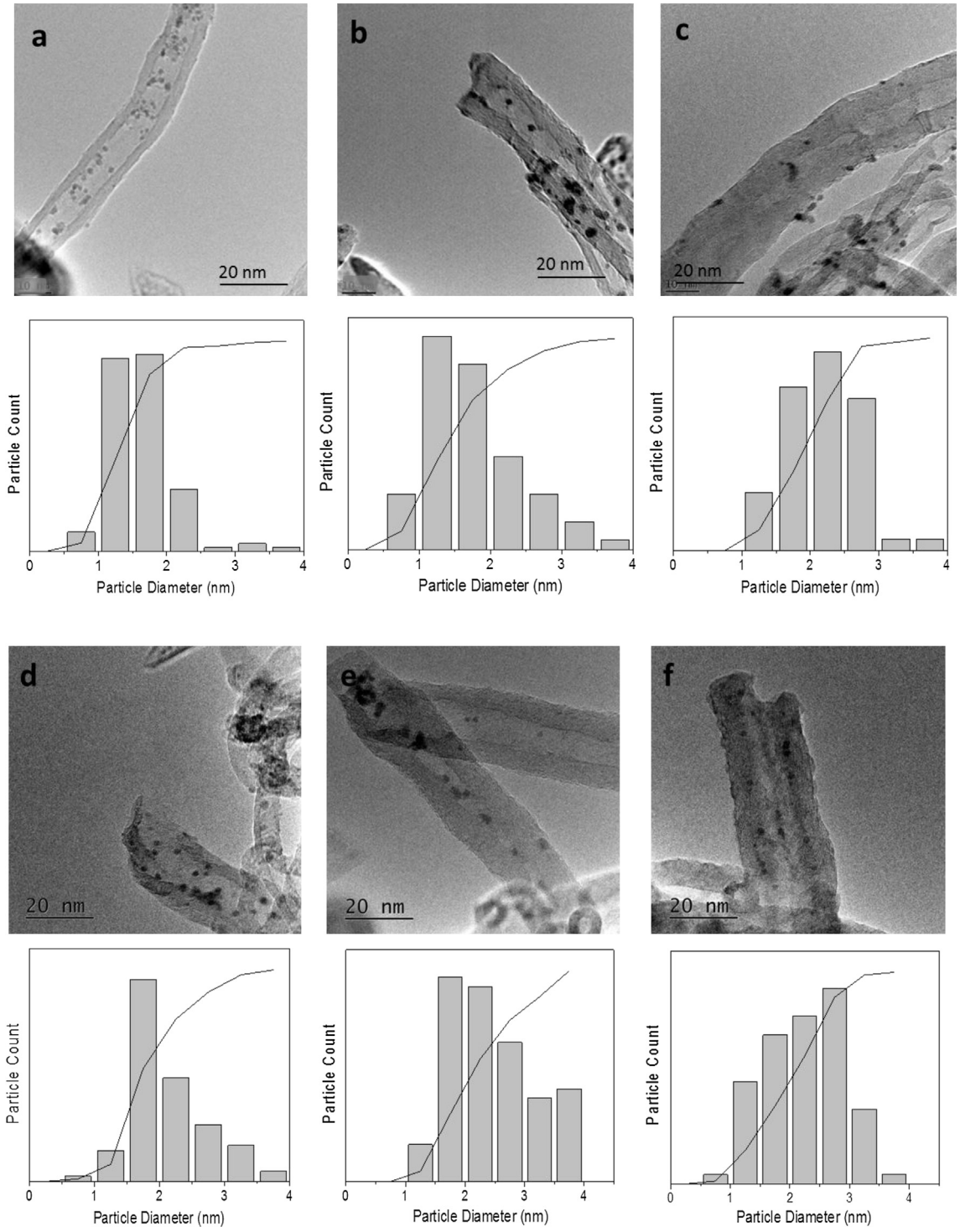


**Fig. 4 – TEM images and particle size histograms of 7 wt.% Ru/CNT catalysts. (a). 0 wt.% Cs, (b). 4.2 wt.% Cs and (c). 10.0 wt.% Cs, (d). 20 wt.% Cs, (e). 30 wt.% Cs and (f). 50 wt.% Cs.**

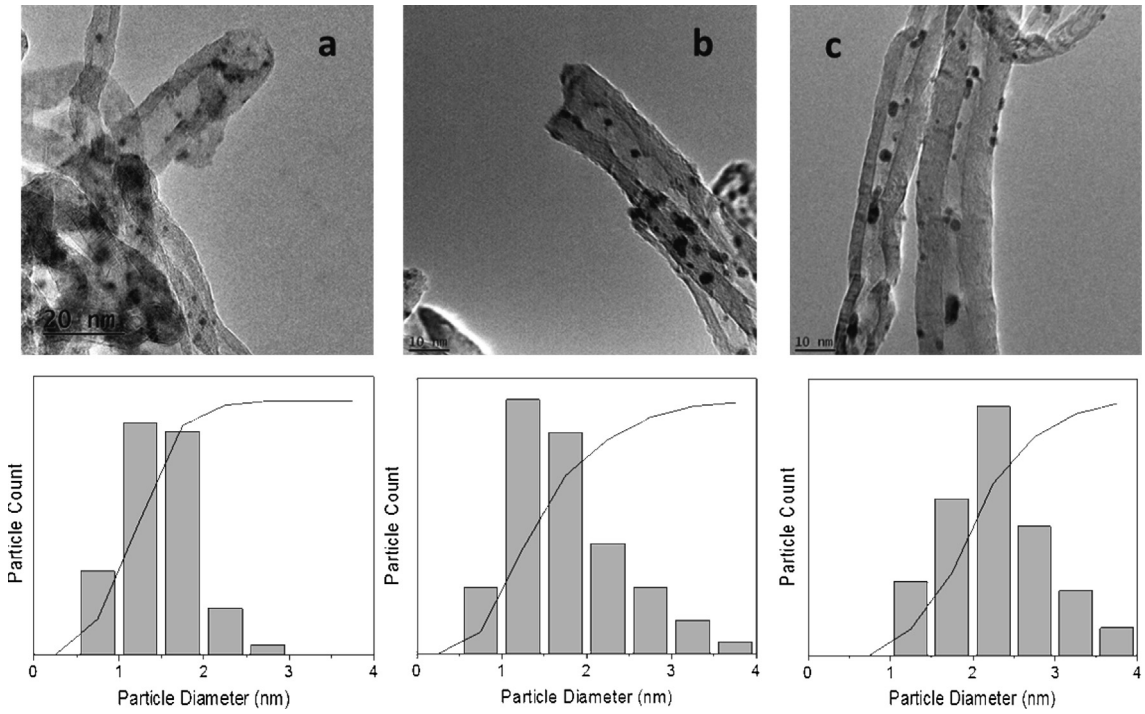


**Fig. 5 – TEM images and particle size histograms of 4.2 wt.% Cs promoted Ru/CNT catalysts. (a). 3.0 wt.% Ru, (b). 7.0 wt.% Ru and (c). 13.2 wt.% Ru.**

size results can be attributed to the limitations of measuring the metal particle sizes by TEM. Cesium is not detectable by TEM even at the higher loading contents studied, its presence on the catalyst was confirmed through EDS experiments.

It is well-accepted in the literature, that the ruthenium B5-type sites [11], a specific arrangement of five ruthenium atoms, are the active sites for the structured sensitive ammonia decomposition reaction [25]. The increase of catalytic activity per mole of ruthenium as the cesium loading increases up to Cs/Ru ratios ~3 (Table 2, TOF values) could lead to the misinterpretation of an increase of ruthenium B5 active site concentration as the cesium loading increases. However, this explanation does not successfully explain the changes on the activation energy suggesting that the main role of cesium is electronic rather than structural [14,16].

A similar study of the effect of ruthenium loading on its particle size was carried out using TEM images (Fig. 5). Up to 13.2 wt.% of ruthenium was loaded on the high surface area carbon nanotubes by incipient wetness impregnation with no apparent effect on the ruthenium particle size distribution as shown in the histograms. The average sizes range from 1.5 to 2.3 nm (Table 1) as the ruthenium content varies from 3.0 to 13.2 wt.%. At higher metal loadings, elongation of some of the metal particles inside the CNT support is observed. Visible

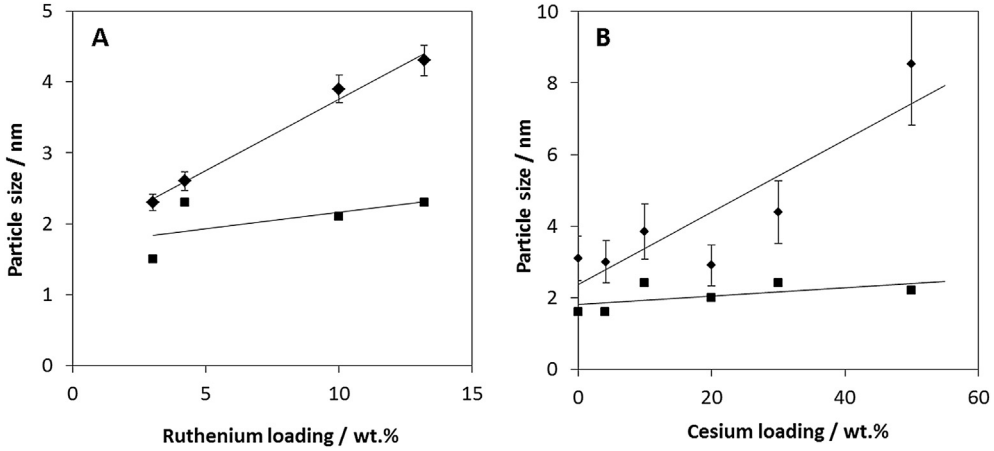


**Fig. 6 – Effect of (A). ruthenium loading on 7 wt.% Cs promoted Ru/CNT catalysts and (B). cesium loading on 7 wt.% Ru/CNT catalysts on average ruthenium particle size measured by (◆) CO pulse chemisorption and (■) TEM.**

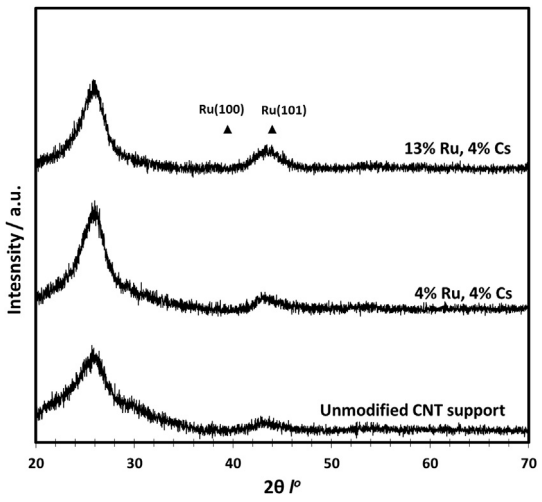


**Fig. 7 – X-Ray diffraction spectra of carbon nanotubes, 4 wt.% Ru 4 wt.% Cs/CNT and 13.2 wt.% Ru 4 wt.% Cs/CNT. Ruthenium diffraction peaks are also shown for reference.**

elongation of nanoparticles suggests that they are generally located inside the carbon nanotubes with a small proportion decorating the external surface. However, in all cases, a similar activity per mole of ruthenium and activation energy is calculated for the ammonia decomposition reaction. Thus, similar active species and concentration per amount of ruthenium is present in all the catalysts independently of the observed particle elongation.

CO pulse chemisorption at 308 K was also used to estimate the ruthenium particle size and metal surface area by quantifying the amount of CO chemisorbed on the metal surface assuming a CO/Ru stoichiometry ratio of 2 and a ruthenium density of 12.45 g/cm$^3$ [26]. In this case, it is observed that CO pulse chemisorption overestimates the ruthenium particle size compared to the data obtained by TEM. At low ruthenium and cesium loadings, the small differences between techniques could be caused by the assumption of hemispherical metal particles (support – metal contact angle of 90°) by the CO chemisorption method. However, the disparity of average ruthenium sizes estimated by both techniques further increases as the ruthenium and cesium loadings increase, as shown in Fig. 6. As observed by TEM, at high ruthenium loadings, partial encapsulation inside the carbon nanotubes support and consequent elongation of the particle takes place which partially blocks the access of CO to the ruthenium surface, consequently overestimating its average particle size (Fig. 6(a)) by decreasing the measured metal surface area (Table 1).

Additionally, the difference between average particle sizes estimated by TEM and CO pulse chemisorption as a function of the cesium promoter content (Fig. 6(b)) further supports the previous observations related to the location of cesium within the catalytic system. As stated above, at low cesium content (Cs/Ru ratio below 3), although cesium is present on the ruthenium surface and proximity having a significant promotion effect, it preferentially adsorbs on the CNT support, leaving the ruthenium surface easily accessible to CO during the pulse chemisorption analyses. Thus, similar ruthenium particle sizes are estimated by both TEM and CO chemisorption methods. However, as the cesium loading increases, it selectively covers the ruthenium surface and consequently makes it inaccessible to CO. In this way, the latter method overestimates the ruthenium size, aligned with the decrease of ruthenium surface area when the Cs/Ru ratio is higher than 3 (Table 1). This observation is also in agreement with the

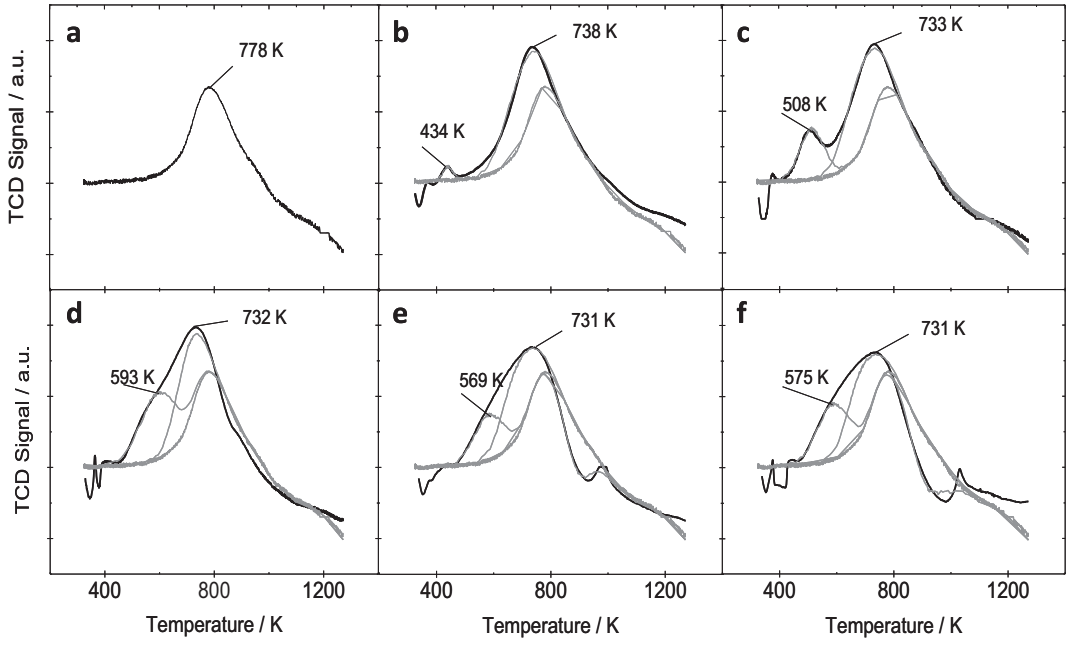


**Fig. 8 – Temperature programmed reduction of (a). CNT, (b). 7 wt.% Ru/CNT, (c). 7 wt.% Ru, 10 wt.% Cs/CNT, (d). 7 wt.% Ru, 20 wt.% Cs/CNT, (e). 7 wt.% Ru, 30 wt.% Cs/CNT and (f). 7 wt.% Ru, 50 wt.% Cs/CNT catalysts.**

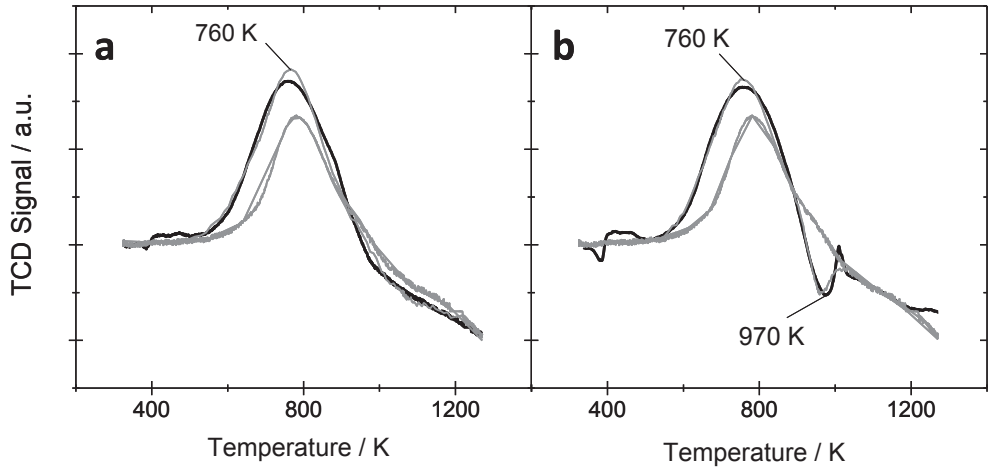


**Fig. 9 – Curve fitting of TPR showing the effect of Cs loading on un-modified carbon nanotubes (a) 20% wt. Cs and (b) 50% wt. Cs.**

decrease of catalytic activity observed at high promoter loadings (Fig. 3) due to the ammonia inaccessibility to the active sites and supports previous observations of cesium increasingly decorating the ruthenium surface as the Cs/Ru ratio increases [15].

Fig. 7 shows the XRD spectra of (4.2 wt.%) cesium promoted Ru/CNT catalysts with different ruthenium loadings. The spectra of the carbon nanotubes support is shown for reference showing broad diffraction peaks at 25.8 and 43.2 $2\theta$ values. No diffraction peaks corresponding to ruthenium are shown independently of its loading which is in agreement with the TEM observation of its low particle size (<3 nm) [13]. No diffraction peaks corresponding to reduced cesium at 19.9°, 28.3°, 34.8°, 40.5°, 45.4° and 50° or any of its proposed chemical forms such as CsOH are observed. It is likely that cesium is present in a disordered form as observed in the literature by HR-TEM studies [15].

Temperature programme reduction of the different catalysts under hydrogen flow was carried out to further understand the interaction between the ruthenium, the cesium promoter and the CNT support and its effect on the final catalytic activity towards ammonia decomposition. Temperature programme reduction of the carbon nanotubes shows a considerable hydrogen uptake from 650 K with a maximum at 778 K (Fig. 8). The presence of cesium only on the CNT surface (20 wt.% Cs/CNT) shows a higher hydrogen intake with respect to the CNT support without a temperature shift of the peak, probably due to the reduction of the cesium hydroxide precursor (CsOH) to substoichiometric $Cs_2O$ in which cesium is partially reduced [23]. Additionally, the presence of cesium also shows a negative peak at ~950 K when compared to the results for the unmodified carbon nanotubes (Fig. 9).

TPR of ruthenium supported on un-promoted CNT catalysts (7 wt.% Ru/CNT) shows two additional peaks with respect to the CNT support. The first negative peak at ~300 K is caused by the decomposition of the ruthenium nitrosyl nitrate precursor with an associated release of nitrate species and water [23]. The second hydrogen uptake peak at ~430 K is associated with the reduction of ruthenium in line with reported values in the literature between 400 and 450 K [13]. The combined presence of ruthenium and cesium in the catalysts (Ru–Cs/CNT) markedly modifies the reduction temperature of both components. The peak temperature and the integration area for the ruthenium reduction peak increase from 430 K to 570 K as the cesium loading increases. The hydrogen consumption during the reduction calculated by integration of this peak suggests a degree of ruthenium reduction increasing from 14% for 0 wt.% Cs, to 88% for 10 wt.% Cs and 120% for 20 wt.% Cs catalysts respectively (all catalysts containing 7 wt.% Ru). This 'over-reduction' of ruthenium is explained by the partial reduction of cesium occurring on the surface of the ruthenium nanoparticle accounting for the additional hydrogen uptake. This finding is in accordance with the results previously published by Rarog-Pilecka et al. [23] who found by in-situ XRD that $CsNO_3$ is converted to CsOH at 373–393 K and then reduced to a partially reduced substoichiometric oxide of $Cs_2O$ in which the degree of cesium reduction varied from 0.25 to 0.45 at around 430 K. Based on our current results, we can now confirm that cesium reduces only on the surface of the ruthenium nanoparticle as no cesium reduction is observed to occur at this temperature for the samples with no ruthenium. The reduction of cesium on the surface of ruthenium at temperatures between 470 and 570 K can be explained by the capability of ruthenium of dissociating hydrogen [27] which consequently spills over reducing the cesium in either direct contact to ruthenium or in the close surroundings. Reduced cesium on the surface of ruthenium would act as a strong electron donor and this explains the powerful effect that the addition of CsOH has upon the ruthenium catalyst for activity towards ammonia decomposition.

## Conclusions

Hydrogen production from ammonia decomposition is shown at temperatures below 500 K using ruthenium supported on carbon nanotubes catalysts promoted with cesium which has a strong effect in reducing the activation energy of the reaction. A combination of characterisation methods

Applied Catalysis B: Environmental 172 (2015) 129–135

Contents lists available at ScienceDirect

Applied Catalysis B: Environmental

journal homepage: www.elsevier.com/locate/apcatb

# Low temperature $H_2$ production from ammonia using ruthenium-based catalysts: Synergetic effect of promoter and support

Alfred K. Hill, Laura Torrente-Murciano *

*Department of Chemical Engineering and Centre for Sustainable Chemical Technologies, University of Bath, Bath BA27AY, UK*

ARTICLE INFO

*Article history:*
Received 6 November 2014
Received in revised form 21 January 2015
Accepted 10 February 2015
Available online 11 February 2015

*Keywords:*
Ammonia decomposition
In-situ $H_2$ production
Low temperature activation
Ruthenium
Promoters

ABSTRACT

Low temperature hydrogen production via ammonia decomposition is achieved by the synergetic combination of a highly conductive support and an electron donating promoter in a ruthenium-based system, with activity at temperatures as low as 450 K. The high conductivity of graphitized carbon nanotubes allows for greater electronic modification of the ruthenium nanoparticles by cesium located in close proximity but without direct contact, avoiding the blockage of the active sites. This development of low temperature catalytic activity represents a breakthrough toward the use of ammonia as chemical storage for in-situ hydrogen production in fuel cells.



## 1. Introduction

Environmental concerns regarding the detrimental effects of anthropogenic $CO_2$ emissions into the atmosphere are increasingly leading the scientific community to the development of sustainable alternative fuels [1]. Hydrogen has long been considered as a suitable alternative as a carbon-free road transport fuel for high energy efficient proton exchange membrane fuel cells (PEM-FC), however, efforts to achieve a sufficient hydrogen storage density remain well short of the targets set by the US Department of Energy (DoE) for feasible safe portable systems [2]. With a hydrogen storage capacity at moderate pressure (<10 bar) that exceeds liquid hydrogen [3], ammonia's potential as a hydrogen vector is currently limited by the lack of a catalytic system capable of releasing hydrogen on-demand at temperatures aligned with those of the PEM-FC (~370 K).

The development and optimization of ammonia synthesis in the so-called Haber-Bosch process for more than 150 years has provided the foundations of the current efforts for the development of catalytic systems for the decomposition of ammonia [4]. Despite the reversibility of the reaction, new challenges arise in the decomposition path, especially at low reaction temperatures (<600 K) due to the low thermodynamic equilibrium conversions and the recombinative desorption of nitrogen adatoms as the rate determining step [5]. Engineering solutions such as membrane systems [6] can successfully integrate hydrogen production and in-situ separation maximizing ammonia utilization and avoiding poisoning of the fuel cell catalysts. This leaves the development of a low temperature catalytic system as the key challenge to unveiling ammonia as an energy vector toward the so-called hydrogen economy.

Despite considerable progress in the field, current catalytic systems can only achieve significant ammonia decomposition conversion at temperatures around 600 K [7] and consequently, its potential for on-demand hydrogen production at low temperatures has been disregarded. The only few previous studies of low temperature ammonia decomposition in the literature [8,9] suggest the feasibility of the system using ruthenium-based catalysts and their catalytic enhancement by the use of electron donating promoters such as cesium or potassium. We have recently demonstrated that optimization of the Ru/Cs ratio on Ru/CNT systems facilitates the production of hydrogen from ammonia at low temperatures. The activation energy is reduced via electronic modification of the active sites which facilitate the nitrogen recombinative desorption on the ruthenium surface [10]. In this work, we show the extraordinary enhanced activity of promoted ruthenium nanoparticles supported on graphitized carbon nanotubes (CNT) at temperatures as low as 450 K, revealing new insights into the synergetic effect of the promoter and a highly conductive support on the electronic modification of the ruthenium sites.

* Corresponding author: Tel.: +44 1225 38 5857; fax: +44 1225 38 5713.
*E-mail address:* ltm20@bath.ac.uk (A.K. Hill).

http://dx.doi.org/10.1016/j.apcatb.2015.02.011

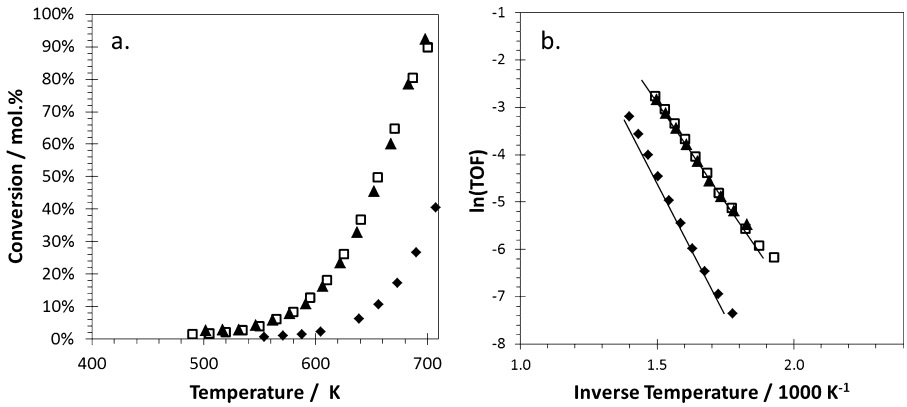


**Fig. 1.** (a) Ammonia decomposition conversion as a function of reaction temperature showing the effect of graphitization of the CNT support in un-promoted Ru catalysts (b) Arrhenius' plot (♦) 7 wt% Ru/CNT, (□) 7 wt% Ru/graphitized-CNT at 2073 K and (▲) 7 wt% Ru/graphitized-CNT at 2273 K Reaction conditions are detailed in the experimental section.

## 2. Experimental procedure

Multi-walled carbon nanotubes (Sigma Aldrich, OD 6–9 nm, length 5 μm, $S_{BET}$ 253.0 $m^2\,g^{-1}$) were graphitized at 2070 and 2270 K during 1 h in an ultra-high vacuum furnace. All catalysts were synthesised by incipient wetness impregnation using $Ru(NO)(NO_3)_3$ (Alfa Aesar) and $CsOH.xH_2O$ (Sigma Aldrich, $x = 0.17$) as ruthenium and cesium precursors. After impregnation of the aqueous solutions, the catalysts were dried at 350 K under vacuum for 3 h and then reduced under hydrogen at 500 K for 1.5 h. Nitrogen adsorption analyses were carried out at 77 K using a Micromeritics ASAP 2020 instrument. The surface area was calculated using the Brunauer, Emmett and Teeler (BET) method. Ruthenium particle size distribution was estimated by microscopy using a JEOL TEM-2100 200 kV ultra-high resolution transmission electron microscope. Samples were prepared by dispersing the samples in ethanol (0.5 mg $mL^{-1}$). A drop of the dispersion was added to a Lacey carbon-coated copper mesh grid and dried under vacuum. CO pulse chemisorption analyses were carried out at 310 K using a Micromeritics Autochem II instrument equipped with a thermal conductivity detector (TCD). Samples were pre-treated for one hour at 525 K under helium flow to desorb water or any other impurity from the catalyst surface. Temperature programme reduction (TPR) experiments were carried out in the same equipment. In this case, the samples were degassed at 775 K under flowing Argon for 20 min prior to TPR analyses up to 1275 K using a temperature ramp rate of 10 K $min^{-1}$ under 30 mL $min^{-1}$ flow of 5% $H_2$/Ar. Raman analyses were carried out using a Renishaw in Via Raman microscope using a 532 nm green Renishaw Diode Laser.

Ammonia decomposition reactions were carried out in a continuous packed bed reactor with a gas hourly space velocity of 5200 $ml_{NH3}\cdot g_{cat}^{-1}\cdot h^{-1}$ using 25 mg of catalyst in a silica bed. The reactor system was equipped with mass flow and temperature controllers. All the pipes were heated to 333 K to avoid any ammonia condensation and consequently corrosion. During each catalytic study, the reaction temperature was ramped from around 450 K to 850 K at 2.6 K $min^{-1}$ using a Carbolyte tubular furnace with PID control. Reactor exit gas was analysed using an on-line gas chromatography fitted with a Hayesep Q column and thermal conductivity detector. The mass balance closure precision was within a ±10% error.

## 3. Results and discussion

Graphitization of commercial multi-walled carbon nanotubes (CNT) substantially increases the ammonia decomposition conversion of unpromoted ruthenium catalysts while decreasing the minimum temperature of activation by ~100 K (Fig. 1a). The turnover frequency values at 600 K are an order of magnitude higher in the case of the graphitized catalysts with a substantial decrease in activation energy from 96.7 to 67.6 kJ $mol^{-1}$ for the commercial and graphitized CNTs support, respectively, (Fig. 1b). None of the supports show any measurable conversion in the absence of ruthenium.

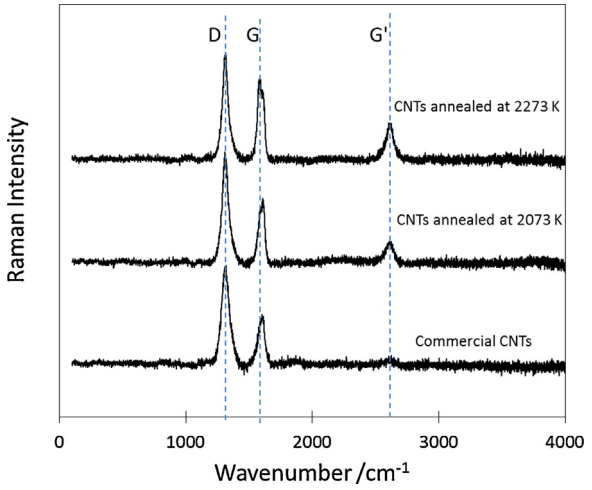


**Fig. 2.** Raman spectra of commercial multi-walled CNT and after graphitisation at 2073 and 2273 K under vacuum.

Annealing of the CNT at 2070 K and 2273 K under ultra-high vacuum modifies the chemical and physical surface properties of the support, increasing the axial alignment of the tubes and increasing the crystallite size [11], shown by a variation of the relative intensity of the peaks in the Raman spectra (Fig. 2).

The D band at 1350 $cm^{-1}$ is representative of the disorder in graphitic carbon and the G and G' bands at 1580 $cm^{-1}$ and 2700 $cm^{-1}$ are produced by graphitic in-plane vibrations from $sp^2$-bonded carbon and 2D vibrations respectively and its prominence reflects the presence of graphitic carbon [12]. The lower $I_D/I_G$ ratio of the annealed CNT with respect to the commercial ones suggests a more graphitic structure after the thermal treatment as shown in Table 1.

Graphitization is accompanied by the removal of any potential presence of residual iron catalyst remaining from the CNT's synthesis [11] and defects in the graphitic walls of the material. This healing of the CNT surface has a minor detrimental effect on the surface area of the material (Table 1) however it strongly promotes the elimination of functional groups on the CNT's surface [11]. Chemical

**Table 1**
Effect of graphitization at 2070 K on the CNT's physical properties.

| Support | Surface area[a] $m^2\ g^{-1}$ | Pore diameter[b] nm | Raman intensity $I_D/I_G$ |
|---|---|---|---|
| Commercial CNT | 253 | 27.6 | 2.6 |
| Graphitised CNT @2070 K | 220 | 28.4 | 1.9 |
| Graphitised CNT @2270 K | 235 | 28.0 | 1.5 |

[a] Calculated via $N_2$ physisorption at 77 K using BET equation.
[b] Using the BJH desorption data.

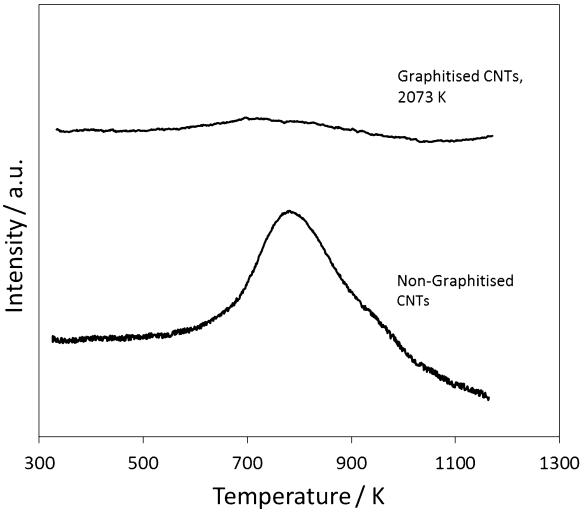


**Fig. 3.** Temperature programmed reduction (TPR) of commercial multi-walled CNT and after graphitisation at 2070 K under vacuum.

functionalization by acid oxidation and the introduction of phenolic, carboxyl, and lactone groups is common practice during the purification stages in the CNT's synthesis [13]. In general, these oxygen surface complexes are known to be thermally unstable and their removal during the graphitization process is here verified by temperature programmed reduction characterization (Fig. 3). While reduction of surface oxygen complexes is observed between 670 and 1270 K in the commercial CNT, negligible hydrogen consumption is observed in the annealed sample as expected due to the lack of such groups in its surface, verifying its graphitization.

Functional surface groups and defects on carbon materials are known to act as anchoring points for the metal active nanoparticles, improving their dispersion across the surface [14] which are mostly removed during graphitization. In any case, ruthenium particles present similar size distribution when supported on commercial CNT and graphitized CNT (Fig. 4). The surface area of the Ru-supported catalysts does not significantly vary respect to their respective supports. Other authors have previously claimed that metal nanoparticles might tend to locate more preferentially on the outer surface of the graphitized CNT due their higher degree of order compared to the inner walls [15] but we do not have a clear evidence of this phenomena. Unfortunately, XRD spectra of these catalysts do not provide useful information related the average crystallite size of the ruthenium particles due to the overlap of the ruthenium and support diffraction peaks.

Instead, the activity enhancement is believed to be caused by an increase of the CNT's electron conductivity during graphitization which consequently modifies the metal-support interaction. The defects and functional groups on the surface of CNT reduce the effective band overlap of the support, leading to an increase in the electrical resistivity [16]. Their removal during graphitization has been shown to greatly increase the material's conductivity [17]. According to that study, the CNT's conductivity increases exponentially with the graphitization temperature below 1770 K. Further increments in the annealing temperature only lead to small incremental enhancements of the conductivity. Indeed, similar catalytic activity toward ammonia decomposition is observed with 7 wt% ruthenium catalysts supported on graphitized CNT at 2070 and 2270 K, respectively, (Fig. 1). Graphitization results in a higher electron density in the CNT's outside walls and a high conductivity which facilitates the electron transfer between the support and the ruthenium particles promoting the recombination of nitrogen, making the catalytic system active at lower temperatures.

Interestingly, a similar modification of the ruthenium sites achieved by graphitization of the CNT support is observed by the addition of 4 wt% cesium as electron donating promoter to the non-graphitized catalysts (Fig. 5, solid triangles and solid line, respectively), with a similar activation energy. Thus, we further investigated the combined effect of cesium loading and the use of graphitized CNT in the modification of the ruthenium activity.

Fig. 5 shows a remarkable synergetic effect of the combination of cesium to ruthenium sites supported on graphitized CNT's. 7 wt% Ru-4 wt% Cs/graphitized CNT presents activity toward decomposition at temperatures as low as 450 K, with a respective decrease of the activation energy as shown in Table 1. However, surprinsingly, higher cesium loadings does not further enhance the catalytic activity neither decreases the minimum temperature of activity, as previously observed for the Ru-based catalysts on commercial CNT [10].

The variations on the catalytic activity of Cs-promoted ruthenium catalysts supported on graphitized CNT are not caused by relevant variations on the ruthenium particle size distribution as shown by representative TEM pictures in Fig. 6. Although the particle size distribution seems to be shifted toward bigger particles as the cesium loading increases, the differences (<1 nm) are within the experimental error associated to TEM particle sizing despite care been taken in imaging multiple locations within each sample. The cesium loading does not either seem to have an effect on the preferential distribution of the ruthenium nanoparticles in the inside or outside surface of the carbon nanotubes. Indeed, in Fig. 6 we have intentionally shown pictures were most of the ruthenium nanoparticles are situated inside and outside the CNT's to demonstrate the lack of a systematic trend. It is important to note that cesium is not detectable by TEM even at the high loadings used herein.

The similitude on ruthenium particle size in the Cs-promoted ruthenium supported on graphitized CNT observed by TEM is not in agreement with the exposed metallic surface areas measured by CO chemisorption (Table 2). This disagreement suggest the partial coverage of the ruthenium sites by cesium, especially at high Cs loadings, blocking the CO access during the CO chemisorption analysis. Considering this, the Cs/Ru molar ratio is expected to have an effect in this phenomena. Indeed, Fig. 7 shows a sharp increase in the ammonia decomposition rate of reaction by the addition of cesium which reaches a maximum activity at a Cs/Ru molar ratio of 0.6, above which the activity decreases.

The addition of cesium has a double effect on the catalytic activity of ruthenium-based catalysts. On one hand, cesium located on the surface of ruthenium or its close proximity produces a beneficial electronic modification of the ruthenium, responsible of the ammonia decomposition catalytic activity enhancement. On the

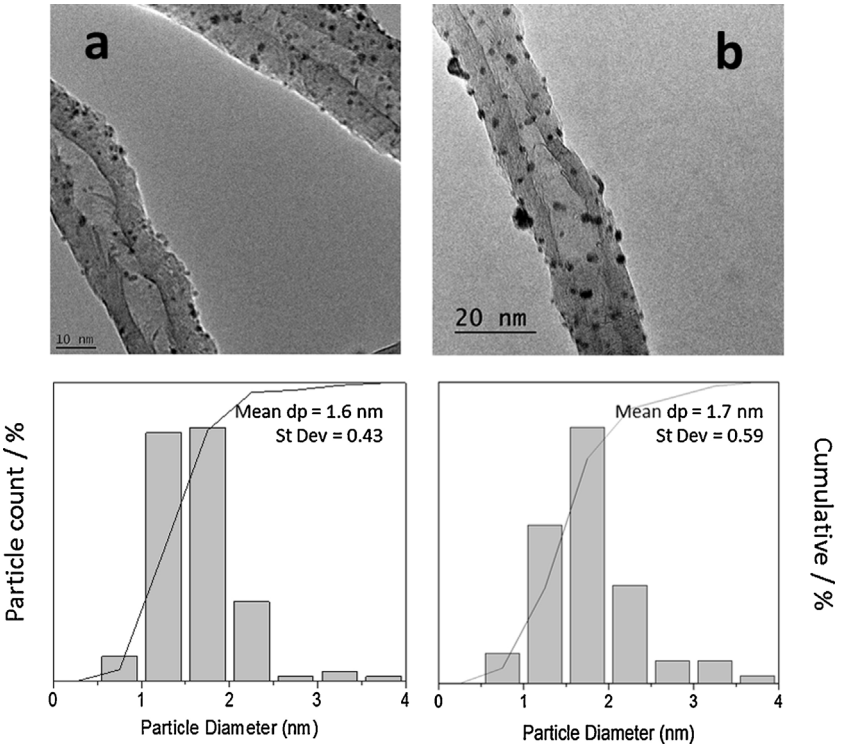


**Fig. 4.** TEM images and particle size histograms of 7 wt% Ru/CNT catalysts (a) Commercial CNT and (b) Graphitised CNT at 2070 K. Particle size distributions are calculated from different locations measuring between ~100 nanoparticles.

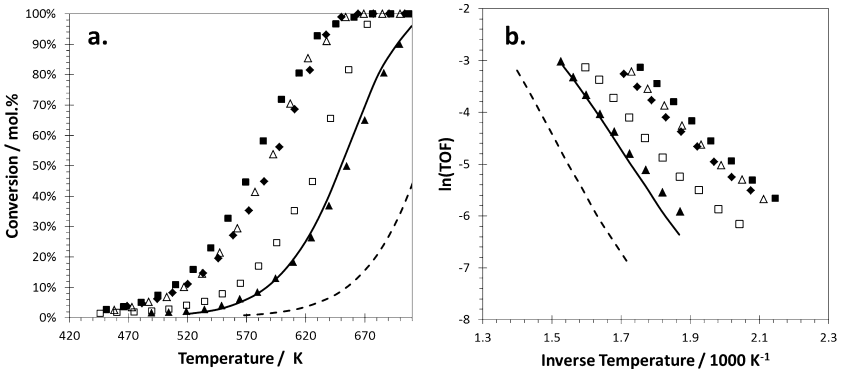


**Fig. 5.** (a) Ammonia decomposition conversion as a function of reaction temperature showing the synergetic effect of graphitization of the CNT support and addition of Cs promoter in Ru catalysts (b) Arrhenius' plot (▲) 7 wt% Ru/graphitized CNT, (■) 7 wt% Ru 4 wt% Cs/graphitized CNT, (△) 7 wt% Ru 10 wt% Cs/graphitized CNT, (♦) 7 wt% Ru 20 wt% Cs/graphitized CNT and (□) 7 wt% Ru 30 wt% Cs/graphitized CNT. Dashed line: 7 wt% Ru/CNT and solid line: 7 wt% Ru 4 wt% Cs/CNT for comparison. Reaction conditions are detailed in the experimental section.

**Table 2**
Effect of CNT's graphitization and cesium loading on 7 wt% Ru/CNT catalysts for the decomposition of ammonia reaction.

| Support | Cesium loading/wt% | Cs/Ru ratio | Ru average particle size[a]/nm | CO adsorbtion[b]/mol CO $g^{-1}$ | TOF @600 K[c]/$mol_{NH3}$ $mol^{-1}{}_{Ru}$ $h^{-1}$ | Activation energy/kJ $mol^{-1}$ |
|---|---|---|---|---|---|---|
| Commercial CNT | 0 | – | 1.6 | 3.0 | 6.5 | 96.7 |
| Commercial CNT | 4 | 0.6 | 1.6 | 2.8 | 41.4 | 78.6 |
| Commercial CNT | 20 | 2.8 | 2.0 | 2.8 | 154.4 | 59.3 |
| Graphitized CNT | 0 | – | 1.6 | 2.3 | 48.9 | 67.6 |
| Graphitized CNT | 4 | 0.6 | 1.7 | 2.2 | 242.3 | 53.5 |
| Graphitized CNT | 10 | 1.4 | 2.1 | 3.0 | 207.0 | 49.5 |
| Graphitized CNT | 20 | 2.8 | 2.4 | 1.1 | 176.4 | 49.6 |
| Graphitized CNT | 30 | 4.6 | 2.6 | 1.4 | 122.4 | 61.7 |

[a] Average particle size determined by TEM.
[b] CO chemisorption at 310 K.
[c] Reaction conditions are detailed in the experimental section.

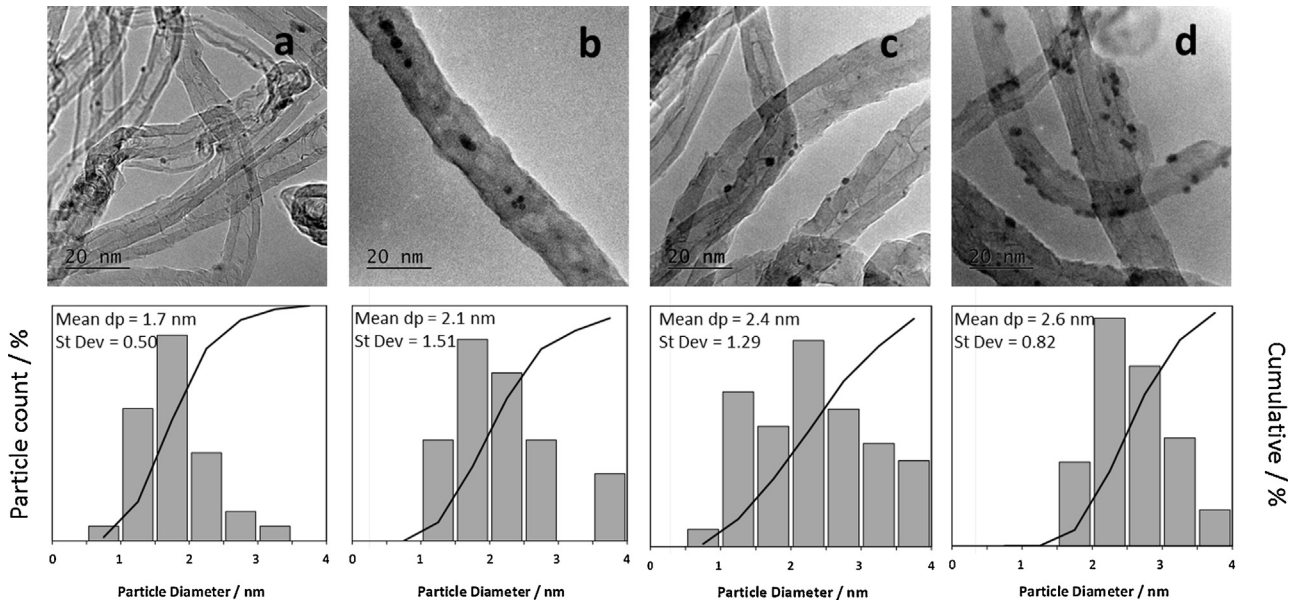


**Fig. 6.** TEM images and particle size histograms of Cs-promoted 7 wt% Ru/graphitized CNT catalysts (a) 4 wt% Cs, (b) 10 wt% Cs, (c) 20 wt% Cs and (d) 30 wt% Cs. Particle size distributions are calculated from different locations measuring between ~100 nanoparticles.

other hand, cesium located on the surface of ruthenium blocks the access of ammonia to the ruthenium active sites, having a detrimental effect on the overall activity. The volcano curve on the effect of cesium loading on the reaction rate is the manifestation of this double effect (Fig. 7).

The different optimum Cs/Ru molar ratio of the CNT and the graphitized CNT supports offers insights about the actual role of promoter, support and their synergetic effect. Although graphitization of the CNT is likely to modify the relative heat of adsorption of the promoter on the ruthenium and the support surface, cesium does not seem to preferentially adsorb on the ruthenium surface on the graphitized CNT catalysts compared to the same catalyst with the commercial CNT support as suggested by CO chemisorption analyses (Table 2). Similar amounts of CO are chemisorbed in all the catalytic systems, with graphitized and commercial CNT supports, suggesting a similar exposure of ruthenium metallic surface. The differences are related to the slight variations in ruthenium particles size and the coverage of the ruthenium nanoparticles by cesium, especially at high cesium loadings (>20 wt%) [10].

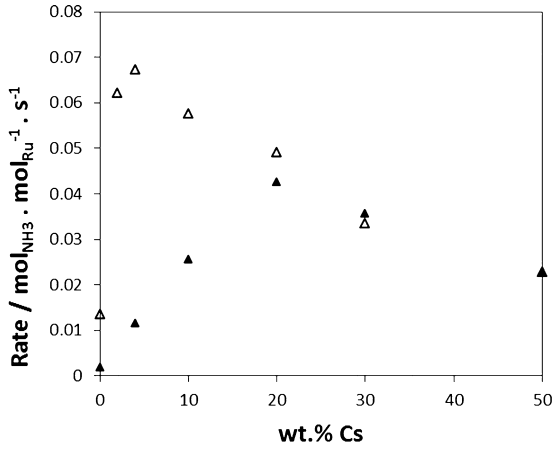


**Fig. 7.** Effect of cesium loading on the ammonia decomposition rate of reaction at 600 K using 7 wt% Ru/CNT catalysts (▲) Commercial CNT (△) graphitized-CNT at 2070 K. Reaction conditions are detailed in the experimental section.

The degree of electronic modification of ruthenium by the presence of cesium can be elucidated by temperature programmed reduction analyses (Fig. 8). Ruthenium particles present the same reduction temperature at ~440 K when supported in both commercial and graphitized CNT in the absence of cesium which suggests similitudes on particle size and metal-support interaction. The reduction temperature and integrated area of this peak (values on Table 3) increase as the cesium loading increases due to the simultaneous reduction of the ruthenium and the cesium located on its surface [10].

The shift of the ruthenium reduction temperature as the cesium loading increases suggests the simultaneous electronic modification of both elements when in contact to each other. While cesium-only supported on CNT does not reduce below ~600 K, the ruthenium's capability of dissociating hydrogen [18] allows the reduction of cesium on direct contact with ruthenium at considerably lower temperatures [10]. Graphitization of the CNT support facilitates the hydrogen spillover to the surrounding area, allowing the reduction of cesium in the ruthenium proximity which is speculated to correspond to the reduction peak ~380 K. In this way, ruthenium supported on graphitized CNT is electronically modified simultaneously by the cesium located in its surface and the cesium located in its close proximity.

The high electron conductivity of the graphitized CNT reciprocally allows the electronic modification of the ruthenium sites by the cesium situated by this wide surrounding area (distance modification), developing activity at lower reaction temperatures. This promotional effect results in a higher electron density in the ruthenium particles reflected in lower activation energy of 53.5 kJ mol$^{-1}$ compared to the 78.6 kJ mol$^{-1}$ achieved with the equivalent Ru-Cs system in commercial CNT (Cs/Ru molar ratio of 0.6).

An increase of the Cs/Ru ratio decreases the number of ruthenium active sites accessible to the reaction due to cesium deposition on its surface, which is reflected in a decrease of the amount of CO chemisorbed (Table 2). While this is beneficial in the commercial CNT catalyst as only the cesium located in the ruthenium surface has a promotional effect, small amounts of cesium are enough to achieve the necessary electronic modification of ruthenium by distance promotion. Consequently, a Cs/Ru molar ratio loading above 0.6, decreases the activity of the Ru/graphitized CNT system.

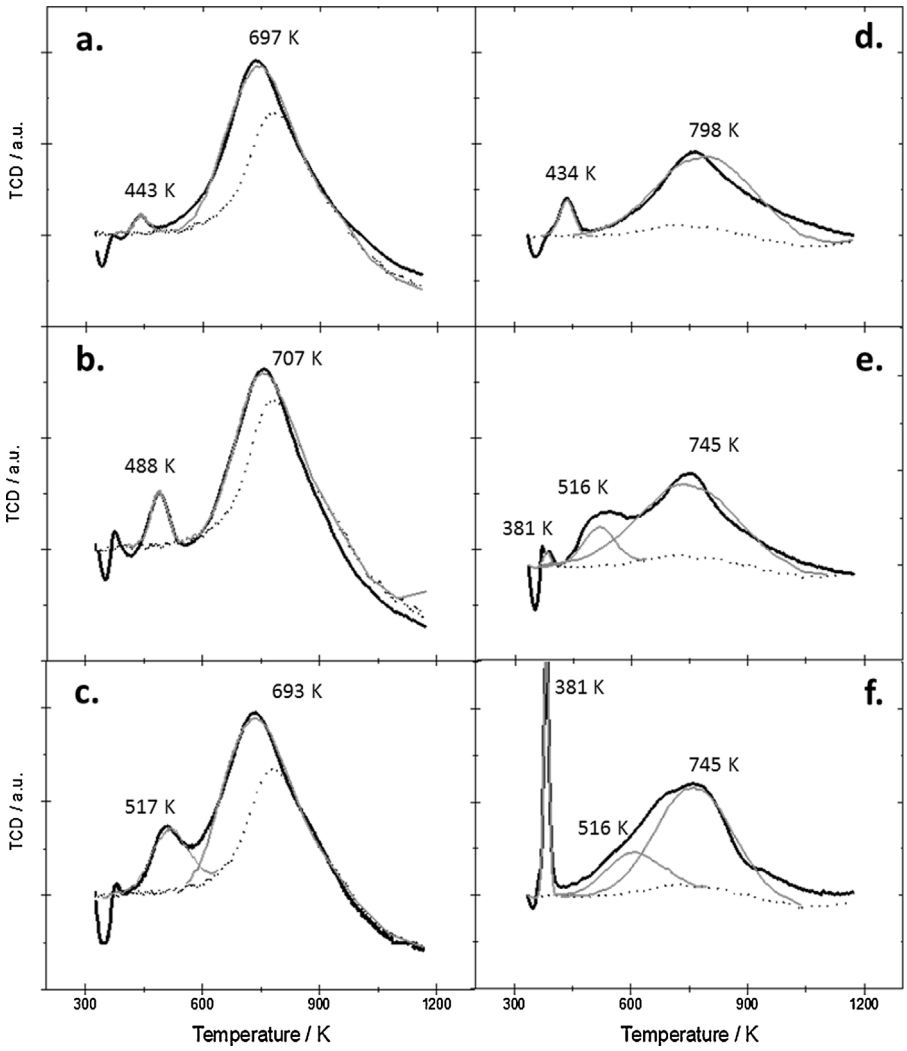


**Fig. 8.** Temperature programme reduction of (a) 7 wt% Ru/CNT, (b) 7 wt% Ru 4 wt% Cs/CNT, (c) 7 wt% Ru 10 wt% Cs/CNT, (d) 7 wt% Ru/graphitised CNT, (e) 7 wt% Ru 4 wt% Cs/graphitised CNT and (f) 7 wt% Ru 10 wt% Cs/graphitised CNT.

**Table 3**
Integration of peaks in TPR analyses shown in Fig. 8.

| | Catalyst | Peak 1 | | Peak 2 | |
|---|---|---|---|---|---|
| | | Peak Temp/K | $H_2$ consumed/mmol $g^{-1}$ | Peak Temp/K | $H_2$ consumed/mmol $g^{-1}$ |
| Fig. 4a | 7 wt% Ru 0 wt% Cs/commercial CNT | – | – | 443 | 0.0009 |
| Fig. 4b | 7 wt% Ru 4 wt% Cs/commercial CNT | – | – | 488 | 0.003 |
| Fig. 4c | 7 wt% Ru 10 wt% Cs/commercial CNT | – | – | 517 | 0.008 |
| Fig. 4d | 7 wt% Ru 0 wt% Cs/graphitized CNT | – | – | 433 | 0.0019 |
| Fig. 4e | 7 wt% Ru 4 wt% Cs/graphitized CNT | 378 | 0.0005 | 487 | 0.005 |
| Fig. 4f | 7 wt% Ru 10 wt% Cs/graphitized CNT | 382 | 0.0050 | 517 | 0.008 |

## 4. Conclusions

In ruthenium-based catalysts, a highly conductive support allows the "distance" promotion by electron donating elements such as cesium without blocking the access to the active sites. This synergetic effect facilitates the development of low temperature activity toward ammonia decomposition providing guidelines for further catalyst design and the development of bi-metallic systems. Specifically, core-shell nanoparticles might be capable of intrinsically modifying the ruthenium's electronic properties to reduce the use of this scare and expensive metal or even replace it. The feasibility of ammonia as large-scale hydrogen storage chemical system and its capability of producing hydrogen on-demand at suitable temperatures for fuel cell systems rely on this success.

## Acknowledgments

The authors would like to acknowledge the UK Engineering and Physical Science Research Council (grant number EP/K016334/1) for funding, the DTC in the Centre for Sustainable Chemical Technologies (grant number EP/G03768X/1) for AKH's studentship and the Research Catalysis Group at Harwell (RCaH) for access to the TEM microscopy facilities.

## References


[1] I.P.o.C. Change, Fifth Assessment report: Climate Change (AR5), 2013.
[2] US Department of Energy Targets for Onboard Hydrogen Storage Systems for Light-Duty Vehicles September, 2009.
[3] A. Klerke, C.H. Christensen, J.K. Norskov, T. Vegge, Ammonia for hydrogen storage: challenges and opportunities, J. Mater. Chem. 18 (2008) 2304–2310.
[4] A. Boisen, S. Dahl, J.K. Norskov, C.H. Christensen, Why the optimal ammonia synthesis catalyst is not the optimal ammonia decomposition catalyst, J. Catal. 230 (2005) 309–312.
[5] M.C.J. Bradford, P.E. Fanning, M.A. Vannice, Kinetics of NH3 decomposition over well dispersed Ru, J. Catal. 172 (1997) 479–484.
[6] F.R. Garcia-Garcia, L. Torrente-Murciano, D. Chadwick, K. Li, Hollow fibre membrane reactors for high H-2 yields in the WGS reaction, J. Membr. Sci. 405 (2012) 30–37.
[7] F. Schuth, R. Palkovits, R. Schlogl, D.S. Su, Ammonia as a possible element in an energy infrastructure: catalysts for ammonia decomposition, Energy Environ. Sci. 5 (2012) 6278–6289.
[8] A. Klerke, S.K. Klitgaard, R. Fehrmann, Catalytic ammonia decomposition over ruthenium nanoparticles supported on nano-titanates, Catal. Lett. 130 (2009) 541–546.
[9] R.Z. Sorensen, A. Klerke, U. Quaade, S. Jensen, O. Hansen, C.H. Christensen, Promoted Ru on high-surface area graphite for efficient miniaturized production of hydrogen from ammonia, Catal. Lett. 112 (2006) 77–81.
[10] A.K. Hill, L. Torrente-Murciano, In-situ H-2 production via low temperature decomposition of ammonia: Insights into the role of cesium as a promoter, Int. J. Hydrog. Energy 39 (2014) 7646–7654.
[11] R. Andrews, D. Jacques, D. Qian, E.C. Dickey, Purification and structural annealing of multiwalled carbon nanotubes at graphitization temperatures, Carbon 39 (2001) 1681–1687.
[12] A.C. Ferrari, J. Robertson, Interpretation of Raman spectra of disordered and amorphous carbon, Phys. Rev. B 61 (2000) 14095–14107.
[13] H.P. Boehm, Surface oxides on carbon and their analysis: a critical assessment, Carbon 40 (2002) 145–149.
[14] F. Rodriguez-Reinoso, The role of carbon materials in heterogeneous catalysis, Carbon 36 (1998) 159–175.
[15] W.Q. Zheng, J. Zhang, B. Zhu, R. Blume, Y.L. Zhang, K. Schlichte, R. Schlogl, F. Schuth, D.S. Su, Structure-function correlations for Ru/CNT in the catalytic decomposition of ammonia, ChemSusChem 3 (2010) 226–230.
[16] J.W. Mintmire, C.T. White, Electronic and structural properties of carbon nanotubes, in: M. Endo, S. Iijima, M.S. Dresselhaus (Eds.), Carbon Nanotubes, Pergamon, Oxford, 1996, pp. 37–46.
[17] D. Mattia, M.P. Rossi, B.M. Kim, G. Korneva, H.H. Bau, Y. Gogotsi, Effect of graphitization on the wettability and electrical conductivity of CVD-carbon nanotubes and films, J. Phys. Chem. B 110 (2006) 9850–9855.
[18] B. Fastrup, On the interaction of N-2 and H-2 with Ru catalyst surfaces, Catal. Lett. 48 (1997) 111–119.

reveal the strong interaction of the cesium promoter with both the ruthenium and the carbon nanotubes support; cesium is partially located on the surface of the ruthenium where it undergoes partial reduction between 450 and 570 K in parallel with the ruthenium reduction, acting as a powerful electron donor. However, an excess of cesium can have a detrimental steric effect, making the ruthenium active sites inaccessible.

## Acknowledgments

The authors would like to acknowledge the UK Engineering and Physical Sciences Research Council (grant number EP/K016334/1) for funding, the DTC in the Centre for Sustainable Chemical Technologies (grant number EP/G03768X/1) for AKH's studentship and the Research Catalysis Group at Harwell (RCaH) for access to the TEM microscopy facilities.

## REFERENCES

[1] Schlapbach L, Zuttel A. Hydrogen-storage materials for mobile applications. Nature 2001;414:353–8.
[2] Suh MP, Park HJ, Prasad TK, Lim DW. Hydrogen storage in metal-organic frameworks. Chem Rev 2012;112:782–835.
[3] Dillon AC, Heben MJ. Hydrogen storage using carbon adsorbents: past, present and future. Appl Phys A-Mater Sci Process 2001;72:133–42.
[4] Satyapal S, Petrovic J, Read C, Thomas G, Ordaz G. The US Department of Energy's National Hydrogen Storage Project: progress towards meeting hydrogen-powered vehicle requirements. Catal Today 2007;120:246–56.
[5] Klerke A, Christensen CH, Norskov JK, Vegge T. Ammonia for hydrogen storage: challenges and opportunities. J Mater Chem 2008;18:2304–10.
[6] Sorensen RZ, Hummelshoj JS, Klerke A, Reves JB, Vegge T, Norskov JK, et al. Indirect, reversible high-density hydrogen storage in compact metal ammine salts. J Am Chem Soc 2008;130:8660–8.
[7] Schuth F, Palkovits R, Schlogl R, Su DS. Ammonia as a possible element in an energy infrastructure: catalysts for ammonia decomposition. Energy Environ Sci 2012;5:6278–89.
[8] Boisen A, Dahl S, Norskov JK, Christensen CH. Why the optimal ammonia synthesis catalyst is not the optimal ammonia decomposition catalyst. J Catal 2005;230:309–12.
[9] Bradford MCJ, Fanning PE, Vannice MA. Kinetics of $NH_3$ decomposition over well dispersed Ru. J Catal 1997;172:479–84.
[10] Tsai W, Weinberg WH. Steady-state decomposition of ammonia on the Ru (001) surface. J Phys Chem 1987;91:5302–7.
[11] Garcia-Garcia FR, Guerrero-Ruiz A, Rodriguez-Ramos I. Role of B5-type sites in Ru catalysts used for the $NH_3$ decomposition reaction. Top Catal 2009;52:758–64.
[12] Ganley JC, Thomas FS, Seebauer EG, Masel RI. A priori catalytic activity correlations: the difficult case of hydrogen production from ammonia. Catal Lett 2004;96:117–22.
[13] Yin SF, Xu BQ, Zhou XP, Au CT. A mini-review on ammonia decomposition catalysts for on-site generation of hydrogen for fuel cell applications. Appl Catal A-Gen 2004;277:1–9.
[14] Rossetti I, Pernicone N, Forni L. Promoters effect in Ru/C ammonia synthesis catalyst. Appl Catal A-Gen 2001;208:271–8.
[15] Larichev YV, Shlyapin DA, Tsyrul'nikov PG, Bukhtiyarov VI. Comparative study of rubidium and cesium as promoters in carbon-supported ruthenium catalysts for ammonia synthesis. Catal Lett 2008;120:204–9.
[16] Rossetti I, Mangiarini F, Forni L. Promoters state and catalyst activation during ammonia synthesis over Ru/C. Appl Catal A-Gen 2007;323:219–25.
[17] Rarog-Pilecka W, Szmigiel D, Kowalczyk Z, Jodzis S, Zielinski J. Ammonia decomposition over the carbon-based ruthenium catalyst promoted with barium or cesium. J Catal 2003;218:465–9.
[18] Garcia-Garcia FR, Torrente-Murciano L, Chadwick D, Li K. Hollow fibre membrane reactors for high H-2 yields in the WGS reaction. J Membr Sci 2012;405:30–7.
[19] Klerke A, Klitgaard SK, Fehrmann R. Catalytic ammonia decomposition over ruthenium nanoparticles supported on nano-titanates. Catal Lett 2009;130:541–6.
[20] Sorensen RZ, Klerke A, Quaade U, Jensen S, Hansen O, Christensen CH. Promoted Ru on high-surface area graphite for efficient miniaturized production of hydrogen from ammonia. Catal Lett 2006;112:77–81.
[21] Huang DC, Jiang CH, Liu FJ, Cheng YC, Chen YC, Hsueh KL. Preparation of Ru-Cs catalyst and its application on hydrogen production by ammonia decomposition. Int J Hydrogen Energy 2013;38:3233–40.
[22] Shitova NB, Dobrynkin NM, Noskov AS, Prosvirin IP, Bukhtiyarov VI, Kochubei DI, et al. Formation of Ru-M/Sibunit catalysts for ammonia synthesis. Kinet Catal 2004;45:414–21.
[23] Rarog-Pilecka W, Miskiewicz E, Jodzis S, Petryk J, Lomot D, Kaszkur Z, et al. Carbon-supported ruthenium catalysts for $NH_3$ synthesis doped with caesium nitrate: activation process, working state of Cs-Ru/C. J Catal 2006;239:313–25.
[24] Anderson EE, Zumwalt LR, Wessman GL. Fission product trapping-sorption of cesium by activated charcoal, Nucl Sci Eng 1962;12:106.
[25] Rarog-Pilecka W, Miskiewicz E, Szmigiel D, Kowalczyk Z. Structure sensitivity of ammonia synthesis over promoted ruthenium catalysts supported on graphitised carbon. J Catal 2005;231:11–9.
[26] Kobayash M, Shirasak T. Chemisorption of CO on ruthenium metals and ruthenium-silica catalysts. J Catal 1973;28:289–95.
[27] Fastrup B. On the interaction of N-2 and H-2 with Ru catalyst surfaces. Catal Lett 1997;48:111–9.